Structure-function relationships of acene based organic semiconductors for use in organic field-effect transistors and organic photovoltaic devices.

A DISSERTATION SUBMITTED TO THE FACULTY OF THE GRADUATE SCHOOL OF THE UNIVERSITY OF MINNESOTA BY

Lafe Joseph Purvis

IN PARTIAL FUFILLMENT OF THE REQUIREMENTS FOR THE DEGREE OF DOCTOR OF PHILOSOPHY

Advisor: Christopher J. Douglas

July 2018

Lafe Joseph Purvis

THE UNIVERSITY OF MINNESOTA

First I need to thank Prof. Chris Douglas for his support and guidance during my graduate career at the University of Minnesota. Chris thank you for helping me acquire a better understanding of organic chemistry and allowing me to pursue my interests which have lead in rather unexpected directions. You pushed me to take advantage of all opportunity to enhance my graduate education and for that I will always be grateful.

Thank you to Micheal Toney, the entire Toney group, and Stanford Synchrotron Radiation Lightsource for hosting me at SLAC for 6 months and teaching me new X-ray characterization techniques.

I would like to thank all my lab mates for their discussing science, Marvel movies, commiserating over beers and above all their friendship. You have helped make these 5 years fly by.

Finally to my family, there would have been no way for me to accomplish this without your continuous and unwavering support. When everything was going wrong I could always find the support I need in you. Thank you.

Abstract:

The ability to readily synthesize derivatives of semi-conducting organic molecules through iterative synthesis allows for the facial tuning of both electron and physical properties. This has led to their use in devices such as field-effect transistors, light emitting diodes, and photovoltaics, bringing organic devices from the bench top to everyday use. Acenes, molecules consisting of annulated benzenes, have garnered interest for use in both single-crystals and thin films devices. However, if organic semiconductors (OSCs) are ever to compete with inorganic semiconductors, a complete structure function relationship (SFR) is required. This will require the development of efficient synthetic strategies, evaluation of solid-state packing, and device performance. Charge transport in OSCs is greatly affected by HOMO/LUMO energies of the molecule, solid state molecular packing, and thin film morphology. Through functionalization of the acene core, HOMO/LUMO energies can be modified yielding n-type (electron-acceptor) or p-type (electron-donating) materials. However, the addition of functional groups to acenes can also drastically alter solid-state packing resulting in new solid-state morphologies which can profoundly affect device efficiency. To vertically advance the field of organic electronics a complete understanding of SFR of new OSC must be determined in order to allow for the rational design of the next generation of OSC molecules. Over the course of my research I have synthesized two modified acene system to study SFRs of organic semiconductors: asymmetrically substituted diarylindenotetracenes (ASIs) and functionalized rubrenes.

Derivatives of ASIs containing either electron donating or electron withdrawing groups were synthesized and their electronic properties were studied using UV/Visible

light spectroscopy, fluorescence spectroscopy, and cyclic voltammetry (CV). Stability of these new OSC was determined by thermogravimetric analysis (TGA) and differential scanning calorimetry (DSC). To examine the solid-state packing, single crystals of ASIs were grown and crystal morphologies were determined via single-crystal X-ray diffraction experiments. Organic photovoltaic devices were prepared using four ASI derivatives as the active layer n-type material and the electronic properties were determined via UV/Visible light spectroscopy, fluorescence spectroscopy, and OPV performance was measured via I-V curves. To correlate thin film morphology and OPV performance solid-state characterization was performed utilizing atomic force microscopy (AFM), grazing incidence wide-angle X-ray scattering (GIWAXS) and near-edge X-ray absorption fine structure spectroscopy (NEXAFS). With both the electronic and physical properties of ASIs determined correlations between ASI molecular structure, thin film morphologies and OPV device performance could be made. Through our study of ASIs we have advanced the field of OSC research and increased our understanding of SFRs of n-type semiconductors.

Two different studies were done to examine the effect of functionalization on the p-type semiconductor rubrene. First, the effect of fluorination on the solid-state packing of rubrene derivatives was studied. Several fluorinated rubrene derivatives were synthesized and single crystals were grown for single-crystal X-ray experiments to examine changes in molecular solid-state packing. By closely studying both inter and intramolecular interactions in each crystal we found that intermolecular interaction, and specifically C–F···X intermolecular interactions, are a major contributor to crystal packing and molecular

orientation in the solid state. Second, to study the effect of nitrogen substitution on both electronic and physical properties of rubrene, a synthetic strategy was developed to prepare 5,6,11,12-tetraphenylnaphtho [2,3-g] quinoline, azarubrene. The total synthesis of this rubrene derivative is still in progress.

Table of content:

List of Figures

Chapter 3:

Chapter 6:

List of Schemes:

List of Tables:

Chapter 2: Page

Chapter 3:

List of Abbreviations:

ADT	Anthradithiophene
AFM	Atomic force micrsocopy
Ag	Silver
AgCl	Silver chloride
$AlCl_3$	Aluminum chloride
Al_2O_3	Aluminum oxide
B_2O_3	Boron trioxide
$BF_3{\cdot}OEt_2$	Boron trifluoride diethyl etherate
BHJ	Bulk heterojunction
BONS	Bicontinuous-ordered nanostructure solar cells
CAM	Cerium ammonium molybdate
CV	Cyclic voltammatry
cm	Centimeters
C–H–π	Carbon hydrogen–pi bonding
CoF_3	Cobalt (III) fluoride
D	Days
DAP	Diaminopentacene
DCM	Dichloromethane
DDQ	2,3-dichloro-5,6-dicyano-1,4-benzoquinone

DFT	Density-functional theory
DHDAP	Dihydrodiaminopentacene
DHTAP	Dihydrotetraminopentacene
DSC	differential scanning calorimetry
E	Energy
EA	Electron affinity
Et	Ethyl
EtAc	Ethyl acetate
eV	Electron Volts
ESI	Electrospray ionization
Fc	Ferrocene
$FeCl_3$	Iron (III) chloride
FET	Field-effect transistor
FF	Fill Factor
g	grams
GC-MS	Gas chromatography mass spectrometry
GC-QTOF	Gas chromatography quaternary time-of-flight
GIWAXS	Grazing incident wide-angle X-ray Scattering
H_2SO_4	Sulfuric acid

h	Hours
HCl	Hydrochloric acid
HI	Hydroiodic acid
HOMO	Highest occupied molecular orbital
HRMS	High resolution mass spectrometry
Hz	Hertz
i-Pr	*Iso*propyl
IE	Ionization energy
IP	Ionization potential
IR	Infrared spectroscopy
ITO	Indium Tin Oxide
J_{sc}	Short-circuit current
K_2CO_3	Potassium carbonate
k	Boltzmann constant
keV	Kiloelectron Volts
LED	Light-emitting diode
LRMS	Low resolution mass spectrometry
LR-TDDFT	Linear response time-dependent density-functional theory
LUMO	Lowest unoccupied molecular orbital
M	Molarity
Me	Methyl

$MeSO_3H$	Methanesulfonic acid
MHz	Megahertz
min	Minutes
mL	Milliliter
mmol	Millimole
$MoCl_5$	Molybdenum(V) chloride
NaCl	Sodium chloride
NBO	Natural bond orbital
NEXAFS	Near-edge X-ray absorption fine structure
NIR	Near infrared radiation
$BF_3 \cdot Et_2O$	Boron trifluoride diethyl etherate
*n*Bu	Butyl
n-BuLi	Butyl lithium
$NaHCO_3$	Sodium bicarbonate
nm	Nanometers
NMe_2	*N*,*N*-dimethyl amine
NPA	Natural population analysis
ODCB	Orthodichlorobenzene
OFET	Organic field-effect transistors
OLED	Organic light-emitting diode
OMe	Methoxy

OPV	Organic photovoltaic
OSC	Organic semiconductor
OTS	Octadecyltrichlorosilane
Ox	Oxidation
PAH	Polycyclicaromatic hydrocarbons
PCBM	Phenyl-C_{61}-butyric acid methyl ester
PCE	Power conversion efficiency
PCl_5	Phosphorus pentachloride
PDI	perylene diimide
$PdCl_2$(dppf)	[1,1'-bis(diphenylphodphino)ferrocene]palladium(II) dichloride
$PdCl_2(PPh_3)_2$	Bis(triphenylphosphinepalladium(II) dichloride
PEN	Pentacene
PEPPSI-IPR™	[1,3-Bis(2,6-Diisopropylphenyl)imidazole-2-ylidene](3-chloropyridyl)palladium(II) dichloride
$PhNO_2$	Nitrobenzene
PIFA	[Bis(trifluoroacetoxy)iodo]benzene

P_{max}	Maximum power
$POCl_3$	Phosphoryl trichloride
ppm	Parts per million
PVT	Physical vapor transport
PVD	Physical vapor deposition
Red	Reduction
r.t.	Room temperature
SFR	Structure-function relationship
SPR	Structure-property relationship
$SnCl_4$	Tin(IV) chloride
$SnCl_2$	Tin(II) chloride
T	Temperature
TAP	Tetraminopentacene
tBu	*tert*-Butyl
TCPS	Tricyclopropyl
TEA	Triethylamine
TES	Triethylsilyl
TFA	Trifluoroacetic acid
TGA	Thermal gravimetric analysis
THF	Tetrahydrofuran
TIPS	Tri-*iso*propylsilyl
TIBS	Tir-*iso*butyl

TLC	Thin layer chromatography
TMS	Trimethylsilyl
UV	Ultraviolet
V	Volts
V_{oc}	Open-circuit voltage
Vis	Visible
XRD	X-ray diffraction
1–D	One-Dimensional
^{1}H NMR	Hydrogen-1 nuclear magnetic resonance
^{13}C NMR	Carbon-13 nuclear magnetic resonance
^{19}F NMR	Fluorine-19 nuclear magnetic resonance
2–D	Two–Dimensional
λ_{max}	Lambda maximum
Å	Angström
η	Power conversion efficiency
μAMP	Microamps
Φ	Fluorescence quantum yield
^{o}C	Degrees Celsius
ν	Wavenumber

Chapter 1: General Introduction

1.1 Applications of organic electronics:

Ever since polythiophene was employed as the semiconducting layer of a field-effect transistor back in 1986 the field of organic electronics has exploded to encompass an enormous range of applications.[1] Organic electronics have the potential for a wide range of application across many fields; from sensors for medical and defense technologies, to photovoltaics for energy production. Additionally, organic electronics have several advantages over their inorganic counter parts including the potential for the production of flexible, lightweight, low cost, and easily processed devices.[2] The vast potential of organic electronics has resulted in greater focus from both the academic and industrial research communities in an attempt to rapidly advance the field.[3]

Organic electronic devices have already seen commercial success as both displays and lighting sources utilizing the fluorescence properties of organic molecule to produces highly efficient organic light emitting diodes (OLED).[4] This is, in large part, due to the ability to design organic molecules with the desired electronic and physical properties, i.e. the desired color of OLED. Through the addition of functional groups it is possible to tune the highest occupied molecular orbitals (HOMO) and the lowest unoccupied molecular orbitals (LUMO) energies, solubilities, crystal packing, and solid-state properties. The recent surge in commercial organic electronic devices is due, in large part, to the ease with which organic semiconductors (OSCs) can be tuned to the desired properties via chemical modification. However, there are several reasons for the limited use of OSCs in commercial devices, two critical reasons being the limited stability of OSC molecules and the cost of device fabrication. The limited stability of small molecule OSC are primarily due to

reactivity with oxygen in the air or degradation in the device. Efforts to produce more stable OSCs has relied heavily on modulation of HOMO/LUMO levels via the addition of functional groups. However, the addition of functional groups to an OSC often changes its solid-state packing morphology leading to further, sometime unexpected, changes to device performance.

Overall, the ability to design organic semiconductors with specific electronic properties has resulted in OSCs finding use as organic light emitting diodes (OLED), field-effect transistors (OFET), photovoltaics (OPV), and molecular sensors (**Figure 1**).[3] The development of new and more efficient OSCs is limited by the extent of our knowledge of structure-function relationships in OSC. Therefore, to rapidly develop new and more efficient OSC our understanding of structure function relationships in OSC must improve.

Figure 1.1: Two example of thin film displays using OLED technology[3]

1.2 Structure-function relationships in acene base organic semiconductors

Understanding structure-function relationships allows scientists to predict how the addition of a new functional groups to a molecule will affect the desired function and properties of the final device. As our understanding of SFRs increase, scientists are better able to rationally designed new molecules with the desired properties. To further our understanding of structure-function relationships of OSC, new molecules need to be thoroughly evaluated from the molecular level all the way to the device.

Over the past decades hundreds of acenes derivatives have been synthesized with a wide range of functional groups. The addition of functional groups to a small molecule OSC often results in changes to solubility, crystal structure, stability, and substrate interactions, all of which can affect device performance.[5] While a functional group may be added to make a molecule more electron rich, i.e. alkoxy groups, they also tend to change packing in both the single crystal and the thin film. This altered packing affects both physical and electronic solid-state properties, and therefore OSC performance, usually in unpredictable ways. For example, calculations performed by the Brédas group demonstrated that electron transport efficiency decreases exponentially with π-stacking distance increases in acene OSC. Also, that small changes in molecular alignment can affect both electron and hole transport.[6]

Another way to tune OSC electronic properties in the final device is to alter fabrication conditions. Current fabrication methods of high performing OSC devices do allow for a high level of morphological control but, require large amounts of material and are less scalable, and thereby increasing device cost. One way to significantly reduce the cost of organic electronic devices is to develop OSCs that can be solution processed into

high performance thin films. The addition of functional groups, i.e. alkoxy, amine, alkyl, often improve acene OSC solubility in organic solvents. However, the same functional groups can impact HOMO/LUMO energies and solid-state morphology. In fact, controlling the morphology of solution processed thin films is a major problem yet to be solved.[3,7] As an alternative approach, studies have demonstrated that the addition of cynano, fluoro, methyl, and other functional groups, can affect how an OSC interacts with the substrate, greatly effecting thin film morphology and device performance relative to the parent molecule.[8 9] Therefore, to fully understand the structure-function relationships (SFR) of new OSC molecules full electronic and physical characterization needs to be performed starting at the molecular level and ending with the device. To demonstrate the importance of understanding SFRs in small molecule OSC a brief over view of the SFR of pentacene derivatives will be presented.

1.3 Structure-function relationships in pentacene derivatives

Pentacene is the prototypical small molecule used as an OSC. First used as a small molecule OSC back in the 1960's, pentacene and its derivatives have been extensively studied using a wide variety of functional groups to modify both electronic and physical properties. In the solid-state pentacene stacks in a herringbone packing motif. However, upon the addition of functional groups to the acene core, researchers have been able to modify the solid-state packing. Several groups have prepared derivatives of pentacene to study how the addition of functional groups to this small molecule OSC affects both electronic and physical properties.

The Nuckells groups showed that N-H substitution of pentacenes resulted in molecules that formed highly ordered thin films that were more stable in OFETs than the

parent pentacene, **1.1**, (**Figure 1.2**). Although when the OFET performance was measured, the N-H substituted pentacene derivative demonstrated decreased on/off ratios, 10^3, and hole mobility, from 10^{-3} to 10^{-5} cm^2/Vs, compared to the unsubstituted pentacene.[10 11] From the X-ray diffraction experiments they found that the crystal packing motifs of the N-substituted pentacene derivatives was highly dependent on the solvent system used. XRD experiments of single crystals prepared from DMF showed that compound **1.2** (**Figure 1.2**) formed hydrogen bonds between the N-H substituent and the carbonyl of DMF. However, when single crystals were grown from non-hydrogen bonding solvents compound **1.2** now formed the traditional herringbone packing motif, as seen in pentacene. The hole mobility of compound **1.2** was found to be the lowest of all the N-H pentacene derivatives, 10^{-5}. Just by shifting the substitution location over one benzenoid ring, compound **1.3**, the Nuckells groups was able to increase the hole mobility 100-fold, though still considerably lower than unsubstituted pentacene. Later experiments on thin film morphology of compound **1.3** performed by the Miao group demonstrated that the poor hole mobility was, in large part, due to substrate interactions.[12] By pretreating the SiO_2 substrate with OTS and depositing dihydrodiazapentacene **1.3** at 100 ˚C the hole mobility increased from 10^{-5} to 10^{-1} cm^2/Vs, outperforming **1.2**.

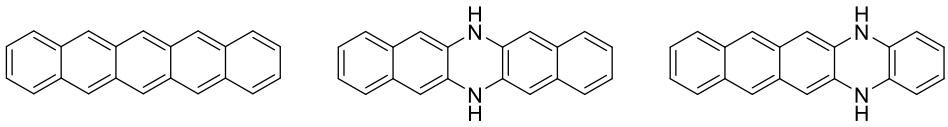

1.1 1.2 1.3

Figure 1.2: Shows, **1.1**) pentacene, and **1.2** and **1.3**) two different N-H substituted pentacene derivatives

The addition of electron withdrawing groups to pentacene allowed the Tokito group to convert the pentacene molecule from a p-type semiconductor to an n-type semiconductor (**Figure 1.3**). By substituting all of the hydrogen of the pentacene, **1.1**, with a more electronegative fluorine, **1.4**, they were able produce OFETs with electron mobility of 0.024 cm^2/Vs. From single crystal X-ray experiments, they found that compound **1.4** still packed in the herringbone packing motif. Interestingly, the much smaller π-π stacking distance, 3.21 Å, was observed in the 1-D direction due to the electron deficient nature of the perfluoropentacene. X-ray diffraction experiments performed on the thin film also showed very similar packing of perfluoropentacene in both the single crystal and thin film with comparable d-spacing.

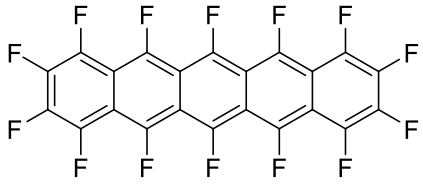

1.4

Figure 1.3: Shows **1.4**) perfluoropentacene

TIPS-pentacene, a well-studied pentacene derivative, was originally designed to increase solubility in organic solvents as well improve π-stacking.[13] However, it was found that not only did the addition of the alkynyl-TIPS functional groups increase solubility, but also drastically changed solid-state molecular packing. Instead of the herringbone packing motif, compound **1.5** (**Figure 1.4**) was found to obtain a 2-D brick packing motif. This change in molecular ordering resulted in a large increase in the hole mobility to around 1 cm^2/Vs.[14] Studies of thin film morphologies later demonstrated a drastic difference in thin film morphology as well. Thin films of unsubstituted pentacene were observed to interact

with the substrate in an edge-on orientation standing on the long axis.[15] With the addition of the TIPS functional groups the molecule now interacted with the substrate via the TIPS group, perfectly aligning the π-system of TIPS-pentacene in the direction of charge transport.[16] Changing the TIPS functional group to a TES functional group (**1.6**) **(Figure 1.4**) resulted in a change of the solid-state packing morphology from 2-D brick to slipped 1-D. As a result, there was a decrease in the alignment of the pentacene backbone in the thin film, resulting in a decreased hole mobility, 10^{-5} cm^2/Vs.[17] [18]

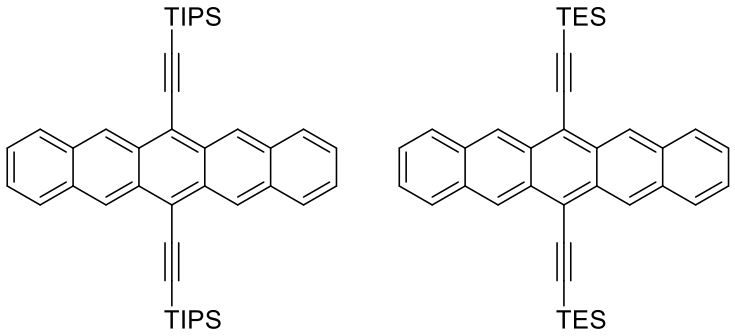

1.5 **1.6**

Figure 1.4: Shows, **1.5**) TIPS-pentacene, **1.6**) TES-pentacene

When the Anthony group converted the end phenyl ring of **1.5** and **1.6** to thiophene functional groups they observed a complete reversal of solid state packing structure-function relationship compared to compounds (**Figure 1.5**). With the addition of the thiophene functional groups, compound **1.7** obtained the slipped 1-D packing motif seen in TES-pentacene while compound **1.8** formed the 2-D brick packing motif of TIPS-pentacene. Also, the hole mobility of TES-anthradithiophene now outperformed the TIPS-anthradithiophine, 1 cm^2/Vs and 10^{-4} cm^2/Vs respectively, due to the improved solid state packing highlighting the importance of proper alignment of the acene core.[19]

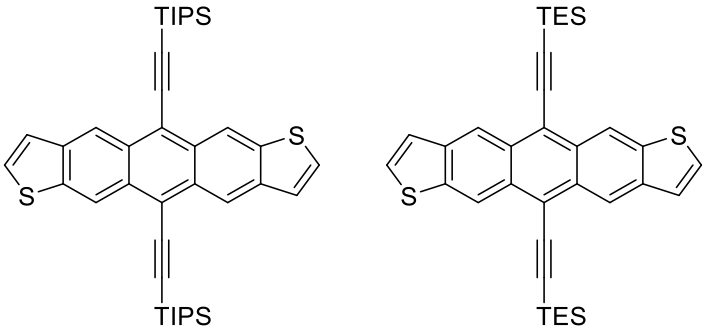

1.7 **1.8**

Figure 1.5: **1.7**) TIPS-anthradithiophene, **1.8**) TES-anthradithiophene

Another example of TIPS-pentacene derivatization performed by the Anthony group found that the addition of cyclic alkoxy groups (**Figure 1.6**) resulted in molecules with increased stability and solubility in organic solvent.[20] Compound **1.10** and **1.11** were also found form a slipped 2-D brick packing motif in the single crystal, similar to TIPS-pentacene, while to compound **1.9** formed a slipped 1-D packing motif with no overlap of the pentacene backbone. The absorbance spectra of compound **1.9** was red-shifted relative to the unsubstituted TIPS-pentacene. This would be expected due to the electron donating nature of alkoxy group. Surprisingly, however, compounds **1.10** and **1.11** were blue-shifted relative to TIPS-pentacene. This indicated that the more rigid alkoxy groups prevented donation of the oxygen lone pair to the pentacene backbone causing a decrease in electron density of the pentacene due to the increased electronegativity of the oxygens. Cyclic voltammetry (CV) experiments of compound **1.11** demonstrated an improved thin film stability, and energy match with the metal substrate, of the TIPS-pentacene derivative on gold.[21] Compared to TIPS-pentacene, when compound **1.11** was used as the donor material in an OPV, it was found that both the efficiencies (η) 0.56 %, and the fill factor (FF) 0.40, had improved due to the increased short-circuit current (J_{sc}) 2.5 mA/cm^2. The improved J_{sc}

of compound **1.11** was determined to be a result of more efficient charge extraction due to improved energy alignments at the interface, resulting from the addition of the dioxolane functional groups.[22]

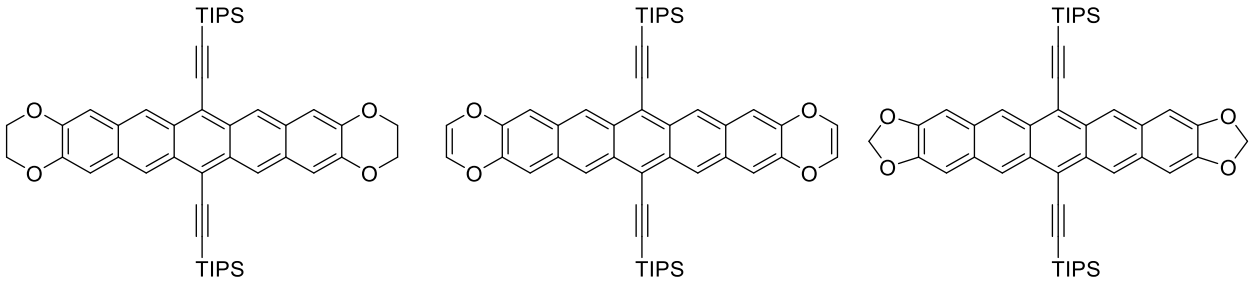

Figure 1.6: Shows the three different alkoxy substituted TIP-pentacene molecules prepared by the Anthony group.

The Malliaras group studied how the addition of electron withdrawing groups to the pentacene core of TIPS-pentacene, compound **1.12**, (**Figure 1.7**) affected crystal packing and charge transport. By substituting hydrogens with either fluorine, bromine, or cyano groups they were able to tune the crystal packing, HOMO/LUMO levels and charge transport. They found that, while symmetric substitution of the cyano functional groups resulted in a 1-D π-stacking motif, symmetric, or asymmetric, substitution of fluorine groups resulted in the same 2-D brick packing motif observed in unsubstituted TIP-pentacene. They also found that the symmetric fluorine substitution of compound **1.12** (**Figure 1.7**) resulted in the smallest interplane spacing at 3.28 Å, and the highest hole mobility of 0.045 cm^2/Vs, whereas compound **1.5**, TIPS-pentacene, hole mobility was found to be 0.001 cm^2/Vs.[23] When grazing incident wide-angle X-ray scattering (GIWAXS) experiments were performed on neat thin films of symmetrically fluorine

substituted compound **1.12**, the crystal structure in the films was found to be the same as the single-crystal.[24] The lack of significant difference in single crystal packing and thin film morphology between the fluorinated TIPS-pentacene derivatives is a result of the TIPS functional group. As previously stated the TIPS group was originally found to help orient the molecule in the thin film. In the single crystal this results in increase π-π interactions and a 2-D brick packing motif. In the thin film TIPS-pentacene interacts with the substrate via the TIPS group maintaining efficient thin film packing resulting in improved device performance.

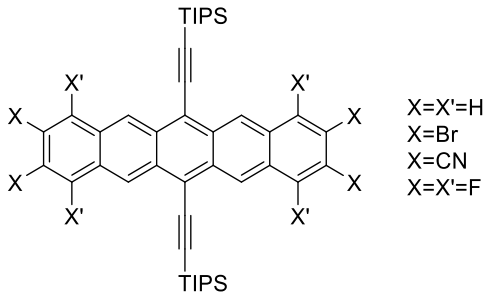

1.12

Figure 1.7: Shows the different sites of functionalization on the TIPS-pentacene core.

Several groups have explored how varying the alkyl group. i.e. from TIPS to TES, TIBS, etc, affects molecular ordering, thin film morphology, and device performance. As discussed above, changing the TIPS group to a TES group can drastically alter the single crystal packing motif. Compounds **1.5** and **1.8** obtained a 2-D brick packing motif while compounds **1. 6** and **1.7** demonstrated slipped 1-D. Previous reports by the Anthony group showed that the addition of trialkylsily functional groups resulted in a sandwich-herringbone packing motif outperforming those that resulted in the 2-D brick packing motif in OPVs.[25] Expanding on these results the Chabynic group performed GIWAXS

experiments, on both neat and bulk-heterojunction (BHJ) thin films, of three different trialkysilyl groups, compounds **1.13**, **1.14**, and **1.15**, (**Figure 1.8**), and a small molecule donor.[26] They first demonstrated that the packing motifs observed in the single-crystal structures of **1.13** and **1.15** were also formed in the neat thin films, 2-D brick and sandwich-herringbone, respectively. Examining the OPV performance of each compound they found that compound **1.15** produced devices with the largest PCE, 0.28 %. The improved OPV performance of compound **1.15** was due to the higher J_{sc}, 0.60 to 0.66 mA/cm^2. When Chabynic and co-workers examine the GIWAXS data for the annealed BHJ thin films of **1.13** they observed the reflections corresponding to single-crystal structures of both the donor and the acceptor **1.13**. For the annealed BHJ thin films of **1.15** they again observed the reflections corresponding to the single-crystal structures of both molecules. The improved J_{sc} was directly related to the improved charge transport efficiency of the sandwich-herringbone packing motif of compound **1.15**. Correlating the OPV performance with thin film X-ray scattering data the Chabynic groups was able to demonstrate that the difference in thin film morphology between **1.13** and **1.15**, and the resulting improved charge transport, led to the enhanced OPV performance.

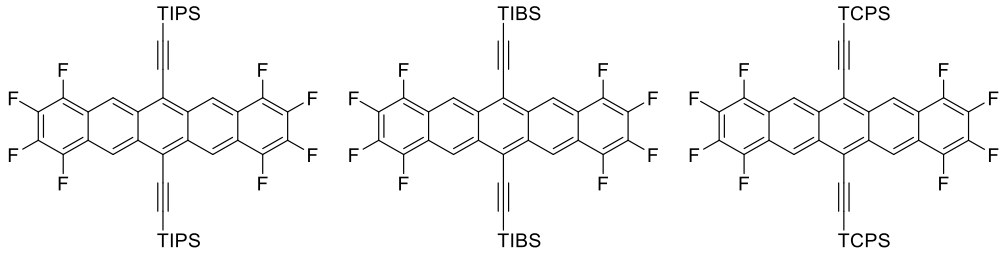

1.13 **1.14** **1.15**

Figure 1.8: Shows the pentacene derivatives studied by the Chabynic group **1.13**) F8TIPS-pentacene, **1.14**) F8TIBS-pentacene, **1.15**) F8TCPS-pentacene.

SFR studies of pentacene derivatives have demonstrated that the addition of functional groups to pentacene result in changes to the electronic, physical and solid-state properties, all of which affect organic electronic device performance. Trialkylsilyl functionalization pentacenes resulted in a drastic change to thin film morphology. By functionalizing the pentacene core of trialkylsilyl-pentacene, it was possible to tune the electronics of the molecules with little affect to the solid-state packing and thin film morphology. Conversely, both the solid-state packing and thin film morphology could be modified by varying the trialkylsilyl functional group with minimal effect on the electronic of the pentacene core. This was due to the fact that trialkylsilyl-pentacene interacts with the substrate via the trialkylsilyl groups dictating packing while not directly affecting the pentacene core.

By thoroughly studying the SFR of pentacene and TIP-pentacene derivatives, a roadmap to the rational design of the next generation of OSC pentacene derivatives was obtained.

To develop the next generation of OSC the same level of detailed studies need to be performed on more OSC small molecules. The greater our understanding of structure-function relationships in new OSC, the faster we can develop the next generation of improved OSC. To that end, I present the study of structure function relationship in acene base organic semiconductors, asymmetrically substituted indenotetracenes and rubrenes.

1.4 References:

(1) Tsumura, A.; Koezuka, H.; Ando, T. *Appl. Phys. Lett.* **1986**, *49*, 1210.

(2) *Org. Elect., Mater., Manufac., and Appl.*; Klauk, H., Ed.; Weinheim : Wiley-VCH: Germany, 2006.

(3) Forrest, S. R. *Nature* **2004**, *428*, 911.

(4) de Mello, J.; Anthony, J.; Lee, S. *Chem. Phys. Chem.* **2015**, *16*, 1099.

(5) Anthony, J. E. *Chem Rev* **2006**, *106*, 5028.

(6) Coropceanu, V.; Cornil, J.; da Silva Filho, D. A.; Olivier, Y.; Silbey, R.; Bredas, J. L. *Chem. Rev.* **2007**, *107*, 926.

(7) Rivnay, J.; Jimison, L. H.; Northrup, J. E.; Toney, M. F.; Noriega, R.; Lu, S.; Marks, T. J.; Facchetti, A.; Salleo, A. *Nat. Mater.* **2009**, *8*, 952.

(8) Dobler, C.; Tönshoff, C.; Bettinger, H. F.; Chassé, T.; Casu, M. B. *J. Phys. Chem. C* **2017**, *121*, 13660.

(9) Wasikiewicz, J. M.; Abu-Sen, L.; Horn, A. B.; Koelewijn, J. M.; Parry, A. V. S.; Morrison, J. J.; Yeates, S. G. *J. Mater. Chem. C* **2016**, *4*, 7309.

(10) Gundlach, D. J.; Lin, Y. Y.; Jackson, T. N.; Nelson, S. F.; Schlom, D. G. *IEEE Electron Device Lett.* **1997**, *18*, 87.

(11) Miao, Q.; Nguyen, T. Q.; Someya, T.; Blanchet, G. B.; Nuckolls, C. *J. Am. Chem. Soc.* **2003**, *125*, 10284.

(12) Tang, Q.; Zhang, D.; Wang, S.; Ke, N.; Xu, J.; Yu, J. C.; Miao, Q. *Chem. Mater.* **2009**, *21*, 1400.

(13) Anthony, J. E.; Brooks, J. S.; Eaton, D. L.; Parkin, S. R. *J. Am. Chem. Soc.* **2001**, *123*, 9482.

(14) Park, S. K.; Jackson, T. N.; Anthony, J. E.; Mourey, D. A. *Appl. Phys. Lett.* **2007**, *91*, 063514.

(15) Nabok, D.; Puschnig, P.; Ambrosch-Draxl, C.; Werzer, O.; Resel, R.; Smilgies, D.-M. *Phys. Rev. B* **2007**, *76*.

(16) Giri, G.; Verploegen, E.; Mannsfeld, S. C.; Atahan-Evrenk, S.; Kim, D. H.; Lee, S. Y.; Becerril, H. A.; Aspuru-Guzik, A.; Toney, M. F.; Bao, Z. *Nature* **2011**, *480*, 504.

(17) Sheraw, C. D.; Jackson, T. N.; Eaton, D. L.; Anthony, J. E. *Adv. Mater.* **2003**, *15*, 2009.

(18) James, D. T.; Frost, J. M.; Wade, J.; Nelson, J.; Kim, J. S. *ACS Nano* **2013**, *7*, 7983.

(19) Payne, M. M.; Parkin, S. R.; Anthony, J. E.; Kuo, C. C.; Jackson, T. N. *J. Am. Chem. Soc.* **2005**, *127*, 4986.

(20) Payne, M. M.; Delcamp, J. H.; Parkin, S. R.; Anthony, J. E. *Org. Lett.* **2004**, *6*, 1609.

(21) Griffith, O. L.; Anthony, J. E.; Jones, A. G.; Shu, Y.; Lichtenberger, D. L. *J. Am. Chem. Soc.* **2012**, *134*, 14185.

(22) Lane, P. A.; Palilis, L. C.; Kushto, G. P.; Kafafi, Z. H.; Purushothaman, B.; Anthony, J. E. *Proc. of SPIE* **2008**, *7052*, 70521J.

(23) Swartz, C. R.; Parkin, S. R.; Bullock, J. E.; Anthony, J. E.; Mayer, A. C.; Malliaras, G. G. *Org. Lett.* **2005**, *7*, 3163.

(24) Sherman, J. B.; Moncino, K.; Baruah, T.; Wu, G.; Parkin, S. R.; Purushothaman, B.; Zope, R.; Anthony, J.; Chabinyc, M. L. *J. Phys. Chem. C* **2015**, *119*, 20823.

(25) Lim, Y.-F.; Shu, Y.; Parkin, S. R.; Anthony, J. E.; Malliaras, G. G. *J. Mater. Chem.* **2009**, *19*, 3049.

(26) Sherman, J. B.; Purushothaman, B.; Parkin, S. R.; Kim, C.; Collins, S.; Anthony, J.; Nguyen, T.-Q.; Chabinyc, M. L. *J. Mater. Chem. A* **2015**, *3*, 9989.

Project 1: Structure-Function Relationships of Asymmetrically Substituted Indenotetracenes: Novel N-type Semiconductor.

Chapter 2: The Synthesis and Characterization Asymmetrically Substituted Indenotetracene: A Novel Electron-Deficient Organic Semiconductor.

2.1 Introduction:

The increasing demand for cheaper, faster, and smaller electronic devices has driven chemists to develop a large number of novel small-molecule organic semiconductors (OSC) resulting in more efficient organic light emitting diodes (OLED), organic photovoltaics (OPV), and organic field-effect transistors (OFET). The discovery of new electron donating, p-type, materials have resulted in steady improvement of OPV efficiency. However, the lack of development of new small-molecule, electron-acceptor, n-type materials, for use in OPVs has hindered the progress of OPV technology.[1] The dearth of n-type materials for OPVs is seen as a major impediment to the further development of OPVs, and large scale energy production. To date, the two primary n-type materials used in OPVs have been perylene diimides (PDI) and fullerenes. Fullerenes and PDIs are both highly efficient electron acceptors due to their high electron affinity and efficient charge transport, however, despite having good solid-state properties that allow for efficient electron transport, these compounds are not ideal materials for OPVs.

Almost all derivatives of both fullerenes and PDIs have poor solubility in organic solvents, limited stability in air or OPVs, and relatively high cost. The poor solubility and limited stability restricts OPV fabrication methods and decreases OPV lifetime. A major drawback of fullerenes is also their poor absorption of light in the visible region. This relative transparency necessitates a thicker absorber layer in order to produce sufficient

light-generated charge carriers (excitons). Although the thicker absorber layer does result in greater exciton generation, it also decreases charge extraction efficiency in device due to the short diffusion length of excitons in the organic material, approximately 10 nm.[2-5] As a result of the properties of PDIs and fullerenes, these material are not seen as commercially viable n-type materials for in OPVs for large scale energy production.

Recently, efforts to overcome the inherent deficiencies of both PDIs and fullerenes have led to the development of several novel, non-fullerene small molecule electron acceptors.[6-12] In 2016 the Chen group reported the development of a new inden-1-ylidene based small molecule electron acceptor which achieved 8 % power conversion efficiency (PCE) in a bulk heterojunction (BHJ) OPV with a polymer donor.[13] The Hou group has also recently reported a record 13 % PCE OPV using a novel, non-fullerene, n-type semiconductor, again in a BHJ OPV with a polymer donor.[14] Through rational design, small molecule, non-fullerene, electron acceptors have the potential to greatly improve OPV performance, by designing new materials for strong visible light absorption, tunable[15] highest occupied molecular orbital (HOMO)/lowest unoccupied molecular orbital (LUMO) energy levels, and improved processability and photostability.[16-18] Among these novel electron acceptors, indene-fused aromatic compounds have shown promise as possible replacements for fullerenes in OPVs. [19-21]

The intrinsic electron deficiency of indene-containing molecules originates from the anti-aromatic 4n π-system. The drive towards aromaticity, a 4n+2 π-system, makes materials containing indenes good electron acceptors. The Plunkett group and Haley group have independently developed new organic n-type materials based on the indene scaffold for use in OPVs.[8,22,23] Corannulenes have also shown the ability to act as an electron

transport material in thin film devices.[21,24] Both the cyclopentane-fused polycyclic aromatic hydrocarbons, indacene, and other indene based materials are well suited as electron accepting material due to the high electron affinity. Indene functionalized electron acceptor have demonstrated LUMOs below -3.5 eV and HOMOs below -5.5 eV, allowing for n-type behavior. Also, these material have demonstrated good solubility in organic solvents, and can be readily derivatized. Recently, the Chen group fabricated OPVs using indene based rubicene derivatives as the electron accepting material which demonstrated a PCE of 3 % and an extremely high V_{oc} of 1.2 V.[25]

Our group previously reported the development of symmetrically substituted indenotetracenes (SSI).[26] Symmetrically substituted indenotetracences were prepared via a Kumada-Corriu coupling between 5,6,11,12-tetrachlorotetracene and a phenyl Grignard containing either an electron donating or an electron withdrawing groups. These conditions resulted in an oxidative cyclization on one side of the tetracene core resulting in the formation of an indene moiety. (**Scheme 2.1**).

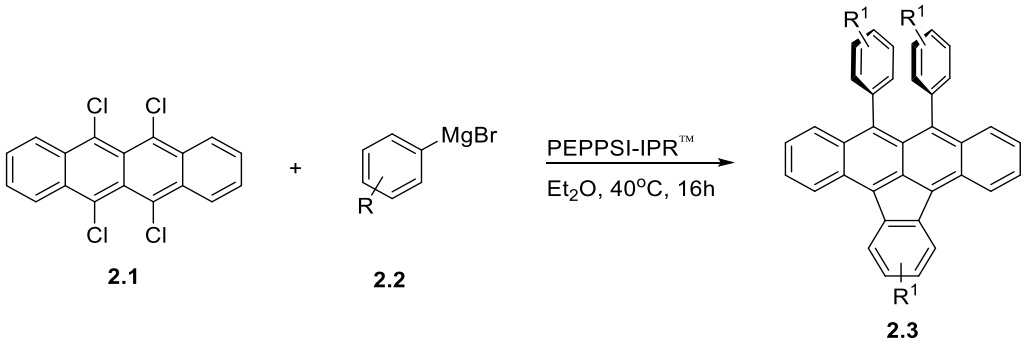

Scheme 2.1: Synthesis of symmetrically substituted diarylindenotetracene via Kumada coupling

To further examine the electronic and physical properties of these molecules, and further our understanding of structure-function relationship, we prepared asymmetrically substituted diarylindenotetracenes (ASI) as a new n-type organic semiconductors.

2.2 Synthesis background:

To allow for rapid diversification, and thorough structure-function relationship studies, a divergent synthetic strategy was employed for the preparation of ASIs. This new synthetic strategy enabled us to quickly synthesize several ASI derivatives. To allow for late stage diversification and rapid derivatization the synthesis of ASIs was designed with two, branching, functionalization points.

The divergent synthetic strategy can be easily seen in the retrosynthetic analysis (**Scheme 2.2**). As shown in **Scheme 2.2** the first disconnection of the ASI to arrive at a 9-chloro-10-phenylindeno[1,2,3-*fg*]tetracene intermediate (**2.5**) and a phenyl Grignard (**2.6**) is accomplished via a Kumada-Corriu cross-coupling. Intermediate **2.5** can be obtain by a disconnection using a oxidative cyclization leading to a 5-chloro-6,11-diphenyltetracene derivative (**2.7**). To arrive at intermediate (**2.9**), 6-chloro-5,12-dione, two sequential disconnections were envisaged. The first, a reductive re-aromatization to arrive at compound **2.8**, and the second being an arylation to compound **2.9**. Finally, to arrive at commercially available starting material two separate Friedel-Crafts acylations can be used. With the first Friedel-Crafts acylation disconnect produces 2-(1-hydoxy-2-naphthoyl) benzoic acid (**2.11**) and the second gives the starting materials phthalic anhydride (**2.13**) and napthalen-1-ol substituted (**2.12**).

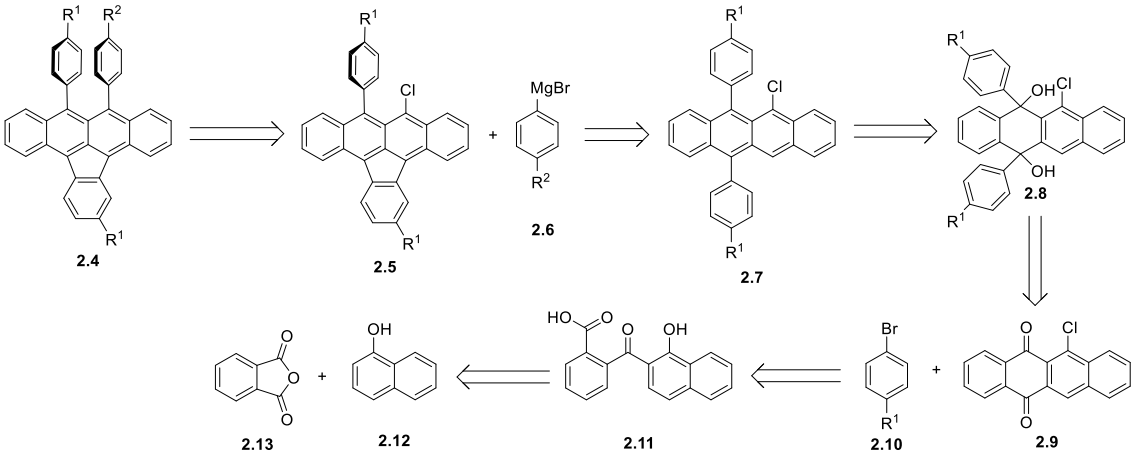

Scheme 2.2: Retrosynthetic route for the divergent synthesis of asymmetrically substituted diarylindenotetracenes

The key synthetic transformation toward the synthesis of the ASI derivatives is the oxidative cyclization which forms the indene ring thereby making the molecule electron deficient (**Scheme 2.3**). To perform that oxidative cyclization, we envisaged using Scholl reaction conditions.

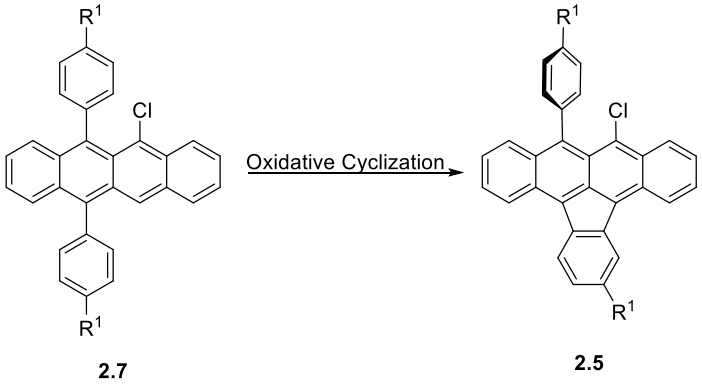

Scheme 2.3: Synthesis of the indene scaffold of the asymmetrically–substituted diarylindenotetracene

The first example of oxidative cyclization of aromatic hydrocarbons was published by Roland Scholl back in 1868 using either arsenic acid or silver oxide.[27-30] In 1873 Dianin achieved a high yielding oxidative coupling of 2-naphthol using the Lewis acid $FeCl_3$.[29] A few decades later, the first example of an intramolecular oxidative coupling was published in 1910 by Scholl and Mansfeld using $AlCl_3$ neat at 140 ˚C.[29] Since then, oxidative aromatic cross-couplings have been accomplished using a wide variety of oxidizing agents, $AlCl_3$, $FeCl_3$, PIFA, CoF_3, $MoCl_5$, or DDQ/$MeSO_3H$, under widely varying conditions. There has been considerable effort expended to determine the mechanism of the Scholl reaction. Currently, two mechanisms are proposed for the Scholl reaction (**Figure 2.1**). The reaction can proceed via either an arenium cationic mechanism if protonation occurs first or a radical-cation if oxidation occurs first, and the products are highly dependent on the specific reaction conditions.[28] While a specific mechanism for the Scholl reaction has yet to be determined, it is thought that reactions using mild Lewis acids at low temperatures proceed via the radical-cation mechanism, while reactions employing strong Lewis acids at elevated temperatures operate through the arenium cation mechanism.[29]

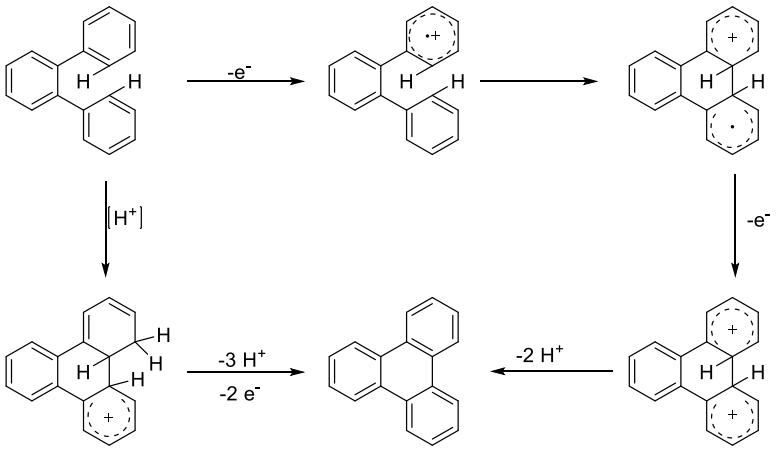

Figure 2.1: Competing mechanistic theories for oxidative aromatic coupling

In previous syntheses of indene containing polycyclic aromatic hydrocarbons (PAH), such as rubicene, the indene moieties were prepared via intramolecular palladium-catalyzed aryl-aryl cross-coupling or pentannulation.[31,32] Recently, Scholl reaction conditions have been used in the synthesis of indene containing PAH compounds. Chi and coworkers published the synthesis bisindeno-annulated pentacene molecules under Scholl reaction conditions using $FeCl_3$ as the oxidizing agent.[33,34]

For the synthesis of ASIs, two different Scholl reaction conditions were employed. The original synthetic strategy, developed by Wayne Gu, used $AlCl_3$ in nitrobenzene. Using this method Wayne was able to synthesize nine ASI derivatives. However, due to synthetic challenges with some functional groups, and for ease of synthesis, conditions were changed to use DDQ/$MeSO_3H$.

2.3 Results and discussion:

2.3.1 Synthesis:

Starting with commercially available phthalic anhydride (**2.13**) and 1-hydroxyl naphthalene (**2.12**), the first Friedel–Crafts acylation was performed using the Lewis acid boron trioxide (**Scheme 2.4**). The crude reaction mixture was then refluxed in water for 1 hour to obtain compound (**2.11**), 2-(1-hydroxy-2-naphthoyl)benzoic acid.

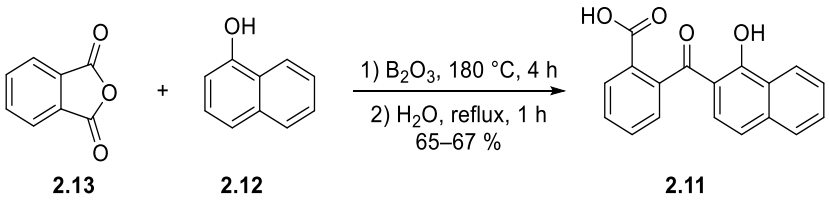

2.13 **2.12** **2.11**

Scheme 2.4: Synthesis of asymmetric 2-(1-hydroxy-2-naphthoyl) benzoic acid (**2.11**)

Compound **2.11** was then treated with PCl_5 forming the acid chloride of compound **2.11**. The acid chloride was subsequently reacted with sulfuric acid accomplishing the second Friedel-Crafts acylation and producing 6-chlorotetracene-5,12-dione, compound (**2.9**), in good yields, 50% over 2 steps (**Scheme 2.5**).[35] Using the above conditions compound (**2.9**) was synthesized on 0.1 molar scale, which, was then be used in all subsequent synthesis.

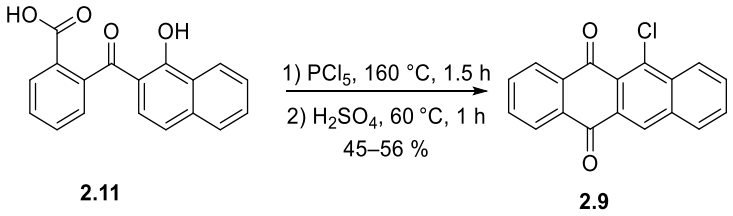

Scheme 2.5: Synthesis of 6-chlorotetracene-5,12-dione (**2.9**).

Arylation of compound **2.9** was the first diversification point (**Scheme 2.6**). The desired arylbromides (**2.10a-e**) first underwent a lithium halogen exchange at -78 ˚C. The resulting arylithium was then reacted with naphthacenequinone **2.9** producing the diol intermediates **2.8a-e** as mixtures of *syn*/*anti* isomers. The *syn* and *anti* isomers of compounds (**2.8a-e**) were never purified and the products were carried forward as a crude mixture.

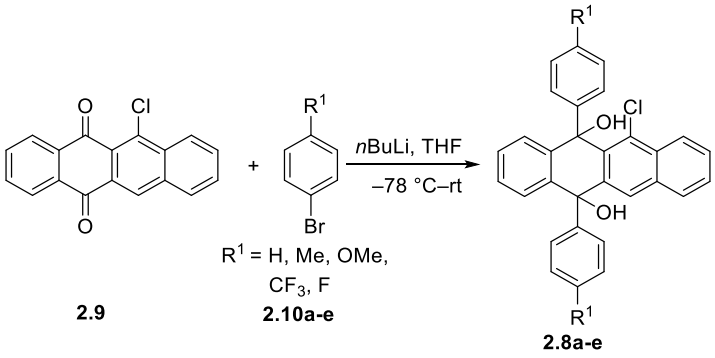

Scheme 2.6: Synthesis of intermediates **2.8a-e**

Next the tetracene backbone was formed via a reductive aromatization. The original condition for reductive aromatization used $SnCl_2$ and HCl in THF. However, the reaction was often very slow and frequently did not go to completion. In an attempt to increase the reaction rate we developed conditions using a Lewis acid. To produce the 5-chloro-6,11-diphenyltetracene intermediates (**2.7a-e**) the crude diols were reduced using $BF_3 \cdot OEt_2$, in the presence of the $SnCl_2$ reducing agent, and refluxed in dioxane for 30 minutes. These new reaction conditions resulted in isolated yields between 46 and 56 % over the 2 steps. The progress of this reaction could be track visually. Where compounds **2.8a-e** were a colorless powder, compounds **2.7a-e** became a bright orange/red color upon formation of the tetracene core.[36,37]

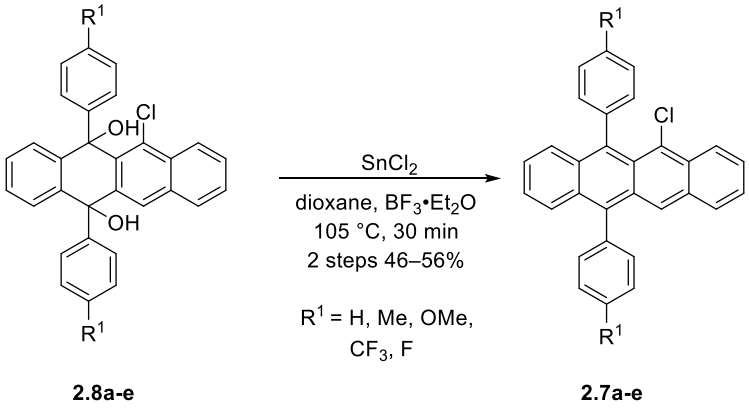

2.8a-e **2.7a-e**

Scheme 2.7: Synthesis of 5-chloro-6,11-diphenyltetracene intermediates (**2.7a-e**).

As stated previously, originally $AlCl_3$ was used to perform the oxidative cyclization in the syntheses of several ASI derivatives.[38] The conditions were later modified to use methanesulfonic acid in the presence of 2,3-dichloro-5,6-dicyano-1,4-benzoquinone (DDQ) (**Scheme 2.8**).[30,38] Using the DDQ/$MeSO_3H$ Scholl reaction conditions compounds (**2.5a-e**) were prepared in yields from 40 to 81 %.

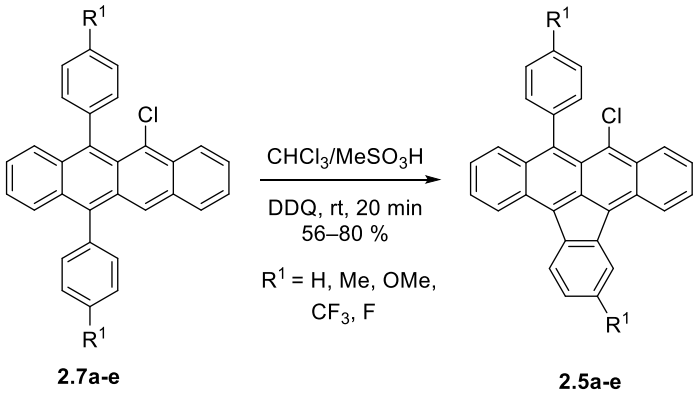

Scheme 2.8: Synthesis of 9-chloro-10-phenylindeno[1,2,3-*fg*]tetracene derivatives (**2.5a-e).**

Once again the formation of intermediates **2.5a-e** could be monitored visually. Upon formation of the indene ring the solution changes from the orange/red color of compounds **2.7a-e**, to a purple/black color. Also, while compound **2.7a-e** was highly fluorescent compound **2.6a-e** produced no visible fluorescence. Interestingly, the regiochemsitry of compounds **2.6a-e** was very specific. Oxidative cyclization was only observed to occur at the C12 carbon of the tetracene core and never at C10. We attributed this high regio-selectivity to steric-repulsion between the C5 chloride and the C6 phenyl group. This steric-repulsion pushes carbons 5 and 6 away from each other, which, in turn pushes the C11 phenyl group closer to the C12 hydrogen.

From compounds **2.5a-e**, the late-stage diversification was accomplished using Kumada-Corriu cross-coupling conditions previously developed in our lab (**Scheme 2.9**).[39] Using PEPPSI-IPR under mild conditions compounds **2.4a-e** were obtain in yields between 54 and 92%.[26,39,40] Via ^{1}HNMR it was observed that the primary impurities in the crude reaction mixtures were the unreacted starting material and dehalogenated indenotetracene (**2.14**) (**Figure 2.2**). In most cases, both the starting material (**2.5**) and impurity **2.14** were

readily separable from the desired product by either column chromatography and/or recrystallization.[41] However, for the di-CF_3 substituted ASI (**2.4d**) we were unable to find purification conditions which separated unreacted starting material **2.5d** from final product. In order to obtain pure **2.4d** the reaction needed to be driven to completion. Increasing the amount of catalyst or the reaction temperature only resulted in more of the dehalogenation by product (**2.14**). Increasing the equivalents of phenylmagnesium bromide resulted in formation of the homodimer, biphenyl, byproduct, which could not be completely separated from the product. In the end switching to a non-ethereal solvent, toluene, resulted in full conversion of **2.5d** to compound **2.4d**. Using the modified reaction conditions pure compound **2.4d** could be easily obtain via recrystallization from the crude reaction mixture. For this project we were able to synthesize a total of 14 ASI derivatives, 5 of which I prepared (**Table 2.1**).[38]

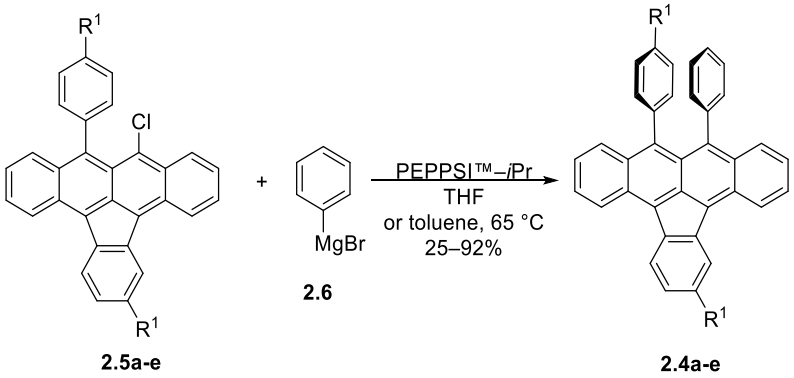

Scheme 2.9: Synthesis of 9,10-diphenylindeno[1,2,3-fg]tetracene derivatives (**2.4a-e**).

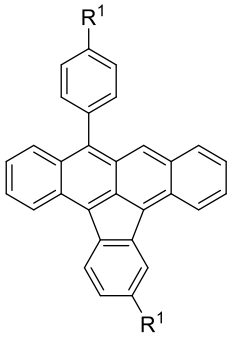

2.14

Figure 2.2: Dechlorination side product from the Kumada-Corriu cross-coupling.

Table 2.1: Functional groups at R^1 and Ar and the yield of three key transformations, preparation of **2.7a-e**, **2.5a-e**, and **2.4a-e**.

Entry	R^1	**2.7**, % yield	**2.5**, % yield	Ar	**2.4**, % yield
1	H	**2.7a**, 27	**2.5a**, 56	Ph [c]	**2.4a**, 63
7	Me	**2.7b**, 53	**2.5b**, 57	Ph [c]	**2.4b**, 57
10	F	**2.7c**, 53	**2.5c**, 81	Ph [c]	**2.4c**, 90
11	CF_3	**2.7d**, 46	**2.5d**, 40	Ph [d]	**2.4d**, 92
12	OMe	**2.7e**, 65	**2.5e**, 69	Ph [c]	**2.4e**, 54

[c] Palladium catalyzed cross-coupling using PEPPSI-iPr™ THF at 65 °C. [d] Palladium catalyzed cross-coupling using PEPPSI-iPr™ in toluene at 65 °C.

2.3.2 Material characterization

2.3.2.1 Crystal structure

For small molecule OPVs exciton dissociation and electron transport generally occurs via Dexter energy transfer.[42] For Dexter energy transfer to occur, tight packing and good orbital overlap is required between neighboring molecules in the solid state. To understand how a material will function as an organic semiconductor it is critical to determine molecular packing in the solid state. Single crystals of 6 ASI derivatives were grown for X-ray diffraction experiments in order to determine solid-state molecular

packing (**Figure 2.3**). Compound **2.4f** was synthesized by Wayne Gu.[38] Single crystals of ASIs **2.4a-f** were grown as small, purple, plate-like crystals via either vacuum sublimation or physical vapor transport using argon as the carrier gas.

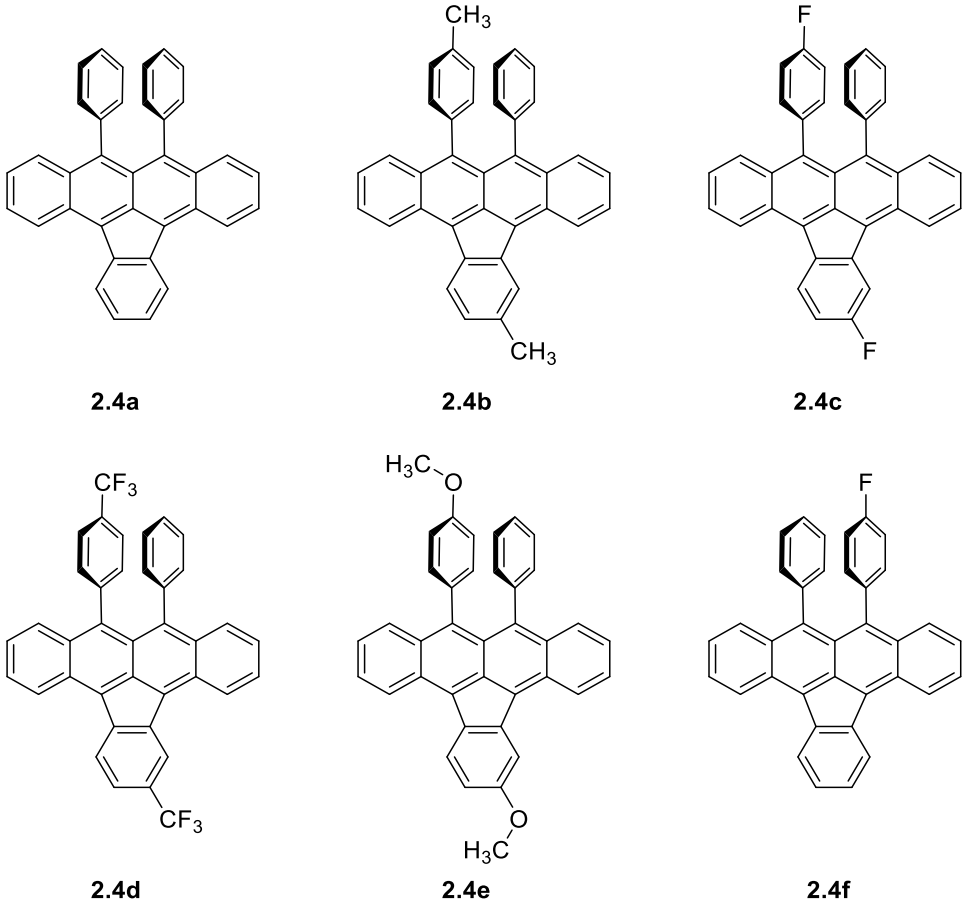

Figure 2.3: Structures of the 6 ASI derivative for which single-crystal X-ray structures were obtained.

Three packing motifs were observed in the single crystals of the 6 ASIs tested: monoclinic C2/*c* or $P2_1/c$, and orthorhombic Pbca.[43] The parent, unsubstituted ASI, compound **2.4a** packed in the monoclinic C2/*c* space group.[26] Substitution of hydrogen with isosteric fluorine, as in **2.4c** and **f**, also resulted in the same C2/*c* space group. When larger functional groups were introduced the crystal packing changed to a monoclinic

$P2_1/c$, derivatives **2.4d** and **2.4e**, and orthorhombic Pbca for **2.4b**.[44] A range of close contact distances between neighboring molecules was observed in all ASIs due to a slight twisting of the indenotetracene core. The observed backbone twist ranged from 0.70˚ in **2.4e**, to 9.67˚ in compound **2.4f**. Average π–stacking distances were determined by generating a plane through the ASI molecule using the atoms of the indene ring, then measuring the distances between neighboring planes (**Figure 2.4**). The monoclinic C2/*c* crystals showed a slipped 1-D (**Figure 2.5**) packing with good overlap of the indenotetracene core and small π–π close contacts averaging around 3.4 Å, (**2.4a**, **2.4c**, and **2.4f**, **Table 2.2**) which would allow for efficient solid-state charge transport.[45] In the solid state compound **2.4b** (orthorhombic Pbca) was observed to pack in a π-stacked herringbone motif (**Figure 2.5)**. Again, we observed good overlap of the indenotetracene cores with π–π distances that averaged 3.46 Å and a closest contact measuring 3.36 Å. In the monoclinic $P2_1/c$ systems, compound **2.4e** showed little overlap of the indenotetracene core due to a horizontal displacement along the indenotetracene backbone; compound **2.4d,** however, demonstrated good overlap, **(Figure 2.6)**. Compound **2.4d** was also unique in that the asymmetric unit contained two molecules giving two different π–π close contacts of 3.28 and 3.26 Å. Compounds for which we obtained single crystal X-ray data were further studied for their electrochemical, optical, and physical properties.

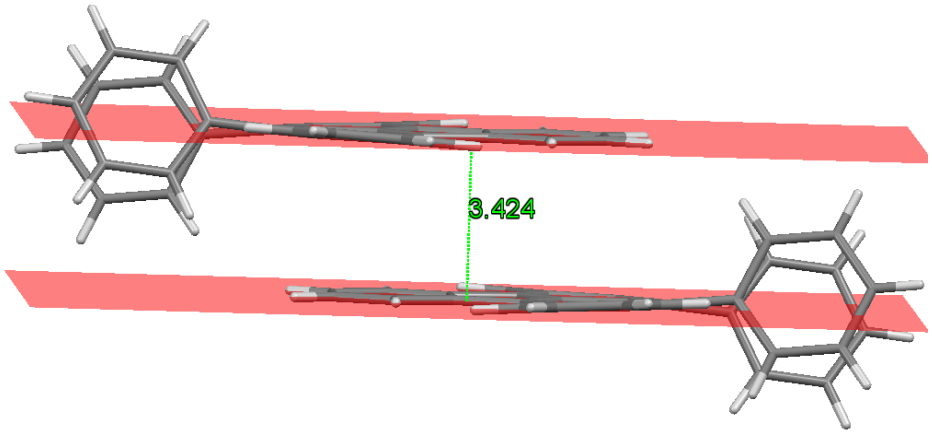

Figure 2.4: For compound **2.4a** the π-π stacking distance was found to be 3.42 Å.

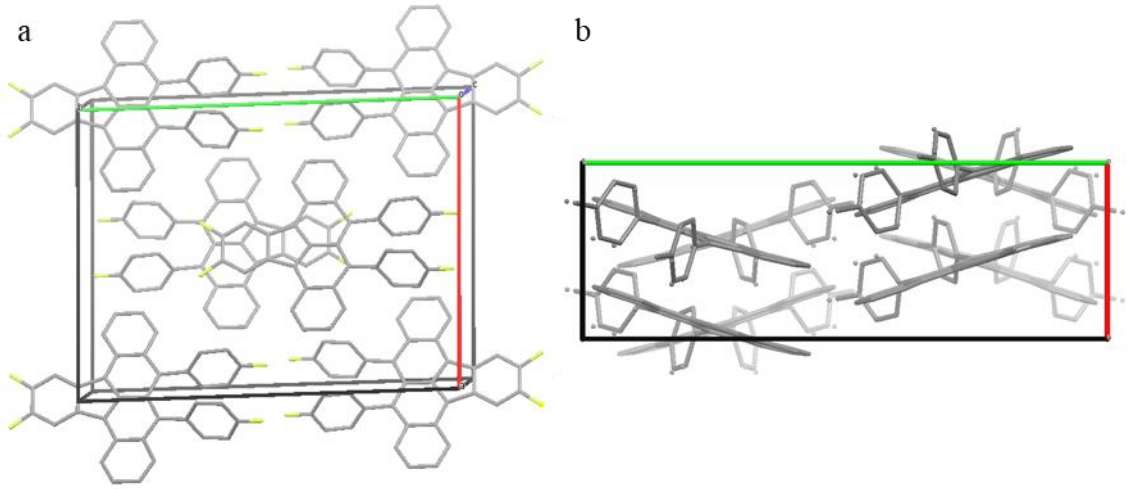

Figure 2.5: a) **2.4c** C2/*c* slipped 1-D π-stacking b) **2.4b** Pbca π-stacked herringbone packing motifs

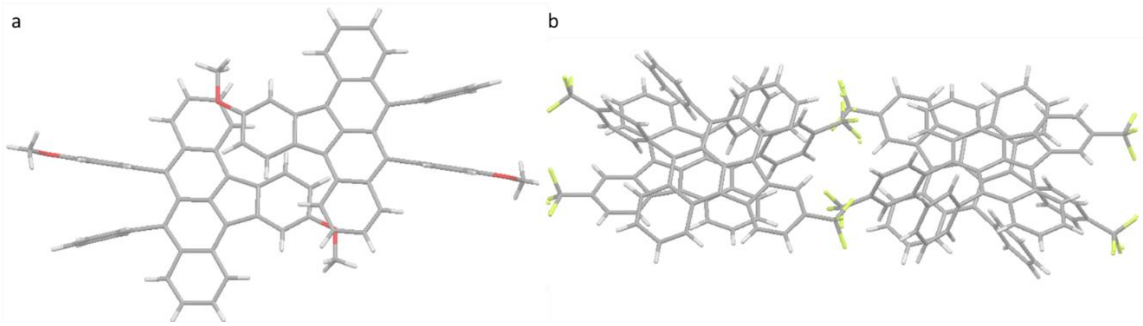

Figure 2.6: Shows the indenotetracene core overlap of a) **2.4e** b) **2.4d.**

Table 2.2: Single crystal packing motifs for compound **2.4a-f** and corresponding tetracene backbone π–π distances.

Crystal system	Packing Motif	Compound	π-spacing Å
Monoclinic	C2/*c*	**2.4a**	3.42
	C2/*c*	**2.4c**	3.42
	C2/*c*	**2.4f**	3.37
	$P2_1/c$	**2.4d**	3.26/3.28[a]
	$P2_1/c$	**2.4e**	3.76
Orthorhombic	Pbca	**2.4b**	3.46

[a] Compound **2.4d** contains two molecules in the asymmetric unit with different π–π distances

2.3.2.2 Thermal stability

Thermal stability and decomposition temperatures, of ASI derivatives **2.4a-f**, were determined using thermogravimetric analysis (TGA) studies. Shown in **Table 2.3**, compounds **2.4a**, **2.4c**, and **2.4d** demonstrated no more than 1% mass loss below 300 ˚C due to sublimation, while **2.4b**, **2.4e**, and **2.4f** did not achieve 1 % mass loss until above 300 ˚C. All ASIs demonstrated good thermal stability measuring less than 5 % mass loss below 325 ˚C and possessing onset temperatures of greater than 343 ˚C.[6,46,47] TGA graphs can be found in the SI of the publish JOC article.[38] With **2.4a-f** demonstrating good thermal stability, we next performed differential scanning calorimetry (DSC) to examine phase transitions.[10,15] Complete DSCs for each compound be found in the JOC paper.[38] The DSC data for compounds **2.4a-d**, and **2.4f** showed no phase change between 0 to 150 ˚C, **Figure 2.7**. With compound **2.4e** a reversible thermal expansion at 115 ˚C was observed, **Figure 2.7**. Upon further heating to 260 ˚C, compounds **2.4a-f** all showed one or more endothermic events suggesting the formation of alternative polymorphs at elevated temperatures. The

measured thermal stability of ASIs was determined to be adequate for resisting decomposition or phase changes at typical OPV device operating temperatures.

Table 2.3: Temperatures of 1%, 5% and decomposition onset

Compound	99%	95%	Onset Point
2.4a	238 ˚C	324 ˚C	380 ˚C
2.4b	312 ˚C	349 ˚C	353 ˚C
2.4c	293 ˚C	327 ˚C	364 ˚C
2.4d	283 ˚C	321 ˚C	343 ˚C
2.4e	336 ˚C	371 ˚C	380 ˚C
2.4f	308 ˚C	357 ˚C	381 ˚C

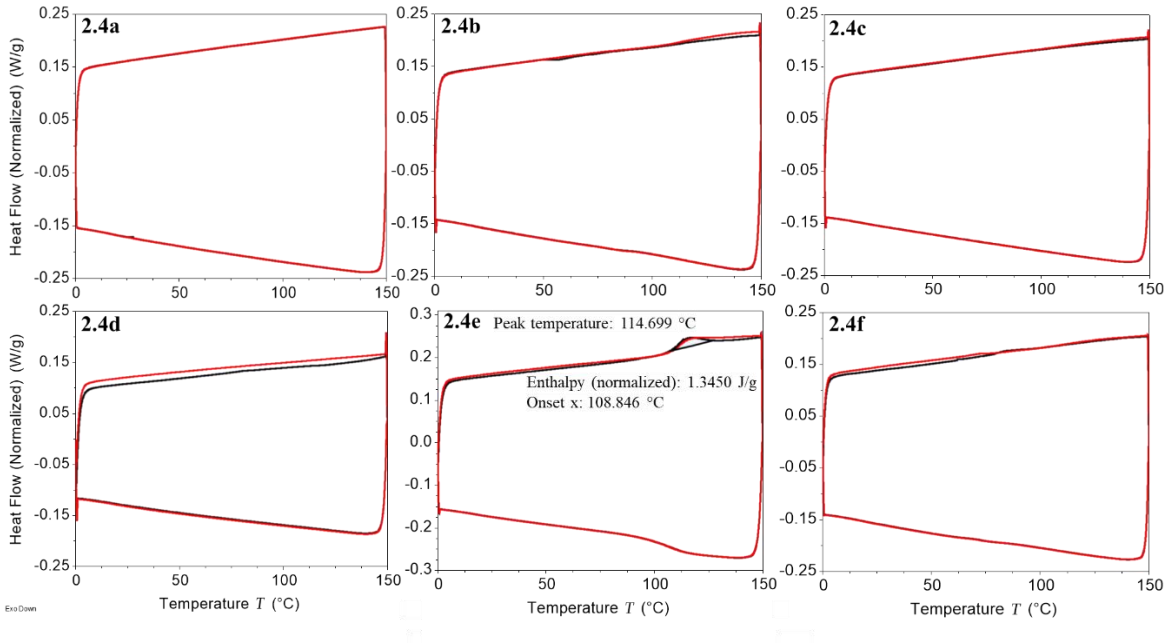

Figure 2.7: Differential scanning calorimetry results for compounds **2.3.10a-f** between 0 and 150 ˚C

2.3.2.3 Electrochemical properties

As stated previously, indenotetracenes possess an electron-deficient π-system due to the anti-aromatic (4n) electron configuration imposed by the five-membered ring. This makes indene containing molecules good candidates for new electron acceptors due to the possibility of accepting two electrons. Two-electron reduction has been observed in other indene-containing molecules.[1,8,48,49] The HOMO and LUMO levels of **2.4a-f** were determined via cyclic voltammetry (CV) referenced to ferrocene (4.8 eV versus vacuum), **Figure 2.8**. HOMO/LUMO levels were estimated from the onset of the oxidation and reduction peaks.[38,46]

Compounds **2.4a-f** all demonstrated at least two reversible, or quasi-reversible, reduction and one oxidation red–ox couples. From the CV experiments, the energy levels of the LUMOs, to which a first electron is added, were determined to be around -4.1 eV while the addition of a second electron was observed between -3.27 and -3.42 eV, **Table 2.4**. The low reduction potentials of ASIs, $E_{1/2}$ = -0.9 to -0.6 V, demonstrated the high electron affinities of the ASI derivatives. All ASIs showed at least one oxidation peak near $E_{1/2}$ = 0.7 V. Estimated HOMO energy levels measured for compounds **2.4a-f** range from -5.40 to -5.67 eV. The HOMO/LUMO energies determined for ASIs were comparable to those determined in other indene-based electron acceptors.[8,49,50]

The HOMO/LUMO energies of ASIs were modulated via substitutions around the indenotetracene core. The addition of an electron donating methoxy group, compound **2.4e**, raised both the HOMO and LUMO in energy. The increased electron density of the indenotetracene core raised the HOMO energies to such a degree that a second oxidation peak could now be observed, **Figure 2.8**. Upon addition of CF_3 groups, **2.4e**, the measured

HOMO energy decreased to -5.67 eV while addition of the first and second electron into the LUMO lowered to -4.25 and -3.42 eV respectively. Addition of the CF_3 functional groups also resulted in the appearance of a third reduction which occurred at -2.67 eV. The band gaps calculated from the measured HOMO/LUMO energy levels are shown in **Table 2.4**. Through a collaboration with the Cramer group, Soumen Goush performed computation analysis of compounds **2.4a-f** using the crystal packing measured by single-crystal X-ray experiments. We found that the energy gaps determined from CV were in good agreement with the calculated energies (**Table 2.7**).

The modulation of HOMO/LUMO levels of ASI derivatives, via substitution with either electron-donating or electron-withdrawing groups, can be understood by examining the corresponding orbital amplitudes (**Figure 2.9**) determined from density functional theory (DFT) calculation. **Figure 2.9** shows that rather than being localized to one specific section of the molecule, e.g. the tetracene unit, both the HOMO and LUMO are delocalized throughout the entire indenotetracene π-system. The HOMO/LUMO energies determined for the ASIs are within the range that would favor electron accepting or ambipolar character for charge transport.[51] The higher LUMO energy levels for electron injection into indenotetracenes, compared to that measured for C_{60}, -4.5 eV, would potentially increase the open circuit voltage of an OPV by increasing the difference between the HOMO of the donor and the LUMO of the acceptor.[52,53,54]

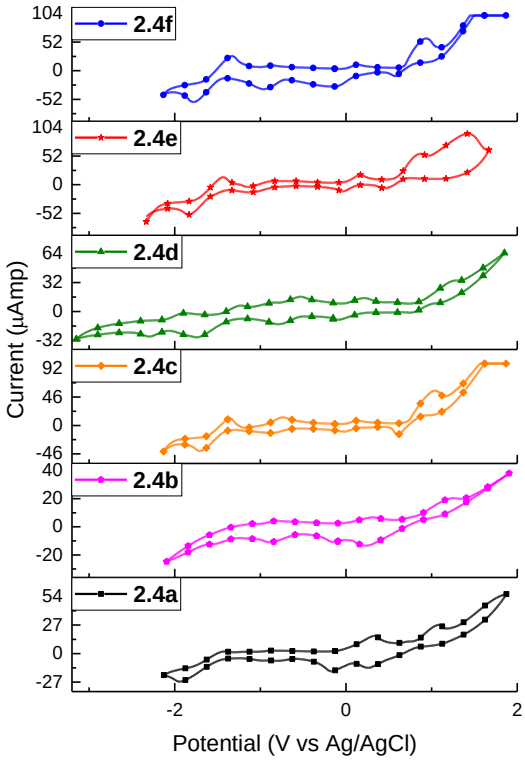

Figure 2.8: Cyclic voltammograms of compounds **2.4a-f**, Fc/Fc^{+} used as standard. Compound **2.4a**, **2.4b**, **2.4d**, **2.4e** were ran at a scan rate of 0.2 V/s, compound **2.4c**, **2.4f** at 0.1 V/s

Table 2.4: Onset potentials, measured HOMO/LUMO energies for compound **2.4a-f**, compared to Fc/Fc^{+}, and energy gap.

Compound	$E_{ox/onset}$ 1 V	$E_{red/onset}$ 1 V	$E_{red/onset}$ 2 V	HOMO eV	LUMO eV	E_g eV	LUMO 2nd electron eV	E_g eV
2.4a	0.72	-0.62	-1.47	-5.52	-4.18	1.34	-3.35	2.17
2.4b	0.74	-0.60	-1.50	-5.54	-4.20	1.34	-3.30	2.24
2.4c	0.72	-0.65	-1.42	-5.52	-4.15	1.37	-3.38	2.14
2.4d	0.87	-0.55	-1.38	-5.67	-4.25	1.42	-3.42	2.25
2.4d	0.60	-0.81	-1.53	-5.40	-3.99	1.41	-3.27	2.13
2.4f	0.68	-0.65	-1.48	-5.48	-4.15	1.33	-3.32	2.16

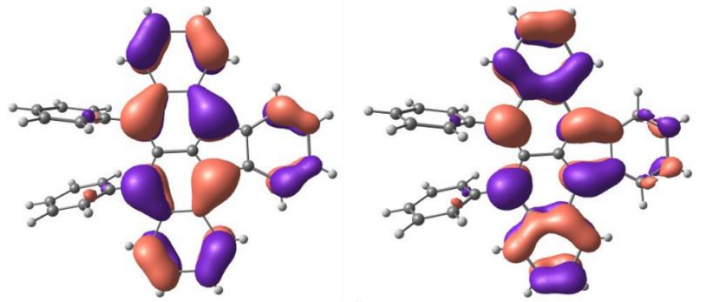

Figure 2.9. Orbital pictures for i) HOMO and ii) LUMO for **2.4a** (single point with M06-2X/6-31+G(d,p)).[55]

2.3.2.4 Optical properties

A major disadvantage of many n-type organic semiconductors is their poor absorptivity of visible light.[16] Having both the electron donor and electron acceptor molecules in OPV be strong visible light absorbers would lead to, thinner active layers and the creation of more light-generated carriers, both of which could potentially improve organic solar cell performance.[52,53,56]

UV/Visible absorption spectroscopy of compounds **2.4a-f** showed strong absorption over a large range of the visible spectrum, 390 to 650 nm.[38] All compounds showed very similar absorbance spectra with minor differences in peak shape, **Figure 2.10**. The variations in peak shape are attributed to the differences in bond vibrational modes/energies and intermolecular interaction in solution. ASIs demonstrated a strong high-energy absorption around 299 nm and weaker mid-range absorption, 350 to 500 nm, which correspond to π–π* transitions of the ASI molecules.[47,57,58] Absorption from 450 to 650 nm is similar to that of other reported indene compounds, resulting from the charge-transfer band, indicating some π–π interaction between molecules in solution.[18,22,50] The

molar attenuation coefficients determined for compounds **2.4a-f**, **Table 2.5**, are comparable to ruthenium dipyridyl complexes and other materials used in dye-sensitized solar cells, which have molar attenuation coefficients around 10^4 M^{-1} cm^{-1} in the visible region.[59] The energy-gap calculated from the charge-transfer band, λ_{onset}, **Table 2.5**, for **2.4a-f** were around 1.9 eV. This agrees with energy-gaps determined from CV measurements, **Table 2.4**, and theoretical linear-response time-dependent density functional theory (LR-TDDFT) calculations (**Table 2.7**). The slightly larger energy-gap measured in by CV experiments is due to the over-potential required to inject an electron into the molecule.

Comparing the absorbance of ASIs molecules to symmetrically substituted indeotetracenes we observed that both have similar molar attenuation coefficients, between 10^4 and 10^5 M^{-1} cm^{-1}. This is to be expected due to the fact that π-conjugation of the indenotetracene cores are same.[26]

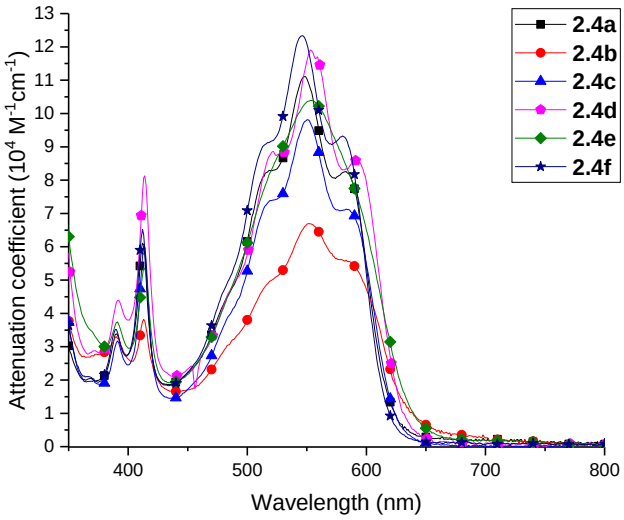

Figure 2.10: Absorption spectra of compounds **2.4a-f**, 10^{-5} M

Table 2.5: λ_{max} and optical band gaps

Compound	λ_{max}	E_g (eV)[a]
2.4a	550	1.98
2.4b	553	1.86
2.4c	551	1.93
2.4d	553	1.96
2.4e	555	1.89
2.4f	546	1.98

[a] Optical band gap was calculated using equation $E_g = \frac{hc}{\lambda}$ where h is Planck's constant, c is the speed of light constant, and λ is the absorption onset.

Fluorescence is the most common path for exciton decay in organic materials, and can decrease OPV efficiency by decreasing exciton (Dexter) energy transfer. **Figure 2.11** shows the absorbance and corresponding fluorescence spectra of compounds **2.4a-f**. Derivatives **2.4a-f** demonstrated weak fluorescence from 600 to 800 nm, which has been observed in other anti-aromatic, 4n, molecules due the excited electron populating the LUMO +1 state.[8] The fluorescence quantum yields (Φ) for compounds **2.4a-f**, **Table 2.6**, were all less than 4 %.

A portion of the very low Φ can be attributed to some re-absorbance due to partial overlap of the absorption and fluorescence spectra. The lack of any significant fluorescence does indicate that non-radiative decay pathways, which may include intersystem crossing and/or intermolecular charge transfer, are occurring in all ASI derivatives.[6,58,60] If operative, these alternate decay pathways could increase the efficiency of OPVs in which ASIs are used as the electron accepting moleucle due to the possible generation of longer lived excitons as well as faster exciton dissociation.[9,17,61]

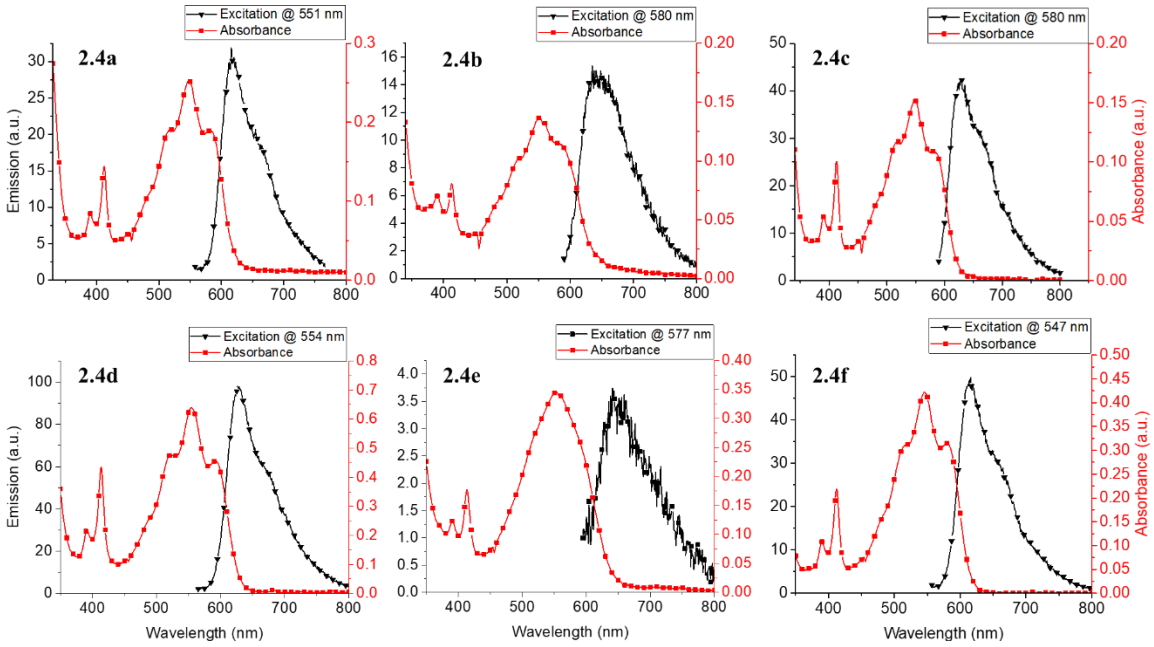

Figure 2.11: Fluorescence and corresponding absorbance spectra compounds **2.4a-f**.

Table 2.6: Calculated fluorescence quantum yield for compounds **2.4a-f** relative to rhodamine b.

Compound	Φ
Rhodamine B	0.7
2.4a	0.018
2.4b	0.016
2.4c	0.042
2.4d	0.029
2.4e	0.0015
2.4f	0.018

2.3.2.5 Theoretical modeling of electronic structure of ASI and charge transport in the solid state:

Through our colaboration with the Cramer group (Soumen Goush) we were able to show that our ASI compounds should function as electron transport or ambipolar material in OPVs. To better understand the excited-state properties of ASIs, LR-TDDFT

calculations were performed for singlet and triplet energies for compound **2.4a-f** (**Table 2.7**). The calculated energies were found to agree well with experimentally determined energy-gaps.

For ASI derivatives **2.4a-d**, **2.4f** the computed hole reorganization energies were found to be moderately smaller than the electron reorganization energies. The addition of an electron donating methoxy group, compound **2.4e**, resulted in a substantial increase in the hole reorganization energy, while leaving the electron reorganization energy relatively unchanged.

The solved single-crystal X-ray structures were used to construct a dimer model from which, the hole and electron transfer integrals were computed. From the computed transfer inetrgals, we found that compounds **2.4a-d**, **2.4f** could function as an electron transport, or ambipolar, OSC in OPVs, whereas compound **2.4e** would potentially function as a hole transport material. The calculated electron transfer integrals ASI derivative **2.4a-f** are comparable that perylene diimides, 10 to 200meV, a proven small molecule electron transport OSC.[62 63]

Considering both the reorganization energies and charge transfer integrals, computational results predict that compounds **2.4a-d**, **2.4f** could function as a new series of n-type semiconductors in OPVs. A full description of the compoutaional calculation and the resulting values can be found in our paper published in JOC.[38]

Table 2.7: LR-TDDFT first singlet and triplet excitation energies (eV, M06-2X/6-31+G(d,p).[a]

Derivative	Singlet excitation energy	Triplet excitation energy
2.4a	2.5	1.2
2.4b	2.4	1.1
2.4c	2.4	1.1
2.4d	2.3	1.1
2.4e	2.3	1.1
2.4f	2.4	1.1

[a]M06-L/6-31+G(d,p) geometries

Table 2.8: Reorganization energies (meV) predicted for various diarylindenotetracene derivatives.[a]

Derivative	Hole Reorganization energy	Electron Reorganization Energy
2.4a	114	136
2.4b	128	152
2.4c	150	169
2.4d	116	184
2.4e	224	167
2.4f	131	160

[a]M06-L/6-31+G(d,p)

Table 2.9: Absolute values for effective transfer integral (meV, PBE0/6-31G(d)) predicted for compounds **2.4a-f**. [64]

Compounds	Crystal Packing	Transfer integrals Electron (meV)	Transfer integrals Hole (meV)
2.4a	C2/c	32	5
2.4b	Pbca	34	4
2.4c	C2/c	19	28
2.4d	$P2_1/c$	87/53[a]	82/81[a]
2.4e	$P2_1/c$	19	57
2.4f	C2/c	44	7

[a] Compound **2.4d** contains two molecules in the asymmetric unit with slightly different π–π distances. Transfer integrals were calculated for both distances

2.4 Conclusion and future work:

In summary, a new class of electron transport material based on the indene scaffold, asymmetrically substituted indenotetracenes (ASI), has been successfully prepared. Electrochemical and physical characterizations demonstrated the potential of ASIs as a novel electron transport material in OPVs. ASI derivatives were shown to strongly absorb over a broad range of the visible spectrum, with little to no concomitant fluorescence, potentially increasing short circuit current. The higher LUMO levels of ASIs relative to C_{60} should allow for increased open circuit voltage. ASIs also demonstrated good thermal stability which could correlate with improved OPV lifetimes. Single-crystal X-ray diffraction experiments showed tight π-stacking and good backbone overlap in the solid state, allowing for efficient solid-state charge transport. Using the solved crystal structure, ASI derivatives **2.4a-d**, **2.4f** were predicted to function as either electron transport or ambipolar OSC in organic photovoltaics.

Our findings demonstrate the potential of asymmetrically substituted indenotetracenes to function as a novel class of non-fullerene electron transport materials in organic photovoltaics with the potential to improve device lifetime and efficiency.

There are two future directions that the synthesis and characterization part of this project could take. In the short term, one could produce ASI derivatives with slight modifications of the functional groups to examine the effects on solid-state packing and electronic properties, using the existing chemistry. This could include either examining new functional groups such as CH_2F and CHF_2, moving the position of the current class of

functional, or new functional group pairings (**Figure 2.12**). This would create new intermolecular interactions in the solid state potentially resulting in new solid-state packing with improved electron transport properties.

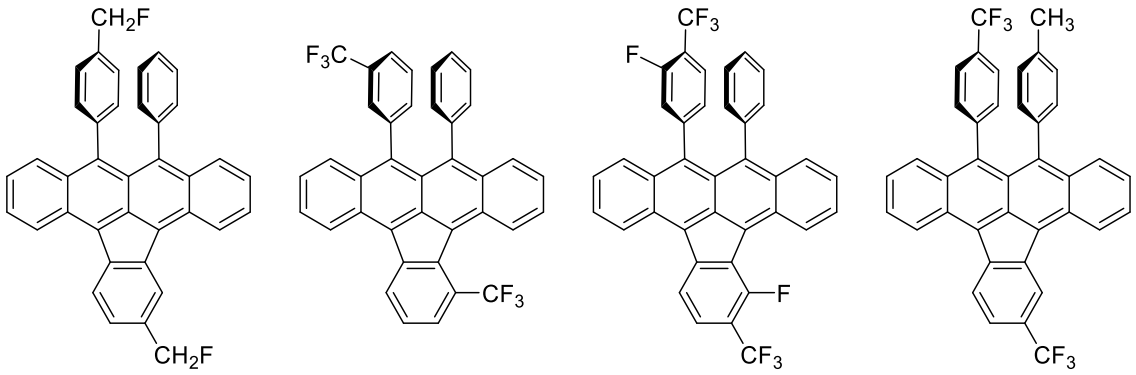

2.15 **2.16** **2.17** **2.18**

Figure 2.12: Indicates possible future synthetic targets using the current synthetic strategy.

A longer term, and potentially more interesting continuation of this work, would be to begin functionalization off the tetracene core. While some derivatives could use the current procedure, **Figure 2.13**, others would require an entirely new synthesis to be developed (**Figure 2.14**). Addition of small functional groups off the tetracene, such as fluorine and methyl groups, would affect the solid-state packing by creating new intermolecular interaction and could result in improved π-stacking and charge transport. The addition of thiophene and phenyl functional groups would result in increased delocalization of the ASI π-system potentially increasing intermolecular interaction in the solid-state which my improve charge transport through ASI thin films.

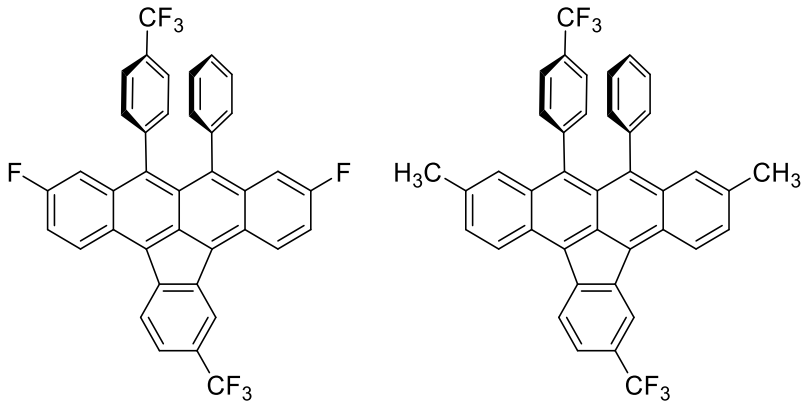

2.19 **2.20**

Figure 2.13: Shows ASI derivatives functionalized off the tetracene core

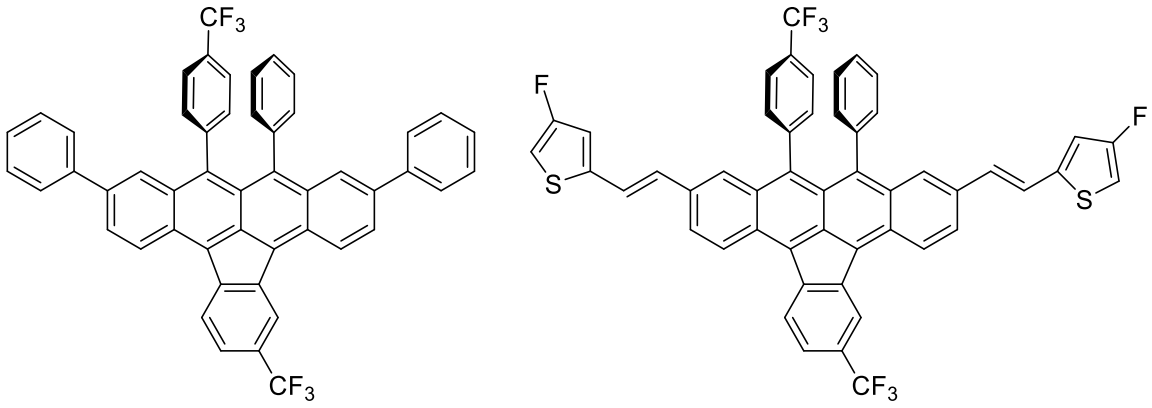

2.21 **2.22**

Figure 2.14: Shows ASI derivatives functionalized off the tetracene core

The ASI derivatives in **Figures 2.13** and **2.14** would not only drastically change solid-state packing, but also significantly alter visible light absorption, HOMO/LUMO energies, and charge transport.

2.5 Experimental:

Materials and reagents

All materials were purchased through commercial sources. Freshly distilled THF and toluene were used in synthesis of all ASI molecules. -(1-hydroxy-2-naphthoyl)benzoic acid (**2.11**) and 6-chlorotetracene-5,12-dione (**2.9**) were synthesized using a previously published procedure.[35]

Measurements and characterization

Melting temperatures for all compounds were performed on samples precipitated from solution. The melting temperature is defined as the temperature at which the powder anneals to a film rather than a free-flowing liquid. High-resolution mass spectrometry (HRMS) using GC-MS was performed on a quadrupole time-of-flight mass spectrometer with a solid injection probe. Method: inlet temperature 250 ˚C, source temperature 280 ˚C. The initial temperature was 80 ˚C and increased to 325 ˚C over 6 minutes and then held for 2.3 minutes. High-resolution mass spectrometry (HRMS) using ESI was performed on time-of-flight instruments.

^{1}H NMR (300, 400, or 500 MHz), and ^{13}C NMR (75, 100, or 125 MHz), ^{19}F NMR (282 or 470 MHz) spectra were recorded on FT NMR instruments. All NMR spectra were reported as δ values in ppm referenced to chloroform (7.26 ppm), methylene chloride (5.32 ppm) or tetramethylsilane (TMS, 0.00 ppm) for ^{1}H, chloroform (77.00 ppm) for ^{13}C, and hexafluorobenzene (-163.00 ppm) for ^{19}F NMR. ^{13}C NMR spectra are reported to the nearest 0.01 ppm due to the large number of close signals.

Infrared (IR) spectra were obtained as films on NaCl plates using an infrared spectrophotometer in transmission mode.

X-ray diffraction experiments were performed via single-crystal XRD using a diffractometer with graphite monochromater using CuKα radiation (λ=1.5418) at 123 K ω scans and MoK α radiation (λ=0.71073) at 298 K ω scans. Crystals of **2.4a**, **2.4d**, **2.4c**, and **2.4f** were grown via physical vapor transport (PVT) using the following technique: the temperature of the sublimation region was adjusted for each compound and ranged between 150 and 230 ˚C, depending on the compound. The crystal growth was held between 140 and 200 ˚C. The thermal gradient in the crystal growth region was created by wrapping thermal tape at continually wider intervals down the crystal growth region. Argon was used as the carrier gas. Argon flow rate was set via an oil bubbler at one bubble in the oil bubbler every 1 to 2 seconds. The crystals were grown in the PVT chamber over a 1 to 3 day period. Crystals of **2.4b**, **c** were grown via sublimation between 180 and 200 ˚C over 3 days under high vacuum. In the solid state, compounds **2.4a-f** are configurationally disordered resulting in having to place the substitutions symmetrically about the diarylindenotetracene core with 50 % occupancy.

Differential scanning calorimetry experiments were performed by heating compounds **2.4a-f**. to 150 ˚C at 10 ˚C/ min for two cycles then heating to 260 ˚C in a differential scanning calorimeter.

Thermogravimetric analysis was performed by heating samples from 24 to 550 ˚C at a rate of 10 ˚C/ minute in a nitrogen atmosphere.

Cyclic voltammetry measurements were performed at 5 mM in anhydrous tetrahydrofuran previously degassed with Argon. A silver/silver chloride reference electrode, gold working electrode, and platinum ground were used for CV experiments. Tetrabutylammonium

perchlorate was used as the electrolyte and ferrocene as the standard. Cyclic voltamagrams were collected at varying concentrations and sweep rates with all showing similar Red/Ox character. Ferrocene oxidation onset was referenced to zero.

Absorbance measurements were performed on a UV/Visible spectrometer, scanned from 1000nm to 100nm as follows: indenotetracene compounds **2.4a-**f were dissolved in dichloromethane (10 mL). Serial dilutions were performed in factor of ten increments (10^{-3}, 10^{-4}, 10^{-5}, 10^{-6} M) and absorbance was measured. Serial dilutions were performed using a 10 mL volumetric flask and 1 mL volumetric pipet. Attenuation coefficients (ε) were calculated from absorbance spectra corrected for dichloromethane.

Fluorescence experiments were performed on a fluorescence spectrophotometer in either ethanol or dichloromethane. The fluorescence quantum yield was calculated using rhodamine b in ethanol excited at 510 nm. The quantum yield for rhodamine b under these conditions was previously reported, $\Phi = 0.7$.[65,66] Absorption and fluorescence measurements for compounds **2.4a-f** were performed at 10^{-5} M.

Synthesis

6-chloro-5,12-diphenyl-5,12-dihydrotetracene-5,12-diol (2.8a):

To a flame dried 100 mL 3-neck round bottom flask was added anhydrous THF (10 mL), which was cooled to –77 ˚C. bromobenzene (0.075 mL, 0.112 g, 0.715 mmol) was added to THF at –77 ˚C followed by n-butyllithium (2.5 M in hexanes, 0.257 mL, 0.643 mmol). The mixture was stirred at –77 ˚C for 10 minutes to form phenyllitium. In a flame dried 250 mL 3-neck round bottom flask anhydrous THF (10 mL) and 6-chloro-5,12-naphthacenequinone **2.9** (0.0801 g, 0.2383 mmol) were combined and cooled to –77 ˚C. The phenyllitium was transferred into the 250 mL round bottom containing the slurry of

THF and 6-chloro-5,12-naphthacenequinone via cannula at a constant flow. The mixture was allowed to react at –77 ˚C for 2 hours then allowed to warm to room temperature and stirred for an additional hour. The reaction was quenched with water (2 mL). The crude reaction mixture was concentrated to a solid and carried forward without purification.

5-chloro-6,11-diphenyltetracene (2.7a):

The resultant residue, compound **2.8a**, was placed in a 100 ml round bottom flask and dissolved in 15 mL THF. The saturated solution of $SnCl_2$ (0.226 g, 1.192 mmol) and BF_3•OEt_2 (0.088 mL, 0.101 g, 0.714 mmol) were then added to the reaction flask. The reaction mixture was heated to reflux (106 ˚C) and reflux was maintained for 30 minutes. The reaction mixture was then allowed to cool to room temperature and quenched with saturated aqueous $NaHCO_3$ solution, followed by addition of solid $NaHCO_3$ until the aqueous portion is basic as indicated by pH paper. The precipitate that formed was removed via filtration over Celite®. The filtered solid was washed with chloroform (3 × 250 mL). The filtrate and chloroform washes were combined and washed once with water, once with saturated brine, dried over $MgSO_4$, concentrated and placed under high vacuum overnight. The crude product was dissolved in boiling chloroform followed by the addition of room temperature methanol and placed in the refrigerator (5 °C) overnight. This gave compound **2.7a**, an orange/red solid (2 steps 0.0266 g, 0.064 mmol, 27 %): mp 188-189 ˚C; ^{1}H NMR (300 MHz, $CDCl_3$) δ 8.39 (d, *J* = 9.1 Hz, 1H), 8.32 (s, 1H), 7.75 (d, *J* = 8.5 Hz, 1H), 7.68–7.62 (m, 5H), 7.61–7.58 (m, 1H), 7.54–7.52 (m, 5H), 7.49–7.47 (m, 2H), 7.45–7.42 (m, 1H), 7.34–7.31 (m, 1H);

9-chloro-10-phenylindeno[1,2,3-*fg*]tetracene (2.5a):

Compound **2.7a** (518 mg, 1.25 mmol) was dissolved in chloroform (20 mL) and the solution was purged with nitrogen for 3 minutes. Methanesulfonic acid was then added (80 mL) and the solution was purged with nitrogen for 5 minutes. 2,3-Dichloro-5,6-dicyano-1,4-benzoquinone (DDQ) (0.341 g, 1.50 mmol) was added to the mixture of chloroform and methanesulfonic acid and the solution was again purged with nitrogen for an additional 5 minutes. The reaction was stirred under nitrogen atmosphere for 3h, wrapped in aluminum foil to shield the mixture from light. The reaction progress was monitored by ^{1}H NMR and TLC, looking for the disappearance of fluorescence of the **2.7a** spot. The reaction was quenched by adding saturated $NaHCO_3$ solution (approximately 100 mL, CAUTION: Gas evolution, exothermic) to the reaction followed by pouring the reaction mixture into a separatory funnel containing solid $NaHCO_3$ (at least 10g CAUTION: Gas evolution, exothermic). After allowing to cool to room temperature, the mixture was extracted with chloroform (3 × 200 mL) and the remaining solid $NaHCO_3$ was dissolved in water. The chloroform washes were combined and washed repeatedly with saturated $NaHCO_3$ solution until the aqueous portion is clear and nearly colorless (faint yellow, usually five washes). Then the organic portion was washed repeatedly with water until the aqueous layer was no longer yellow. The organic layer was then washed with brine, dried over magnesium sulfate, concentrated and placed under high vacuum overnight. The crude product **2.5a** was dissolved in boiling chloroform followed by the addition of room-temperature methanol and the mixture was placed in the refrigerator (5 °C) overnight. Compound **2.5a** was collected by vacuum filtration as a purple solid (0.2906 g, 0.705 mmol, 56 %): mp 262–263 ˚C; ^{1}H NMR (300 MHz, $CDCl_3$) δ 8.89 (dd, J = 8.2, 6.9Hz, 2H), (d, J = 9.1Hz, 1H),

8.56–8.51 (m, 2H), 7.71 (d, *J* = 9.1 Hz, 1H), 7.67–7.62 (m, 2H), 7.57–7.55 (m, 3H), 7.54–7.50 (m, 3H), 7.46–7.44 (m, 2H), 7.34 (ddd, *J* = 1.0, 6.5, 9.2 Hz, 1H);

9,10-diphenylindeno[1,2,3-*fg*]tetracene (2.4a):

To a flame-dried 100 mL round-bottom flask, **2.5a** (291 mg, 0.706 mmol), PEPPSI-IPr (20.0 mg, 0.0282 mmol) and 15 mL freshly distilled THF were added. The flask was then sealed with a septum and placed under a nitrogen atmosphere. The solution was heated to 65 °C then phenylmagnesium bromide in THF (1 M, 1.058 mL, 1.058 mmol) was added. The reaction was stirred at 65 °C for 16 hours. The reaction was then quenched with a saturated solution of NH_4Cl and extracted with EtOAc (3 × 50 mL). The organic layers were combined, dried over $MgSO_4$ and concentrated under vacuum. The crude product was purified by recrystallization from hot chloroform with methanol to give a purple/black solid, compound **2.4a** (0.201 mg, 0.443 mmol, 63%): mp 271–272 ˚C; ^{1}H NMR (300 MHz, $CDCl_3$) δ 8.93 (d, *J* = 8.8 Hz, 2H), 8.61 (dd, *J* = 5.6, 3.2 Hz, 2H), 7.59 (m, 2H), 7.53 (dd, *J* = 5.6, 2.8 Hz, 2H), 7.36 (d, *J* = 9.2 Hz, 2H), 7.21 (ddd, *J* = 7.2, 6.4, 0.8 Hz, 2H), 7.05 (m, 6H), 6.93 (m, 4H);

6-chloro-5,12-di-p-tolyl-5,12-dihydrotetracene-5,12-diol (2.8b):

6-chloro-5,12-di-p-tolyl-5,12-dihydrotetracene-5,12-diol was synthesized analogously to 6-chloro-5,12-diphenyl-5,12-dihydrotetracene-5,12-diol, compound **2.8a**. The crude product was carried to the next step without purification.

5-chloro-6,11-di-p-tolyltetracene (2.7b):

5-chloro-6,11-di-p-tolyltetracene was synthesized analogously to 5-chloro-6,11-diphenyltetracene, compound **2.7a**, to give an red/orange solid (2.36 g, 5.33 mmol, 53 %

over 2 step): mp 197–198 ˚C; ^{1}H NMR (300 MHz, $CDCl_3$) δ 8.39 (d, *J* = 9.1 Hz, 1H), 8.35 (s, 1H), 7.76 (d, *J* = 8.1 Hz, 1H), 7.68–7.61 (m, 2H), 7.48–7.39 (m, 5H), 7.35 (s, 4H), 7.31 (d, *J* = 6.5 Hz, 1H), 7.27–7.23 (dd, *J* = 5.6, 1.9 Hz, 2H), 2.59 (s, 3H), 2.56 (s, 3H).

10-chloro-2-methyl-9-(p-tolyl)indeno[1,2,3-*fg*]tetracene (2.5b):

10-chloro-2-methyl-9-(p-tolyl)indeno[1,2,3-fg]tetracene was synthesized analogously to 9-chloro-10-phenylindeno[1,2,3-fg]tetracene, compound **2.5a**, to give an purple solid (0.5000 mg, 0.915 mmol, 81%): mp 197–198 °C; ^{1}H NMR (300 MHz, $CDCl_3$) δ 8.86 (dd, *J* = 8.9, 15.1 Hz, 2H), 8.59 (d, *J* = 9.1 Hz, 1H), 8.40 (d, *J* = 9.1 Hz, 1H), 8.32 (s, 1H), 7.73 (d, *J* = 9.1 Hz, 1H), 7.62–7.53 7.65 (dd, *J* = 9.95, 6.5 Hz, 2H), 7.61-7.57 (m, 1H), 7.53 (dd, *J* = 9.72, 5.9 Hz, 2H), 7.38-7.35 (m, 2H), 7.32-7.29 (m, 4H), 2.62 (s, 3H), 2.56 (s, 3H).

2-methyl-10-phenyl-9-(*p*-tolyl)indeno[1,2,3-*fg*]tetracene (2.4b)

In a flame dried 250 mL 2-neck round bottom flask, anhydrous THF (150 mL), compound **2.5b** (0.819 mg, 1.862 mmol), and PEPPSI–IPR™ (0.051 g, 0.074 mmol) were added and the solution was purged with nitrogen for 10 minutes. The reaction was heated to 65 ˚C, at which point phenyl magnesium bromide was added (1 M in THF, 2.793 mL, 0.5064 g, 2.793 mmol). The solution was heated, and maintained, at 65 ˚C under a nitrogen atmosphere and wrapped in aluminum foil overnight. The reaction was monitored by ^{1}H NMR. Upon complete consumption of **2.5b**, the reaction was allowed to cool to room temperature and quenched with water (2 mL). THF was removed in vacuo, then the resulting solid was dissolved in chloroform (600 mL). The organic extract was washed once with saturated $NaHCO_3$ solution, once with water, once with brine, dried over $MgSO_4$, concentrated, and placed under high vacuum overnight. Crude compound **2.4b** was dissolved in boiling chloroform followed by the addition of room temperature methanol

and placed in the refrigerator (5 °C) overnight. Compound **2.4b** was collected by vacuum filtration as a purple solid (0.515 g, 1.067 mmol, 58%); mp 179–180 °C; ^{1}H NMR (300 MHz, $CDCl_3$) δ 8.89 (dd, *J* = 8.9, 15.9 Hz, 2H), 8.45 (d, *J* = 7.8 Hz, 1H), 8.41 (s, 1H), 7.62–7.55 (m, 2H), 7.45 (d, *J* = 9.1 Hz, 1H), 7.35 (dd, *J* = 11.9, 6.7 Hz, 2H), 7.20 (dd, *J* = 9.2, 6.4 Hz, 2H), 7.13 (dd, *J* = 8.3, 6.4 Hz, 1H), 7.03 (t, *J* = 7.4 Hz, 2H), 6.91 (dd, *J* = 5.2, 3.1 Hz, 2H), 6.83–6.78 (m, 4H), 2.65 (s, 3H), 2.32 (s, 3H).

6-chloro-5,12-bis(4-fluorophenyl)-5,12-dihydrotetracene-5,12-diol (2.8c):

To a flame dried 100 mL 3-neck round bottom flask was added anhydrous THF (50 mL), which was cooled to –77 ˚C. 1-bromo-4-fluorobenzene (1.965 mL, 3.130 g, 17.89 mmol) was added to THF at –77 ˚C followed by n-butyllithium (2.5 M in hexane, 6.439 mL, 24.53 mmol). The mixture was stirred at –77 ˚C for 10 minutes to form 4-fluorophenyllitium. In a flame dried 250 mL 3-neck round bottom flask anhydrous THF (150 mL) and 6-chloro-5,12-naphthacenequinone **2.9** were combined and cooled to –77 ˚C. The 4-fluorophenyllitium was transferred into the 250 mL round bottom flask containing the slurry of THF and 6-chloro-5,12-naphthacenequinone via cannula at a constant flow. The mixture was allowed to react at –77 ˚C for 2 hours then allowed to warm to room temperature and stirred for an additional hour. The reaction was quenched with water (2 mL). The crude reaction mixture was concentrated to a solid and carried forward without purification.

5-chloro-6,11-bis(4-fluorophenyl)tetracene (2.7c):

The crude reaction mixture of compound **2.8c** was dissolved in 100 mL of dioxane and poured into a 250 mL round bottom flask. Tin (II) chloride (5.652 g, 29.81 mmol) and BF_3•OEt_2 (2.207 mL, 2.538 g, 17.89 mmol) were added to the 250 mL round bottom. The

reaction mixture was heated to reflux (106 ˚C) and reflux was maintained for 45 minutes. The reaction mixture was then allowed to cool to room temperature and quenched with saturated aqueous $NaHCO_3$ solution, followed by addition of solid $NaHCO_3$ until the aqueous portion is basic as indicated by pH paper. The precipitate that formed was removed via filtration over Celite®. The filtered solid was washed with chloroform (3 × 250 mL). The filtrate and chloroform washes were combined and washed once with water, once with saturated brine, dried over $MgSO_4$, concentrated and placed under high vacuum overnight. The crude product was dissolved in boiling chloroform followed by the addition of room temperature methanol and placed in the refrigerator (5 °C) overnight. This gave compound **2.7c**, an orange/red solid (2 steps 1.425 g, 3.160 mmol, 53%): mp 207–208 ˚C; ^{1}H NMR (500 MHz $CDCl_3$) δ 8.40 (d, *J* = 9.1 Hz, 1H), 8.28 (s, 1H), 7.77 (d, *J* = 8.6 Hz, 1H), 7.66 – 7.60 (m, 1H), 7.60–7.55 (m, 1H), 7.50–7.47 (m, 3H), 7.45–7.34 (m, 6H), 7.30–7.27 (m, 2H), 7.25–7.23 (m, 1H); ^{13}C NMR (126 MHz $CDCl_3$) δ 163.5 (d, *J* = 21.8 Hz), 161.5 (d, *J* = 20.7 Hz), 137.8 (d, *J* = 3.6 Hz), 137. 2, 135.1, 135.0 (d, *J* = 3.6 Hz), 133.0 (d, *J* = 7.9 Hz), 132.9 (d, *J* = 7.8 Hz), 132.0, 130.8, 130.3, 130.2, 129.4, 128.8, 128.6, 127.3 (d, *J* = 6.8 Hz), 126.6, 126.3, 125.7, 125.6, 125.5, 125.4, 125.0, 115.8 (d, *J* = 21.3 Hz), 114.8 (d, *J* = 21.3 Hz) (not all carbon signals are resolved); ^{19}F NMR (379 MHz) δ -115.43–-115.60 (m) -116.84 (ddd, *J* = 14.3, 8.8, 5.6 Hz); IR (Thin Film) ν 3073, 1602, 1509, 1461, 1389 cm^{-1}; HRMS (GC-QTOF) m/z: $[M]^+$ Calcd for $C_{30}H_{17}ClF_2$ 450.0987, found 450.0972.

10-chloro-2-fluoro-9-(4-fluorophenyl)indeno[1,2,3-*fg*]tetracene (2.5c):

Compound **2.3.7c** (1.425 g, 3.165 mmol) was dissolved in chloroform (20 mL) and the solution was purged with nitrogen for 3 minutes. Methanesulfonic acid was then added (80 mL) and the solution was purged with nitrogen for 5 minutes. 2,3-Dichloro-5,6-dicyano-1,4-benzoquinone (DDQ) (0.862 g, 3.798 mmol) was added to the mixture of chloroform and methanesulfonic acid and the solution was again purged with nitrogen for an additional 5 minutes. The reaction was stirred under nitrogen atmosphere for 3h, wrapped in aluminum foil to shield the mixture from light. The reaction progress was monitored by ^{1}H NMR and TLC, looking for the disappearance of fluorescence of the **2.7c** spot. The reaction was quenched by adding saturated $NaHCO_3$ solution (approximately 100 mL, CAUTION: Gas evolution, exothermic) to the reaction followed by pouring the reaction mixture into a separatory funnel containing solid $NaHCO_3$ (at least 10g CAUTION: Gas evolution, exothermic). After allowing to cool to room temperature, the mixture was extracted with chloroform (3 × 200 mL) and the remaining solid $NaHCO_3$ was dissolved in water. The chloroform washes were combined and washed repeatedly with saturated $NaHCO_3$ solution until the aqueous portion is clear and nearly colorless (faint yellow, usually five washes). Then the organic portion was washed repeatedly with water until the aqueous layer was no longer yellow. The organic layer was then washed with brine, dried over magnesium sulfate, concentrated and placed under high vacuum overnight. The crude product **2.5c** was dissolved in boiling chloroform followed by the addition of room temperature methanol and the mixture was placed in the refrigerator (5 °C) overnight. Compound **2.5c** was collected by vacuum filtration as a purple solid (1.150 g, 2.561, 81%): mp 295–296 ˚C; ^{1}H NMR (400 MHz $CDCl_3$) δ 8.81 (d, *J* = 8.9 Hz, 1H), 8.60 (d, *J* = 9.2 Hz, 1H), 8.46 (dd, *J* = 8.6, 5.3 Hz, 1H), 8.18 (dd, *J* = 9.9, 2.3 Hz, 1H), 7.77–7.64 (m, 2H), 7.66–7.61 (m, 1H),

7.59–7.52 (m, 1H), 7.44–7.33 (m, 3H), 7.30–7.27 (m, 2H), 7.25–7.15 (m, 1H);); ^{19}F NMR (379 MHz, CDCl3) δ -115.68 (td, *J* = 9.3, 5.2 Hz), -115.94 – -116.09 (m); IR (Thin Film) ν 2917, 1602, 1507, 1460, 1395 cm^{-1}; HRMS (GC-QTOF) m/z: $[M]^+$ Calcd for $C_{30}H_{15}ClF_2$ 448.0830; found 448.0813. A suitable ^{13}C NMR spectrum could not be obtained due to poor solubility.

2-fluoro-9-(4-fluorophenyl)-10-phenylindeno[1,2,3-*fg*]tetracene (2.4c):

In a flame dried 250 mL 2-neck round bottom flask, anhydrous THF (150 mL), compound **2.4c** (1.0981 g, 2.451 mmol), and PEPPSI–IPR™ (0.067 g, 0.09 mmol) were added and the solution was purged with nitrogen for 10 minutes. The reaction was heated to 65 ˚C, at which point phenyl magnesium bromide was added (1 M in THF, 3.677 mL, 0.667 g, 3.677 mmol). The solution was maintained at 65 ˚C under a nitrogen atmosphere and wrapped in aluminum foil overnight. The reaction was monitored by ^{1}H NMR. Upon complete consumption of **2.4c**, the reaction was allowed to cool to room temperature and quenched with water (2 mL). THF was removed in vacuo, then the resulting solid was dissolved in chloroform (600 mL). The organic extract was washed once with saturated $NaHCO_3$ solution, once with water, once with brine, dried over $MgSO_4$, concentrated, and placed under high vacuum overnight. Crude compound **2.4c** was dissolved in boiling chloroform followed by the addition of room temperature methanol and placed in the refrigerator (5 °C) overnight. Compound **2.4c** was collected by vacuum filtration as a purple solid (1.076 g, 2.193 mmol, 90%): phase change 265 ˚C, sublimes 278 ˚C; ^{1}H NMR (500 MHz $CDCl_3$) δ 8.87 (d, *J* = 8.9 Hz, 1H), 8.82 (d, *J* = 8.9 Hz, 1H), 8.54 (dd, *J* = 8.5, 5.3 Hz, 1H), 8.29 (dd, *J* = 9.9, 2.4 Hz, 1H), 7.71–7.58 (m, 2H), 7.48–7.34 (m, 2H), 7.28–7.20 (m, 4H), 7.17–

7.08 (m, 2H), 6.97–6.93 (m, 2H), 6.93–6.84 (m, 2H), 6.85–6.67 (m, 1H); ^{13}C NMR (125 MHz $CDCl_3$) δ 133.2, 133.1, 131.6, 129.4, 129.2, 129.0, 128.0, 127.7, 127.4, 126.5, 124.9, 124.8, 124.7 (d, *J* = 6.8 Hz), 123.3, 114.23 (d, *J* = 21.4 Hz), 113.1 (d, *J* = 22.8 Hz), 111.8 (d, *J* = 24.9 Hz) (not all carbon signals are resolved); ^{19}F NMR (379 MHz, CDCl3) δ -116.27 (td, *J* = 9.3, 5.2 Hz), -117.61 – -117.81 (m); IR (Thin Film) ν 2957, 2916, 2849, 1601, 1508, 1469, 1460 cm^{-1}; HRMS (GC-QTOF) m/z: [M]+ Calcd for $C_{36}H_{20}F_2$ 490.1533; found 490.1526.

6-chloro-5,12-bis(4-(trifluoromethyl)phenyl)-5,12-dihydrotetracene-5,12-diol (2.8d): 6-chloro-5,12-bis(4-(trifluoromethyl)phenyl)-5,12-dihydrotetracene-5,12-diol was synthesized analogously to 6-chloro-5,12-bis(4-fluorophenyl)-5,12-dihydrotetracene-5,12-diol, compound **5c**. The product was carried to the next step without purification.

5-chloro-6,11-bis(4-(trifluoromethyl)phenyl)tetracene (2.7d):

5-chloro-6,11-bis(4-(trifluoromethyl)phenyl)tetracene (**2.7d**) was synthesized analogously to 5-chloro-6,11-bis(4-fluorophenyl)tetracene, compound **2.7c**, to give an orange/red solid (2 steps, 2.309 g, 4.191 mmol, 46%): mp 249-250 ˚C; ^{1}H NMR (500 MHz $CDCl_3$) δ 8.38 (dd, *J* = 8.3, 1 Hz , 1H), 8.21 (s, 1H), 7.96 (d, *J* = 7.9 Hz, 1H), 7.82 (d, *J* = 7.9 Hz, 1H), 7.79 (d, *J* = 8.7 Hz, 1H), 7.66 (d, *J* = 7.8 Hz, 2H), 7.61 (d, *J* = 7.8 Hz, 2H), 7.57–7.45 (m, 3H), 7.38 (dd, *J* = 8.7, 6.1 Hz, 1H), 7.30 (dd, *J* = 7.1, 3.2 Hz, 2H); ^{13}C NMR (125 MHz $CDCl_3$) δ 146.0, 143.1, 136.9, 134.9, 131.8, 131.7, 131.5, 130.9, 130.4, 130.3 (q, 36 Hz) 129.6, 129.5 (q, 36 Hz), 129.0, 128.7, 128.6, 127.6, 127.0, 126.3, 126.1, 126.1, 125.2, 124.9, 125.7 (q, 4 Hz), 124.7 (q, 4 Hz) 124.5 (q, 270 Hz) 124.3 (q, 270 Hz) (not all carbon signals are resolved); ^{19}F NMR (379 MHz, $CDCl_3$) δ -63.36, -63.62; IR (Thin Film) ν 3074,

1616, 1461, 1406, 1324 cm^{-1}; HRMS (GC-QTOF) m/z: $[M]^+$ Calcd for $C_{32}H_{17}ClF_6$ 550.0923; found 550.0941.

10-chloro-2-(trifluoromethyl)-9-(4-(trifluoromethyl)phenyl)indeno[1,2,3-*fg*]tetracene (2.5d):

10-chloro-2-(trifluoromethyl)-9-(4-(trifluoromethyl)phenyl)indeno[1,2,3-fg]tetracene was synthesized analogously to 10-chloro-2-fluoro-9-(4-fluorophenyl)indeno[1,2,3-fg]tetracene, compound **2.5c**, to give a purple/black solid (0.8479 g, 1.545 mmol, 40%): mp 259–260 ˚C; ^{1}H NMR (400 MHz $CDCl_3$) δ 8.89 (d, *J* = 8.9 Hz, 1H), 8.84 (d, *J* = 8.8 Hz, 1H), 8.71 (s, 1H), 8.64 (d, *J* = 8.2 Hz, 1H), 8.58 (d, *J* = 9.1 Hz, 1H), 7.87–7.81 (m, 2H), 7.82–7.68 (m, 3H), 7.64–7.55 (m, 4H), 7.41 (dd, *J* = 10.1, 6.4 Hz, 1H); ^{19}F NMR (379 MHz, CDCl3) δ -63.05, -63.45; IR (Thin Film) ν 3071, 1679, 1617, 1595, 1432, 1405, 1324 cm^{-1}; HRMS (GC-QTOF) m/z: $[M]^+$ Calcd for $C_{32}H_{15}ClF_6$ 548.0766; found 548.0774. A suitable ^{13}C NMR spectrum could not be obtained due to poor solubility.

10-phenyl-2-(trifluoromethyl)-9-(4-(trifluoromethyl)phenyl)indeno[1,2,3-*fg*]tetracene (2.4d):

In a flame dried 250 mL 3-neck round bottom flask, anhydrous toluene (150 mL), compound **2.5d** (0.8038 g, 1.467 mmol), and PEPPSI–IPR™ (0.040 g, 0.05868 mmol) were added and the solution ws purged with nitrogen for 10 minutes. The reaction was heated to 65 ˚C at which point phenylmagnesium bromide was added (1 M in THF, 2.200 mL, 2.200 mmol). The solution was maintained at 65 ˚C under a nitrogen atmosphere wrapped in aluminum foil overnight. The reaction was monitored by ^{1}H NMR. Upon complete consumption of **2.5d**, the reaction was allowed to cool to room temperature and

quenched with water (2 mL). Toluene was removed in vacuo and the resulting solid was dissolved in chloroform (600 mL). The chloroform solution was washed once with saturated $NaHCO_3$ solution, once with water, once with brine, dried over $MgSO_4$, concentrated, and placed under high vacuum overnight. The crude product was dissolved in boiling chloroform followed by the addition of room temperature methanol and placed in the refrigerator (5 °C) overnight. Compound **2.5d** was collected by vacuum filtration, a purple/black solid (0.7947 g, 1.346 mmol, 92%): mp 228–229 ˚C; ^{1}H NMR (400 MHz $CDCl_3$) δ 8.94 (d, *J* = 9.0 Hz, 1H), 8.90 (d, *J* = 8.9 Hz, 1H), 8.82 (s, 1H), 8.71 (d, *J* = 8.2 Hz, 1H), 7.82 (d, *J* = 8.1 Hz, 1H), 7.73–7.64 (m, 2H), 7.41 (d, *J* = 9.0 Hz, 1H), 7.37–7.25 (m, 5H), 7.22–7.14 (m, 1H), 7.14–6.96 (m, 4H), 6.92 (dd, *J* = 8.1, 1.3 Hz, 1H); ^{13}C NMR (125 MHz $CDCl_3$) δ 143.9, 142.2, 141.6, 140.3, 134.2, 133.6, 131.8, 131.6, 130.2, 129.6, 129.5, 129.5, 129.4, 128.9, 128.8, 128.7, 128.5, 128.4, 128.4, 127.5, 127.0, 125.2, 125.4, 124.2 (q, *J* = 3.7 Hz), 124.0, 123.7, 123.5, 120.6, 120.6 (not all carbon signals are resolved); ^{19}F NMR (379 MHz, $CDCl_3$) δ -62.92, -64.91; IR (Thin Film) ν 3060, 235l, 1615, 1551, 1448, 1364, 1324 cm^{-1}; HRMS (GC-QTOF) m/z: $[M]^+$ Calcd for $C_{38}H_{20}F_6$ 590.1469; found 590.1450.

6-chloro-5,12-bis(4-methoxyphenyl)-5,12-dihydrotetracene-5,12-diol (2.8e):

6-chloro-5,12-bis(4-methoxyphenyl)-5,12-dihydrotetracene-5,12-diol was synthesized analogously to 6-chloro-5,12-bis(4-fluorophenyl)-5,12-dihydrotetracene-5,12-diol, compound **5c**. The product was carried to the next step without purification.

5-chloro-6,11-bis(4-methoxyphenyl)tetracene (2.7e):

5-chloro-6,11-bis(4-methoxyphenyl)tetracene (**2.7e**) was synthesized analogously to 5-chloro-6,11-bis(4-fluorophenyl)tetracene, compound **2.7c**, to give an orange/red solid (2 steps, 1.0323 g, 2.173 mmol, 55%): mp 205–206 ˚C; ^{1}H NMR (500 MHz $CDCl_3$) δ 8.40 (dd, *J* = 8.3, 1 Hz, 1H), 8.36 (s, 1H), 7.77 (d, *J* = 8.7 Hz, 1H), 7.74–7.67 (m, 1H), 7.68–7.62 (m, 1H), 7.49–7.40 (m, 3H), 7.39–7.30 (m, 3H), 7.29–7.23 (m, 2H), 7.23–7.14 (m, 2H), 7.15–7.06 (m, 2H), 4.01 (s, 2H), 3.98 (s, 3H); ^{13}C NMR (125 MHz $CDCl_3$) δ 159.2, 158.8, 137.8, 135.6, 134.2, 132.5, 132.4, 132.2, 131.3, 130.5, 130.4, 130.1, 129.5, 128.8, 128.6, 127.4, 126.9, 126.9, 126.5, 125.8, 125.3, 125.1, 125.0, 114.0, 113.1, 55.4, 55.3. (not all carbon signals are resolved); IR (Thin Film) ν 2953, 2834, 1607, 1511, 1460, 1388 cm^{-1}; HRMS (GC-QTOF) m/z: $[M]^+$ Calcd for $C_{32}H_{23}ClO_2$ 474.1387; found 474.1382.

10-chloro-2-methoxy-9-(4-methoxyphenyl)indeno[1,2,3-*fg*]tetracene (2.5e):

10-chloro-2-methoxy-9-(4-methoxyphenyl)indeno[1,2,3-fg]tetracene was synthesized analogously to 10-chloro-2-fluoro-9-(4-fluorophenyl)indeno[1,2,3-fg]tetracene, compound **2.5c**, to give an purple/black solid (0.341 g, 0.721 mmol, 69%): mp 260–264 ˚C; ^{1}H NMR (400 MHz $CDCl_3$) δ 8.83 (d, *J* = 5.1 Hz, 1H), 8.81 (d, *J* = 5.2 Hz, 1H), 8.63 (d, *J* = 9.1 Hz, 1H), 8.43 (d, *J* = 8.5 Hz, 1H), 8.08 (d, *J* = 2.3 Hz, 1H), 7.77 (d, *J* = 9.1 Hz, 1H), 7.67 (dd, *J* = 9.3, 5.9 Hz, 1H), 7.60 (dd, *J* = 9.3, 5.9 Hz, 1H), 7.55 (dd, *J* = 8.7, 6.9 Hz, 1H), 7.41–7.30 (m, 3H), 7.18–7.09 (m, 2H), 7.05 (dd, *J* = 8.5, 2.3 Hz, 1H), 4.07 (s, 3H), 4.01 (s, 3H); IR (Thin Film) ν 3058, 2934, 2832, 1606,1576, 1510, 1460, 1431, 1397 cm^{-1}; HRMS (GC-QTOF) m/z: $[M]^+$ Calcd for $C_{32}H_{21}ClO_2$ 472.1230, found 472.1237. Due to poor solubility, a ^{13}C NMR spectrum could not be obtained.

2-methoxy-9-(4-methoxyphenyl)-10-phenylindeno[1,2,3-*fg*]tetracene (2.4e):

2-methoxy-9-(4-methoxyphenyl)-10-phenylindeno[1,2,3-fg]tetracene, compound **2.4e**, was synthesized analogously to 2-fluoro-9-(4-fluorophenyl)-10-phenylindeno[1,2,3-fg]tetracene, compound **8c**, to give a purple solid (0.2020 g, 0.393 mmol, 54%): mp 212–213 ˚C; ^{1}H NMR (400 MHz $CDCl_3$) δ 8.85 (d, *J* = 8.9 Hz, 1H), 8.83 (d, *J* = 8.9 Hz, 1H), 8.47 (d, *J* = 8.5 Hz, 1H), 8.15 (d, *J* = 2.3 Hz, 1H), 7.58 (ddd, *J* = 8.8, 6.4, 1.0 Hz, 2H), 7.55 (ddd, *J* = 8.8, 6.4, 1.0 Hz, 2H), 7.44 (d, *J* = 9.1 Hz, 1H), 7.36 (d, *J* = 9.1 Hz, 1H), 7.23–7.17 (m, 2H), 7.14–7.04 (m, 4H), 6.93 (dd, *J* = 8.0, 1.2 Hz, 2H), 6.57 (dd, *J* = 8.6, 2 Hz, 1H), 4.07 (s, 2H), 3.84 (s, 2H); ^{13}C NMR (125 MHz $CDCl_3$) δ δ 159.1, 157.8, 141.5, 141.2, 140.6, 139.2, 134.4, 133.9, 133.0, 132.7, 132.5, 131.6, 131.1, 130.8, 129.3, 129.3, 128.8, 128.1, 127.4, 127.2, 127.1, 126.0, 124.7, 124.7, 124.4, 124.3, 123.8, 123.5, 113.0, 111.7, 110.9, 55.8, 55.3. (not all carbon signals are resolved); IR (Thin Film) ν 3000, 2954, 2834, 1675, 1607, 1573, 1511, 1461, 1441, 1411, 1389, 1360, 1315 cm^{-1}; HRMS (GC-QTOF) m/z: $[M]^+$ Calcd for $C_{38}H_{26}O_2$ 514.1933; found 514.1926.

2.6 References:

(1) Zhou, Y.; Ding, L.; Shi, K.; Dai, Y. Z.; Ai, N.; Wang, J.; Pei, J. *Adv. Mater.* **2012**, *24*, 957.

(2) Zhang, J.; Li, C. Z.; Williams, S. T.; Liu, S.; Zhao, T.; Jen, A. K. *J. Am. Chem. Soc.* **2015**, *137*, 2167.

(3) Kim, Y.; Park, G.; Choi, S.; Lee, D.; Cho, M.; Choi, D. *J. Mater. Chem. C* **2017**, *5*, 7182.

(4) Hwang, Y. J.; Li, H.; Courtright, B. A.; Subramaniyan, S.; Jenekhe, S. A. *Adv. Mater.* **2016**, *28*, 124.

(5) Meng, D.; Sun, D.; Zhong, C.; Liu, T.; Fan, B.; Huo, L.; Li, Y.; Jiang, W.; Choi, H.; Kim, T.; Kim, J. Y.; Sun, Y.; Wang, Z.; Heeger, A. J. *J. Am. Chem. Soc.* **2016**, *138*, 375.

(6) Hendsbee, A. D.; Sun, J. P.; Rutledge, L. R.; Hill, I. G.; Welch, G. C. *J. Mater. Chem. A* **2014**, *2*, 4198.

(7) Jones, B. A.; Ahrens, M. J.; Yoon, M. H.; Facchetti, A.; Marks, T. J.; Wasielewski, M. R. *Angew. Chem., Int. Ed.* **2004**, *43*, 6363.

(8) Chase, D. T.; Fix, A. G.; Rose, B. D.; Weber, C. D.; Nobusue, S.; Stockwell, C. E.; Zakharov, L. N.; Lonergan, M. C.; Haley, M. M. *Angew. Chem. Int. Ed.* **2011**, *50*, 11103.

(9) Li, M. M.; Liu, Y. T.; Ni, W.; Liu, F.; Feng, H. R.; Zhang, Y. M.; Liu, T. T.; Zhang, H. T.; Wan, X. J.; Kan, B.; Zhang, Q.; Russell, T. P.; Chen, Y. S. *J. Mater. Chem. A* **2016**, *4*, 10409.

(10) Rananaware, A.; Gupta, A.; Kadam, G.; Duc La, D.; Bilic, A.; Xiang, W.; Evans, R., A.; Bhosale, S., V. *Mater. Chem. Front.* **2017**, *1*, 2511.

(11) Gupta, A.; Rananaware, A.; Srinivasa Rao, P.; Duc La, D.; Bilic, A.; Xiang, W.; Li, J.; Evans, R., A.; Bhosale, S., V.; Bhosale, S., V. *Mater. Chem. Front.* **2017**, *1*, 1600.

(12) Liu, F.; Zhou, Z.; Zhang, C.; Vergote, T.; Fan, H.; Liu, F.; Zhu, X. *J. Am. Chem. Soc.* **2016**, *138*, 15523.

(13) Li, M.; Liu, Y.; Ni, W.; Liu, F.; Feng, H.; Zhang, Y.; Liu, T.; Zhang, H.; Wan, X.; Kan, B.; Zhang, Q.; Russell, T. P.; Chen, Y. *J. Mater. Chem. A* **2016**, *4*, 10409.

(14) Zhao, W.; Li, S.; Yao, H.; Zhang, S.; Zhang, Y.; Yang, B.; Hou, J. *J. Am. Chem. Soc.* **2017**, *139*, 7148.

(15) Diao, Y.; Shaw, L.; Bao, Z.; Mannsfeld, S. C. B. *Energy Environ. Sci.* **2014**, *7*, 2145.

(16) Eftaiha, A. F.; Sun, J. P.; Hill, I. G.; Welch, G. C. *J. Mater. Chem. A* **2014**, *2*, 1201.

(17) Kondratenko, M.; Moiseev, A. G.; Perepichka, D. F. *J. Mater. Chem.* **2011**, *21*, 1470.

(18) Li, S. X.; Yan, J. L.; Li, C. Z.; Liu, F.; Shi, M. M.; Chen, H. Z.; Russell, T. P. *J. Mater. Chem. A* **2016**, *4*, 3777.

(19) Shen, Z.; Xu, B.; Liu, P.; Hu, Y.; Yu, Y.; Ding, H.; Kloo, L.; Hua, J.; Sun, L.; Tian, H. *J. Mater. Chem. A* **2017**, *5*, 1242.

(20) Jiang, H.; Ferrara, G.; Zhang, X.; Oniwa, K.; Islam, A.; Han, L.; Sun, Y. J.; Bao, M.; Asao, N.; Yamamoto, Y.; Jin, T. *Chemistry* **2015**, *21*, 4065.

(21) Deng, Y.; Xu, B.; Castro, E.; Fernandez-Delgado, O.; Echegoyen, L.; Baldridge, K., K.; Siegel, J., S. *Euro. J. Org. Chem.* **2017**, *2017*, 4338.

(22) Lee, C. H.; Plunkett, K. N. *Org. Lett.* **2013**, *15*, 1202.

(23) Zhu, X. J.; Bheemireddy, S. R.; Sambasivarao, S. V.; Rose, P. W.; Guzman, R. T.; Walther, A. G.; DuBay, K. H.; Plunkett, K. N. *Macromolecules* **2016**, *49*, 127.

(24) Lu, R. Q.; Zheng, Y. Q.; Zhou, Y. N.; Yan, X. Y.; Lei, T.; Shi, K.; Zhou, Y.; Pei, J.; Zoppi, L.; Baldridge, K. K.; Siegel, J. S.; Cao, X. Y. *J. Mater. Chem. A* **2014**, *2*, 20515.

(25) Chen, H.-Y.; Golder, J.; Yeh, S.-C.; Lin, C.-W.; Chen, C.-T.; Chen, C.-T. *RSC Advances* **2015**, *5*, 3381.

(26) Gu, X.; Luhman, W. A.; Yagodkin, E.; Holmes, R. J.; Douglas, C. J. *Org. Lett.* **2012**, *14*, 1390.

(27) Zhai, L.; Shukla, R.; Rathore, R. *Org. Lett.* **2009**, *11*, 3474.

(28) Zhai, L.; Shukla, R.; Wadumethrige, S. H.; Rathore, R. *J. Org. Chem.* **2010**, *75*, 4748.

(29) Grzybowski, M.; Skonieczny, K.; Butenschon, H.; Gryko, D. T. *Angew. Chem. Int. Ed. Engl.* **2013**, *52*, 9900.

(30) Rempala, P.; Kroulik, J.; King, B. T. *J. Am. Chem. Soc.* **2004**, *126*, 15002.

(31) Smet, M.; Van Dijk, J.; Dehaen, W. *Syn. Lett.* **1999**, *4*, 495.

(32) Eversloh, C., L. ; Avlasevich, Y.; Li, C.; Mullen, K. *Chemistry* **2011**, *17*, 12756.

(33) Lakshminarayana, A., N.; Chang, J.; Luo, J.; Zheng, B.; Huang, K. W.; Chi, C. *Chem. Commun.* **2015**, *51*, 3604.

(34) Wu, J.; Pisula, W.; Mullen, K. *Chem. Rev.* **2007**, *107*, 718.

(35) Buchholtz, F.; Zelichenok, A.; Krongauz, V. *Macromolecules* **1993**, *26*, 906.

(36) It must be noted, to remove all the inorganic tin from the product the reaction has to be made basic, filtered over diatomaceous earth and further purified via recrystallization from hot chloroform with methonal.

(37) Miao, Q.; Chi, X.; Xiao, S.; Zeis, R.; Lefenfeld, M.; Siegrist, T.; Steigerwald, M. L.; Nuckolls, C. *J. Am. Chem. Soc.* **2006**, *128*, 1340.

(38) Purvis, L. J.; Gu, X.; Ghosh, S.; Zhang, Z.; Cramer, C. J.; Douglas, C. J. *J. Org. Chem.* **2018**, *83*, 1828.

(39) Yagodkin, E.; Douglas, C. J. *Tet. Lett.* **2010**, *51*, 3037.

(40) O'Brien, C. J.; Kantchev, E. A.; Valente, C.; Hadei, N.; Chass, G. A.; Lough, A.; Hopkinson, A. C.; Organ, M. G. *Chem. Eur. J.* **2006**, *12*, 4743.

(41) Compounds 2.4d-e were chraterized by ^{1}H, ^{13}C, ^{19}F NMR and IR. HRMS was done via QTOF and ESI. Single-crystal X-ray structures were obtain for compounds 2.4d-e, f.

(42) Dexter, D., L., *J. Chem. Phys.* **1953**, *21*, 836.

(43) CIFs found in the supporting information of JOC paper.

(44) The degree of indenotetracene core overlap and pi-stacking distance were measured form the solved crystal structures.

(45) Coropceanu, V.; Cornil, J.; da Silva Filho, D. A.; Olivier, Y.; Silbey, R.; Bredas, J. L. *Chem. Rev.* **2007**, *107*, 926.

(46) Sonar, P.; Williams, E. L.; Singh, S. P.; Manzhos, S.; Dodabalapur, A. *Phys. Chem. Chem. Phys.* **2013**, *15*, 17064.

(47) Lan, L. Y.; Chen, Z. M.; Ying, L.; Huang, F.; Cao, Y. *Org. Elect.* **2016**, *30*, 176.

(48) Valenti, G.; Bruno, C.; Rapino, S.; Fiorani, A.; Jackson, E. A.; Scott, L. T.; Paolucci, F.; Marcaccio, M. *J. Phys. Chem. C* **2010**, *114*, 19467.

(49) Zhu, X. J.; Yuan, B. X.; Plunkett, K. N. *Tet. Lett.* **2015**, *56*, 7105.

(50) Bheemireddy, S. R.; Ubaldo, P. C.; Rose, P. W.; Finke, A. D.; Zhuang, J.; Wang, L.; Plunkett, K. N. *Angew. Chem. Int. Ed.* **2015**, *54*, 15762.

(51) Zhou, K.; Dong, H.; Zhang, H. L.; Hu, W. *Phys. Chem. Chem. Phys.* **2014**, *16*, 22448.

(52) Li, H. Y.; Earmme, T.; Subramaniyan, S.; Jenekhe, S. A. *Adv. Eng. Mater.* **2015**, *5*, 1402041.

(53) Zhou, F.; Jehoulet, C.; Bard, A. J. *J. Am. Chem. Soc.* **1992**, *114*, 11004.

(54) Kulshreshtha, C.; Kim, W., G.; Lampande, R.; Huh, H., D.; Chae, M.; Kwon, H., J. *J. Mater. Chemi. A* **2013**, *1*, 4077.

(55) Zhao, Y.; Truhlar, D. *Theor. Chem. Account.* **2007**, *120*, 215.

(56) Kwon, O. K.; Park, J. H.; Kim, D. W.; Park, S. K.; Park, S. Y. *Adv. Mater.* **2015**, *27*, 1951.

(57) Shi, X.; Liu, S.; Liu, C.; Hu, Y.; Shi, S.; Fu, N.; Zhao, B.; Wang, Z.; Huang, W. *Chem. Asian J.* **2016**, *11*, 2188.

(58) Lu, X.; Fan, S.; Wu, J.; Jia, X.; Wang, Z. S.; Zhou, G. *J. Org. Chem.* **2014**, *79*, 6480.

(59) Frischmann, P. D.; Mahata, K.; Wurthner, F. *Chem. Soc. Rev.* **2013**, *42*, 1847.

(60) Huss, A. S.; Pappenfus, T.; Bohnsack, J.; Burand, M.; Mann, K. R.; Blank, D. A. *J. Phys. Chem. A* **2009**, *113*, 10202.

(61) Li, C.; Liu, M.; Pschirer, N. G.; Baumgarten, M.; Mullen, K. *Chem. Rev.* **2010**, *110*, 6817.

(62) Vura-Weis, J.; Ratner, M. A.; Wasielewski, M. R. *J. Am. Chem. Soc.* **2010**, *132*, 1738.

(63) Ide, J.; Mereau, R.; Ducasse, L.; Castet, F.; Olivier, Y.; Martinelli, N.; Cornil, J.; Beljonne, D. *J. Phys. Chem. B* **2011**, *115*, 5593.

(64) Adamo, C.; Barone, V. *J. Chem. Phy.* **1999**, *110*, 6158.

(65) Arbeloa, F. L.; Ojeda, R. P.; Arbeloa, L. I. *J. Lumin.* **1989**, *44*, 105—112.

(66) Grabolle, M.; Spieles, M.; Lesnyak, V.; Gaponik, N.; Eychmuller, A.; Resch-Genger, U. *Anal. Chem.* **2009**, *81*, 6285.

Chapter 3: Structure-Function Relationship Between Thin Film Morphology and Organic Photovoltaic Performance of Devices Containing Asymmetrically Substituted Indenotetracenes.

3.1 Introduction:

3.1.1 General introduction:

For OSCs to operate efficiently, the molecular orientation, crystallinity, π-stacking as well as other aspects of thin film morphology, need to be controlled. There have been several studies examining different methods for controlling thin film morphology via processing techniques and/or using solvent additives.[1,2] While these new fabrication methods do demonstrate the ability to control thin film morphology, they are also highly dependent on the inherent properties of the OSC used and often require extensive optimization. Controlling solution-possessed OSC thin film morphology via functional group manipulation is another tool currently being widely researched. Historically, the functional groups employed have been heteroatoms such as N, O, or S, which can form strong intermolecular interactions. Large alkyl groups have also been used to modulate molecular ordering in the solid state, the most famous example being TIPS-pentacene.[3-5] The major disadvantage of these functional groups is that they tend to drastically change the solid-state crystal structure due to strong intermolecular interactions. For example, while pentacene orients in a herringbone packing motif in the solid-state, TIPS-pentacene arranges in a 2-D brick motif. As described earlier, changes in packing motif can dramatically alter the electron transport character of the material.[6] Alternatively, organofluorines form comparatively weak intermolecular interactions, which makes them ideal for modulating thin film morphologies.

The substitution of hydrogen with isosteric fluorine is commonly used to modulate electronic properties and improve photochemical stability.[7-9] New intermolecular C–F··X interactions, resulting from functionalization with fluorine, have been observed to affect solid-state crystal packing.[10-13] The same C–F··X intermolecular interactions that affect solid-state packing have also been observed to affect thin film morphology, and in turn, device efficiency.[14]

To better predict how functionalization of organic semiconductors affects thin film morphology and device performance, a more complete understanding of the relationship between structure and function needs to be developed.[15] This is especially true for small molecule organic semiconductors where the substitution of a single functional group can have a profound effect on solid-state properties. Recently, studies have begun to examine the effects of fluorination on thin film morphology and device performance. While there have been extensive studies on thin films of perfluorinated small molecule organic semiconductors, *e.g.* perfluoropentacene and perfluorophthalocyanines, there have been very few studies examining the effects of partial fluorination on thin film processing and morphology.[16-21] Fewer still are the number of studies done which examine morphological changes of solution-processed thin films resulting from partial fluorination of small molecule OSCs.[22-24] Therefore, to better understand the SFR of fluorines in OSC, we studied the effects of partial fluorination on solution-processed thin film morphology and device performance using asymmetric indenotetracenes (ASIs), compounds **2.4a-d**.

The analysis and conclusions of these experiments rely heavily upon synchrotron X-ray characterization techniques to determine solid-state crystal packing and thin film morphology. The observed thin film morphology was then correlated to the performance

of organic photovoltaics containing ASIs as the photodiode. Therefore, a brief introduction and background on solid-state characterization using synchrotron X-ray techniques and OPV performance measurements will be presented.

3.1.2 Thin film grazing incidence X-ray diffraction background:

The principles of X-ray diffraction are the same when using either a point source, such as copper, or a synchrotron. Diffraction effects are only observed when the wavelength of the radiation used is the same as the length scale of the periodic structures in a crystal.[25] For organic crystals, the interatomic distance of molecules within the crystal lattice is between 1.5 to 4 Å. This length scale inside an organic crystal corresponds to X-ray radiation between 3 to 8 keV in energy. In all crystals scattering does not occur from individual atoms or molecules but from crystallographic lattice planes. The ordering of each plane in the lattice is defined by its Miller indices *hkl*. For example, the lattice planes with Miller indices (100), (110), and (111) all represent unique geometric crystallographic lattice planes in the crystal. The distance between each of these planes is given by d_{hkl}, the interplanar spacing (d-spacing). For a monoclinic crystal systems, the unit cell lengths, a, b, and c, are not equal. The angles α, between c and b, and γ, between a and b, are both equal to 90˚, while the β angle, between a and c, does not equal 90˚. This unit cell geometry results in the d-spacing equation given in **equation 3.1**,

$$\frac{1}{d^2} = \frac{1}{(\sin\beta)^2}\left(\frac{h^2}{a^2} + \frac{k^2(\sin\beta)^2}{b^2} + \frac{l^2}{c^2} - \frac{2hl\cos\beta}{ac}\right) \qquad (\mathbf{3.1})$$

where *h*, *k*, and *l* are the Miller indices for a given plane, a, b, and c are the lengths of the crystallographic unit cell, and β is the angle between a and c unit cell vectors. When the d-spacing in a crystal results in coherent scattering of the impinging X-rays, the conditions

for maximum intensity are reached. This occurs when the conditions satisfy the Bragg equation (**equation 3.2**),

$$2d_{hkl} \sin \theta_B = \lambda \quad \textbf{(3.2)}$$

where d_{hkl} is the interplanar spacing, θ_B is the Bragg angle (this is the angle that results in a measurable interference peak), and λ is the wavelength of the X-ray. This can also be represented visually as shown in **Figure 3.1**.

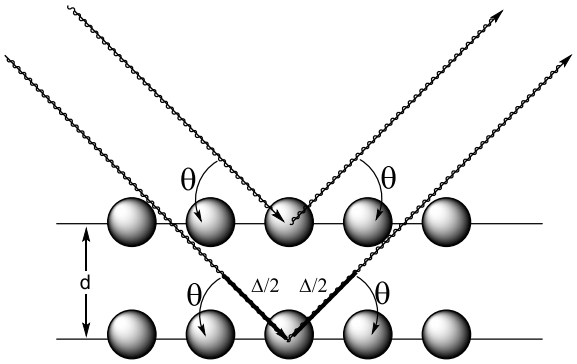

Figure 3.1: A visual representation of the Bragg equation.

When one performs an X-ray diffraction experiment what is observed are reflections which have a reciprocal relationship to corresponding crystallographic lattice plane. The reciprocal-space lattice parameters of the observed reflection relate to the real-space lattice parameters via **equations 3.3**,

$$a^* = \frac{b \times c}{V}, \quad b^* = \frac{a \times c}{V}, \quad c^* = \frac{a \times b}{V} \quad \textbf{(3.3)}$$

where a^*,b^*, and c^* are the reciprocal-space lattice parameters, a, b, and c are the real-space lattice parameters, and V is the real-space unit cell volume. The volume of a monoclinic unit cell is calculated using **equation 3.4**,

$$V = abc \sin \beta \quad \textbf{(3.4)}$$

where again a, b, and c are the lattice parameters of the monoclinic unit cell and β is the angle between a and c unit cell vectors. Using these equation, the reciprocal-space diffraction pattern obtained from the X-ray diffraction experiment is converted into a real-space crystal structure. When attempting to determine crystal structure and morphology in thin films, the most common experimental configure is grazing incidence wide-angle X-ray scattering (GIWAXS). Since the experiments herein rely on the use of an area detector, rather than a point detector, I will only be discussing the former.

The small entrance angle of the GIWAXS configuration increases the path length of the X-ray through the thin film. This allows for greater sampling of the thin film, increasing structural information obtained from the diffraction pattern. When utilizing an area detector, a significant amount of data can be obtained very quickly. The grazing incident geometry results in distortion of reciprocal space in the raw diffraction pattern.[26] [27] Polarization and χ corrections are applied and the intensity versus scattering vector components, qz and qxy, are plotted.[28] From the 2-D qzqxy plot the molecular orientation within the thin film can be assigned. Diffraction in the qxy plane results from lattice planes aligned in an edge-on manner to a substrate. Similarly, diffraction in the qz direction results from lattice planes is oriented face-on to a substrate (**Figure 3.2**). In 2-D X-ray diffraction experiments the qz is defined as the out of plane, or OOP, direction.

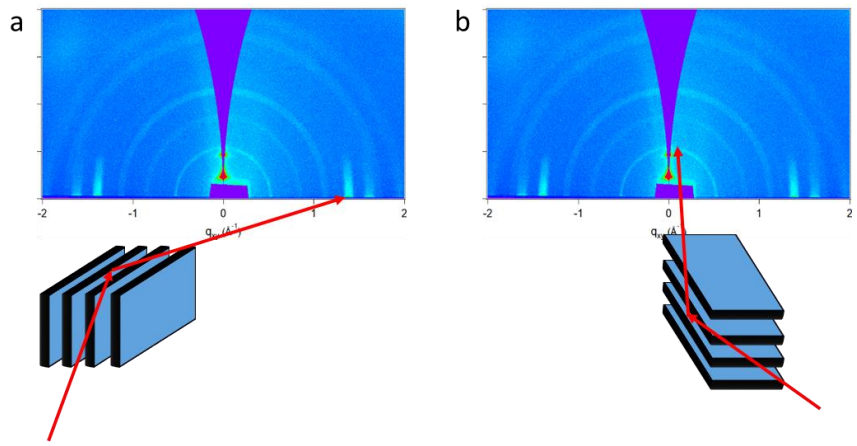

Figure 3.2: Shows the lattice plane orientations, a) in-plane and b) out-of-plane scattering in a 2-D qzqxy diffraction pattern.

The diffraction pattern also indicates the texture in the film. As shown in **Figure 3.3**, when crystallites are randomly oriented in a thin film X-ray diffraction results in a rings. The more isotopic the crystal orientation in the thin film becomes, the more spot-like the diffraction pattern becomes.

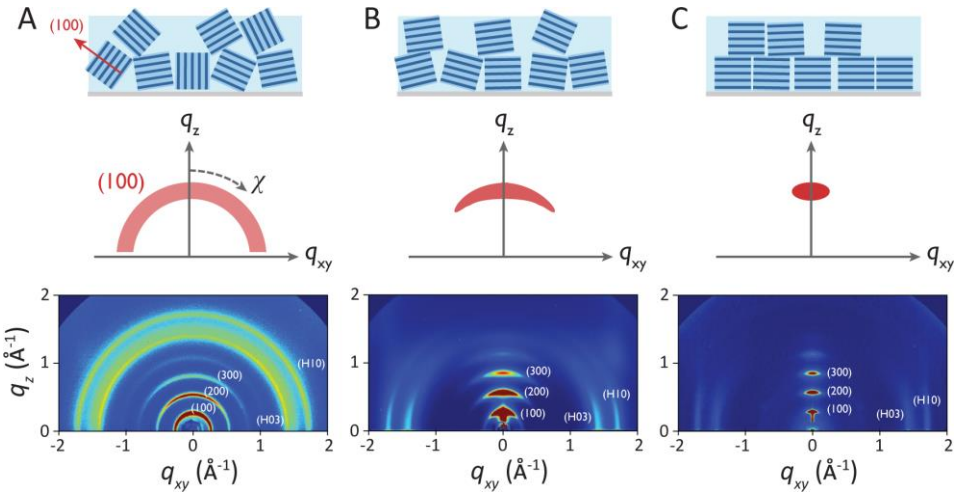

Figure 3.3: Shows the thin film texture and resulting diffraction pattern, a) randomly oriented thin film, b) preferred out-of-plane orientation, c) highly ordered thin films. Figure was taken from a review article.[29]

From the 2-D diffraction pattern, it is possible to determine both the crystal structure and molecular orientation in the thin film. Line scans can then be produced by integrating 2-D GIWAXS data over a given polar angle, giving a 1-D I vs q graph. By taking a line scan from χ = -30 to 90˚, an I vs q graph can be generated which corresponds to the powder diffraction pattern of the thin film. The I vs q powder diffraction pattern can be used to determine crystal structure as well as crystal size in the thin film.

3.1.3 Thin film X-ray absorption background:

The discovery of the shell structure of electrons has led to the development of several spectroscopic techniques for determining the properties of solids.[30] An extremely useful spectroscopic technique for determining the accurate orientation of molecules in an organic thin film is near edge X-ray absorption fine structure, or NEXAFS. The term comes from the fact that the molecular orientation in the thin film can be determined by examining the fine structure near the absorption edge. For low-Z atoms, such as carbon, nitrogen, oxygen, etc., with K-shell binding energies between 250 to 750 eV a great deal of information can be obtained about the molecule and its local environment.

The first NEXAFS experiment demonstrating a difference in K-shell near edge fine structure between CO and NO chemisorbed onto Ni(100) was published in 1981 by Stöhr and coworkers at SLAC.[31] In the case of aromatic hydrocarbons such as benzene, naphthalene, and phenanthroline, the highly directional nature of the bonding in the π-system can be used to accurately determine molecular orientation in a film. By changing the angle of the incident X-ray from parallel to normal to the substrate, and monitoring the change in absorbance, 285 ± 1 eV for C1s-π* and 294 ± 1 eV C1s-σ* resonance, the molecular orientations of aromatic hydrocarbons in thin films were determined.[30] The first

example of this was published in 1983 by the Muetterties group. By examining the K-edge absorption spectra of both carbon and nitrogen, Muetterties and coworkers were able to determine the molecular orientation of chemisorbed benzene, toluene, and pyridine. Since these original experiments, NEXAFS has been used to determine the molecular orientation of a wide range of polycyclic aromatic hydrocarbons, e.g. pentacenes, coronenes, and polymers.[32,33,20]

3.1.4 Evaluating organic photovoltaic performance:

All solar cells are evaluated by measuring the current (I)-voltage (V) characteristics of the device (**Figure 3.4**). **Figure 3.4** shows a schematic drawing of a current-voltage curve. To determine OPV performance, I-V curves are measured under AM 1.5 illumination. Open circuit voltage (V_{oc}) is the measured voltage with no current flowing through the cell. The V_{oc} is proportional to the energy difference between the HOMO of the donor molecule and the LUMO of the acceptor molecule; the larger the difference the higher the V_{oc}. The short circuit current (J_{sc}) is the maximum current in the solar cell when the voltage is zero. In a solar cell, the J_{sc} is a measure of the cell's ability to generate and collect light-generated charge carriers. The Fill Factor (FF) is a measure of the squareness of the I-V curve and the quality of the solar cell; it is determined by **equation 3.5**. From these values the maximum power (P_{max}) and the power conversion efficiency (PCE, η) can be determined. The P_{max} of a solar cell is calculated using **equation 3.6**, while the η is a measure of the fraction of incident light converted into usable electricity (**equation 3.7**). Maximum efficiency is achieved when V_{oc}, J_{sc}, and FF are as large as possible.

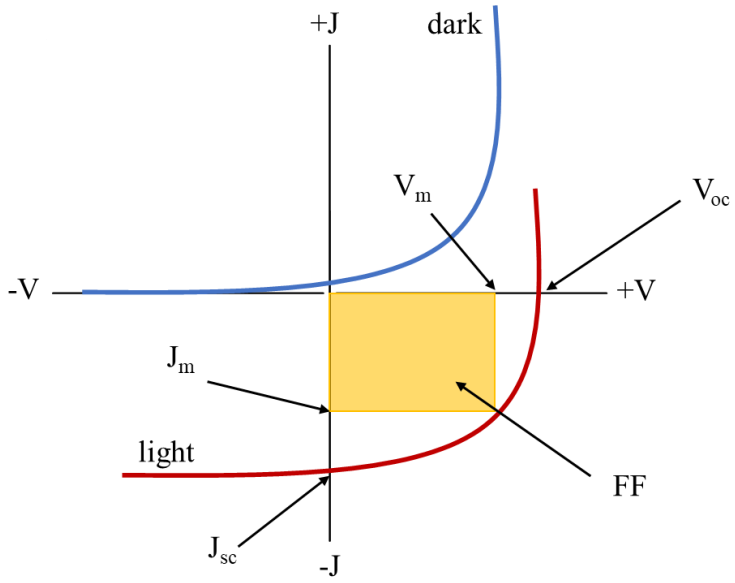

Figure 3.4: Shows a schematic depiction of a current-voltage curve

$$FF = \frac{V_m \times J_m}{V_{oc} \times J_{sc}} \quad \textbf{(3.5)}$$

$$P_{max} = V_{oc} \times J_{sc} \times FF \quad \textbf{(3.6)}$$

$$\eta = \frac{P_{max}}{P_{in}} \quad \textbf{(3.7)}$$

Using a combination of GIWAXS, NEXAFS, atomic force microscopy (AFM), and UV/Visible light absorption spectroscopy, we were able to determine thin film morphologies in OPVs containing ASI derivatives as the photodiode and correlate the observed molecular orientation to organic photovoltaic performance.

3.2 Results and discussion:

3.2.1 Thin film crystal structure determination:

The molecular packing in the thin film can often differ from what was observed in the bulk single-crystal, sometime substantially. To determine the crystal structure in the thin films, experimental I vs q patterns were compared to the calculated powder diffraction

pattern generated from the solved single crystal of compounds **2.4a-d**, shown in **Figure 3.5**. Experimental I vs q patterns were generated by integrating the 2-D diffraction patterns from χ = -30 to 90˚ where χ is defined with 0˚ = out-of-plane (OOP).

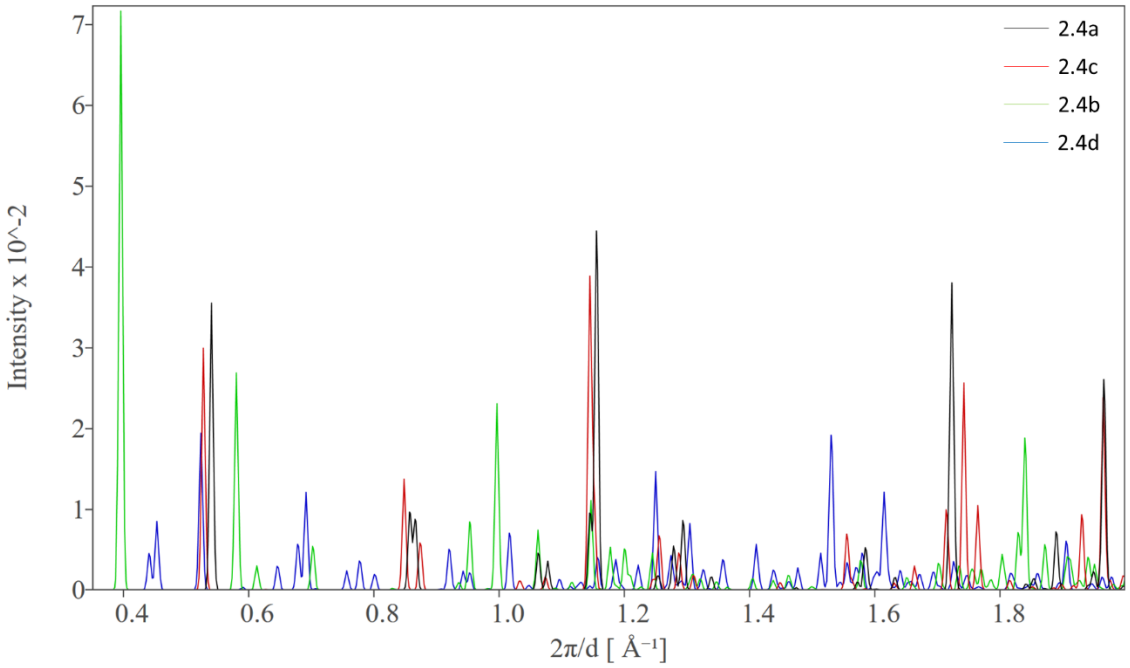

Figure 3.5: Calculated powder diffraction pattern for the crystal structures of C2/*c* compounds **2.4a**, **2.4c**, Pbca compound **2.4b**, and $P2_1/c$ compound **2.34d**.

For compound **2.4b**, which demonstrated a Pbca single-crystal structure, the thin film 2-D diffraction pattern demonstrated only polycrystalline diffraction for the all thin films on ITO/ZnO and for the thin film produced from $CHCl_3$:ODCB on Si/SiO_2 . The thin films prepared from MeTHF:Toluene on Si/SiO_2 did produce some increased diffraction signals that suggested the presence of a Pbca crystal structure; however, the thin film was still primarily polycrystalline (Appendix **Figure A1-A4**). **Figure 3.2.1.2** compares the

experimental and theoretical I vs q plots. Due to the highly polycrystalline nature of the thin film, no specific crystal structure could be determined.

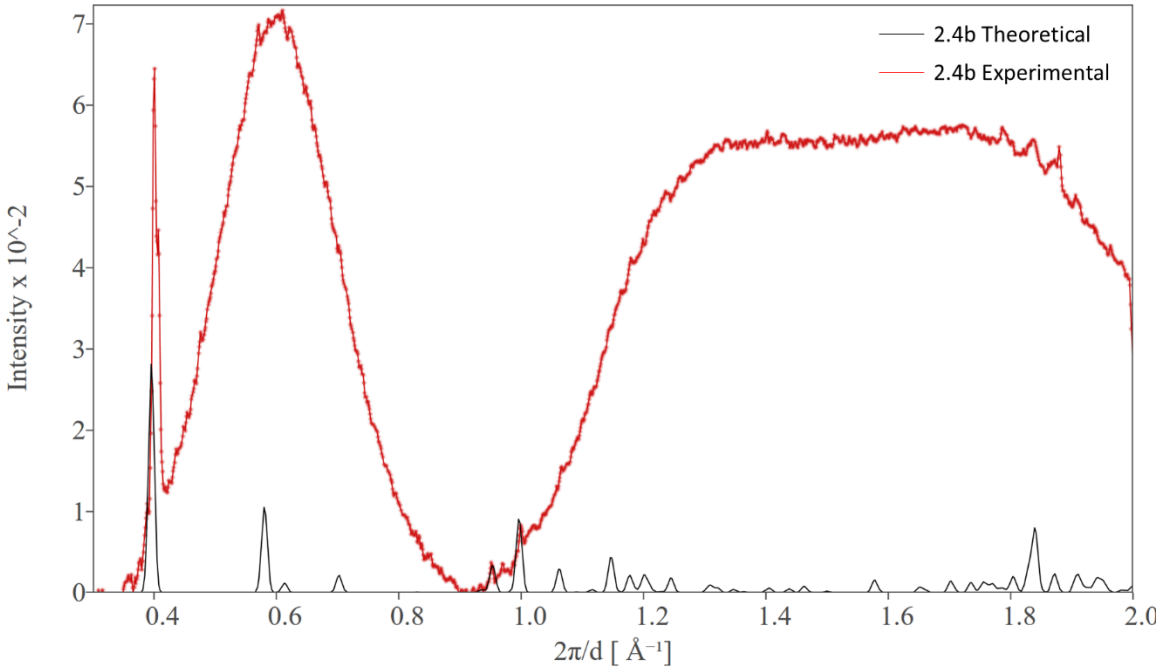

Figure 3.6: Compound **2.4b** theoretical powder diffraction pattern, the experimental I vs q plot prepared form (2:3) MeTHF:toluene solvent system Si/SiO_2 substrate and annealed at 60 ºC are shown.

Compound **2.4d**, which produced a $P2_1/c$ single-crystal structure, gave only polycrystalline X-ray scattering from the thin films (Appendix **Figures A5-A8**). **Figure 3.7** shows the experimental I vs q plot of polycrystalline thin film of compound **2.4d**. Because of the polycrystalline nature of the thin films, no specific crystal structure could be determined.

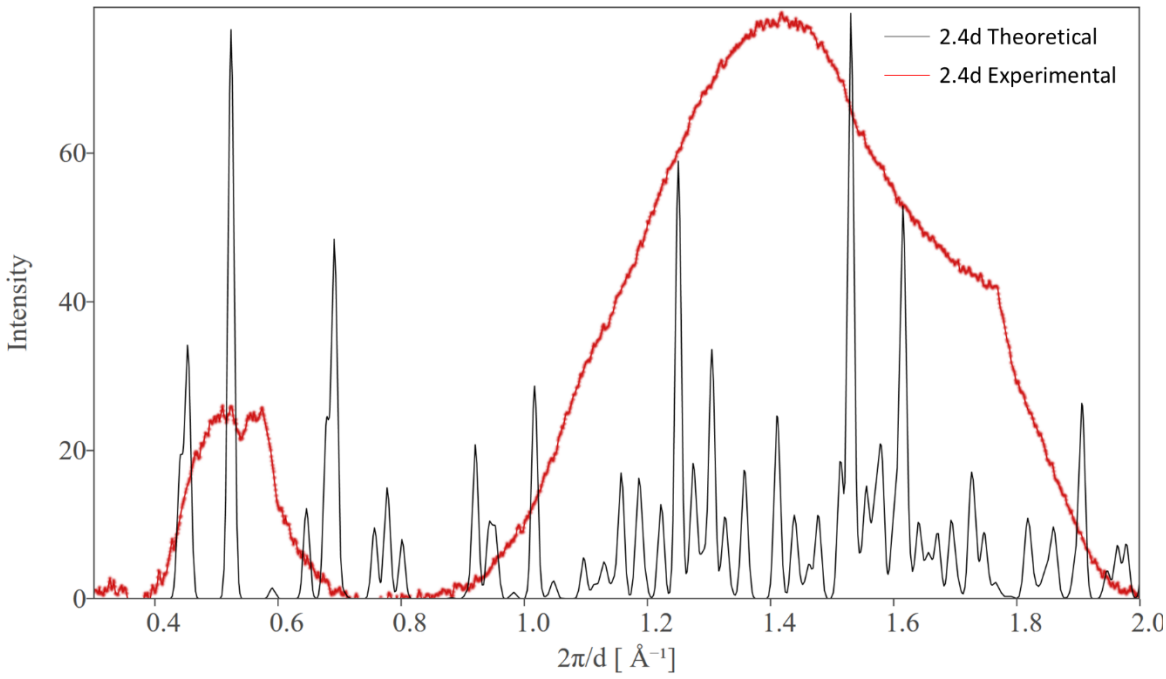

Figure 3.7: Compound **2.4d**, theoretical powder diffraction pattern, the experimental I vs q plot prepared form (2:3) MeTHF:toluene solvent system Si/SiO_2 substrate as-cast are shown. The drop in signal intensity above 1.7 $Å^{-1}$ is due to masking of interference from the Si/SiO_2 substrate.

For compounds **2.4a** and **c**, the experimental I vs q patterns were compared to several theoretical crystal systems and lattice parameters to determine whether the observed changes in peak positions were the result of either a new crystal system in the spin-coated thin films or changes in lattice parameters in the C2/*c* crystal system (Appendix **Figures A10**-**A16**). The peak broadening observed in the experimental I vs q is a result of the X-ray wavelength 0.974 Å and small crystallite size in the film, both of which can be modeled using Crystaldiffract (Appendix **Figure A17**). Peak fitting was done by modeling experimental I vs q using a Gaussian (**Figure 3.8**). The fitting was determined to be good

if the simulated diffraction pattern from the cumulative fit peak matched the experimental I vs q diffraction pattern, and if relative peak intensities, FWHM, and q peak positions of the experimentally determined I vs q peaks matched the theoretical values of a specific crystal structure (**Table A1**). The modeling of the experimental I vs q data indicated that the observed pattern matched well with the theoretical powder diffraction pattern for the C2/*c* crystal structure with small changes in the lattice parameters. **Figure 3.9** compares the theoretical diffraction, using the modified lattice parameters, of compound **2.4c** with the experimentally determined I vs q plot. (The remaining I vs q comparisons can be found in the appendix **Figures A18-A21**.) By comparing the experimental I vs q plots generated for the GIWAXS experiments and the theoretical I vs q plots from the solved single-crystal structure, the crystal structure in the thin films was determine to be the monoclinic C2/*c*. **Table 3.1** shows the modified lattice parameters of the crystal structures found in the thin films of compounds **2.4a** and **c**.

There are several possible reasons for the observed differences in the lattice parameters between the single crystal X-ray and thin films of compounds **2.4a** and **c**. Single crystal X-ray experiments were performed at -150 ˚C while all 2-D GIWAXS experiments were performed at room temperature. While one would expect the volume of the lattice to simply increase as temperature is increased, the smaller lattice volume of the room temperature samples can be explained by the observed changes in the lattice parameters and relaxation of the crystal system into a more stable crystal structure containing a smaller lattice volume. The different lattice parameters could have also resulted from small changes in lattice energies due to interactions with the substrate.

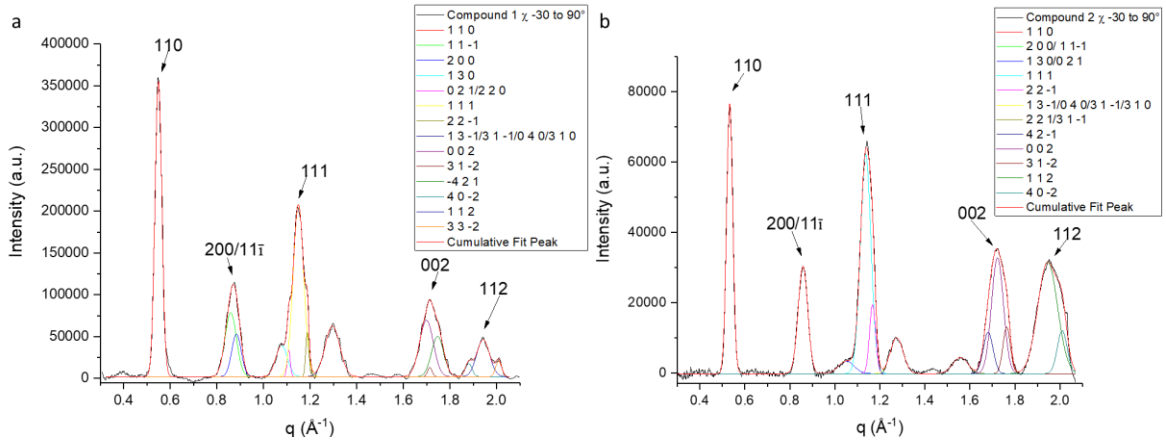

Figure 3.8: Fitted I vs q (hkl) patterns plotted on experimental I vs q, a) compound **2.4a** MeTHF:toluene on Si/SiO_2 at room temperature b) compound **2.4c** $CHCl_3$:ODCB on Si/SiO_2 annealed at 150 ˚C

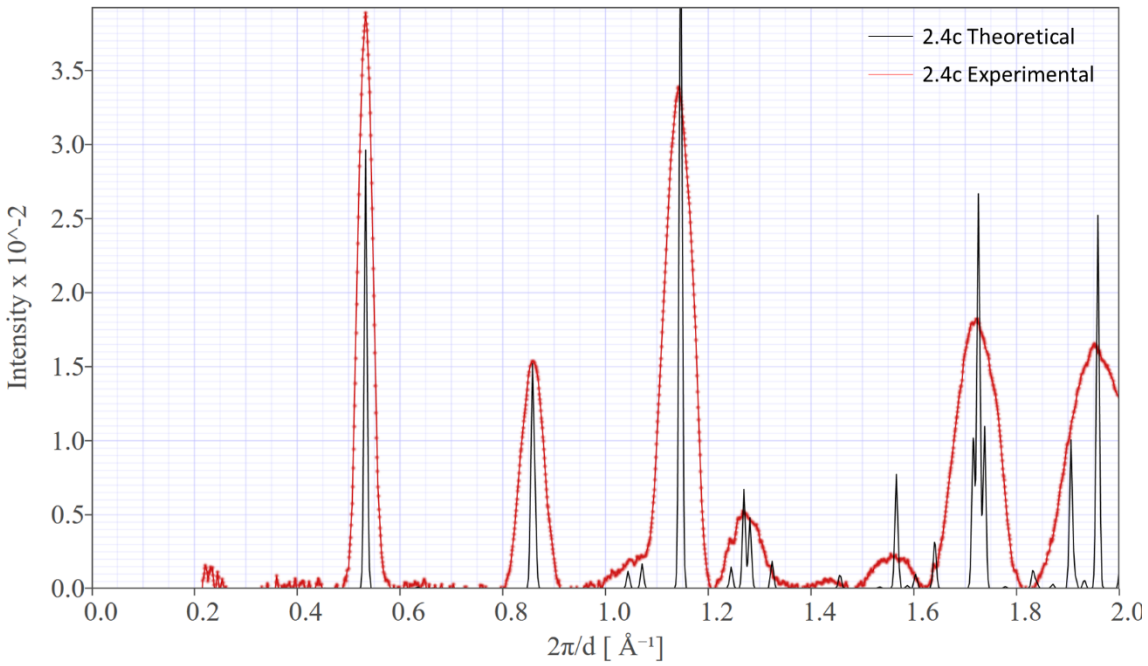

Figure 3.9: The theoretical powder diffraction patterns with the modified lattice parameters of compound **2.4c** thin films prepared from $CHCl_3$:ODCB on Si/SiO_2, annealed 150 ˚C.

Table 3.1: The determined alternative lattice parameters. [a] The calculated lattice parameters for the two primary diffraction patterns observed in in the experimental I vs q of compound **2.4a** were calculated and are presented in the table

Compound **2.4a** lattice parameters of the C2/*c* on ITO/ZnO			
	Single crystal held at -150 ˚C	As-cast Thin Film held at room temperature	150 ˚C annealed Thin Film held at room temperature [a]
Volume	2243.4 Å^3	2195.6 Å^3	2238.3/ 2254.5 Å^3
a	15.84 Å	15.43 Å	15.58/ 15.84 Å
b	19.43 Å	19.36 Å	19.16/ 19.42 Å
c	7.96 Å	7.96 Å	8.15/ 8.0 Å
α	90˚	90˚	90˚
β	113.7˚	112.6˚	113.1˚/113.7
γ	90˚	90˚	90˚
Compound **2.4c** lattice parameters of the C2/*c* on Si/SiO_2			
	Single crystal held at -150 ˚C	As-cast Thin Film held at room temperature	150 ˚C annealed Thin Film held at room temperature
Volume	2301.3 Å^3	2255.2 Å^3	2291.2 Å^3
a	15.94 Å	15.93 Å	15.89 Å
b	20.01 Å	19.49 Å	19.80 Å
c	7.76 Å	7.85Å	7.89 Å
α	90˚	90˚	90˚
β	111.7˚	112.4˚	112.7˚
γ	90˚	90˚	90˚

As stated previously, changes in crystal packing would have a dramatic effect on device efficiency. Using the experimentally determined thin film crystal structure lattice parameters for compounds **2.4a** and **c**, crystal structures were simulated using CrystalMaker to examine the changes to molecular packing. Figure **3.10** shows the intermolecular bonding distance in the solved single-crystal X-ray structure. The simulated single-crystal structure of the as-cast thin films of compound **2.4c** produced from $CHCl_3$:ODCB on Si/SiO_2 resulted in a small increase in the 1-D π-stacking distance and decrease of the alkyl spacing, less than 0.1 Å (**Figure 3.11**). Upon annealing at 150 ˚C, a

further increase in both the 1-D π-stacking spacing and alkyl spacing was observed (**Figure 3.12**). Comparing the single-crystal, as-cast, 150 ˚C annealed crystal structures of thin films of compound **2.4a** produced from MeTHF:toluene on Si/SiO_2 we observed no consistent changes in intermolecular interactions between either the 1-D π-stacking or the interplanar spacing.

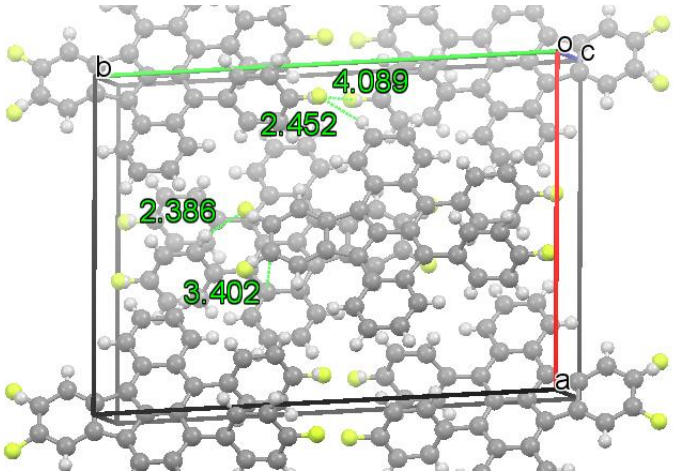

Figure 3.10: Experimentally determined single-crystal structure for compound **2.4c** showing 1-D π-stacking distance, and intermolecular C-F··H interactions between peripheral aryl groups and the indenotetracene core.

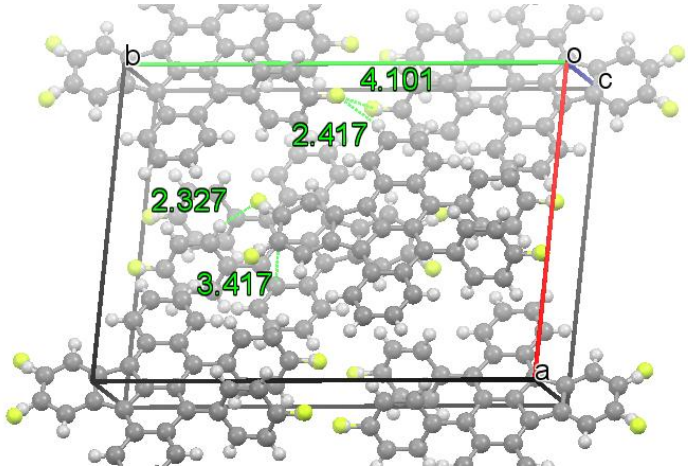

Figure 3.11: Theoretical crystal structure for compound **2.4c** in the as-cast thin film showing 1-D π-stacking distance, and intermolecular C-F··H interactions between peripheral aryl groups and the indenotetracene core.

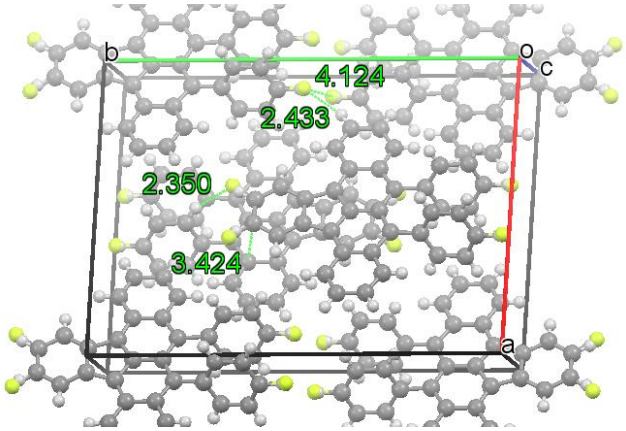

Figure 3.12: Theoretical crystal structure for compound **2.4c** in the thin filmed annealed at 150 ˚C showing 1-D π-stacking distance, and intermolecular C-F··H interactions between peripheral aryl groups and the indenotetracene core.

For compound **2.4c**, the increased 1-D π-stacking and the interplanar spacing in the as-cast thin film coincided with shorter, stronger C–F··H interactions between the fluorines of the indenotetracene core and the hydrogens of the peripheral aryl groups (**Figures 3.10**

and **3.11**). When compound **2.4c** was annealed at 150 ˚C, all C–F··H interaction distances increased but were still less than that observed in the single crystal (**Figure 3.10** and **3.12**).

For compound **2.4a**, we were unable to correlate the change in the crystal packing to any specific changes in intermolecular C–H··H or π-π interactions. From the random changes observed in the intermolecular interactions of compound **2.4a**, we can surmise that at elevated temperatures, the intermolecular C–H··H and π-π interactions were not of sufficient strength to maintain ordered crystal packing in the thin films. The simulated thin film crystal structure of compounds **2.4a** and **c** demonstrate that strategic partial fluorination of OSCs can result in the formation of intermolecular C–F··H interactions in thin films which both orient the molecules and increase the lattice energy, stabilizing the crystal structure.

3.2.2 Thin film morphology analysis:

3.2.2.1 Relating q–peaks to specific crystallographic planes:

Having determined the primary crystal structures in the thin films to be monoclinic C2/*c* for both compounds **2.4a** and **c**, the molecular orientation in the thin film could then be determined. Due to the fact that the small changes in the observed lattice parameters would result in only minimal changes in d-spacing or crystallographic plane angles, the single crystal lattice parameters of both compound **2.4a** and **c** were used to determine molecular orientation in the thin film.

Using the predicted powder diffraction pattern as a reference, each signal of the experimental I vs q plots was assigned to specific crystallographic planes. In both compounds **2.4a** and **c** q = 0.5 $Å^{-1}$ corresponds to the either the 110 or 1$\bar{1}$0 planes, q = 1.14 $Å^{-1}$ to 111 or 1$\bar{1}$1 planes, q = 1.95 $Å^{-1}$ to 112 or 1$\bar{1}$2 planes, and q = 1.17 $Å^{-1}$ to the 002

plane. For both compounds **2.4a** and **c**, the signal at q = 0.8 Å^{-1} can be produced from either the 200 or 11ī planes, but the 200 or 11ī planes were easily differentiated by their relationship/angles to other planes (**Figure 3.13**).

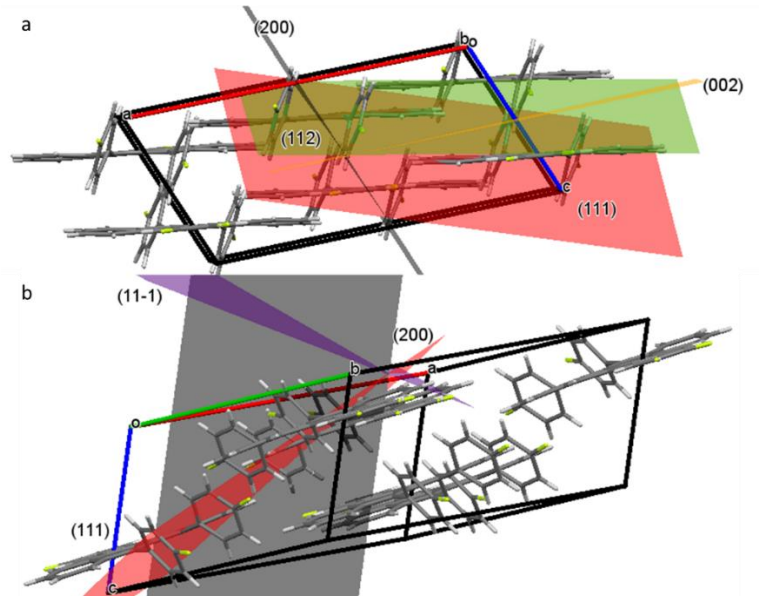

Figure 3.13: a) shows the orientation of the 200 plane relative to 111, 002, and 112; b) shows the orientation of the 11ī plane relative to 200 and 111.

Having established the crystal structure in the film to be C2/*c* for compounds **2.4a** and **c**, **equation 3.8** was used to calculate the angles between planes.[34] In **equation 3.8**, θ is the angle between two planes in the crystal lattice, h_1; k_1; l_1 and h_2; k_2; l_2 are the Miller indices of two crystallographic plane, d_1 and d_2 are the respective d-spacing, a, b, and c are the lengths of each axis of the unit cell, and β is the β angle of the monoclinic unit cell.

$$\cos\theta = \frac{d_1 d_2}{(\sin\beta)^2}\left[\frac{h_1 h_2}{a^2} + \frac{k_1\, k_2\, (\sin\beta)^2}{b^2} + \frac{l_1\, l_2}{c^2} - \frac{(l_1\, h_2 + l_2\, h_1)\cos\beta}{ac}\right] \qquad \textbf{(3.8)}$$

Thin film crystal orientations were preliminarily determined by comparing I vs q of qz from 0 to 20˚ and qxy from 70 to 90˚. A more precise thin film crystal orientation was then determined by obtaining cake-slices of the 2-D diffraction pattern from $\chi = 0$ to 90˚ in 10˚ increments. Changes in q-peak intensities from 0 to 90˚ of specific crystallographic planes were used to identify specific crystal orientations in the films. The crystal orientations determined to be present in the thin film were then used to simulate a 2-D diffraction pattern which was then compared to the experimental 2-D diffraction pattern. Using this method, the molecular orientations of both compounds **2.4a** and **c** were determined for all solution-processed thin films.

3.2.2.2 Intermolecular interactions on Si/SiO_2:

Compound 2.4a:

The as-cast thin film of compound **2.4a** prepared from $CHCl_3$:ODCB on Si/SiO_2 produce a polycrystalline 2-D diffraction pattern, as did the thin films annealed at 100 and 150 ˚C (Appendix **Figure A22**). The 2-D diffraction pattern of the thin film annealed at 60 ˚C did indicate some increased ordering but analysis of the I vs q pattern indicated the presence of several different crystal structures (Appendix **Figure A23**). Angle-resolved NEXAFS also showed no preferential molecular orientation for compound **2.4a** in the thin films on Si/SiO_2 (**Figure 3.14**). The AFM images of compound **2.4a** for the as-cast thin film showed only very smooth film with little to no texture and a root-mean-squrared (rms) roughness of 0.90 nm (**Figure 3.15a**). When thin films of compound **2.4a** were annealed at 150 ˚C, localized large aggregates were observed and the rms roughness increased to 112.59 nm (**Figure 3.15b**). The UV/Vis absorption spectra of compound **2.4a** revealed changes to the solid-state packing upon annealing at different temperatures (**Figure 3.16**).

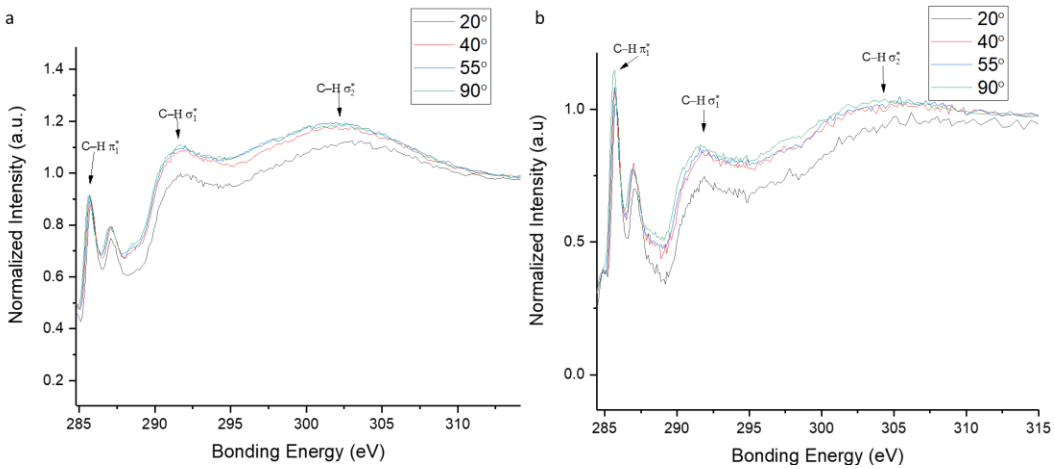

Figure 3.14: Normalized NEXAFS energy spectra of compound **2.4a** prepared from $CHCl_3$:ODCB on Si/SiO_2 a) as-cast thin film b) thin film annealed at 150 ˚C.

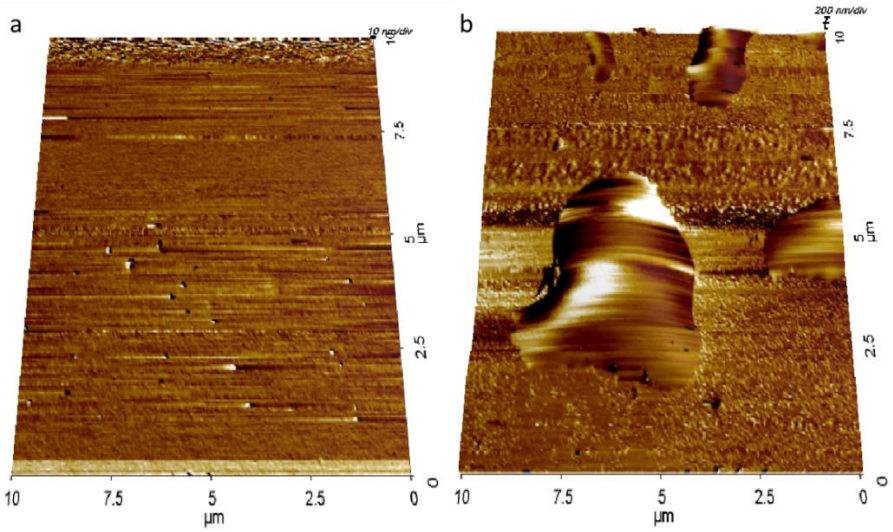

Figure 3.15: AFM images of compound **2.4a** prepared from $CHCl_3$:ODCB on Si/SiO_2 a) is the as-cast thin film b) is the thin film annealed at 150 ˚C

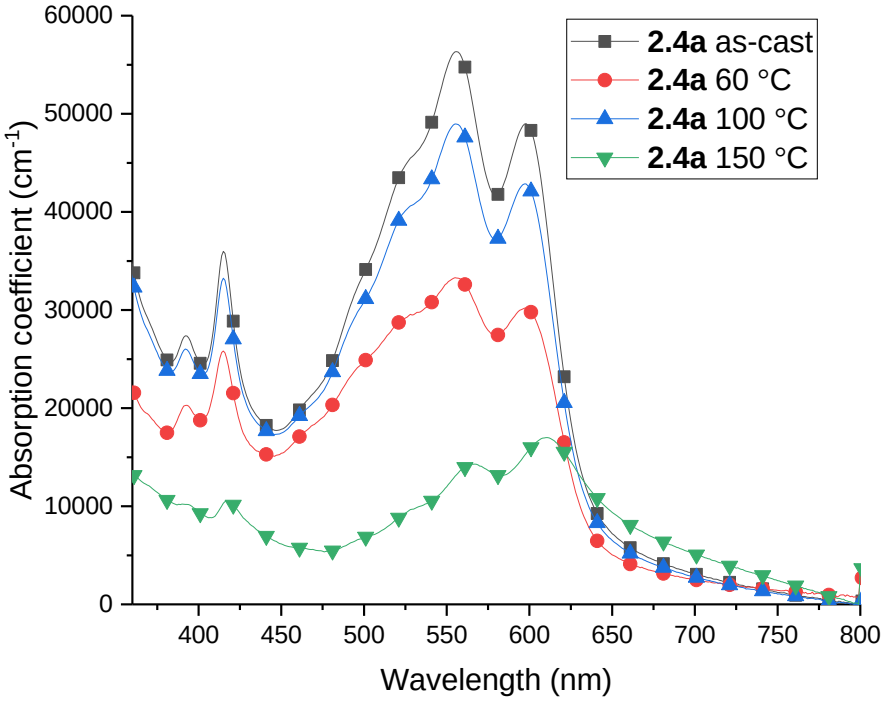

Figure 3.16: UV/Visible light absorption spectra of compound **2.4a** produced from $CHCl_3$:ODCB, as-cast, annealed at 60, 100, or 150 ˚C.

Compound 2.4c:

As-cast thin films:

To determine molecular orientation in the thin films of compound **2.4c**, prepared from $CHCl_3$:ODCB on Si/SiO_2, 9 cake-slices of 10 degrees were taken from $\chi = 0$ to 90˚, converted to I vs q plots, and background corrected. **Figure 3.17A** shows the waterfall plot of the I vs q patterns from $\chi = 0$ to 90˚. The molecular orientation in the thin films was determined by measuring the angle between planes in the solved single-crystal structure and correlating peaks in the experimental I vs q graphs to specific sets of plane orientations from $\chi = 0$ to 90˚.

From the single crystal structure, the angles between the 111 plane and the 110 and 200 planes were found to be 46.6 and 49.3˚, respectively. From the waterfall plot of I vs q graphs, the 111 plane was observed to lay parallel to the substrate, $\chi = 0$ to 20˚. We then correlated the angles between the planes to the specific I vs q signal of (110), 40 to 70˚, and (200), 50 to 80˚, peaks labeled **a**. Crystal orientation of **a** is shown in **Figure 3.17Ba**. Rotating the 111 plane normal to the substrate, we could then correlate the $q = 0.5$ Å^{-1} signals of the 110 plane, tilted between and 50 and 30˚ from qz, with the $q = 0.8$ Å^{-1} signals of the 200 plane, tilted between 70 to 90˚ from qz (peaks labeled **b**) to the thin film crystallite orientation shown in **Figure 3.17Bb**. This indicated that there were multiple crystal orientations present in the thin film. Both the **a** and **b** orientations of compound **2.4c** allow for C–F··Si interactions with the Si/SiO_2 surface. The 2-D diffraction pattern was compared to a simulated diffraction pattern, using the crystallite orientations found in the thin film, modeled using SimDiffract (**Figure 3.18**). In **Figure 3.18**, and all subsequent 2-D diffraction patterns, the theoretical diffraction pattern based on the C2/*c* crystal structure is represented by the dots with the size of the dot representing the relative intensity. The polycrystalline nature of ASI thin films was modeled by rotating select plane within the ASI crystal structure normal to perpendicular to the substrate. The experimentally observed diffraction patters were analyzed by overlaying the combined simulated diffraction pattern of select angles. Comparison of the experimental and modeled diffraction patterns showed that the two primary molecular orientations determined from the I vs q graphs would produce the experimentally observed 2-D diffraction pattern. Angle-resolved NEXAFS was again used to examine the molecular orientation of compound **2.4c** in the thin films. In the normalized NEXAFS spectra, the largest C1s-π* peak intensity occurred at both 20

and 90 degrees with deceased intensity at intermediate angles (**Figure 3.19**). The change in C1s-π* signal intensity was modeled using **equation 3.9**

$$I \propto \frac{1}{2}(P(\cos\theta)^2\,(3(\cos\alpha - 1)^2) + (\sin\alpha)^2) \qquad \textbf{3.9})$$

where I(θ) is the angle-dependent peak intensity, θ is the incident X-ray angle, P is the beam polarization, and α is the calculated average angle from the substrate. The NEXAFS experiments indicated that the π-system of compound **2.4c** had two primary orientations: parallel or perpendicular to the substrate. This indicated a mix of perpendicular and parallel molecular orientations in the thin film of compound **2.4c**. Both NEXAFS and GIWAXS experiments showed compound **2.4c** to be oriented both parallel and perpendicular, and aligned in a manner allowing for intermolecular C–F··Si interactions between **2.4c** and the Si/SiO_2 substrate.

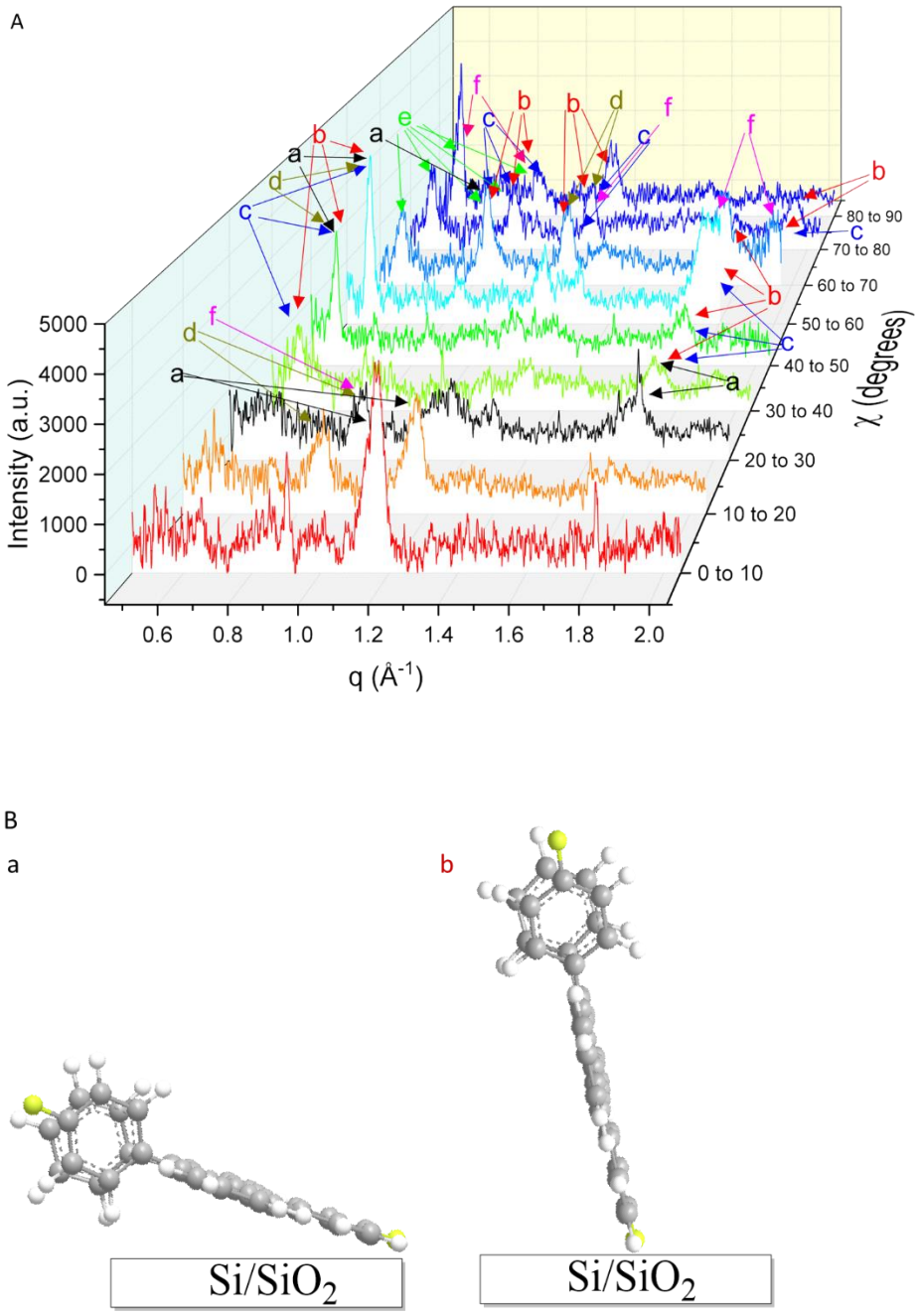

Figure 3.17: A) The waterfall plot of the I vs q from χ = 0 to 90˚. Related peaks are identified by corresponding letters. B) The 2 primary molecular orientations of compound **2.4c** identified in the I vs q and letters of the corresponding peaks, **a** and **b**, in A.

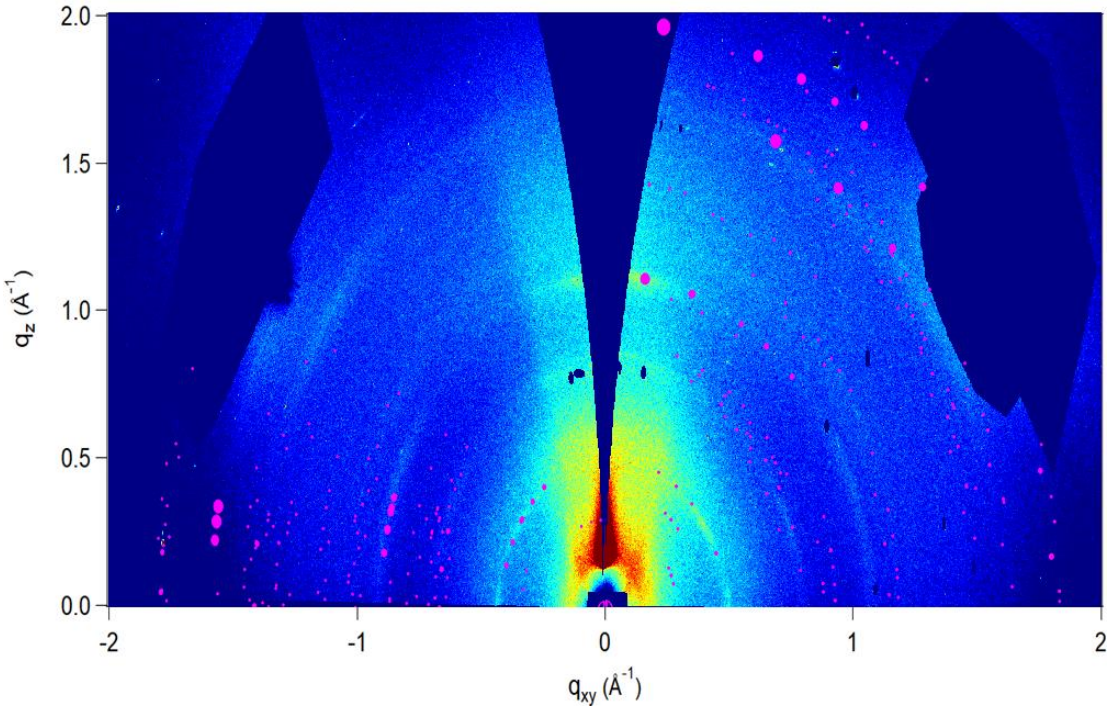

Figure 3.18: The combined 2-D qzqxy diffraction patterns of compound **2.4c** on Si/SiO_2 prepared from a solution of (2:3) $CHCl_3$:ODCB with the 111 plane oriented parallel to the substrate on the right and 200 plane oriented perpendicular to the substrate on the left.

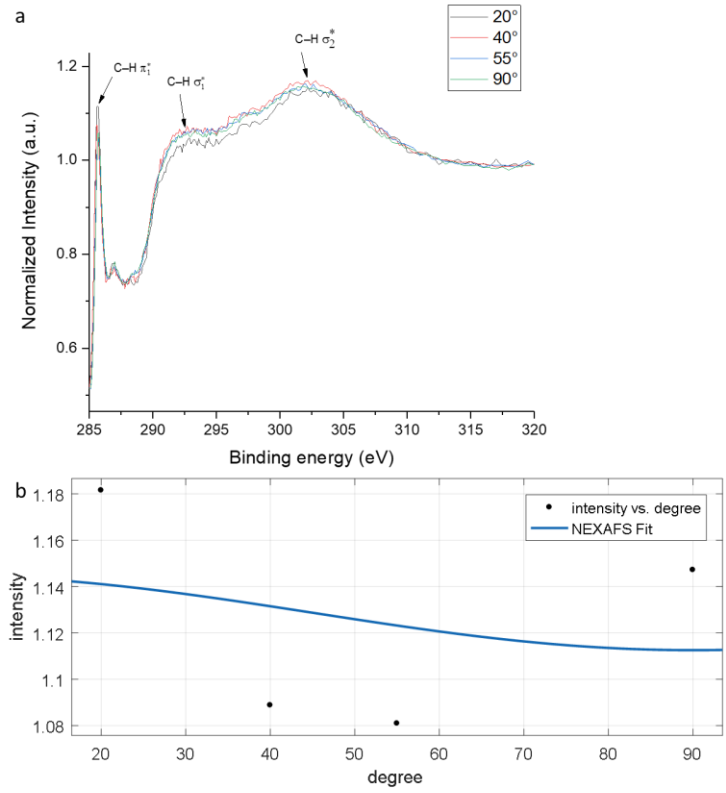

Figure 3.19: (a) The normalized NEXAFS data for incident angles of 20, 40, 55 and 90˚ of the thin film of compound **2.4c** as-cast and b) Fitted area of the π_1^* peak angle of 20, 40, 55 and 90˚ fitted to **equation 3.9**.

Annealed thin films:

Additional I vs q waterfall plots were generated for thin films of compound **2.4c** annealed at 60, 100, and 150 ˚C (**Figure 3.20**). Using the molecular orientations determined in the as-cast thin films, we were able to follow the changes in the molecular orientation in the thin films annealed at different temperatures. Upon annealing compound **2.4c**, we not only observed increased diffraction signal intensity but also increased signal intensity at high q.

Using the waterfall plot, normalized intensities versus χ were plotted for the thin film annealed at 150 ˚C. From these plots we observed that the maximum intensity of the 200 plane occurred between 40 and 50˚ while the maximum intensity for the 110 and 111 planes occurred between 60 to 70˚ and 0 to 10˚, respectively (**Figure 3.21**). Modeling the observed crystallographic orientations onto the experimental 2-D diffraction pattern, we found good agreement with the experimentally-observed diffraction pattern (**Figure 3.22**). From the GIWAXS data, we concluded that the bulk of the thin film must be oriented parallel to the substrate with a slight tilt (**Figure 3.17Ba**). We also observed that the crystallites originally oriented perpendicular to the substrate at room temperature (**Figure 3.17Bb**) did not change molecular orientation upon annealing at any temperature. NEXAFS spectra of compound **2.4c** thin films annealed at 150 ˚C showed the same large increase in C1s-π* signal at 20˚ and C1s-σ* signal at 90˚, similar to the as-cast thin film. When the NEXAFS data was fitted using **equation 3.9**, it was clear that some fraction of compound **2.4c** was still oriented perpendicular to the Si/SiO_2 substrate, the large C1s-π* at 90˚, even after annealing at 150 ºC (**Figure 3.23**).

The increased crystallinity, observed upon annealing of thin films of compound **2.4c**, was seen in both the 2-D diffraction patterns, the increased signal intensity, and AFM images of the surface. AFM images of the room temperature thin films showed smooth regions with large, localized grains ranging from 17 to 75 nm in height resulting in an rms roughness of 7.29 nm (**Figure 3.24a**). When thin films of compound **2.4c** were annealed at 150 ˚C, a large change in morphology was observed. AFM images of the thin films of compound **2.4c** indicated that the surface thin film morphology had transitioned from a primarily smooth film, with some local granular structure, to the highly textured film

shown in **Figure 3.24b**. Post 150 ˚C annealing, grain size became much more homogeneous, 10 to 40 nm, while the rms roughness almost doubled to 14.29 nm.

The increased signal intensity from the 111, 002, and 112 planes also indicates an increase in short-range molecular ordering and increased π-stacking in the film. The changes in π-stacking in the thin films were also observed via UV/Vis (**Figure 3.25**). As annealing temperature was increased from 60 to 150 ˚C, a clear increase of the absorbance at 598 nm was seen. The increased absorbance was a result of increased short range ordering/π-stacking in the thin films of compound **2.4c**.

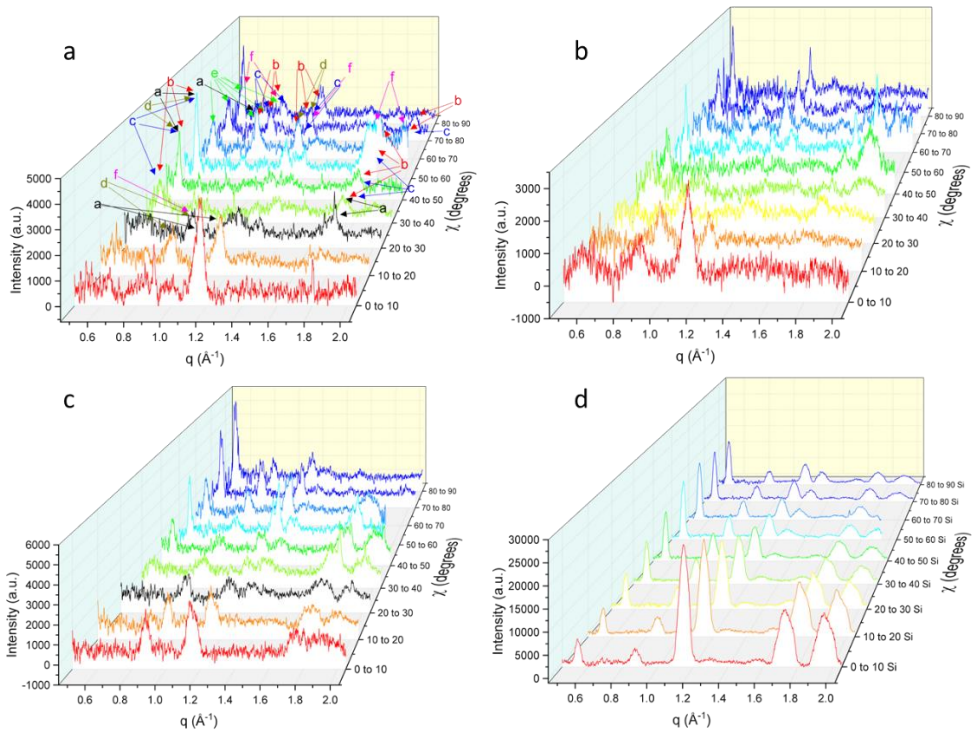

Figure 3.20: Waterfall plots of I vs q from 0 to 90˚ of compound **2.4c** thin films produced from $CHCl_3$:ODCB on Si/SiO_2, a) as-cast, b) annealed at 60 ˚C, c) annealed at 100 ˚C, d) annealed at 150 ˚C.

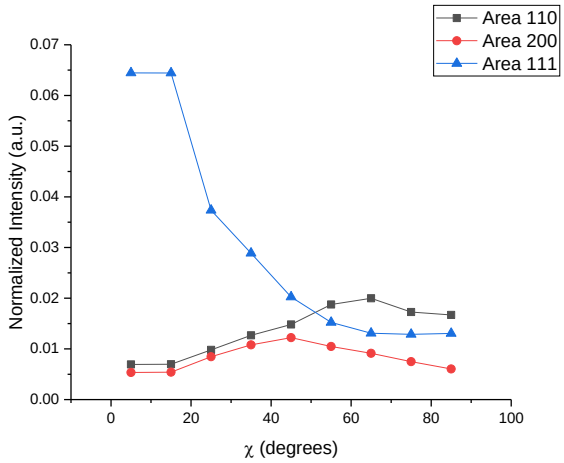

Figure 3.21: Intensity versus cake slice angle, 0 to 90˚, of the 110, 200, and 111 diffraction peaks of compound **2.4c**.

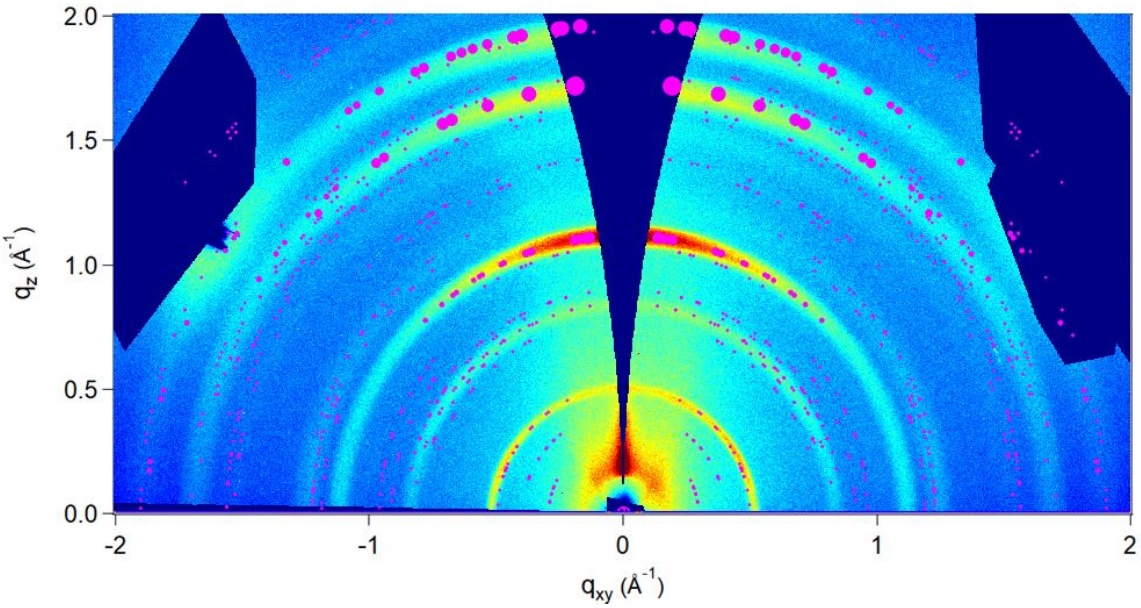

Figure 3.22: Thin film qzqxy diffraction patterns of compound **2.4c** from $CHCl_3$:ODCB on Si/SiO_2 annealed at 150 ˚C. 111, 002, and 112 planes oriented parallel to the Si/SiO_2 substrate and tilted between 0 to 20 degrees.

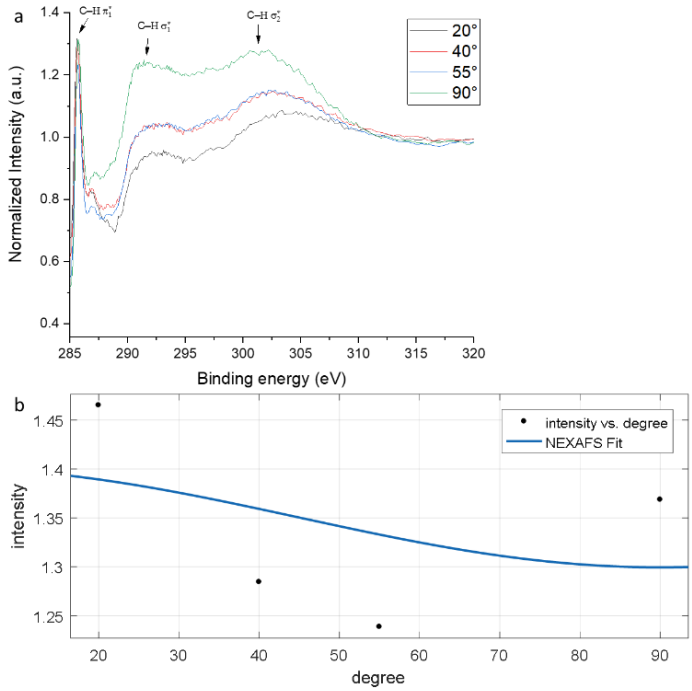

Figure 3.23: (a) The normalized NEXAFS data for incident angles of 20, 40, 55 and 90˚ of the thin film of compound **2.4c** annealed at 150 ˚C and b) Fitted area of the π_1^* peak angle of 20, 40, 55 and 90˚ fitted to **equation 3.9**.

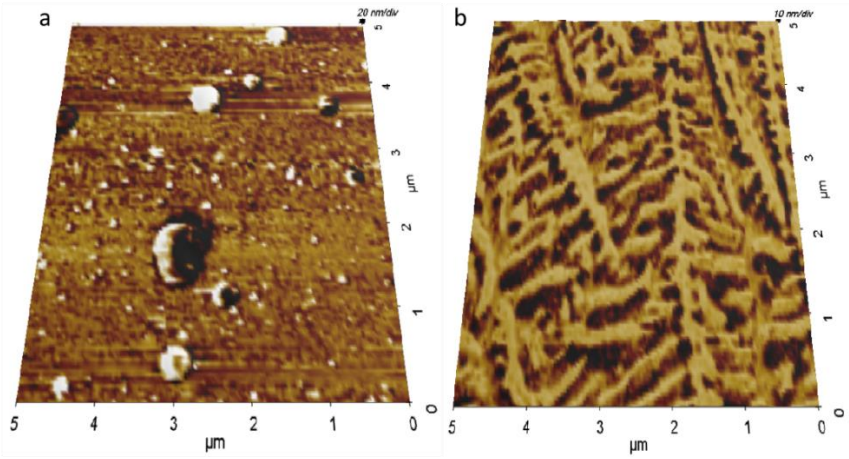

Figure 3.24: Atomic force microscopy images of compound **2.4c** on Si/SiO_2 prepared from $CHCl_3$:ODCB a) the 3-D AFM image of the as-cast thin film b) the 3-D AFM image of the thin film annealed at 150 ˚C.

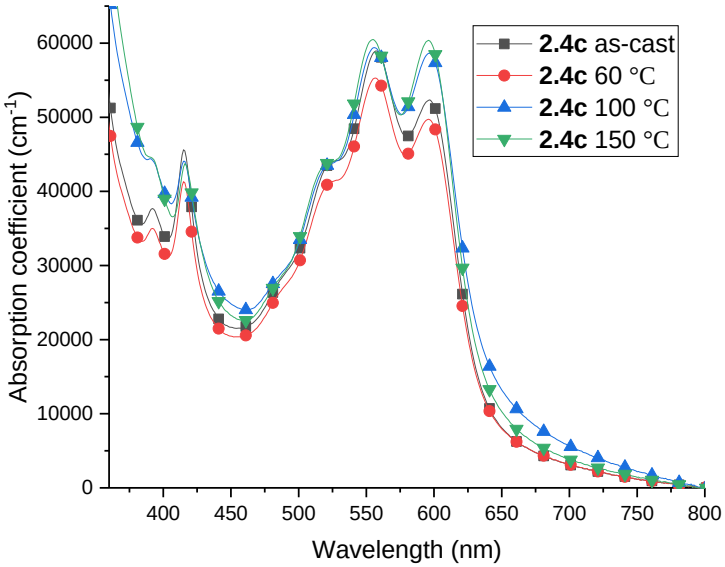

Figure 3.25: UV/Visible absorption spectrum of compound **2.4c** thin films produced from $CHCl_3$:ODCB, as-cast, annealed at 60, 100, or 150 ˚C.

Thin film morphologies of compounds 2.4a and c on Si/SiO_2:

The difference in thin film morphology between compounds **2.4a** and **c** on Si/SiO_2 is a direct result of partial fluorination of the ASI molecules and the resulting intermolecular C–F··X interactions. For organic crystals to form on the surface of a substrate, the lattice energy of the organic crystal must be large enough to overcome any increased barrier to crystallization casued by interactions with the substrate and lattice mismatch.[35]

For thin films of compound **2.4a** prepared from $CHCl_3$:ODCB, the lack of uniform crystalline thin films indicate that the intermolecular C–H··H and π-π interactions between neighboring ASI molecules were insufficient to overcome the increased crystallization

barrier, leading to predominately amorphous/pollycrystalline films with limited thermal stability. Alternatively, intermolecular C–F··X interactions did allow compound **2.4c** to produce ordered crystalline films despite the increased crystallization barrier. To better understand the role of intermolecular C–F··X interactions in the formation of crystalline thin film of compound **2.4c** on Si/SiO_2, we considered both C–F··H interactions between neighboring ASI molecules and C–F··Si interactions with the substrate.

Intermolecular C–F··X interactions in organic crystals do impart some stabilization to the crystal lattice. This lattice stabilization of the **2.4c** crystal system was evident in increased crystal stability at elevated temperatures. The increased lattice energy of solid state compound **2.4c** resulting from C–F··H interactions can be further understood by performing a Hirschfeld analysis. Comparing the Hirschfeld plots of compounds **2.4a** and **c** (**Figure 3.26**) we found that C–F··H form stronger intermolecular interactions then either C–H··H and π-π interactions. This is evidenced by shorter intermolecular distance between C–F··H interactions. We also found that C–F··X interactions comprise a significant fraction of all the interactions that occur in the crystal lattice of compound **2.4c**, at 26.7 % (Appendix **Figure A26**). This additional stabilization, resulting from the intermolecular C–F··X interactions, could have allowed compound **2.4c** to form thin films with highly ordered crystalline domains, thus overcoming any increased barrier to crystallization caused by interactions with the Si/SiO_2 substrate and lattice mismatch.

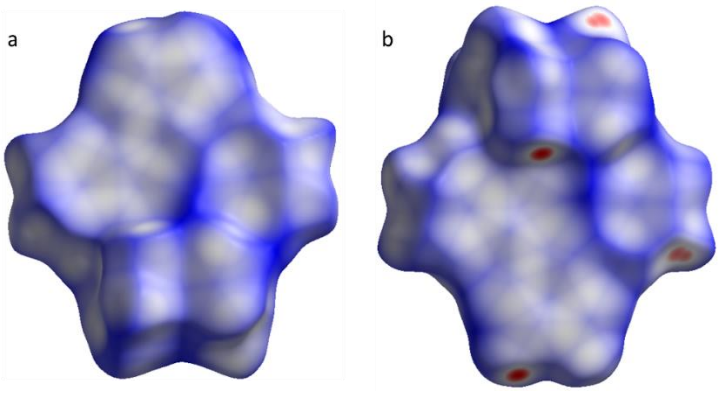

Figure 3.26: Hirschfeld surface maps of, a) compound **2.4a**, and b) compound **2.4c**.

Compounds containing organofluorines have also been observed to interact strongly with several different substrates. The as-cast thin films of compound **2.4c** were observed to have crystallites align either parallel or perpendicular to the Si/SiO_2 substrate, with an orientation allowing for C–F··Si interaction. These C–F··Si interactions could have lowered the barrier to crystallization enough to produce highly ordered crystalline thin films. Alternatively, molecules of compound **2.4c**, which were oriented perpendicular to the Si/SiO_2, could have formed a buffer layer between the Si/SiO_2 substrate and the bulk of film. This newly formed buffer layer could have allowed compound **2.4c** to orient parallel to the substrate on top of this perpendicular buffer layer. To determine the significance of the C–F··Si interaction on the thin film morphology of compound **2.4c**, the substrate was switched to ITO/ZnO.

3.2.2.3 Intermolecular C–F··X Interactions on ITO/ZnO:

Compound 2.4a:

On Si/SiO_2, thin films of compound **2.4a** were found to be predominantly polycrystalline. Switching the substrate to ITO/ZnO resulted in some molecular ordering; however, the presence of a broad diffraction signal from 0 to 90˚ indicates the films were

still highly polycrystalline with some amorphous character as well (Appendix **Figure A27**).

From analysis of the I vs q plots we found that compound **2.4a** preferentially oriented edge-on (**Figure 3.27**). **Figure 3.28a** and **b** show the two predominant edge-on, perpendicular, molecular orientations of compound **2.4a** determined from the I vs q plots. Simulating the two observed crystal orientations, we found good agreement between the theoretical and experimental 2-D diffraction patterns (**Figure 3.29**).

Annealing compound **2.4a** at 60 ˚C on ITO/ZnO produced a primarily amorphous diffraction pattern and upon further heating to 150 ˚C, several different crystal structures were formed (Appendix **Figure A27b and d**). NEXAFS experiments performed on samples of compound **2.4a** on ITO/ZnO only resulted in two usable data points due to interference from the conducting tape (Appendix **Figure A28**). Because of this, no molecular orientation data could be obtained from the NEXAFS data.

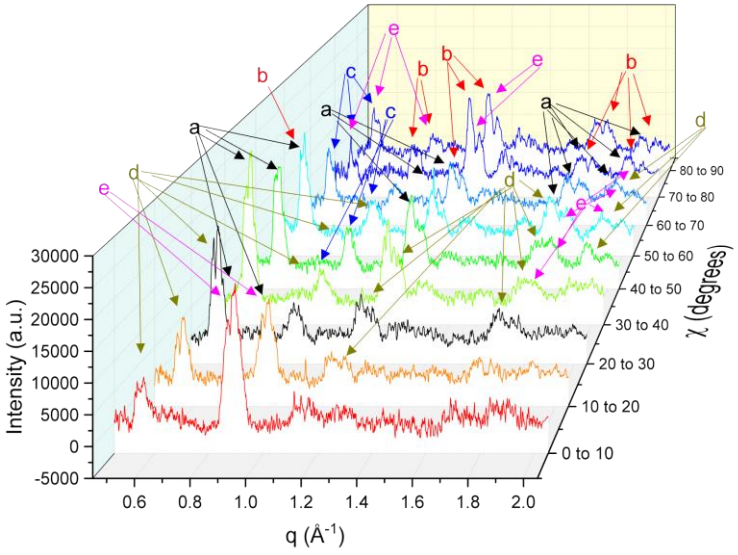

Figure 3.27: The waterfall plot of the I vs q from 0 to 90˚ and crystallographically related peaks are identified with the same letters.

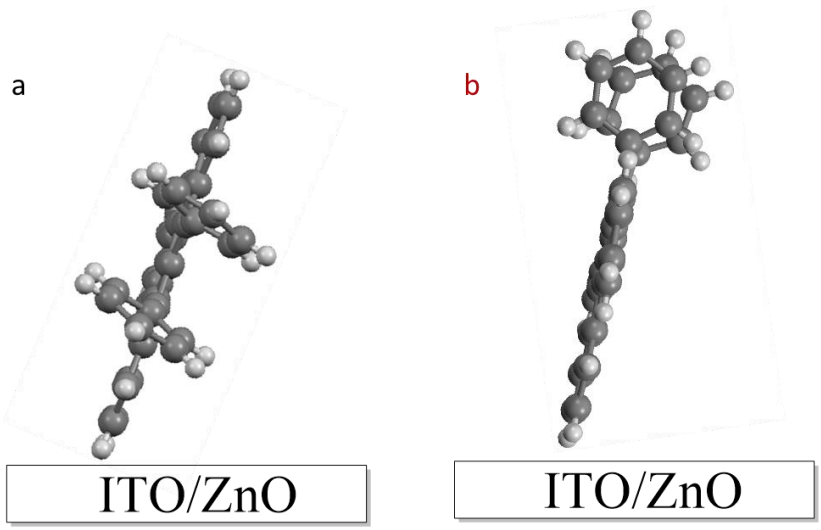

Figure 3.28: Showing the two primary molecular orientations of compound **2.4a** on ITO/ZnO identified in the I vs q waterfall plot with the letters corresponding to the peaks **a** and **b**.

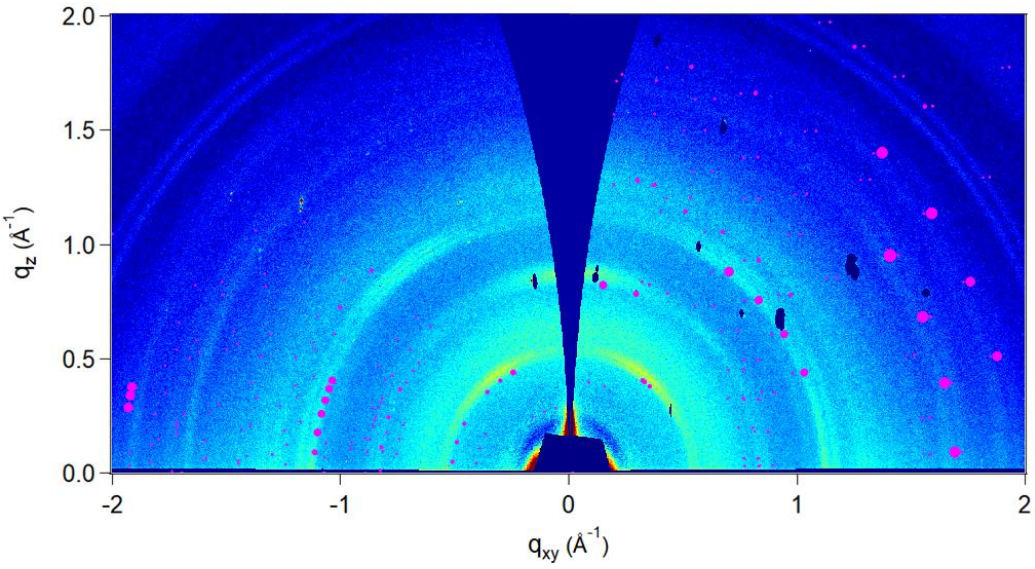

Figure 3.29: The combined 2-D qzqxy diffraction patterns for compound **2.4a** thin film on ITO/ZnO from $CHCl_3$:ODCB solution with 110 and 200 modeled perpendicular to the substrate on the right and 200 modeled parallel to the substrate on the left

Compound 2.4c:

As-cast thin film:

For compound **2.4c**, the 2-D diffraction pattern of the as-cast thin film samples prepared on ITO/ZnO were more similar to compound **2.4a** on ITO/ZnO than compound **2.4c** on Si/SiO_2 (Appendix **Figure A29a**). The thin film of compound **2.4c** was clearly also partly polycrystalline/amorphous, with significant broadening of all diffraction peaks. Even with the weaker diffraction signal, I vs q plots could be generated to determine molecular orientation in the thin film (**Figure 3.30**). From the I vs q patterns, two perpendicular crystal orientations were identified. The 200 plane was found to align in the qz direction with $\chi = 0^{\circ}$ which would result in the crystal orientation indicated in **Figure 3.31a**. The signal corresponding to the 111 and 002 planes, which were observed to be rotated toward qxy, $\chi > 40^{\circ}$, resulting in the crystal orientation indicated in **Figure 3.31b.** Modeling the two observed molecular orientations onto the 2-D diffraction pattern, we saw good agreement with the experimental data (**Figure 3.32**). The normalized NEXAFS spectra confirmed that compound **2.4c** was primarily oriented perpendicular to the ITO/ZnO substrate with the largest C1s-π^* signal occurring at an X-ray incidence angle of 90° (**Figure 3.33**). No accurate molecular orientation could be determined, however, due to a poor fit of the modeled intensity.

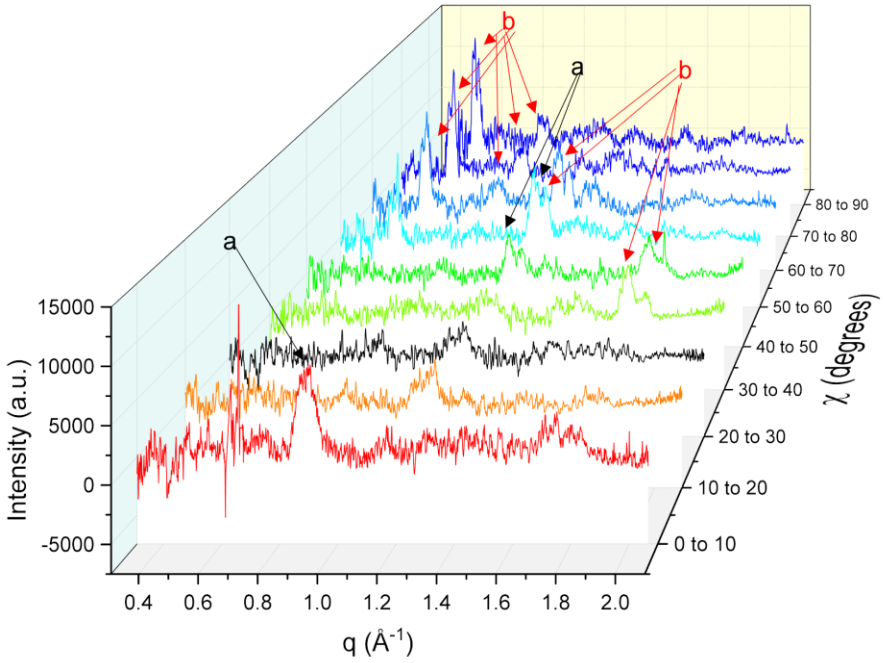

Figure 3.30: The I vs q plots from 0 to 90˚of compound **2.4c** thin film on ITO/ZnO prepared from (2:3) $CHCl_3$:ODCB solution. Crystallographically related peaks are identified with the same letters.

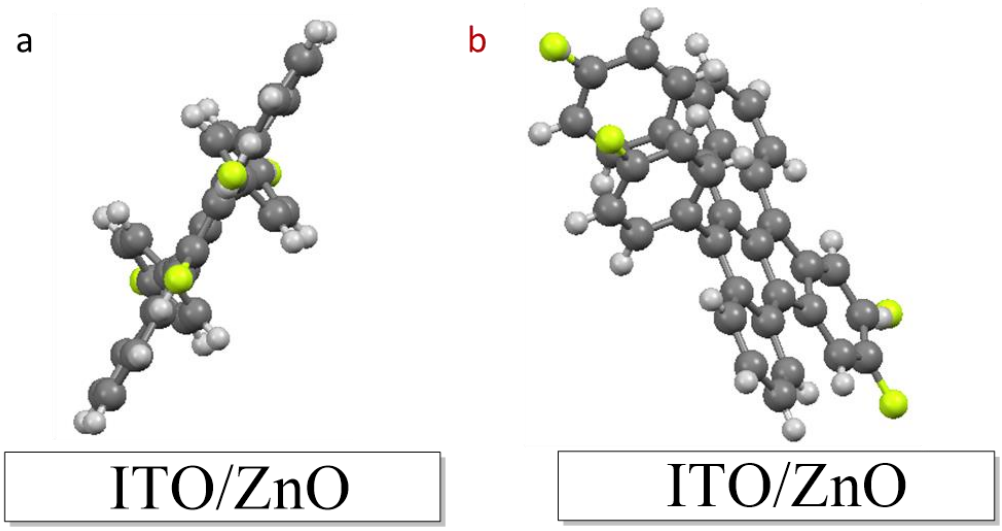

Figure 3.31: Shows the two primary molecular orientations identified in the I vs q waterfall plot with the letters corresponding to the peaks **a** and **b** in **Figure 3.30**.

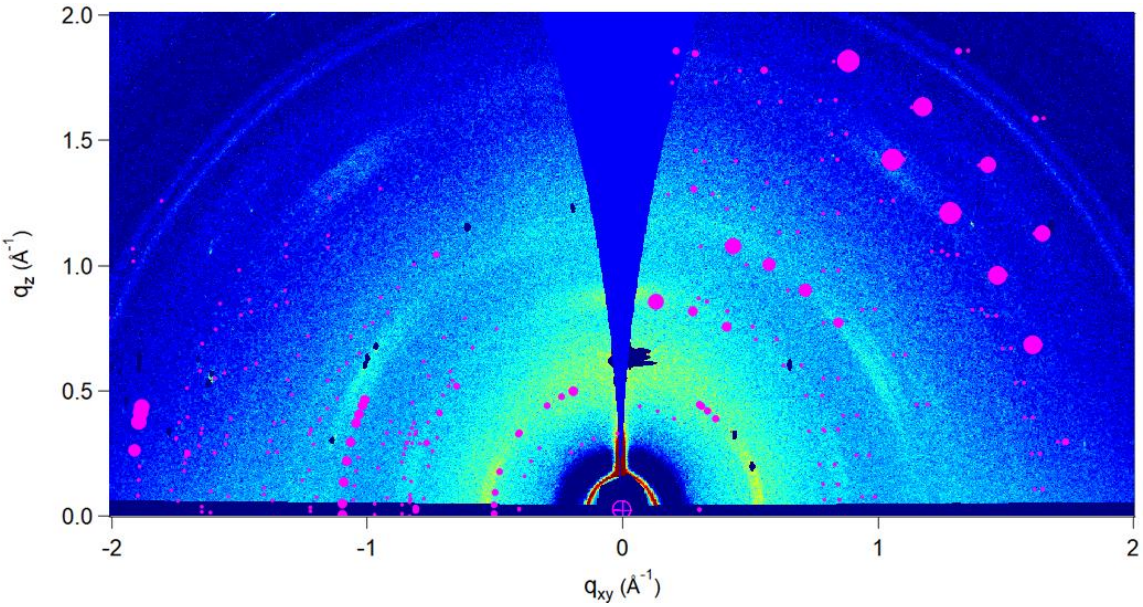

Figure 3.32: Combined 2-D diffraction pattern of compound **2.4c** thin film on ITO/ZnO prepared from (2:3) $CHCl_3$:ODCB solution with 110 plane modeled perpendicular to the substrate on the right and the 200 plane modeled parallel to substrate on the left.

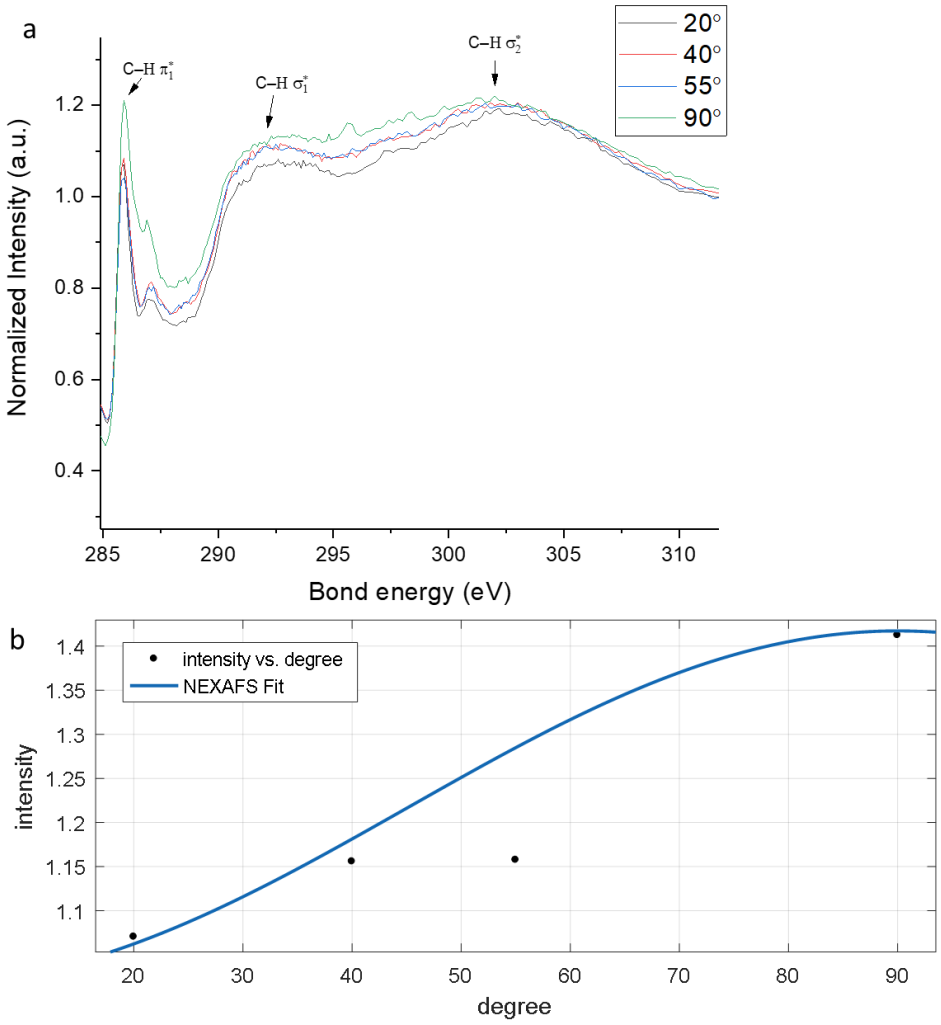

Figure 3.33: a) The normalized NEXAFS spectra for incident angles of 20, 40, 55 and 90˚ of the thin film of compound **2.4c** as-cast and b) the fitted area of the π_1^* peak angle of 20, 40, 55 and 90˚ fitted to **equation 3.9**.

Annealed thin films:

Annealing thin films of compound **2.4c** at 150 ˚C resulted in the films becoming highly ordered (Appendix **Figure A29b**), similar to what was observed for thin films on the Si/SiO_2 substrate. **Figure 3.34a** shows the I vs q plots of compound **2.4c** annealed at 150 ˚C on ITO/ZnO. As previously observed for compound **2.4c** on Si/SiO_2, the 111, 002,

and 112 planes were primarily oriented parallel to the substrate, with the corresponding diffraction signal occurring between χ = 0 to 30˚. This diffraction signal results from compound **2.4c** being oriented parallel to the ITO/ZnO substrate as shown in **Figure 3.34b**. Plotting the normalized intensities of the 110 plane from χ = 0 to 90˚ we saw that rather than having the maximum intensity between 50 and 60˚, as seen on Si/SiO_2, the maximum intensity now occurs between χ = 70 and 90˚ (**Figure 3.34c**). Theoretical diffraction patterns where the 111, 002, and 112 planes are aligned in the χ = 0 and the 110 plane aligned in the χ =90˚, modeled well onto experimental data (**Figure 3.35**). Utilizing NEXAFS experiments, we were able to correlate the change in 2-D diffraction pattern to a change in the preferred molecular orientation in the film. **Figure 3.36a** shows the normalized NEXAFS spectra. The normalized TEY demonstrated a decrease in the C1s-π^* absorbance as well as an increase in the C1s-σ^* absorbance as the incidence angle was increased from 20 to 90˚.

The fitted NEXAFS data (**Figure 3.37b**) indicated that compound **2.4c** was now primarily oriented with an average angle of 43.5 ± 2.4˚ from parallel to the substrate. Since the compound **2.4c** can tilt along two different axes (**Figure 3.37**), however, a second reference angle was needed to determine an accurate molecular orientation in the film. From the single crystal structure, it was observed that the 200 plane could be used to determine the tilt along β. By modeling the possible orientations of the 11$\bar{1}$ and 200 planes on the 2-D diffraction of q = 0.8 $Å^{-1}$, we determined the orientation of compound **2.4c** on ITO/ZnO along the β direction (Appendix **Figure A30**). Using **equation 3.10**, where α is the dipole moment measure by NEXAFS, β is the tilt parallel along the tetracene backbone,

and γ is the tilt of the indenotetracene core, we were able to determine an accurate orientation of compound **2.4c** on the ITO/ZnO substrate.

$$\cos\alpha = \sin\gamma * \cos\beta \qquad (\mathbf{3.10})$$

Using **equations 3.10** the indenotetracene core, γ, was determined to be tilted 49.7±4.4˚ and β was determined to be tilted 16.5˚ ± 5˚. Comparing GIWAXS and NEXAFS data, compound **2.4c** was found to lay parallel to the ITO/ZnO substrate with the molecular orientation shown in **Figure 3.38**.

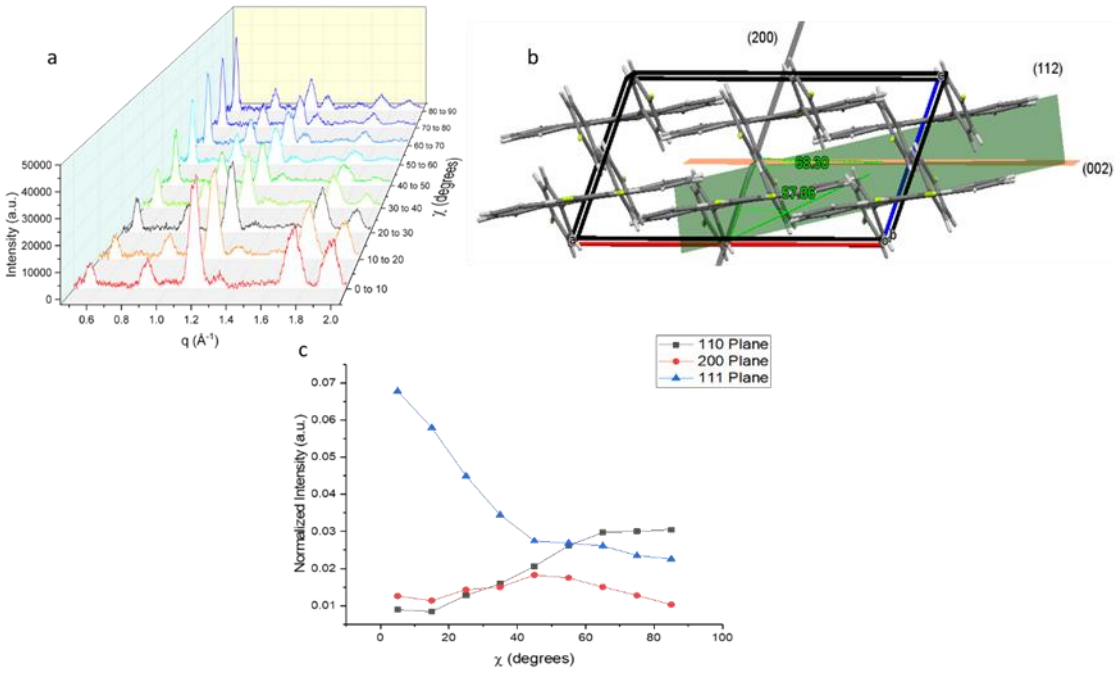

Figure 3.34: a) Shows the I vs q plot from 0 to 90˚, b) gives primary crystal orientations identified in the I vs q waterfall plot with the letters corresponding to the identified peaks in A, and c) shows the plot of the normalized intensity versus cake slice angle, 0 to 90˚, of the 110, 200, and 111 planes.

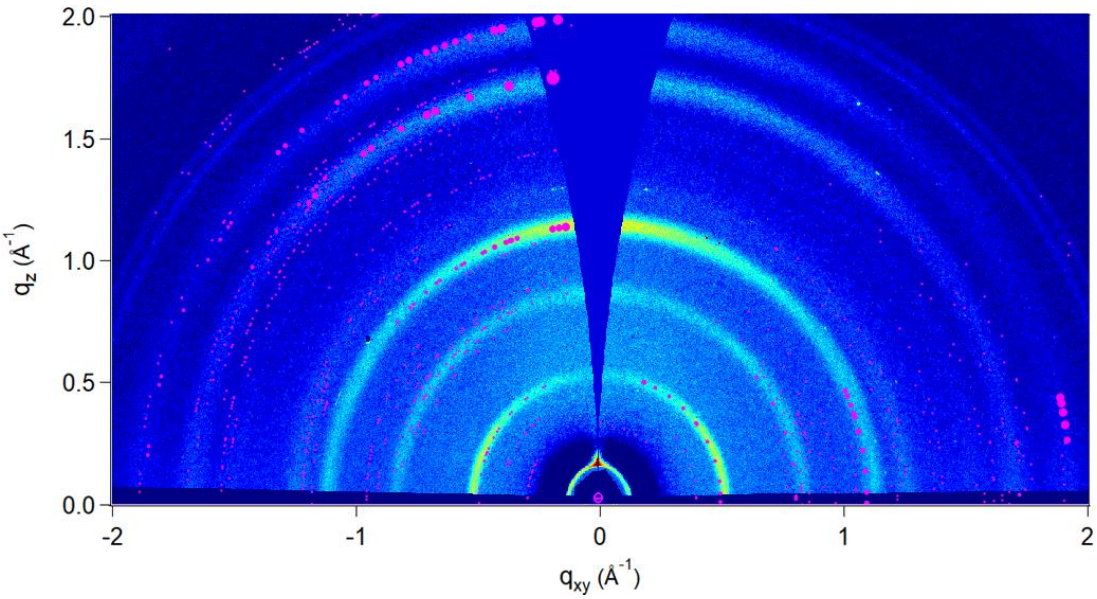

Figure 3.35: The 2-D diffraction patterns of compound **2.4c** thin films prepared from $CHCl_3$:ODCB on ITO/ZnO annealed at 150 ˚C and the overlaid modeled diffraction patterns with 111, 002, and 112 planes modeled parallel to the substrate on the right and 110 modeled perpendicular to substrate on the left.

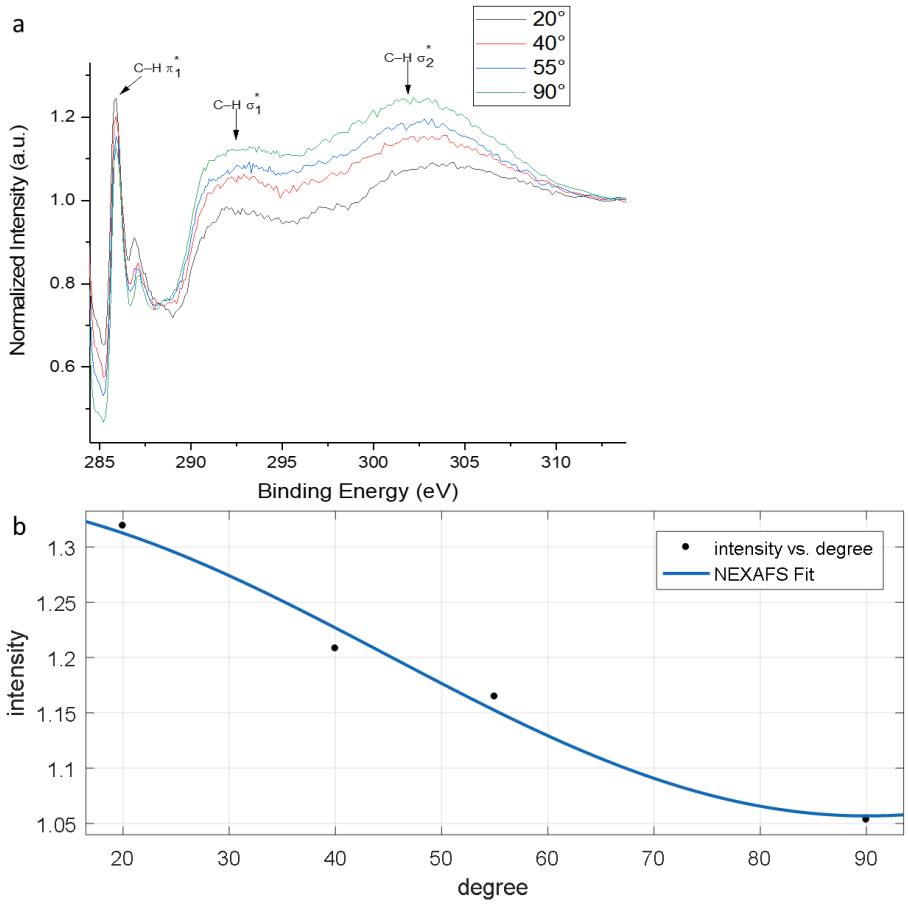

Figure 3.36: Shows a) the normalized NEXAFS data for incident angles of 20, 40, 55 and 90˚ of the thin film of compound **2.4c** annealed at 150 ºC and b) the area of the π_1^* peak angle at 20, 40, 55 and 90˚ fitted to **equation 3.9**.

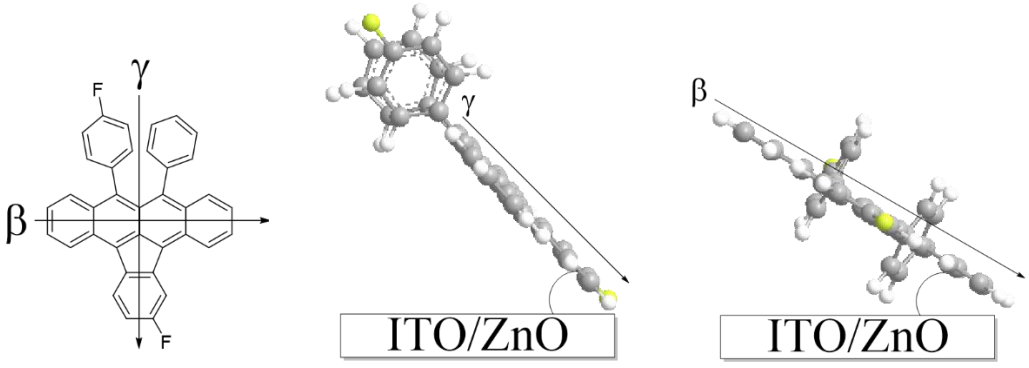

Figure 3.37: The two possible tilt directions of compound **2.4c**

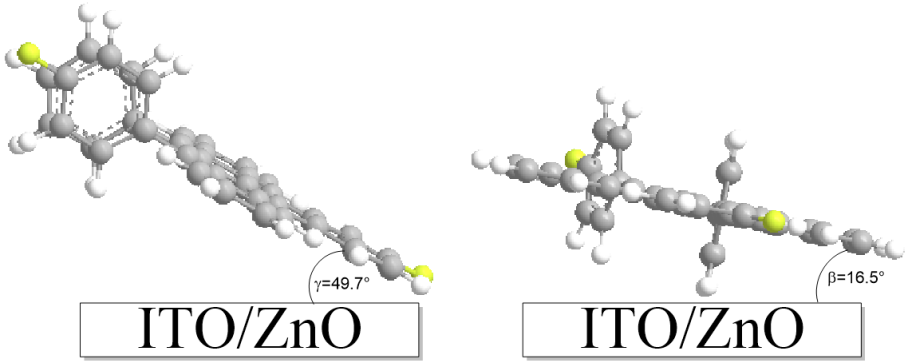

Figure 3.38: The exact molecular orientation of compound **2.4c**

Thin film morphologies of compounds 2.4a and 2.4c on ITO/ZnO:

The difference in thin film morphology between compounds **2.4a** and **c** can again be attributed to intermolecular C–F··X interaction. On ITO/ZnO, compound **2.4a** formed semi-ordered thin films. GIWAXS spectra showed that compound **2.4a** was aligned perpendicular to the ITO/ZnO surface, minimizing interactions between the substrate and compound **2.4a**, which lowered the barrier to crystallization. The minimized substrate interaction between the substrate and **2.4a** allowed for the formation of crystalline thin films at room temperature, though the ordering was quickly disrupted upon heating. Even at 60 ˚C we saw that the intermolecular C-H··H and π-π interactions of **2.4a**, in the solid state, were insufficient to maintain ordered crystal packing.

In contrast, compound **2.4c** on ITO/ZnO was found to have two different molecular orientations between the as-cast and annealed thin films as determined by both GIWAXS and NEXAFS. The molecular orientation of the as-cast thin film of compound **2.4b** was found to be edge-on, similar to as-cast thin films of compound **2.4a**. Upon annealing at 150 ˚C, however, increased C–F··H interactions oriented the ASI molecules in the thin film and produced a highly crystalline thin film with C2/*c* crystal packing.

Thin film morphologies on ITO/ZnO and Si/SiO_2:

A summary of the observed intermolecular interactions, thermal stability, thin film crystal structures and molecular orientation are shown in **Table 3.2**. On Si/SiO_2, **2.4a** demonstrated little to no molecular ordering in the thin films. On ITO/ZnO, compound **2.4a** oriented perpendicular to the substrate minimizing interactions between the ASI molecules and the substrate. Annealing compound **2.4a** on either substrate disrupted intermolecular C-H··X and π-π interactions even at low temperatures.

For compound **2.4c**, the as-cast molecular orientation of the ASI molecules in the thin films, on both Si/SiO_2 and ITO/ZnO, were very similar. From the analysis of the thin films we found that some **2.4c** molecules were oriented with the fluorine groups pointed directly at the Si/SiO_2 substrate. On ITO/ZnO, compound **2.4c** initially interacted with the substrate via intermolecular C-H··X interactions. While the intermolecular C-H··X interactions between compound **2.4c** and the ITO/ZnO substrate were weak and quickly disrupted upon annealing, the C–F··Si interactions between compound **2.4c** and the Si/SiO_2 substrate were very strong and persisted throughout the annealing process, even at 150 ˚C. Comparing the different substrate interactions we can now theorize that the initial perpendicular molecular orientation on the Si/SiO_2 substrate created a stable buffer layer. This buffer layer allowed the above layers of **2.4c** to orient parallel to the Si/SiO_2 substrate even at room temperature due to decreased disruption of compound **2.4c**'s crystal lattice.

From the study of the thin film morphology on Si/SiO_2 and ITO/ZnO, we can conclude that the changes in thin film morphology observed between compounds **2.4a** and **c** must be a direct result of the introduction of C–F··X interactions in the thin film of compound **2.4c**. The final, post-annealing, parallel orientation observed for compound **2.4c**

on both Si/SiO_2 and ITO/ZnO would lead to maximum interaction between the ASI molecules and the substrate surface, thereby increasing the barrier to crystallization. The fact that the same final molecular orientation is observed for compound **2.4c** annealed on both substrates, and not compound **2.4a**, indicates that the parallel orientation in the thin film of **2.4c** is a result of the intermolecular C–F··H interactions between neighboring ASI molecules. For this to occur, intermolecular C–F··H interactions between ASI molecules must impart significant stabilization energy to the crystal lattice allowing, compound **2.4c** to form highly-ordered, and thermally-stable, crystalline thin films from solutions of $CHCl_3$:ODCB while compound **2.4a** could not.

Table 3.2: A summary of the observed intermolecular interactions, thermal stability, thin film crystal structures, and molecular orientation for thin films of compounds **2.4a** and **c** prepared from (2:3) $CHCl_3$:ODCB.

Compound	Substrate	Interactions	Thermal stability	As-cast crystal structure	Molecular orientation	150 ºC annealed crystal structure	Molecular orientation
2.4a	Si/SiO_2	C–H··Si	< 150 ºC	multiple	unknown	multiple	unknown
		C–H··H	< 150 ºC				
		π··π	< 150 ºC				
	ITO/ZnO	C–H··ZnO	< 150 ºC	multiple	unknown	multiple	unknown
		C–H··H	< 150 ºC				
		π··π	< 150 ºC				
2.4c	Si/SiO_2	C–F··Si	> 150 ºC	C2/*c*	perpendicular/parallel	C2/*c*	perpendicular/parallel
		C–F··H	> 150 ºC				
	ITO/ZnO	C–H··ZnO	< 150 ºC	C2/*c*	perpendicular	C2/*c*	parallel

3.2.2.4 Solvation effect on thin film morphology:

Compound 2.4a on Si/SiO_2 and ITO/ZnO as-cast and annealed:

To account for solvent effects on thin film morphology, the spin-coating solvents were changed from (2:3) $CHCl_3$:ODCB to (2:3) MeTHF:toluene. The solution concentrations remained the same between the two solvent systems. The 2-D diffraction patterns of compound **2.4a** produced from MeTHF:toluene on Si/SiO_2 showed increased molecular ordering and crystallinity whereas previously, primarily amorphous/polycrystalline diffraction signals were observed (**Figure 3.39**). Thin films of compound **2.4a** produced from MeTHF:toluene also demonstrated an increased thermal stability compared to $CHCl_3$:ODCB thin films (**Figure 3.39**). The 2-D diffraction patterns produced from thin films of compound **2.4a** prepared on ITO/ZnO looked and behaved similarly to those on Si/SiO_2 (Appendix **Figure A31**), as did the thin films produced from 10 mg/ml solution (Appendix **Figure A32**). The AFM images of the as-cast thin film and the thin film annealed at 150 ˚C were also very similar (**Figure 3.34**). The MeTHF:toluene as-cast thin film showed an increase in the number of grains compared to the thin films prepared from $CHCl_3$:ODCB. As a result of the increase in the number of grains in the MeTHF:toluene thin films that rms roughness increased to 9.21 nm. Unlike the $CHCl_3$:ODCB thin films, however, the rms roughness of the annealed thin film decreased to 5.47 nm. The UV/Vis spectra of the thin films produced from (2:3) MeTHF:toluene showed greater stability in the charge transfer band up to 100 ˚C (**Figure 3.35**). When the thin films were annealed at 150 ˚C, absorbance and the fine structure detail of the thin film were greatly disrupted.

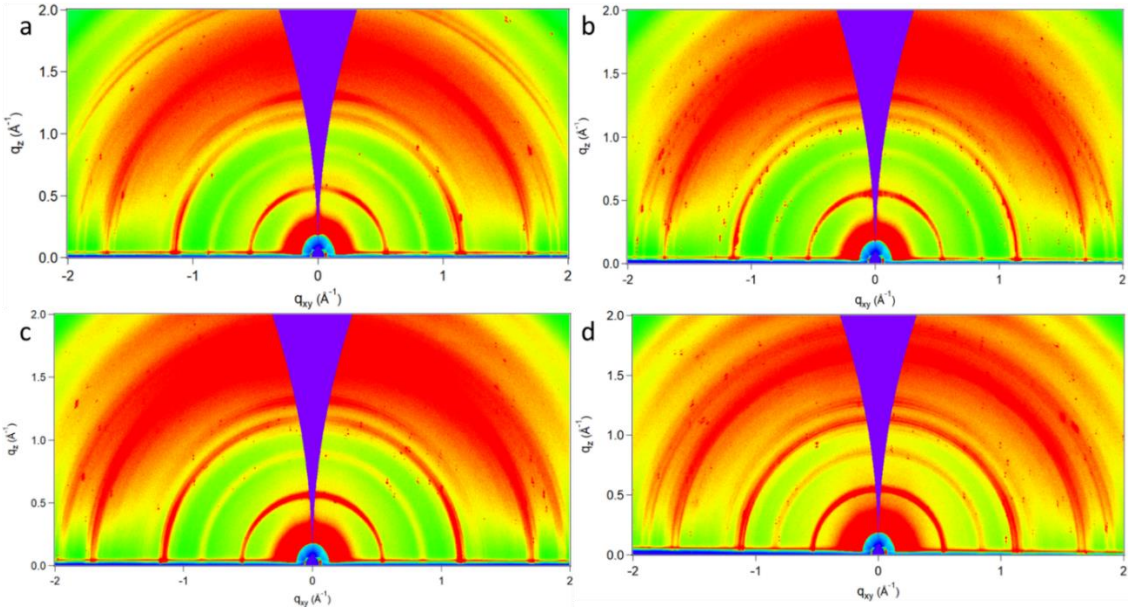

Figure 3.39: 2-D qzqxy patterns of compound **2.4a** thin film from MeTHF:toluene 20 mg/ml on ITO/ZnO, a) as-cast film b) film annealed at 60 ˚C c) thin film annealed at 100 ˚C d) thin film annealed at 150 ˚C

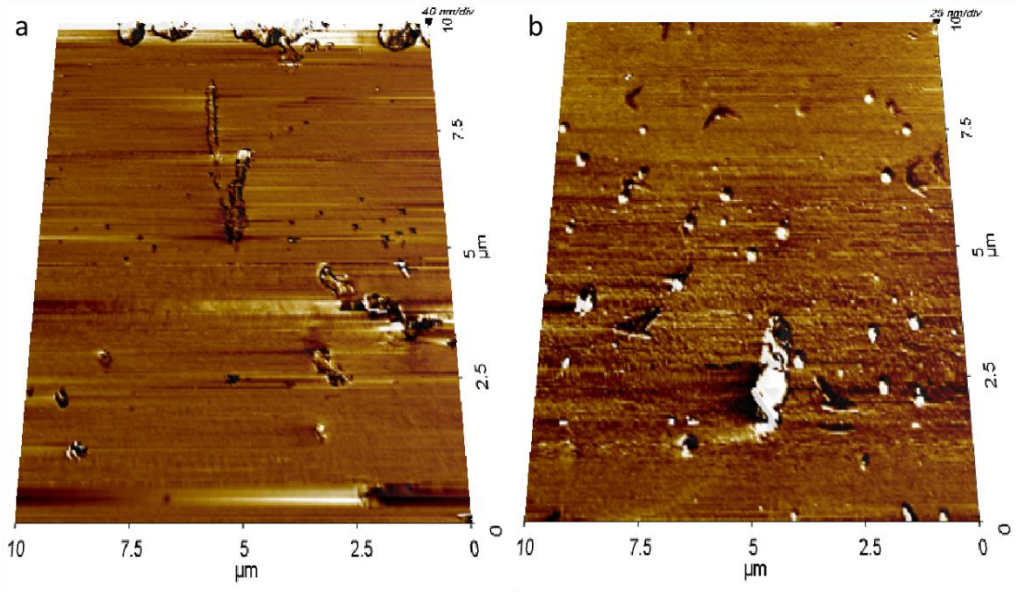

Figure 3.40: 3-D Atomic force microscopy images of compound **2.4a** on Si/SiO_2 produced using MeTHF:toluene, a) as-cast b) thin film annealed at 150 ˚C.

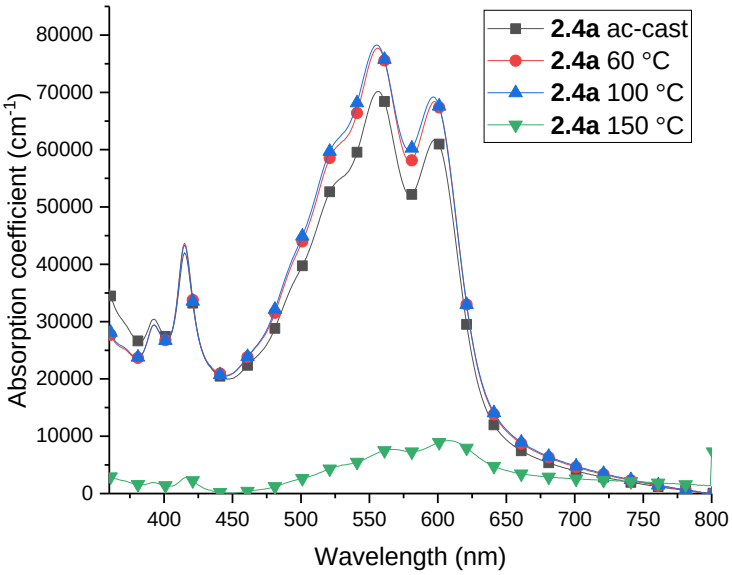

Figure 3.41: UV/Visible light absorption spectra of compound **2.4a** thin films produced from MeTHF:toluene, as-cast, annealed at 60, 100, or 150 ˚C.

Compound 2.4c on Si/SiO_2 and ITO/ZnO as-cast and annealed:

The 2-D diffraction patterns of the as-cast thin film of compound **2.4c** prepared using MeTHF:toluene on Si/SiO_2 indicated that both the crystallinity and the disorder of the thin film had increased (**Figure 3.42a**). By AFM, both crystalline (large crystals) and semi-crystalline (smooth) domains were now observed in the as-cast thin film (**Figure 3.42a**). While the as-cast thin films of compound **2.4c** prepared from MeTHF:toluene were determined to be oriented both perpendicular and parallel, similar to thin films prepared from $CHCl_3$:ODCB, the thin films were now clearly more isotropically oriented.

Thin films of **2.4c** annealed at 150 ˚C demonstrated no significant change in diffraction peak position as seen with the thin films prepared from $CHCl_3$:ODCB. Only slight increases in π-stacking and crystallinity were observed (**Figure 3.42b**) post-annealing at 150 ˚C. The AFM

images of compound **2.4c** annealed at 150 ˚C also showed very little change in thin film morphology upon annealing (**Figure 3.43**). The AFM images of the MeTHF:toluene as-cast thin film was found to have an rms roughness of 22.29 nm with grains sizes between 0.02 and 30 μm^2 (**Figure 3.43a**). The AFM images of the thin film annealed at 150 ˚C showed both crystalline and semi-crystalline regions, similar to the as-cast films, and while the rms roughness increased to 33.20 nm grains sizes decreased to between 0.012 and 11 μm^2 (**Figure 3.43b**). The UV/Vis spectra showed no increase in short range ordering until 150 ˚C (**Figure 3.44**).

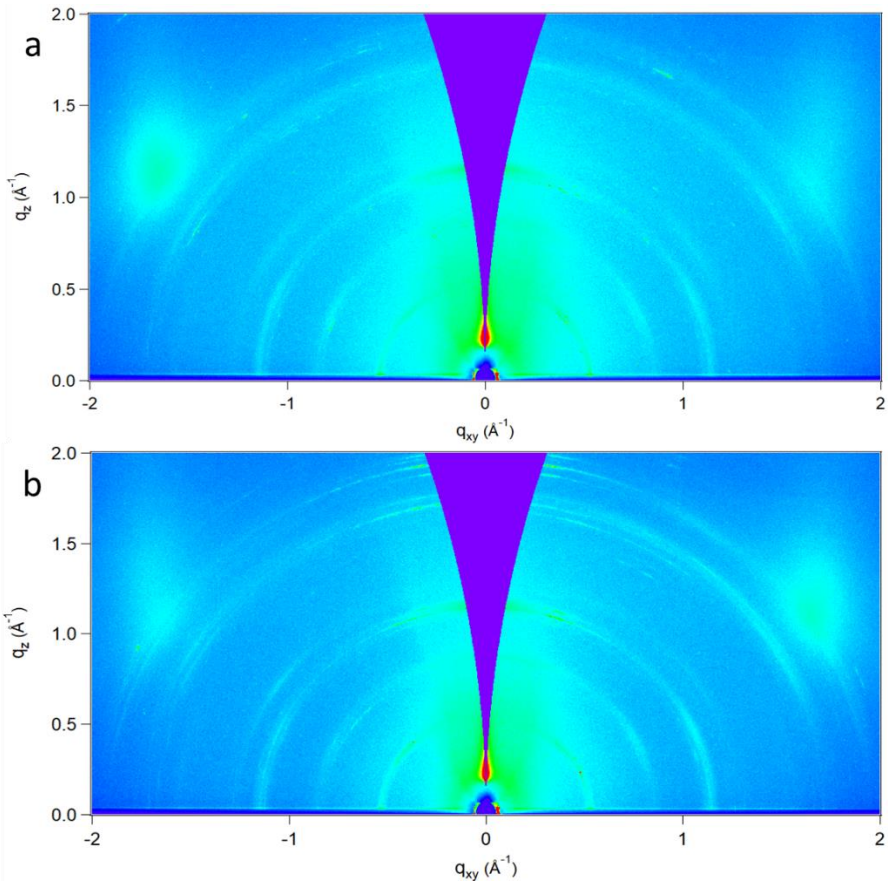

Figure 3.42: 2-D qzqxy patterns of compound **2.4c** thin film from MeTHF:toluene on Si/SiO_2 10 mg/ml, a) as-cast film, b) thin film annealed at 150 ˚C

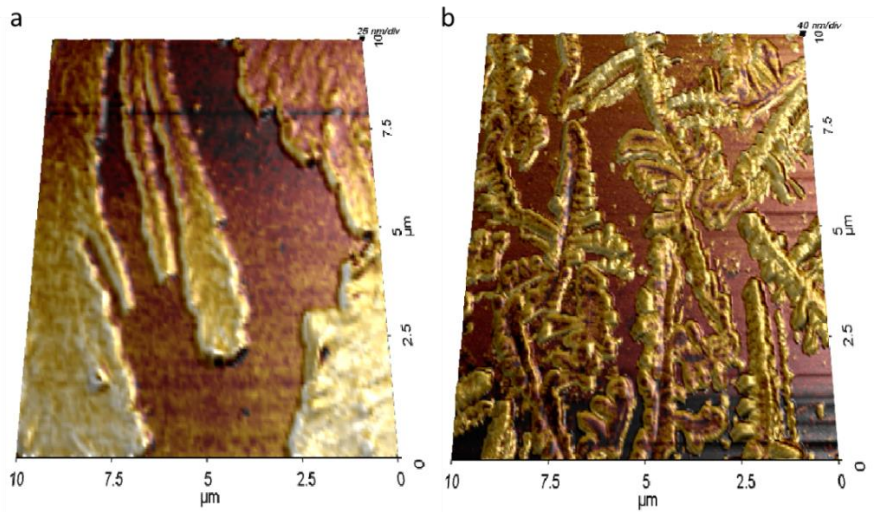

Figure 3.43: 3-D Atomic force microscopy images of compound **2.4c** on Si/SiO_2 produced using MeTHF:toluene, a) as-cast b) thin film annealed at 150 ˚C.

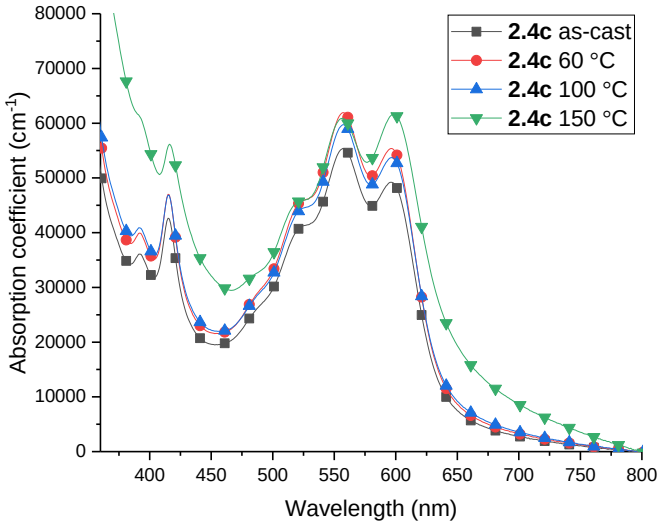

Figure 3.44.: UV/Visible light absorption spectra of compound **2.4c** thin films produced from MeTHF:toluene, as-cast, annealed at 60, 100, or 150 ˚C.

The thin film of compound **2.4c**, produced on ITO/ZnO from 10 mg/ml MeTHF:toluene solution, showed primarily polycrystalline 2-D diffraction pattern, a weak/broad 110 signal at q = 0.52 $Å^{-1}$ and 002 signal around q = 1.72 $Å^{-1}$ (Appendix **Figure A35**). Comparing I vs q at qz = 0

and qxy = 0 we did not observe any significant preferential crystallite orientation in the thin films (Appendix **Figure A36**). Increasing solution concentration to 20 mg/ml did result in an increase in thin-film crystallinity as observed by GIWAXS (**Figure 3.45**). When examined the I vs q plots of thin films prepared from the 20 mg/ml solutions, we observed two molecular of **2.4c**, similar to the molecular orientations observed on the Si/SiO_2 substrate (**Figure 3.46**).

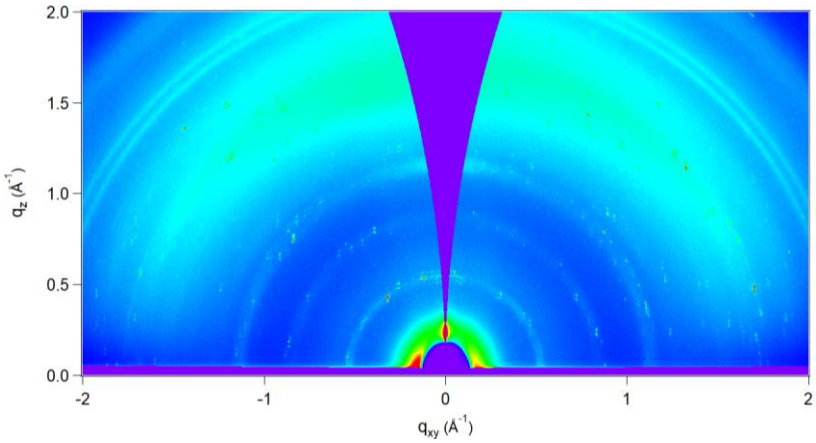

Figure 3.45: 2-D qzqxy patterns of compound **2.4c** thin film from 20mg/ml solution MeTHF:toluene on ITO/ZnO, 20 mg/ml as-cast film

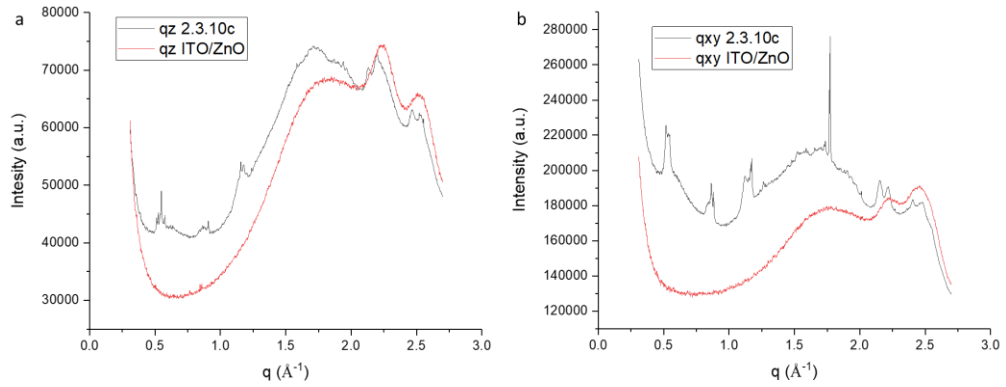

Figure 3.46: I vs q graphs of thin films of compound **2.4c** prepared from 20 mg/ml solution in MeTHF:toluene, overlaid with I vs q graphs of blank ITO/ZnO; a) I vs q from $\chi = 0$ to 20˚ b) show the I vs q from $\chi = 70$ to 90˚

Analysis of solvent effects on thin film morphology of compounds 2.4a and c on both Si/SiO_2 and ITO/ZnO:

A summary of the observed intermolecular interactions, thermal stability, thin film crystal structures and molecular orientation are shown in **Table 3.3**. Experiments comparing $CHCl_3$:ODCB and MeTHF:toluene solvent systems show that while the difference in thin film crystallinity and thin film disorder observed between compounds **2.4a** and **c** were partially due to the choice of solvent, the molecular orientation and increased molecular ordering of thin films of compound **2.4c** were a result of intermolecular C–F··X interaction.

The switch from $CHCl_3$:ODCB to MeTHF:toluene had two significant effects; a decrease in solvation strength and faster second-stage evaporation due to the lower boiling point of toluene verses ODCB, 111 and 180 ˚C resectively.[36,37] Decreasing the solvation strength allowed for increased partitioning of compound **2.4a** in solution allowing for increased intermolecular C-H-H and π-π interactions, between ASI neighbors, overcoming the barrier to crystallization resulting from interactions with the substrate surface although, on both substrates (Si/SiO_2 and ITO/ZnO) compound **2.4a** aligned normal to the substrates minimizing interactions with the substrate.

The thin films of compound **2.4c** produced from MeTHF:toluene on Si/SiO_2 at room temperature had very similar molecular orientation to those produced from $CHCl_3$:ODCB, either parallel or perpendicular. The major difference was the increase in the isotropically-oriented component of the films and an increase in as-cast thin-film crystallinity, both of which can be attributed to the lower boiling point of toluene in the new solvent system. The polycrystalline character of thin films of compound **2.4c** produced from 10 mg/ml solutions on ITO:ZnO can be explained by minimal interaction with the ITO/ZnO surface, which does not allow for initial ordering, and the rapid solvent evaporation decreases solvent residence time, thereby decreasing

ordered crystal growth. Upon increasing the concentration of the solution to 20 mg/ml, initial intermolecular C–F··X interations can occur in solution, producing more ordered films than the less-concentrated solutions.

Table 3.3: A summary of the observed intermolecular interactions, thermal stability, thin film crystal structures, and molecular orientation for thin films of compounds **2.4a** and **c** prepared from (2:3) MeTHF:toluene.

Compound	Substrate	Interactions	Thermal stability	As-cast crystal structure	Molecular orientation	150 ºC annealed crystal structure	Molecular orientation
2.4a	Si/SiO_2	C–H··Si	< 150 ºC	C2/*c*	perpendicular	multiple	perpendicular
		C–H··H	< 150 ºC				
		π··π	< 150 ºC				
	ITO/ZnO	C–H··ZnO	< 150 ºC	C2/*c*	perpendicular	multiple	perpendicular
		C–H··H	< 150 ºC				
		π··π	< 150 ºC				
2.4c	Si/SiO_2	C–F··Si	> 150 ºC	C2/*c*	perpendicular/parallel	C2/*c*	perpendicular/parallel
		C–F··H	> 150 ºC				
	ITO/ZnO	C–H··ZnO	< 150 ºC	C2/*c*	parallel	C2/*c*	parallel

3.2.2.5 Thin film morphology of compounds 2.4b and 2.4d

Compounds 2.4b

As stated previously, the GIWAXS experiments performed on thin films of compounds **2.4b** and **2.4d** did not afford a specific crystal structure. All the GIWAXS patterns for the thin films prepared using compound **2.4b** showed no preferential orientation of the polycrystalline thin films except for the thin film prepared from MeTHF:toluene on Si/SiO_2, (Appendix **Figure A2**). **Figure 3.47** shows the 2-D diffraction pattern of compound **2.4b** prepared from MeTHF:toluene on Si/SiO_2 annealed at 60 ˚C, which does indicate the presence of some ordered crystalline domains. Comparing I vs q along qz, $\chi = 0$, and qxy, $\chi = 90^{\circ}$, we did see a preferred crystal orientation; however, because we were unable to determine the crystal structure of the crystalline domains, no specific molecular orientation could be dertermined (**Figure 3.48**). NEXAFS experiments were performed on thin films of **2.4b** on Si/SiO_2. The NEXAFS spectra showed that the **2.4b** molecules, in the as-cast thin films, preferentially oriented with a $56.7 \pm 1.1^{\circ}$ tilt from the substrate (**Figure 3.49**). While the NEXAFS of the 150 ˚C annealed thin film of **2.4b** did indicate that the **2.4b** molecules were oriented perpendicular to the substrate, due to a poor fit with the modeled data, no specific molecular orientation could be determined (**Figure 3.50**). For NEXAFS experiments performed on thin films of compound **2.4b** on ITO/ZnO, no accurate molecular orientation of **2.4b** could be determined due to interference from the conducting tape at 40, 55, and 90˚(Appendix **Figure A38**). The AFM images of the as-cast thin films prepared from both $CHCl_3$:ODCB (**Figure 3.51**) and MeTHF:toluene (**Figure 3.52**) showed relatively smooth thin film with some larger localized grains. The resulting rms roughness for both films was small. The $CHCl_3$:ODCB

thin film's rms roughness was 0.84 nm while the MeTHF:toluene thin films had an rms roughness of 1.35 nm. Upon annealing at 150 ˚C, the rms roughness for both films increased. Thin films prepared from $CHCl_3$:ODCB now had an rms roughness of 4.07 nm while thin films prepared from MeTHF:toluene had an rms roughness of 2.02 nm. The UV/Vis spectra of the $CHCl_3$:ODCB showed little to no change between the as-cast and annealed thin films (**Figure 3.53a**). The MeTHF:toluene demonstrated a greater absorbance for the as-cast thin film compared to the annealed samples (**Figure 3.53b**).

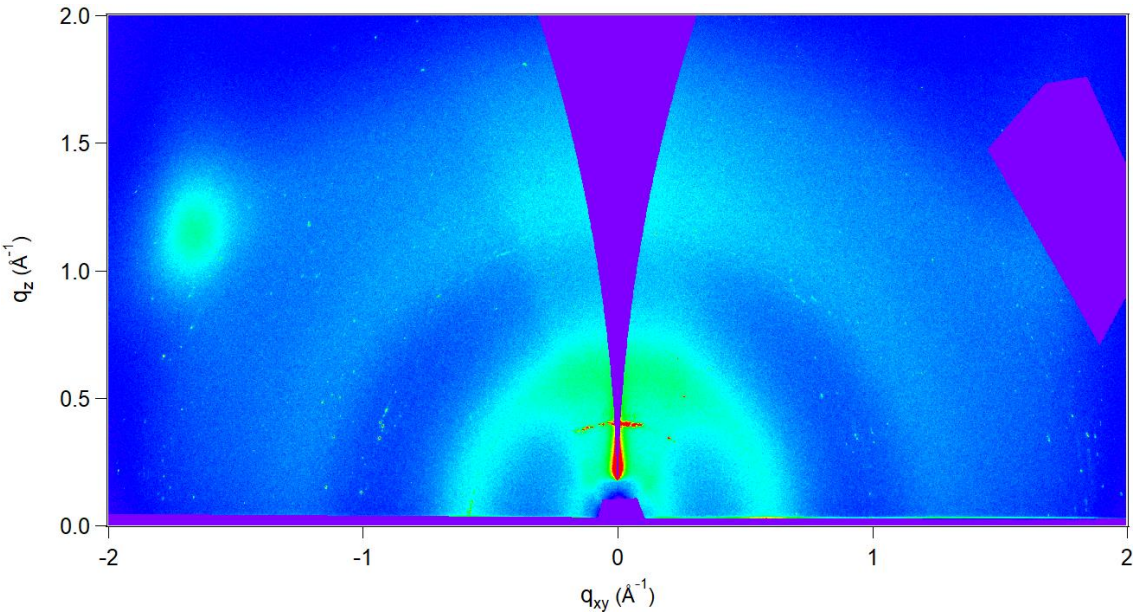

Figure 3.47: 2-D qzqxy patterns of compound **2.4b** thin film from MeTHF:toluene 20 mg/ml on Si/SiO_2 film annealed at 60 ˚C.

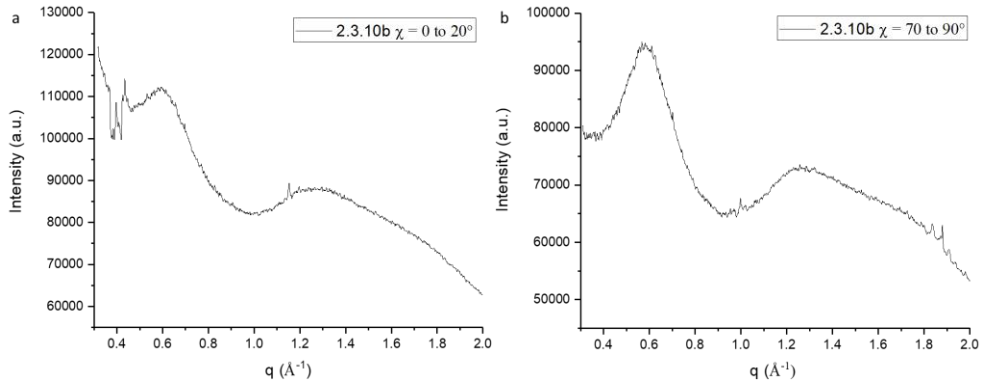

Figure 3.48: I vs q graphs of thin films of compound **2.4b** prepared from solution of MeTHF:toluene, a) from $\chi = 0$ to 20˚ b) and $\chi = 70$ to 90˚.

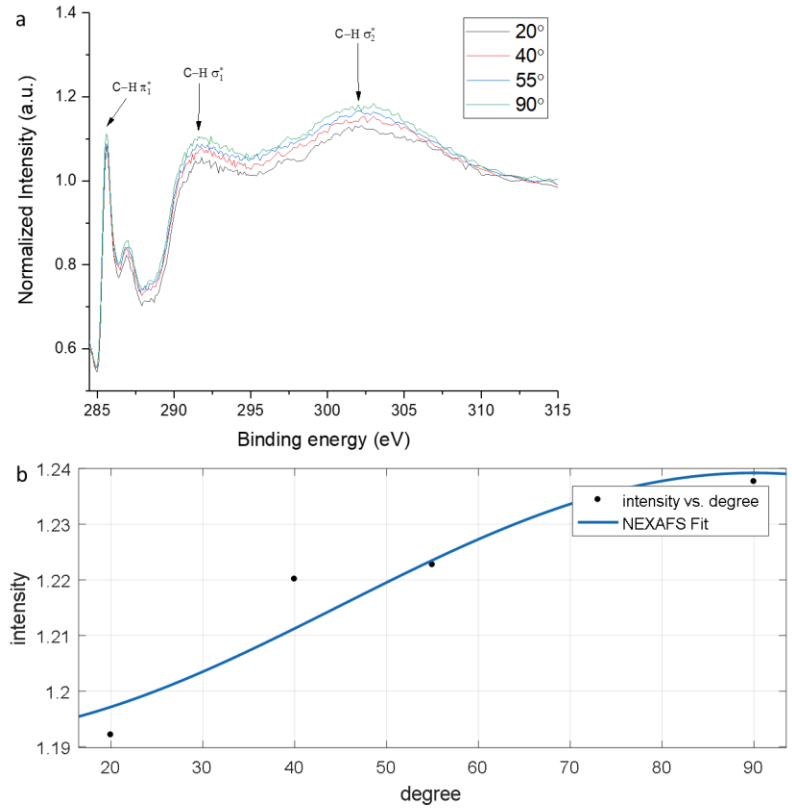

Figure 3.49: Shows a) the normalized NEXAFS data for incident angles of 20, 40, 55 and 90˚ of the thin film of compound **2.4b** as-cast and b) the area of the π_1^* peak angle at 20, 40, 55 and 90˚fitted to **equation 3.9** of the as-cast thin films of compound **2.4b** on Si/SiO_2.

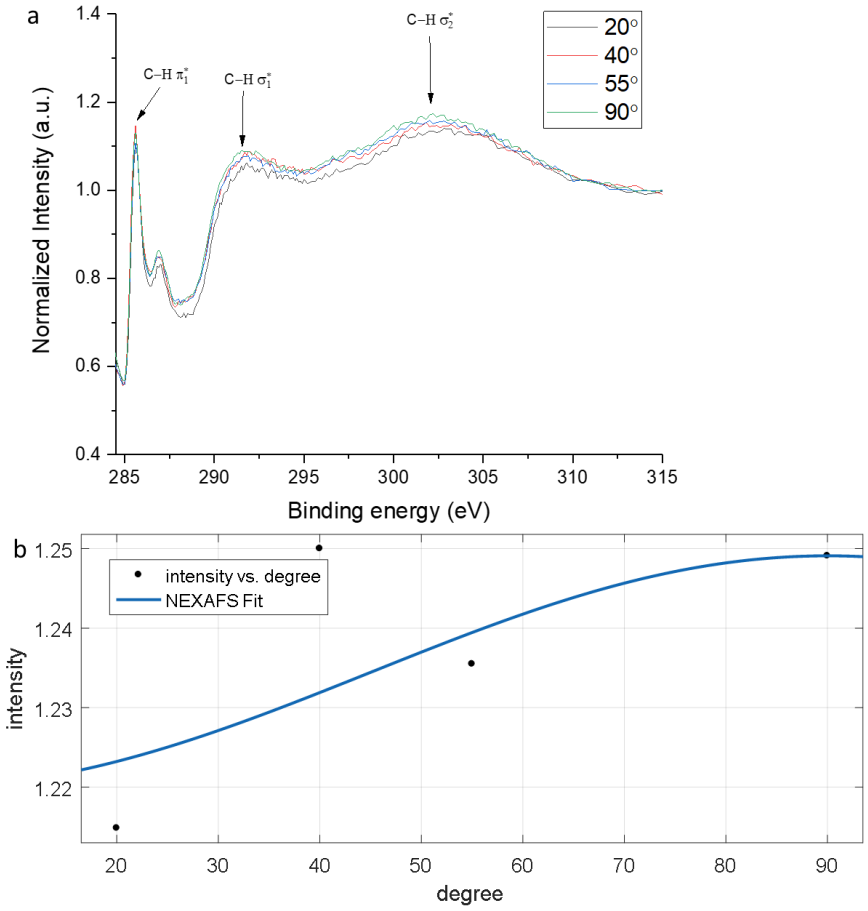

Figure 3.50: Shows a) the normalized NEXAFS data for incident angles of 20, 40, 55 and 90˚ of the thin film of compound **2.4b** annealed at 150 ºC and b) the area of the π_1^* peak angle at 20, 40, 55 and 90˚fitted to **equation 3.9** of the 150 ˚C annealed thin films of compound **2.4b** on Si/SiO_2.

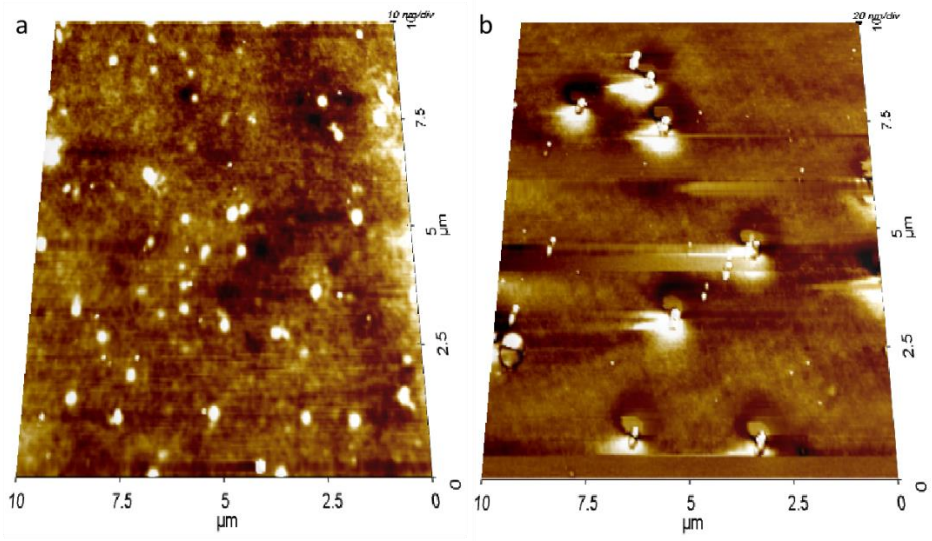

Figure 3.51: 3-D Atomic force microscopy images of compound **2.4b** on Si/SiO_2 produced using $CHCl_3$:ODCB, a) as-cast b) thin film annealed at 150 ˚C.

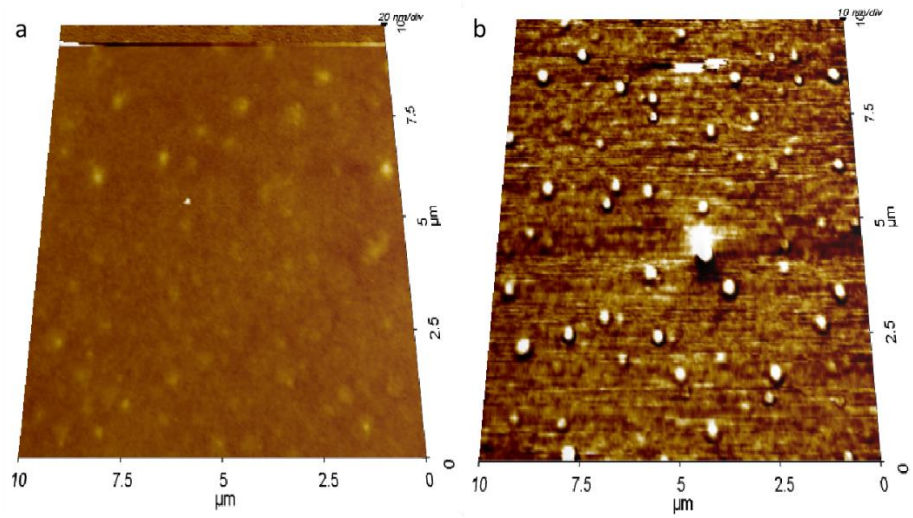

Figure 3.52: 3-D Atomic force microscopy images of compound **2.4b** on Si/SiO_2 produced using MeTHF:toluene, a) as-cast b) thin film annealed at 150 ˚C.

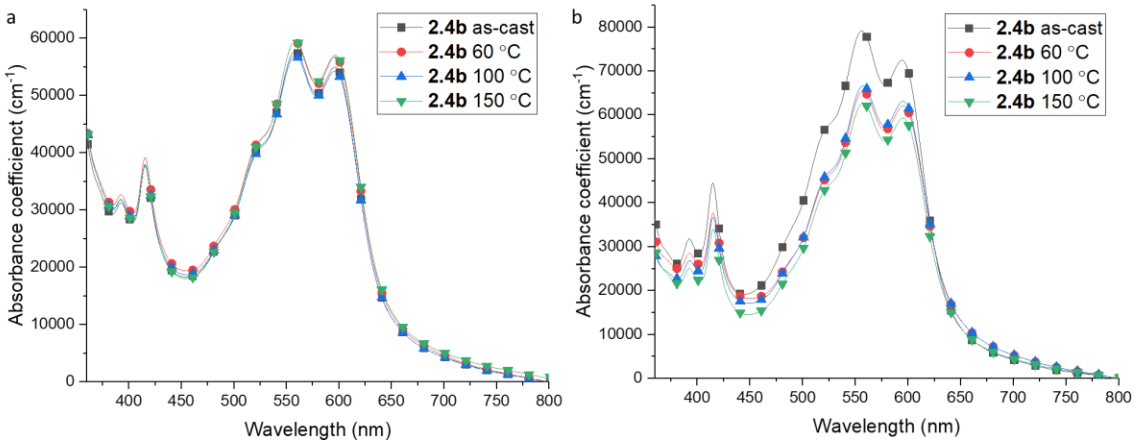

Figure 3.53: UV/Visible light absorption spectra of compound **2.4b** thin films, as-cast, annealed at 60, 100, or 150 ˚C, a) thin films produced from $CHCl_3$:ODCB, b) thin films produced from MeTHF:toluene

Compounds 2.4d

GIWAXS experiments of thin films prepared from compound **2.4d** produced only polycrystalline diffraction patterns for all films with no appearent preferential molecular orientation in the thin films (Appendix **Figure A5-A8**). NEXAFS experiments with thin films on Si/SiO_2 did indicate a preferential perpendicular orientaion of compound **2.4d** between 60.5 ± 3.6˚ (**Figure 3.54**) . After annealing at 150 ˚C, the thin films still had a predominatly perpendicular molecular orientation (**Figure 3.55**). This is indicated by the calculated molecular tilt, 58.8 ± 3.7˚, the R^2 of the fitted data decreased from 0.9, (as-cast), to 0.8. NEXAFS experiment on both the as-cast and the 150 ˚C annealed thin films on ITO/ZnO only gave three usable angles, due to interference for the conducting tape, which is insufficent for determination of accurate molecular orientation. (Apeendix **Figure 43**). Comparing AFM images of the thin films prepared from $CHCl_3$:ODCB and thin films prepared form MeTHF:toluene, we do see some thin film morphology changes. AFM

images of the thin film of compound **2.4d** prepared from $CHCl_3$:ODCB showed uniform films with very little difference in the rms roughness between the as-cast and 150 ˚C annealed thin films, which were 0.69 and 1.13 nm respectively (**Figure 3.56**). Switching to MeTHF:toluene spin-coating solvent two separate phases were observed in both the as-cast and 150 ˚C annealed thin films (**Figure 3.57**). We also observed an increase in the rms roughness of both thin films. The rms roughness for the as-cast film was determined to be 3.10 nm which decreased to 1.43 nm post-annealing at 150 ˚C. This could indicate either two distinct crystal structures in the thin films or two different molecular orientations. Because no specific crystallographic data could be obtain from the GIWAXS data, we are unable to determine specifics. The absorbance at 554 nm, of thin thin preprared from $CHCl_3$:ODCB continuely decreased as annealing teperatures increased (**Figure 3.58a**). For thin films preprared from MeTHF:toluene, absorbance at 554 nm increased when annealed upto 100 ˚C; however, when thin films were annealed 150 ˚C, the absorbance decreased dramatically (**Figure 3.59b**).

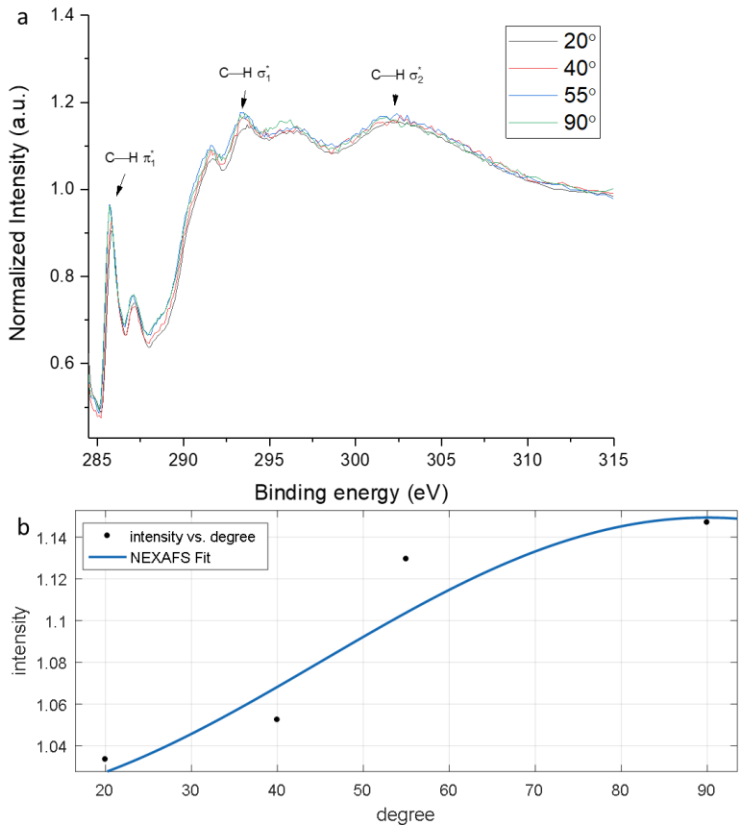

Figure 3.54: Shows a) the normalized NEXAFS data for incident angles of 20, 40, 55 and 90˚ of the thin film of compound **2.4b** as-cast and b) the area of the π_1^* peak angle at 20, 40, 55 and 90˚fitted to **equation 3.9**.

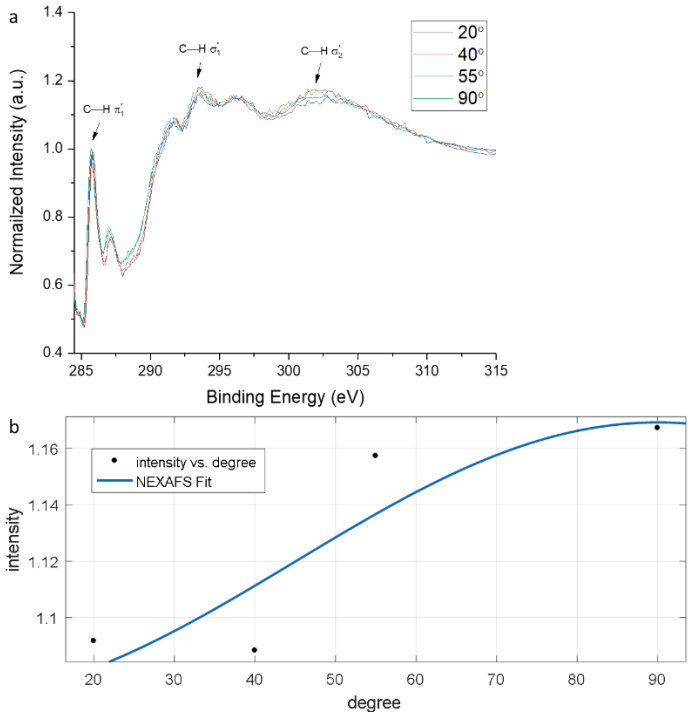

Figure 3.55: Shows a) the normalized NEXAFS data for incident angles of 20, 40, 55 and 90˚ of the thin film of compound **2.4b** annealed at 150 ºC and b) the area of the π_1^* peak angle at 20, 40, 55 and 90˚fitted to **equation 3.9**.

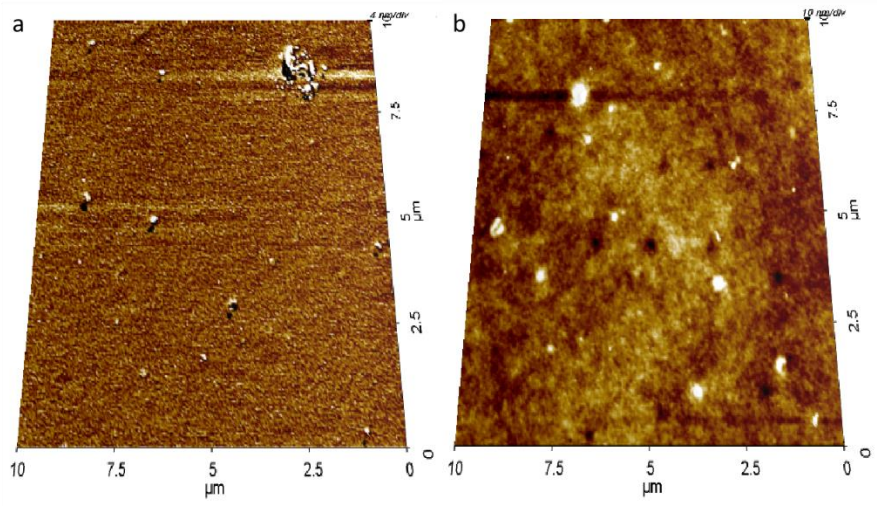

Figure 3.56: 3-D Atomic force microscopy images of compound **2.4d** on Si/SiO_2 produced using $CHCl_3$:ODCB, a) as-cast b) thin film annealed at 150 ˚C.

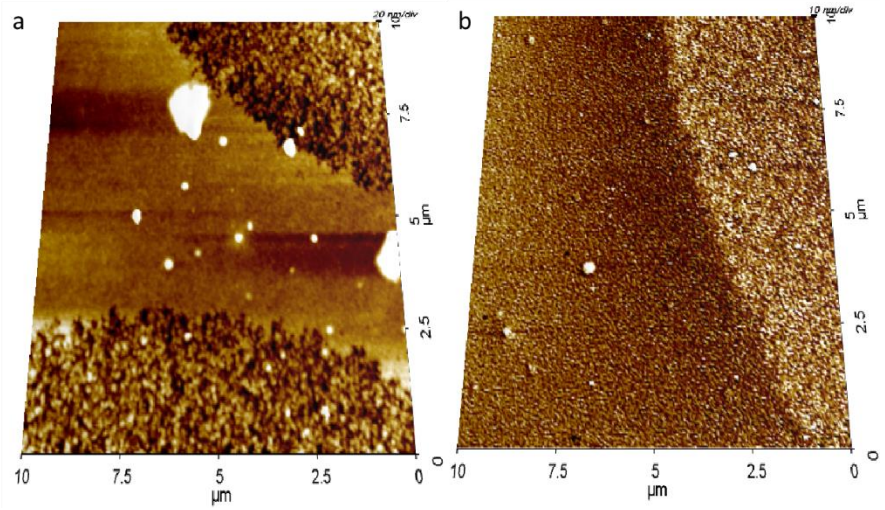

Figure 3.57: 3-D Atomic force microscopy images of compound **2.4d** on Si/SiO_2 produced using MeTHF:toluene, a) as-cast b) thin film annealed at 150 ˚C.

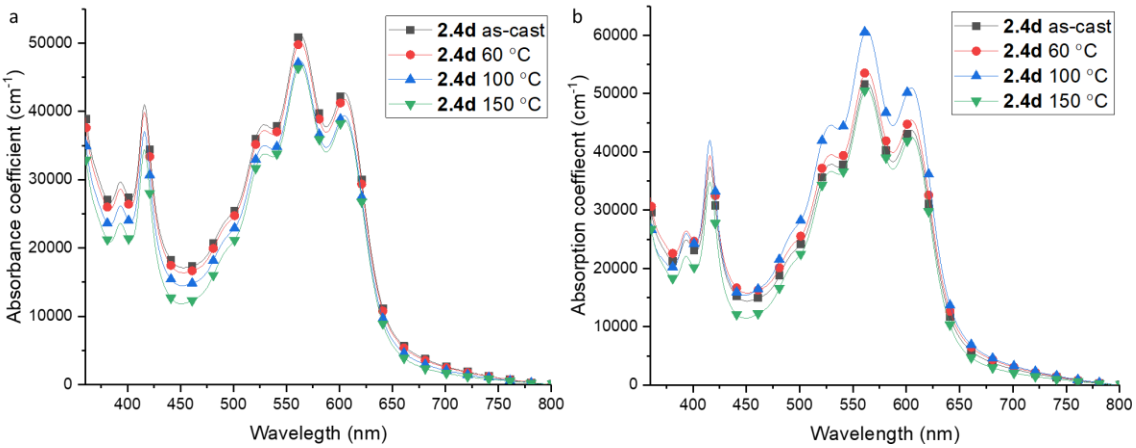

Figure 3.58: UV/Visible light absorption spectra of compound **2.4d** thin films, as-cast, annealed at 60, 100, or 150 ˚C, a) thin films produced from $CHCl_3$:ODCB, b) thin films produced from MeTHF:toluene

Analysis of thin films prepared from compounds 2.4b and d.

While little thin film morphology information could be gained from the GIWAXS, NEXAFS indicated that both compounds **2.4b** and **d** were oriented perpendicular to the Si/SiO_2 substrate in thin films prepared from $CHCl_3$:ODCB. Also, AFM experiments showed that switching the solvent system from $CHCl_3$:ODCB and MeTHF:toluene resulted in greater texturing of the as-cast thin films. As explained earlier this is a result of the decreased solvent residence time and increased second-stage evaporation. The UV/Vis of the thin film prepared from $CHCl_3$:ODCB shows very little difference between the as-cast and annealed thin films. The thin films of compounds **2.4b** and **d** prepared from MeTHF:toluene all showed a decrease in absorbance upon annealing at 150 ˚C.

3.2.2.6 Intermolecular C–F··X interactions effects on organic photovoltaics:

To determine how the different thin film morphologies affect device performance, single-layer organic photovoltaics (OPV) were fabricated. Single-layer OPVs were chosen for these experiments to allow for the direct comparison of the effects of C–F··X interactions on thin film morphology and OPV device performance. The devices were not optimized. All I-V curves for the OPVs employing the as-cast ASI active layer can be found in the appendix **Figure A41-48**.

Compound 2.4a:

Compound **2.4a** demonstrated almost no rectification behavior for thin films produced from either 10 mg/ml or 20 mg/ml solutions using either $CHCl_3$:ODCB or MeTHF:toluene solvent mixtures (Appendix **Table A2**). Both the short-circuit current, J_{sc}, and open-circuit voltage, V_{oc}, were extremely low. In the single-layer architecture, exciton dissociation only occurs at the electrodes. The small J_{sc} was most likely a result of poor exciton splitting due to the single-layer OPV architecture. The small V_{oc} of compound **2.4a**

OPVs was attributed to poor charge extraction and increased charge buildup at the interfaces.

Compound 2.4c:

No rectification behavior was observed for thin films produced from either 10 mg/ml or 20 mg/ml solutions from a $CHCl_3$:ODCB solvent mixture. Upon switching to the MeTHF:toluene solvent system, rectification behavior was observed. OPVs produced from 20 mg/ml solutions showed minimal OPV performance while those produced from 10 mg/ml solutions showed improved performance (**Table 3.4**). The difference in efficiency between the 20 mg/ml and 10 mg/ml thin film could have been due to several factors. One possible reason was that the increased thin film crystallinity, clearly visible in the 2-D diffraction pattern (**Figure 3.45**), could have resulted in greater recombination at grain boundries. OPVs produced using compound **2.4c** showed very similar J_{sc} as those observed for compound **2.4a** (**Figure 3.59**). Upon annealing, we observed a modest improvement in J_{sc} indicating an improvement in both exciton splitting and charge transport. The largest improvement between the two materials was in the V_{oc}. The as-cast OPV produced a V_{oc} of 0.425 V. The difference in V_{oc} observed between compound **2.4a** and **2.4c** demonstrated an improved charge extraction and decreased charge build up in the OPVs prepared using **2.4c**. The improved charge extraction observed in compound **2.4c** was a result of increased interaction between the transport layers due to the parallel molecular orientation in the thin film.

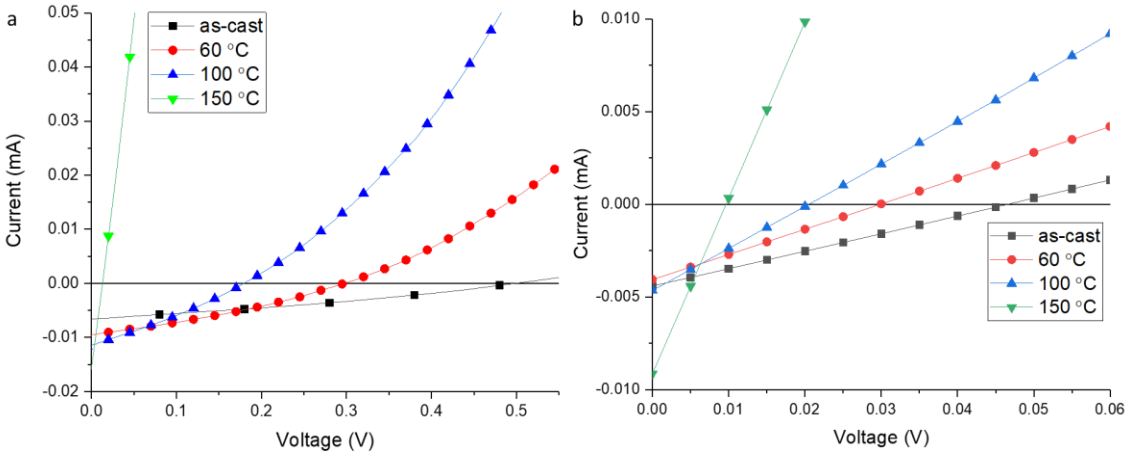

Figure 3.59: Comparison of I-V curves of OPV using **2.4c** in the active layer as-cast, and annealed at 60, 100, and 150 ˚C prepared from (2:3) MeTHF:toluene a) 10 mg/ml solutions b) 20 mg/ml solutions.

Table 3.4: A summary of OPV parameters for ITO/ZnO/compound **2.4c**/MoO_3/Ag. Devices were prepared from 10 or 20 mg/ml solution of either (2:3) $CHCl_3$:ODCB or (2:3) MeTHF:toluene. Four different film processing temperatures were tested: as-cast, annealed at 60, 100, and 150 ˚C. J_{sc} is the short-circuit current, V_{oc} is the open-circuit voltage, and P_{max} is the maximum power output.

(2:3) $CHCl_3$:ODCB				
20 mg/ml	J_{sc} (mA/cm^2)	V_{oc} (V)	P_{max} (mW/cm^2)	Fill Factor
as-cast	-4.82E^{-03}	0.000	0.00E^{+00}	0.000
Annealed 60 ˚C	-1.27E^{-02}	0.000	0.00E^{+00}	0.000
Annealed 100 ˚C	-9.09E^{-03}	0.000	0.00E^{+00}	0.000
Annealed 150 ˚C	-1.40E^{-02}	0.000	0.00E^{+00}	0.000
10mg/ml				
as-cast	-6.94E^{-03}	0.019	3.28E^{-05}	0.222
Annealed 60 ˚C	-7.49E^{-03}	0.006	9.00E^{-06}	0.116
Annealed 100 ˚C	-8.43E^{-03}	0.005	4.80E^{-06}	0.089
Annealed 150 ˚C	-1.76E^{-02}	0.000	0.00E^{+00}	0.000
(2:3) MeTHF:Toluene				
20mg/ml	J_{sc} (mA/cm^2)	V_{oc} (V)	P_{max} (mW/cm^2)	Fill Factor
as-cast	-4.08E^{-03}	0.026	2.67E^{-05}	0.246
Annealed 60 ˚C	-4.05E^{-03}	0.013	1.26E^{-05}	0.182
Annealed 100 ˚C	-4.59E^{-03}	0.015	1.64E^{-05}	0.240
Annealed 150 ˚C	-1.09E^{-02}	0.007	9.73E^{-06}	0.125
10mg/ml				
as-cast	-6.14E^{-03}	0.425	8.12E^{-04}	0.312
Annealed 60 ˚C	-8.91E^{-03}	0.258	7.10E^{-04}	0.306
Annealed 100 ˚C	-1.16E^{-02}	0.171	5.72E^{-04}	0.288
Annealed 150 ˚C	-1.65E^{-02}	0.007	2.05E^{-05}	0.125

Compound 2.4b

Unlike compounds **2.4a** and **c**, OPV devices of compound **2.4b** prepared from $CHCl_3$:ODCB did show minimal power generation (**Table 3.5**). Both the J_{sc} and V_{oc} were very low, but the values were sufficent to give fill factors between 0.19 and 0.25. However,

because of the very low values of the V_{oc}, the calculated fill factors are questionable. Switching solvent system from $CHCl_3$:ODCB to MeTHF:toluene resulted in improved OPV performance. The increased fill factors, between 0.20 and 0.32, were a result of the impoved V_{oc}. Using MeTHF:Toluene as the spin-coating solution resulted in a five fold increase in the the V_{oc}, indicating that the OPVs prepared form MeTHF:Toluene had improved interactions with the interface, allowing for improved charge extraction. Decreasing solution concentration from 20 mg/ml to 10 mg/ml resulted in improved J_{sc} with only small descreaes in the V_{oc}. Annealing thin films of **2.4b** again improved J_{sc} but resulted in a substantial decrease in the V_{oc} (**Figure 3.60**). The improvement in the J_{sc} resulted in an increase in the P_{max} though the FF was unchanged due to the small decrease in the V_{oc}.

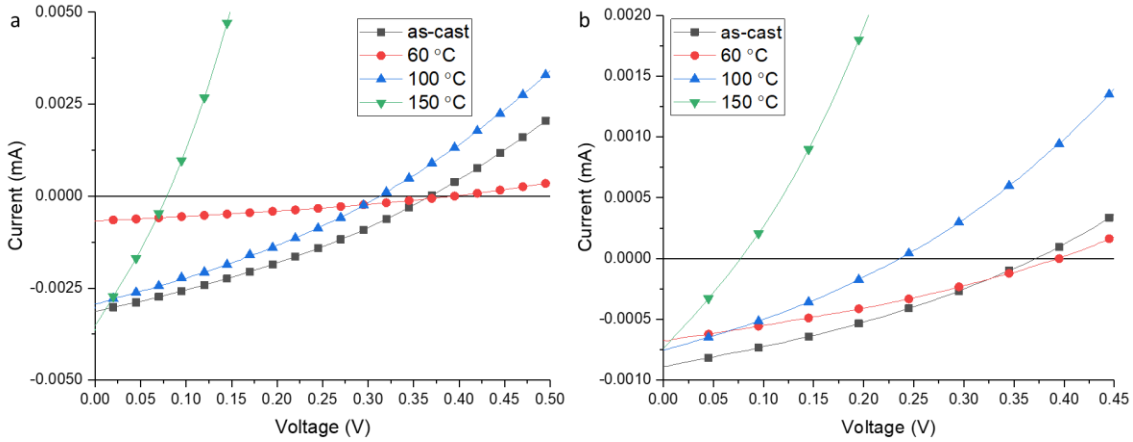

Figure 3.60: Comparison of I-V curves of OPV using **2.4b** in the active layer as-cast, and annealed at 60, 100, and 150 ˚C prepared from (2:3) MeTHF:toluene a) 10 mg/ml solutions b) 20 mg/ml solutions.

Table 3.5: A summary of OPV parameters for ITO/ZnO/compound **2.4b**/MoO_3/Ag. Devices were prepared from 10 or 20 mg/ml solution of either (2:3) $CHCl_3$:ODCB or (2:3) MeTHF:toluene. Four different film processing temperatures were tested: as-cast, annealed at 60, 100, and 150 ˚C. J_{sc} is the short-circuit current, V_{oc} is the open-circuit voltage, and P_{max} is the maximum power output.

(2:3) $CHCl_3$:ODCB				
20 mg/ml	J_{sc} (mA/cm^2)	V_{oc} (V)	P_{max} (mW/cm^2)	Fill Factor
as-cast	-1.14E^{-03}	0.052	1.51E^{-05}	0.257
Annealed 60 ˚C	-1.38E^{-03}	0.045	1.59E^{-05}	0.193
Annealed 100 ˚C	-1.44E^{-03}	0.061	2.29E^{-05}	0.256
Annealed 150 ˚C	-1.53E^{-03}	0.063	2.48E^{-05}	0.197
10mg/ml				
as-cast	-5.07E^{-03}	0.018	2.30E^{-05}	0.247
Annealed 60 ˚C	-4.40E^{-03}	0.072	8.03E^{-05}	0.256
Annealed 100 ˚C	-4.12E^{-03}	0.025	2.56E^{-05}	0.248
Annealed 150 ˚C	-1.04E^{-03}	0.008	2.73E^{-06}	0.133
(2:3) MeTHF:Toluene				
20mg/ml	J_{sc} (mA/cm^2)	V_{oc} (V)	P_{max} (mW/cm^2)	Fill Factor
as-cast	-8.90E^{-04}	0.306	8.41E^{-05}	0.304
Annealed 60 ˚C	-7.32E^{-04}	0.281	6.48E^{-05}	0.322
Annealed 100 ˚C	-7.61E^{-04}	0.178	3.93E^{-05}	0.287
Annealed 150 ˚C	-7.80E^{-04}	0.054	1.06E^{-05}	0.197
10mg/ml				
as-cast	-3.21E^{-03}	0.271	2.68E^{-04}	0.309
Annealed 60 ˚C	-3.08E^{-03}	0.220	2.18E^{-04}	0.322
Annealed 100 ˚C	-3.01E^{-03}	0.206	1.83E^{-04}	0.292
Annealed 150 ˚C	-3.44E^{-03}	0.090	8.72E^{-05}	0.279

Compound 2.4d:

Similar to compound **2.4b**, OPVs containing **2.4d** prepared from $CHCl_3$:ODCB demonstrated minimal rectification behavior. The V_{oc} was again very low indicating inefficient charge extraction and buildup in the device (**Table 3.5**). Changing the solvent

system to MeTHF:Toluene did improve OPV performance of devices prepared from 20 mg/ml solutions. The V_{oc} for the as-cast and annealed active layers increased by almost a factor of 10 for all devices; however, the J_{sc} decreased by half (**Figure 3.61**). The calculated FF for these solar cells ranged from 0.26 to 0.34. The 10-fold increase in the V_{oc} resulted in a matching 10-fold increase in the P_{max}. The performance of OPVs prepared from the 10 mg/ml solutions of MeTHF:Toluene remained unchanged from those prepared from $CHCl_3$:ODCB.

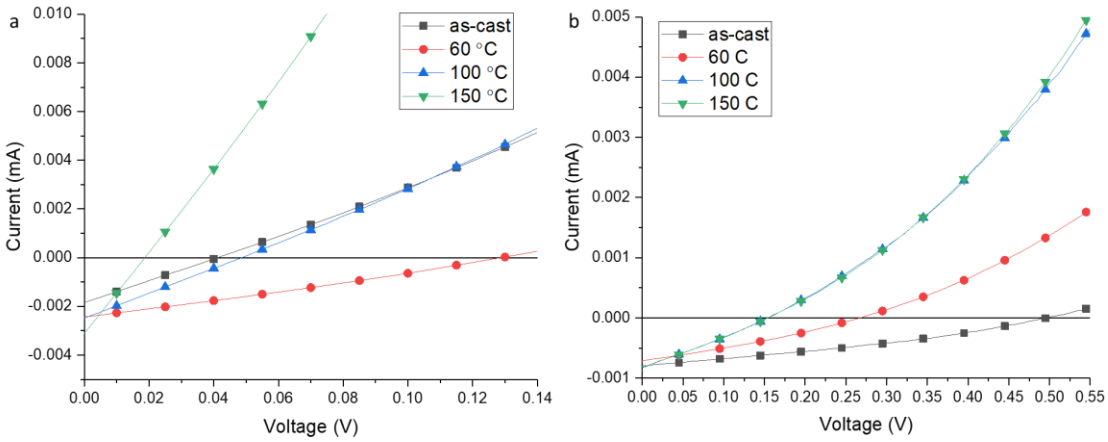

Figure 3.61: Comparison of I-V curves of OPV using **2.4d** in the active layer as-cast, and annealed at 60, 100, and 150 ˚C prepared from (2:3) MeTHF:toluene a) 10 mg/ml solutions b) 20 mg/ml solutions.

Table 3.6: A summary of OPV parameters for ITO/ZnO/compound **2.4d**/MoO_3/Ag. Devices were prepared from 10 or 20 mg/ml solution of either (2:3) $CHCl_3$:ODCB or (2:3) MeTHF:toluene. Four different film processing temperatures were tested: as-cast, annealed at 60, 100, and 150 ˚C. J_{sc} is the short-circuit current, V_{oc} is the open-circuit voltage, and P_{max} is the maximum power output.

(2:3) $CHCl_3$:ODCB				
20 mg/ml	J_{sc} (mA/cm^2)	V_{oc} (V)	P_{max} (mW/cm^2)	Fill Factor
as-cast	-1.20E^{-03}	0.039	1.18E^{-05}	0.249
Annealed 60 ˚C	-1.20E^{-03}	0.007	1.75E^{-06}	0.161
Annealed 100 ˚C	-1.36E^{-03}	0.016	5.43E^{-06}	0.188
Annealed 150 ˚C	-1.37E^{-03}	0.048	1.70E^{-05}	0.215
10mg/ml				
as-cast	-3.18E^{-03}	0.014	9.90E^{-06}	0.174
Annealed 60 ˚C	-3.68E^{-03}	0.007	3.68E^{-06}	0.062
Annealed 100 ˚C	-3.59E^{-03}	0.029	2.51E^{-05}	0.249
Annealed 150 ˚C	-3.82E^{-03}	0.009	7.55E^{-06}	0.175
(2:3) MeTHF:Toluene				
20mg/ml	J_{sc} (mA/cm^2)	V_{oc} (V)	P_{max} (mW/cm^2)	Fill Factor
as-cast	-7.73E^{-04}	0.445	1.16E^{-04}	0.340
Annealed 60 ˚C	-7.16E^{-04}	0.311	7.18E^{-05}	0.321
Annealed 100 ˚C	-7.73E^{-04}	0.102	2.13E^{-05}	0.262
Annealed 150 ˚C	-8.09E^{-04}	0.105	2.26E^{-05}	0.262
10mg/ml				
as-cast	-2.16E^{-03}	0.023	1.12E^{-05}	0.188
Annealed 60 ˚C	-2.15E^{-03}	0.076	4.63E^{-05}	0.203
Annealed 100 ˚C	-2.53E^{-03}	0.035	2.18E^{-05}	0.249
Annealed 150 ˚C	-3.33E^{-03}	0.016	1.25E^{-05}	0.237

OPV device performance and thin film morphology, compound 2.4a and c:

The difference in OPV performance between compound **2.4a** and **2.4c** can again be attributed to the intermolecular C–F··H interactions of compound **2.4c** and the resultant increased lattice energy. From the 2-D diffraction pattern and the I vs q plots, thin films of

compound **2.4a** on ITO/ZnO were observed to preferentially align with the 110 and 200 planes along $\chi = 0^{\circ}$ and the 111, 002, and 112 planes along $\chi = 90^{\circ}$. This indicated an edge-on molecular orientation of compound **2.4a** on the ITO/ZnO substrate which aligned the π–stacking direction parallel to the substrate. Because of this, thin films of compound **2.4a** could not efficiently transport charge through the bulk of the active layer to the interface or between the ASI molecules at the interface and the electron, or hole, transport layers. Comparing the thin film morphology of compound **2.4a** with the OPV performance data, we can conclude that the edge-on molecular orientation of **2.4a** resulted in the observed lack of any rectification behavior.

In the thin films produced using compound **2.4c**, the intermolecular C–F··H interactions aligned compound **2.4c** parallel to the ITO/ZnO substrates, aligning the π-system perpendicular to the substrate. Since compound **2.4c** π-stacked perpendicular to both electrodes, more efficient Dexter energy transfer could occur through the bulk of the ASI active layer to the anode and the cathode. The parallel molecular orientation of **2.4c** also aligned the ASI π-system to allow for stronger interactions with the electron and hole transport layers. The strong interaction at the interface would allow for more efficient exciton dissociation and therefore, improved OPV performance. The inefficient transport of the edge-on orientation also explained the lack of any device performance of the thin films of compound **2.4c** prepared from $CHCl_3$:ODCB. As shown by both GIWAXS and NEXAFS experiments, the as-cast thin films of compound **2.4c** produced from $CHCl_3$:ODCB oriented edge-on to both the Si/SiO_2 and ITO/ZnO substrates prior to annealing at 150 ˚C. Annealing thin films of compound **2.4c** resulted in the thin films

becoming highly crystalline and textured which, while improving J_{sc} and charge transport, decreased V_{oc} due to decreased chrage extraction efficeincy at the interface.

OPV device performance and thin film morphology, compound 2.4b and d:

Due to a lack of structural information about compounds **2.4b** and **d**, the only thing we can conclude is that using the (2:3) MeTHF:Toluene solvent system to prepare the active layer of the OPV tends to improve device performance. The NEXAFS spectra indicated a primarily perpendicular molecular orientation for both **2.4b** and **d** prepared from (2:3) $CHCl_3$:ODCB on Si/SiO_2, but no such conclusions could be drawn for thin films prepared on ITO/ZnO. From the AFM images, we observed that switching to MeTHF:Toluene form $CHCl_3$:ODCB resulted in a rougher, more crystalline, surface. Due to a lack of structural information for the GIWAXS experiments, how these correlate the thin film morphology to OPV device performance remains unclear.

3.3 Conclusion and future work:

A better understanding of how functional groups modulate intermolecular interactions, altering thin film morphology and thereby device performance, is critical to designing the next generation of OSCs. To further expand our understanding of structure-function relations regarding small molecule organic semiconductors, we studied the effect of partial fluorination on solution-processed thin film morphology and OPV device performance of ASIs. Performing GIWAXS, NEXAFS, AFM, and UV/Vis measurements on thin films of compounds **2.4a** and **c** we demonstrated that the substitution of just two hydrogens with isosteric fluorines, **2.4a** and **c**, had a profound effect on ASI thin film morphology. Unfortunately, no SFR insght could be gained for compounds **2.4b** and **d**. The introduction of intermolecular C–F··X interactions in compound **2.4c** increased the

lattice energy of the C2/*c* crystal structure and promoted formation of highly ordered thin films on two different substrates, Si/SiO_2 and ITO/ZnO, from two different solvent systems, (2:3) $CHCl_3$:ODCB and MeTHF:toluene. **Figure 3.62** shows the significant intermolecular interactions formed in thin films of compound **2.4c**. Compound **2.4c** was observed to form strong C–F··Si interactions on Si/SiO_2, which were very stable and facilitated molecular ordering of thin films at room temperature. The increased lattice energy of compound **2.4c**, resulting from intermolecular C–F··H interactions, not only promoted the formation of crystalline thin films and stabilized the thin films at up to 150 ˚C, but also oriented compound **2.4c** to π-stack perpendicular to the Si/SiO_2 and ITO/ZnO substrates. With the π-system aligned perpendicular to both the anode and the cathode, more efficent energy transfer and charge extraction occurred in OPVs using **2.4c**, improving OPV performance. These results demonstrate that the strategic implementation of partial fluorination in small molecule organic semiconductors should be considered a viable tool for morphological control of solution-processed thin films to tune small-molecule organic semiconductor performance.

Future work on this part of the project should include re-running the NEXAFS experiments for compounds **2.4b** and **d** for the thin films on ITO/ZnO. Also, NEXAFS measurements of compound **2.4a**, **b**, **c**, and **d**, prepared from the MeTHF:Toluene solvent system, could be extremely informative. To continue developing our understanding of SFR of ASIs, the same studies should be performed on any of the new ASI derivatives proposed in chapter 2.

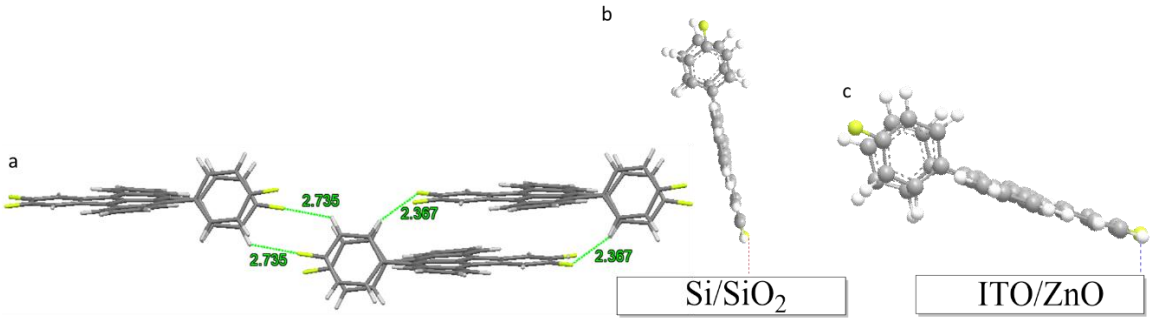

Figure 3.62: Shows the significant intermolecular interactions of compound **2.4c** a) intermolecular C–F··H interaction, b) intermolecular C–F··Si interaction, c) intermolecular C–H··ZnO interaction

3.4 Experimental:

Thin films of compounds **2.4a-d** were fabricated from a mixed solvent system of 2:3 chloroform ($CHCl_3$):orthodichlorobenzene (ODCB) or 2:3 2-Methyltetrahydrofuran (MeTHF):toluene in a nitrogen-filled glovebox. Solutions were prepared by dissolving 15 mg of the compounds in either ODCB or toluene. The suspensions were then heated to 80 ˚C and stirred for 5 minutes in a sealed 2 mL screw top vial. The suspensions were then cooled to 55 ˚C, chloroform or MeTHF was added, and the solutions were stirred for an additional 5 minutes at 55 ˚C. The solutions were then removed from heat, allowed to cool to room temperature, and filtered through a 0.45 μm PTFE syringe filter. Using this procedure, 10 mg/mL and 20 mg/mL solutions of compounds **2.4a-d** were prepared.

Thin films of compounds **2.4a-d** were prepared on either glass, Si with a native oxide layer, or ITO on glass covered with zinc oxide nanoparticles (ITO/ZnO). ITO/glass substrates were cleaned by sequentially sonicating in detergent, deionized water, acetone,

and isopropyl alcohol for 10 minutes each. The substrates were blown dry with N_2 and cleaned with UV/ozone for 20 minutes. ZnO nanoparticles were immediately applied to the cleaned ITO surface from a 2.8 wt% solution in acetone. A 50 μL drop of the ZnO solution was placed on the cleaned substrate and then spun at 7000 rpm for 30 seconds to give a ZnO layer 30 to 40 nm thick. The ITO/ZnO substrate was then transferred to the glovebox and used immediately. The Si and glass substrates were cleaned by sonication in acetone for 15 minutes followed by sonication in isopropyl alcohol for 15 minutes, blow dried with N_2, and finally cleaned with UV/ozone for 20 minutes. The cleaned substrates were directly transferred to the glove box and used immediately.

Thin films were prepared in an oxygen-free and moisture-free nitrogen glovebox. A 50 μl drop of the prepared ASI solution was spread over the substrate to assure even coverage. The substrate was then spin cast at 1000 rpm for 45 s. Compound **2.4a, b** and **d** were prepared from a 10 mg/ml solution for atomic force microscopy (AFM), UV/Visible light absorption spectroscopy (UV/Vis), and near-edge X-ray absorption fine structure spectroscopy (NEXAFS) experiments to give films between 20 to 30 nm thick. Thin films for Grazing incidence wide-angle X-ray scattering (GIWAXS) experiments were prepared from a 20 mg/ml solution due to limited diffraction signal of thinner films. Compound **2.4c** was prepared from a 10 mg/ml solution, to give films between 20 and 30 nm thick, for all experiments. Thin films of compounds **2.4a-d** were prepared on ITO/ZnO for GIWAXS and NEXAFS experiments, Si/SiO_2 for GIWAXS, NEXAFS, and AFM experiments, and glass for UV/Vis experiments. To study thin film properties at variable temperatures four samples were prepared. One was left as-cast, while the remaining three samples were

annealed at 60, 100 or 150 ˚C for 2 minutes in a nitrogen-filled glovebox and then quenched by removal from heat.

Thin film crystal structure and molecular orientation were determined via GIWAXS experiments performed on beamline 11-3 at the Stanford Synchrotron Radiation Lightsource (SSRL) using an X-ray energy of 12.7 keV and a 2-D MACCD detector at a sample-detector distance of 250 mm. The samples were placed in a chamber with flowing He at an incident angle of either 0.16˚ for samples on Si/SiO_2, or 0.12˚ for samples on ITO/ZnO. Samples were calibrated using a LaB_6 standard.[38] To minimize beam damage, samples were exposed to X-rays in five 60 second increments in the same place. The images were then averaged to produce the raw diffraction pattern. The grazing incident geometry results in distortion of reciprocal space in the raw diffraction pattern.[26] [27] Using the WAXStools program, χ and polarization corrections were applied and the intensity versus scattering vector component, qz and qxy, were plotted.[28] No absorbance intensity correction was performed because only peak location and relative intensities within a given scan were of interest. Line scans were produced by integrating 2-D GIWAXS data over a given polar angle. I vs q curves were modeled by first performing a baseline correction then fitting each peak to a Gaussian curve. Baseline correction and peak fitting of I vs q was performed using Origin data analysis software. I vs q graphs obtained from the 2-D GIWAXS were compared to theoretical I vs q powder diffraction patterns generated from the CrystalDiffract software. SimDiffraction program was used to model 2-D GIWAXS diffraction patterns.[39] Mercury software was used to determine intermolecular distances, angle of crystallographic planes, and molecular orientation.[40]

Accurate molecular orientation was determined from NEXAFS measurements performed at beamline 8-2 at the SSRL from 260 to 360 eV with 80 meV resolution. These energies result in the incident X-ray beam being elliptically polarized, with horizontal intensity polarization accounting for 80% of the total beam energy and vertical polarization accounting for 20%. Spectra were collected by recording the total electron yield (TEY) via sample drain current. Carbon K-edge spectra were collected at 20, 40, 55 and 90˚. TEY data was interpreted using Athena program.[41] Normalized TEY data was analyzed using Origin and MATLAB programs.

To characterize changes in film morphology and film thickness, AFM images in non-contact mode were obtained at the Stanford Nano Shared Facilities: Soft & Hybrid Material Facility using Park NX-10. Image analysis was performed using Park systems XEI.

UV/Visible light spectroscopy (UV/Vis) was used to determine changes in π-stacking in the thin films. UV/Vis experiments were done at the Stanford Nano Shared Facilities: Soft & Hybrid Material Facility using the Agilent Cary 6000i UV/Vis/NIR spectrophotometer. Absorbance measurements were performed on thin films of compound **2.4a-d** on glass scanning from 1200 to 200 nm. Data was analyzed using Origin data analysis software.

Organic Photovoltaic fabrication

Organic photovoltaic (OPV) devices were prepared with an inverted architecture, ITO/ZnO/ASI/MoO_3/Ag. OPV active layers were prepared from 10 and 20 mg/ml solutions of compounds **2.4a-d**. A 50 μl drop of the desired ASI solution was spread over the substrate to assure even coverage. The substrate was then spin cast at 1000 rpm for 45

s. The effects of annealing temperatures on OPV performance were studied by preparing four separate devices. The first was left as-cast, while the remaining three samples were annealed at either 60, 100 or 150 ˚C for 2 minutes in a Nitrogen-filled glovebox and then quenched by removal from heat. The electron transport layer and anode were deposited via thermal evaporation, 10 nm thick MoO_3 and 100 nm thick silver respectively, under high vacuum at 10^{-6} torr. Solar cell devices were illuminated under a simulated AM 1.5G solar spectrum (Newport Solar Simulator 94021A) calibrated to a KG5 Si photodiode, and current-voltage curves were collected by a Keithley 2400 analyzer.

3.5 References:

(1) Liao, H.-C.; Ho, C.-C.; Chang, C.-Y.; Jao, M.-H.; Darling, S. B.; Su, W.-F. *Mater. Tod.* **2013**, *16*, 326.

(2) Diao, Y.; Shaw, L.; Bao, Z.; Mannsfeld, S. C. B. *Energy Environ. Sci.* **2014**, *7*, 2145.

(3) Yuan, D.; Huang, D.; Zhang, C.; Zou, Y.; Di, C. A.; Zhu, X.; Zhu, D. *ACS Appl. Mater. Interfaces* **2017**, *9*, 28795.

(4) Zhou, N.; Vegiraju, S.; Yu, X.; Manley, E. F.; Butler, M. R.; Leonardi, M. J.; Guo, P.; Zhao, W.; Hu, Y.; Prabakaran, K.; Chang, R. P. H.; Ratner, M. A.; Chen, L. X.; Facchetti, A.; Chen, M.-C.; Marks, T. J. *J. Mater. Chem. C* **2015**, *3*, 8932.

(5) James, D. T.; Kjellander, B. K.; Smaal, W. T.; Gelinck, G. H.; Combe, C.; McCulloch, I.; Wilson, R.; Burroughes, J. H.; Bradley, D. D.; Kim, J. S. *ACS Nano* **2011**, *5*, 9824.

(6) Park, S. K.; Jackson, T. N.; Anthony, J. E.; Mourey, D. A. *Appl. Phys. Lett.* **2007**, *91*, 063514.

(7) Wasikiewicz, J. M.; Abu-Sen, L.; Horn, A. B.; Koelewijn, J., M.; Parry, A., V. S.; Morrison, J. J.; Yeates, S. G. *J. Mater. Chem. C* **2016**, *4*, 7309.

(8) Dou, J., H.; Zheng, Y., Q.; Yao, Z., F.; Yu, Z., A.; Lei, T.; Shen, X.; Luo, X., Y.; Sun, J.; Zhang, S., D.; Ding, Y. F.; Han, G.; Yi, Y.; Wang, J. Y.; Pei, J. *J. Am. Chem. Soc.* **2015**, *137*, 15947.

(9) McGarry, K. A.; Xie, W.; Sutton, C.; Risko, C.; Wu, Y.; Young, V. G.; Brédas, J.-L.; Frisbie, C. D.; Douglas, C. J. *Chem. Mater.* **2013**, *25*, 2254.

(10) Ogden, W. A.; Ghosh, S.; Bruzek, M. J.; McGarry, K. A.; Balhorn, L.; Young, V.; Purvis, L. J.; Wegwerth, S. E.; Zhang, Z.; Serratore, N. A.; Cramer, C. J.; Gagliardi, L.; Douglas, C. J. *Cryst. Growth Des.* **2017**, *17*, 643.

(11) Yadav, H. R.; Choudhury, A. R. *J. Molec. Struc.* **2017**, *1150*, 469.

(12) Osuna, R. M.; Hernández, V.; Navarrete, J. T. L.; D'Oria, E.; Novoa, J. J. *Theor. Chem. Acc.* **2010**, *128*, 541.

(13) Panini, P.; Chopra, D. *Cryst. Eng. Comm* **2013**, *15*, 3711.

(14) Jiang, H.; Ye, J.; Hu, P.; Wei, F.; Du, K.; Wang, N.; Ba, T.; Feng, S.; Kloc, C. *Sci. Rep.* **2014**, *4*, 7573.

(15) Rivnay, J.; Jimison, L. H.; Northrup, J. E.; Toney, M. F.; Noriega, R.; Lu, S.; Marks, T. J.; Facchetti, A.; Salleo, A. *Nat. Mater.* **2009**, *8*, 952.

(16) Marks, M.; Schmidt, C.; Schwalb, C. H.; Breuer, T.; Witte, G.; Höfer, U. *J. Phys. Chem. C* **2012**, *116*, 1904.

(17) Parkhomenko, R. G.; Sukhikh, A. S.; Klyamer, D. D.; Krasnov, P. O.; Gromilov, S.; Kadem, B.; Hassan, A. K.; Basova, T. V. *J. Phys. Chem. C* **2017**, *121*, 1200.

(18) Breuer, T., Witte, G., *Phys. Rev. B* **2011**, *83*, 155428.

(19) Wong, S. L.; Huang, H.; Huang, Y. L.; Wang, Y. Z.; Gao, X. Y.; Suzuki, T.; Chen, W.; Wee, A. T. S. *J. Phys. Chem. C* **2010**, *114*, 9356.

(20) Breuer, T.; Klues, M.; Liesfeld, P.; Viertel, A.; Conrad, M.; Hecht, S.; Witte, G. *Phys. Chem. Chem. Phys.* **2016**, *18*, 33344.

(21) Klues, M.; Jerabek, P.; Breuer, T.; Oehzelt, M.; Hermann, K.; Berger, R.; Witte, G. *J. Phys. Chem. C* **2016**, *120*, 12693.

(22) Kim, C. H.; Hlaing, H.; Payne, M. M.; Parkin, S. R.; Anthony, J. E.; Kymissis, I. *Chem. Phys. Chem.* **2015**, *16*, 1251.

(23) Sherman, J. B.; Moncino, K.; Baruah, T.; Wu, G.; Parkin, S. R.; Purushothaman, B.; Zope, R.; Anthony, J.; Chabinyc, M. L. *J. Phys. Chem. C* **2015**, *119*, 20823.

(24) Kline, R. J.; Hudson, S. D.; Zhang, X.; Gundlach, D. J.; Moad, A. J.; Jurchescu, O. D.; Jackson, T. N.; Subramanian, S.; Anthony, J. E.; Toney, M. F.; Richter, L. J. *Chem. Mater.* **2011**, *23*, 1194.

(25) Birkholz, M. *Thin Film Analysis by X-ray Scattering*; Wiley-VCH: Weinheim, 2006.

(26) Smilgies, D.-M. *Rev. Sci. Instrum.* **2002**, *73*, 1706.

(27) Baker, J. L.; Jimison, L. H.; Mannsfeld, S.; Volkman, S.; Yin, S.; Subramanian, V.; Salleo, A.; Alivisatos, A. P.; Toney, M. F. *Langmuir* **2010**, *26*, 9146.

(28) Oosterhout, S. D.; Savikhin, V.; Zhang, J.; Zhang, Y.; Burgers, M. A.; Marder, S. R.; Bazan, G. C.; Toney, M. F. *Chem. Mater.* **2017**, *29*, 3062.

(29) Rivnay, J.; Mannsfeld, S. C.; Miller, C. E.; Salleo, A.; Toney, M. F. *Chem. Rev.* **2012**, *112*, 5488.

(30) Stöhr, J. *NEXAFS Spectroscopy*; Springer-Verlag: New York, 1992.

(31) Stöhr, J.; Baberschke, K.; Jaeger, R.; Treichler, R.; Brennan, S. *Phys. Rev. Lett.* **1981**, *47*, 381.

(32) Dobler, C.; Tönshoff, C.; Bettinger, H. F.; Chassé, T.; Casu, M. B. *J. Phys. Chem. C* **2017**, *121*, 13660.

(33) McNeill, C. R.; Watts, B.; Swaraj, S.; Ade, H.; Thomsen, L.; Belcher, W.; Dastoor, P. C. *Nanotechnology* **2008**, *19*, 424015.

(34) Massa, W. *Crystal Structure Determination*; Springer: New York, 2004.

(35) Witte, G.; Wöll, C. *Phys. Status Solidi A* **2008**, *205*, 497.

(36) Dickey, K. C.; Anthony, J. E.; Loo, Y. L. *Adv. Mater.* **2006**, *18*, 1721.

(37) Hu, S.; Dyck, O.; Chen, H.; Hsiao, Y.-c.; Hu, B.; Duscher, G.; Dadmun, M.; Khomami, B. *RSC Adv.* **2014**, *4*, 27931.

(38) Ilavsky, J. *J. Appl. Crystallogr.* **2012**, *45*, 324.

(39) Breiby, D. W.; Bunk, O.; Andreasen, J. W.; Lemke, H. T.; Nielsen, M. M. *J. Appl. Crystallogr.* **2008**, *41*, 262.

(40) Macrae, C. F.; Bruno, I. J.; Chisholm, J. A.; Edgington, P. R.; McCabe, P.; Pidcock, E.; Rodriguez-Monge, L.; Taylor, R.; van de Streek, J.; Wood, P. A. *J. Appl. Crystallogr.* **2008**, *41*, 466.

(41) Ravel, B.; Newville, M. *J. Synch. Radiat.* **2005**, *12*, 537.

Project 2 Crystal Engineering and Structure-Function Relationship in Rubrene Derivaites

Chapter 4: The effects of intermolecular interaction on solid-state crystal packing of fluorinated rubrene derivatives

4.1. Introduction:

4.1.1 General introduction:

Organic molecules have been extensively studied as semiconductors in organic transistors as both thin film and single crystal devices. Due to tight π- stacking and a large amount of long range ordering, single crystals devices have demonstrated the highest charge mobility, between 15-40 cm^2/Vs.[1] [2] For small molecule p-type organic semiconductors single-crystal organic field-effect transistors (OFET) devices have produced the highest mobility.

To produce single crystal OFETs, high quality organic crystals are produced by either solution growth, or physical vapor transport (PVT). The process of growing high quality organic single crystals from solution or by PVT is difficult, as these methods require a large amount of time and material and are therefore not ideal for large scale commercial device production.[3] For this reason single-crystals of organic semiconductors are primarily used for fundamental studies rather than commercial device production.[4] An extremely important fundamental study of organic semiconductors is the study of molecular interactions in the solid-state and the resulting crystal structure and molecular packing. These studies are critical in developing the next generation of OSC and improving OFET performance.

For efficient charge transport to occur in OFETs tight π-stacking and long range molecular ordering in the single-crystals are critical. This is because unlike inorganic system where the ionic interaction falls off at a rate of $1/r^2$, van der Waals interactions in organic systems decrease at a rate of $1/r^6$.[5] As the Brédas group has shown, this results in an exponential decrease in charge transport efficiency as π-π stacking distances increase (**Figure 4.1a**).[6] The Brédas group also demonstrated that the type of solid-state charge transport, n-type or p-type, can vary greatly depending on the degree of acene overlap (**Figure 4.1b**). Therefore, experimentally determining molecular orientation in the solid-state is critical for predicting how efficiently OSC will function in the solid-state.

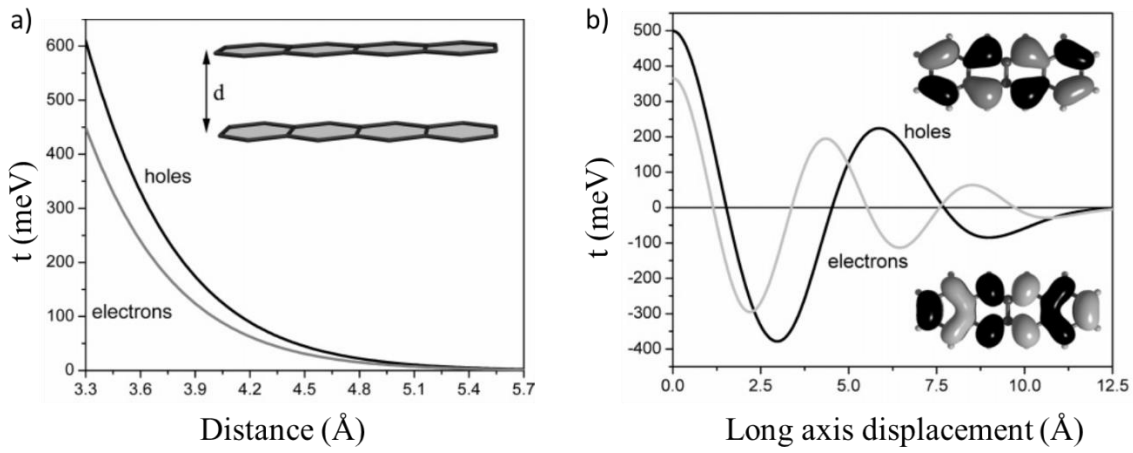

Figure 4.1: Shows a) the dependence of charge transport on π-stacking distance b) the dependence of hole and electron transport on acene overlap. Taken form the Coropceanu paper[6]

Rubrene (5,6,11,12-tetraphenyltetracene, **4.1a**) is a benchmark p-type organic semiconductor with a single crystal organic field-effect transistor (SC-OFET) mobility of up to 20 cm^2 /V s.[7-9] The tight 1D slipped π-stack of the tetracene cores along the b-axis,

in the herringbone packing motif, results in efficient charge transport in single crystal of rubrene. Functionalizing the peripheral phenyl rings can induce more desirable packing, such as tighter π-stacks, to increase charge mobility.[10-12] Rubrene derivatives have also been observed to obtain a variety of crystal systems and packing motifs, with varying amounts of π-overlap. Rubrene itself has been observed in three different polymorphs (orthorhombic, monoclinic, and triclinic), of which only the orthorhombic possesses the packing needed for efficient charge transport.[13] However, the planarity of the tetracene core, which is presumed to be necessary to achieve packing conducive to charge transport, is not always preserved in the solid state of rubrene derivatives.

4.1.2 Fluorinated rubrene derivatives:

Crystal engineering is a material design strategy employed to develop superior single-crystal organic semiconductors.[2,14] To achieve high charge mobility in organic materials, molecules must be designed with energy levels favoring either hole or electron injections, as well as maintaining solid state packing conducive to intermolecular electronic coupling.[15-17] Modification of the π-system by incorporating electron-donating or electron-withdrawing functional groups, is often used to modify energy levels in the molecule, tuning hole and electron transport efficiency.[18,19] Predicting changes in crystal packing due to structural modifications is considerably more difficult. Molecular ordering and solid-state packing are determined by the non-covalent intermolecular interactions occurring in the solid state such as, hydrogen bonding, halogen bonding, dipole−dipole, edge−face, and π−π stacking. Therefore, to engineer organic single crystal non-covalent interaction in a molecule must be modified. The modification of these non-covalent interactions can be

readily accomplished via synthetic modification to a molecular structure. Examples of some synthetic modifications used to tune non-covalent interaction in an organic molecule include the addition aryl or large alkyl groups or incorporation of a heteroatoms.[20,21]

In designing organic semiconductors, fluorine is often used as an isosteric substitution for hydrogen. Due to the difference in electronegativity, however, substitution of hydrogen with fluorine can have significant effects on both the physical and electronic properties of compounds.[22-24] For example the electron density of perfluorphenyl rings is inverted with respect to its non-fluorinated counterpart.[17,25,26] Also, unlike ionic fluoride, which forms strong hydrogen bonds, organofluorine, C–F, forms comparatively weak hydrogen bonds.[27] As a result, fluorination of an organic compound can increase its hydrophobic character. Because of this, organofluorine molecules form very few intermolecular interactions in solution. In the solid state, however, organofluorine molecules form intermolecular interactions that can significantly affect solid-state packing.[28,29] In particular, organofluorine compounds make several types of intermolecular interactions, C–F···H, C–F···F, C–F···π, π_F···H–C, and π_F···π. Although these interactions are relatively weak, organofluorine intermolecular interactions impart between –0.4 to –1 kcal/mol of stabilization per interaction, when several of them occur in one molecule they can produce significant changes in the crystal packing.[95,96] In this work, we reported a systematic study of functionalized rubrenes (**Figure 4.2**) in an attempt to better understand the underlying principles for crystal engineering of fluorinated rubrenes.

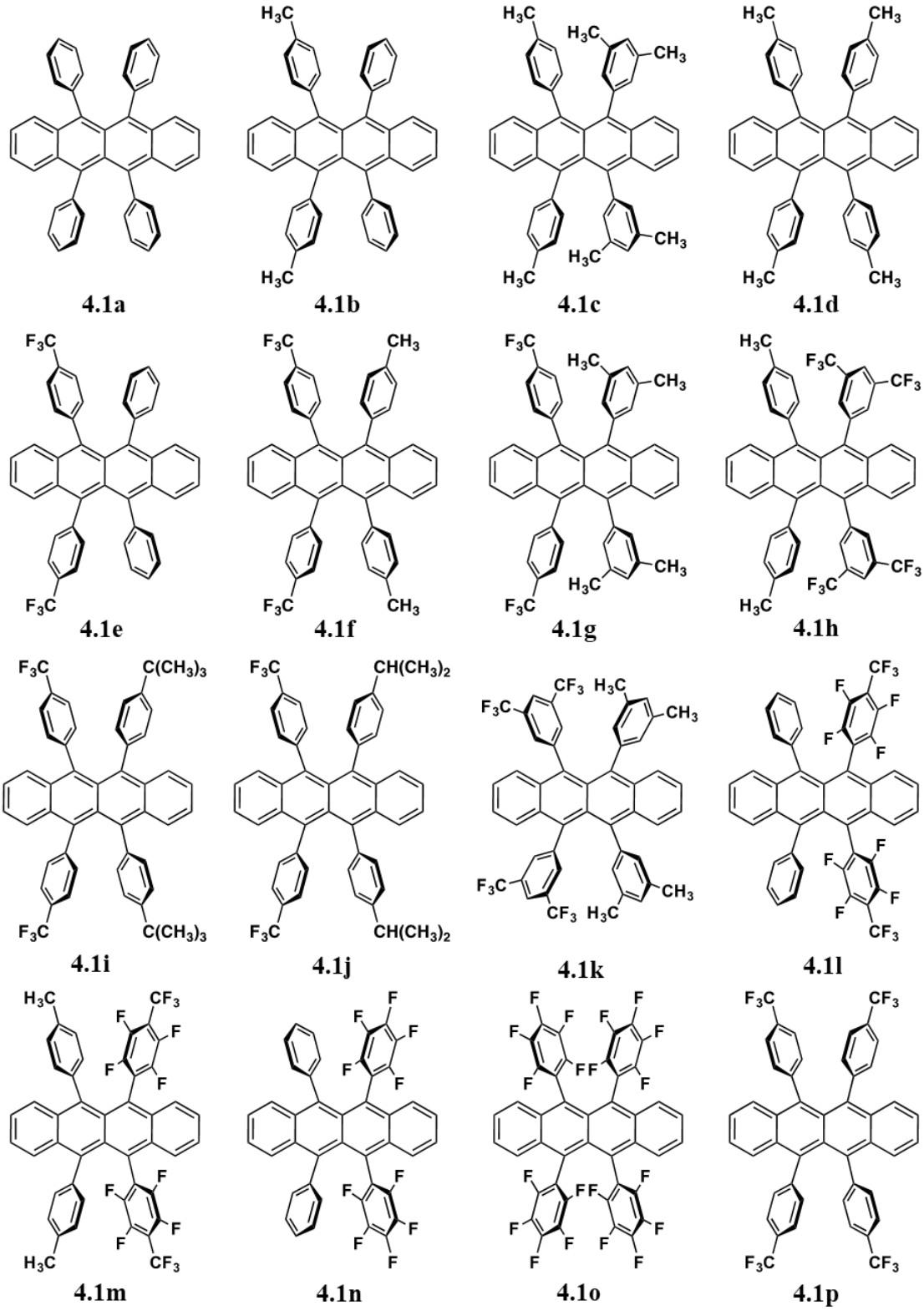

Figure 4.2: Rubrenes examined in this work.

Based on previous work performed in the Douglas group, which follows the work by Siegel et al., we hypothesized that the intramolecular steric and electronic repulsion of the peripheral aryl, groups forced into close proximity on the rubrene core, caused twisting of the tetracene backbone.[30-32] Previous publications by, Brédas, Risko, and coworkers reported calculations supporting the idea that isolated rubrene molecules (and derivatives) twist to reduce the unfavorable exchange-repulsion interaction between the peripheral aryl groups.[33] We thought that the unfavorable intramolecular interactions could be mitigated by pairing electron-rich and electron-deficient peripheral aryl groups. This hypothesis appeared to have some merit based on our early success in crystal engineering of rubrenes. Incorporation of a *para*-CF_3 group on two peripheral aryl groups (**4.1e and f**, **Figure 4.2**), resulted in rubrenes which packed similarly to orthorhombic rubrene with a planar backbone.[12] Further substitution of hydrogens on the peripheral aryl groups with isosteric fluorine resulted in rubrene derivatives with twisted tetracene backbones and altered single crystal packing motifs. [12]

We examined inter- and intramolecular interactions of several new fluorinated rubrenes through a combination of computational studies, chemical synthesis, and X-Ray crystallography. We initially synthesized, crystallized, and obtained X-ray diffraction (XRD) data for a diverse set of fluorine-rich rubrenes. To understand the energies involved in the planarization of rubrenes during crystallization, we also examined the energy barrier for the transition from a twisted to a planar backbone for a variety of fluorinated rubrene derivatives. From the XRD data, we then correlated the amount of twist in the tetracene

backbones and related that to the steric bulk and/or electronics of the peripheral aryl groups. Our analyses led to realization that fluorine-based intermolecular interactions played a much more significant role than intramolecular interactions in determining molecular packing and backbone planarity in single-crystals of rubrenes. Close contacts in the solved single-crystal structures were carefully examine to establish the correlation between chemical structure and crystal packing. Through collaborations with the Gagliardi and Cramer computational groups the reorganization energies and charge transport integrals of select rubrene derivatives were calculated, using the single-crystal packing motifs, to evaluate the charge transport properties of these new packing motifs.

4.2 Synthesis:

Several methods have been developed for the synthesis of rubrene and rubrene derivatives.[12,34,35] The procedure used for the synthesis of 5,12-bis(4-(trifluoromethyl)phenyl)-6,11-bis(3,4,5-trimethylphenyl)tetracene (**4.1q**) allowed for late state diversification, and was previously reported by our group.[12] First a Suzuki-Miyaura coupling was performed between 6,11-dichlorotetracene-5,12-dione (**4.2**) and 1,2,3-trimethylbenzene-*para*-pinacol boronate (**4.3**) to give intermediate **4.4** in 72 % yield (**Scheme 4.1**). Compound **4.2** was obtained from previous large scale reaction using as procedure previously reported from our group.[36]

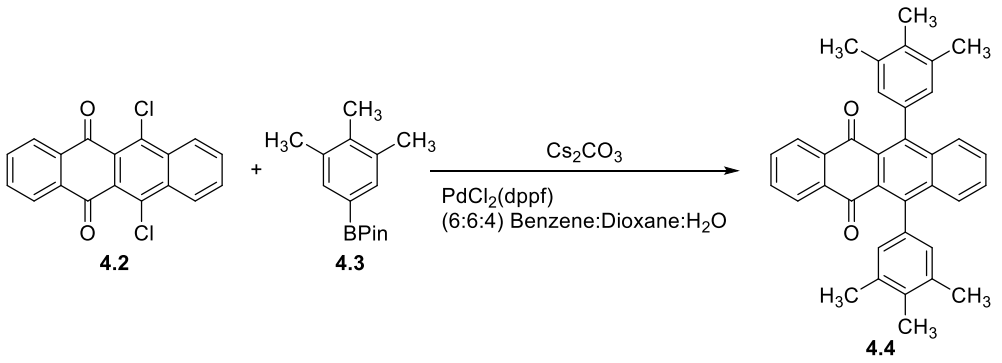

Scheme 4.1: Synthesis of 6,11-dichlorotetracene-5,12-dione (**4.4**)

The second functionalized aryl group was installed by reacting compound **4.4** with the aryl lithium of trifluoromethyl benzene from compound **4.5** producing intermediate **4.6** (**Scheme 4.2**).

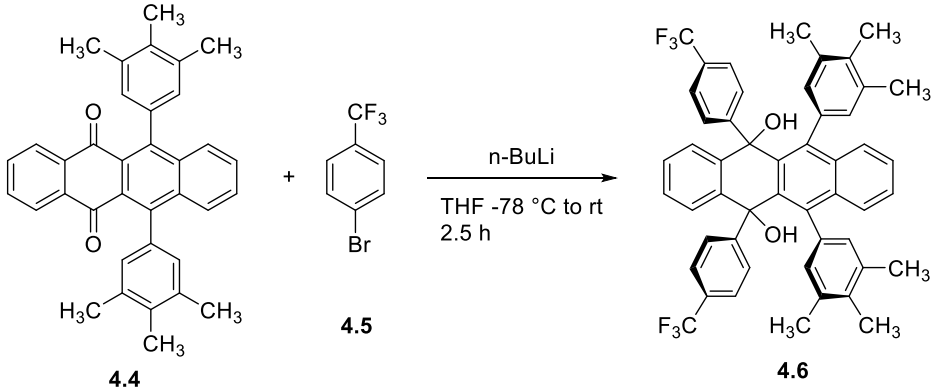

Scheme 4.2: Synthesis of 5,12-bis(4-(trifluoromethyl)phenyl)-6,11-bis(3,4,5-trimethylphenyl)-5,12-dihydrotetracene-5,12-diol (**4.6**)

This produced diol **4.6** as a mixture of diastereomers, which was carried forward as the crude mixture. The final step of reductive aromatization was performed by refluxing the crude mixture of compound **4.6** in acetone with HI to give 5,12-bis(4-(trifluoromethyl)phenyl)-6,11-bis(3,4,5-trimethylphenyl)tetracene (**4.7**) in 57 % yield over two steps (**Scheme 4.3**).

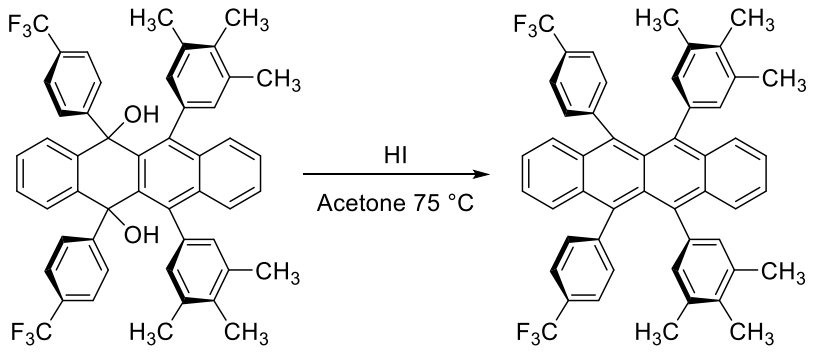

4.6 **4.7**

Scheme 4.3: Synthesis of 5,12-bis(4-(trifluoromethyl)phenyl)-6,11-bis(3,4,5-trimethylphenyl)tetracene (**4.7**)

4.3 Results and discussion:

4.3.1 The limited influence of intramolecular interactions on solid-state conformation

Crystal structures were analyzed using Mercury program. Most planar rubrene derivatives have been observed to pack in a herringbone motif (**Figure 4.3**).[37] However, the non-covalent interactions which favor the formation of planar rubrenes in the solid state are not well understood from a purely experimental perspective. Also, single crystals containing either planar or twisted rubrenes have been studied and found to pack in a wide variety of motifs. To better understand the molecular interactions controlling the solid-state conformation of fluorinated rubrene derivatives, we reevaluated our prior hypothesis that reduction of torsional strain between peripheral aryl groups led to planar rubrenes in the solid-state.

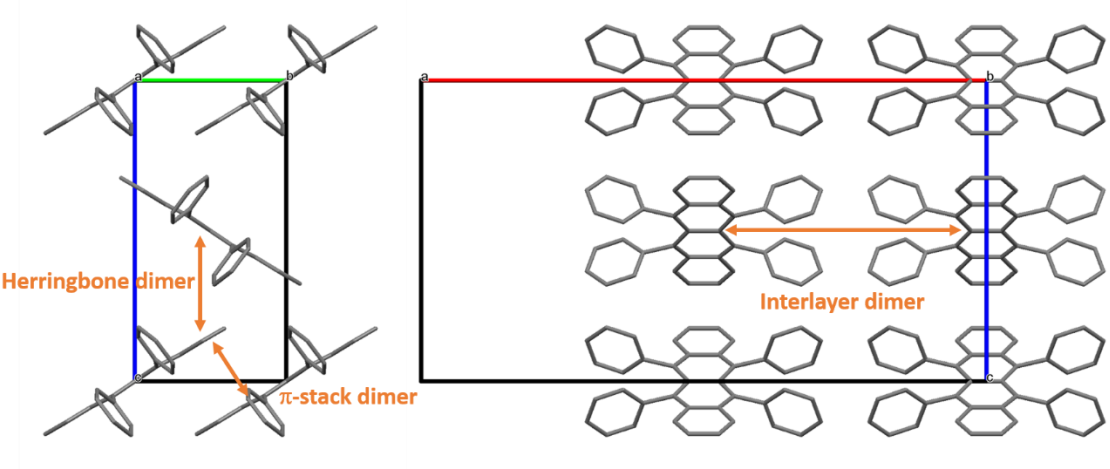

Figure 4.3: Definition of dimers discussed in this paper, intralayer (left) and interlayer (right), using the unit cell of rubrene **4.1a**.

It is a common practice to modulate molecular conformations by modifying intramolecular interactions when studying rubrenes and other organic semiconductors.[38-40] Based on our previous work,[12] the electronic character of the of the peripheral aryl groups did appear to influence molecular orientation in the single-crystal. Rubrenes **4.1b-d**, with only methyl group substitutions, exhibited twisted backbones in the solid state. By replacing a methyl with an electron-withdrawing CF_3 group (**4.1e-g**) we were able to produce single crystals of rubrene containing planar tetracene backbones. These findings also indicated a reduced influence of sterics on the formation of planar rubrene conformations. For example, rubrene **4.1f**, sterically analogous to **4.1d**, was planar. The planarity in **4.1f** suggested that the addition of bulky substituents to the peripheral aryl groups was not the primary factor affecting backbone planarity in the solid state. Calculations by the Brédas group also demonstrated the decreased importance of intramolecular sterics on rubrene conformation. Their results indicated that the unfavorable

exchange-repulsion interactions between the peripheral aryl groups were the primary cause of twisting of the tetracene cores of rubrenes. In designing new rubrene targets, we attempted to reduce exchange-repulsion between the peripheral aryl groups through incorporation of electron-withdrawing substituents. New fluorinated rubrenes **4.1.2.1h**-**p** were prepared, and singles crystals grown, to determine if alleviation of exchange-repulsion resulted in planar, π-stacked, rubrene. For most of the prepared rubrene derivatives, compounds **4.1.2.1h**-**p**, further decreasing the electron density on the peripheral aryl groups resulted in rubrenes which packed in a twisted conformation rather than the predicted planar conformation.

To compare the relative energies, and energetics, of interconversion between twisted and planar backbones density functional theory (DFT) calculation were performed for rubrenes **4.1h** and **4.1k–o**. Souman Gosh, of the Gagliardi and Cramer groups observed that for isolated rubrene molecules, the twisted conformation is the lowest energy state for all derivatives and that all electron deficient rubrenes had a lower energy barrier to planarization than the parent compound.[41] The calculations also indicated that conversion between planar and twisted conformations was essentially a barrierless process for all rubrenes measured.[41] Although the DFT models generally agreed with our prior experimental results, we were unable correlate intramolecular electronics or sterics with planarization energies and the tetracene backbone conformation observed in the solid-state. Since we were unable to explain our experimental results from the computational planarization energies, we looked for alternative ways to relate the backbone twist to substituent effects.

Table 4.1: Crystal data of rubrene derivatives **4.1a-b**, **4.1e-h**, **4.1k-m**, **4.1o**.

Compound		**4.1a**	**4.1b**	**4.1e**	**4.1f**	**4.1g**	**4.1h**	**4.1k**	**4.1l**	**4.1m**	**4.1o**
Crystal System[a]		O	O	O	O	O	M	M	M	M	T
Space Group		Cmca	$Pna2_1$	Pnma	Pbcm	Pbcm	$P2_1/c$	$P2_1$	$C2/c$	$P2_1/n$	Pī
Twist (degrees)	molecule 1	0	41.2	0	0	0	19.9	39.5	28.9	28.4	0
	molecule 2[b]							40			0
Centroid-to-Centroid distance (Å)	molecule 1	3.54	3.44/ 3.75[c]	3.43	3.42	3.47	3.38/ 3.43[c]	3.45/ 3.43[c]	3.4	3.34/ 3.41[c]	3.33
	molecule 2[b]							3.45/ 3.42[c]			3.39
Aryl Splay Angle (degrees)	molecule 1	25.3	29.2/ 16.3[c]	18.5	18.2	18.5	23.1/ 19.1[c]	17.5/ 18.8[c]	23.3	18.6/ 13.7[c]	13.7
	molecule 2[b]							16.6/ 19.9[c]			17
Aryl Slip Angle (degrees)	molecule 1	26.7	45.3/ 34.1[c]	23.2	24.7	30.8	24.5/ 26.9[c]	34.0/ 34.3[c]	18.5	31.5/ 34.1[c]	28.3
	molecule 2[b]							36.3			30.3

Note: [a] O = orthorhombic, M = monoclinic, T = triclinic; [b] molecule 2 indicates two molecules in the asymmetric unit; [c] indicates values are inequivalent across the tetracene core. A description of how values were measured for each parameter can be found in the SI with table S3.

No rubrene derivative was observed to crystalize with the peripheral aryl groups perfectly eclipsed. Instead, rings can splay (**Figure 4.4a**) or slip past each other (**Figure 4.4b**); in many cases, the whole tetracene backbone twists (**Figure 4.4c**) to reduce the repulsion. We measured each of these phenomena for our new rubrene derivatives and

summarized values for selected compounds in **Table 4. 1**.[41] Our analysis found no direct correlations between the degree of electron deficiency of the peripheral aryl groups with any one parameter (splay, slip, or twist). We also found no correlation between the splay and slip angles or between splay and slip angles with the degree of backbone. In an attempt to simplify the analysis, the centroid-to-centroid (CtC) distances (**Figure 4.4d**) of the peripheral aryl groups was used to determine the extent exchange-repulsion. If twisting of the backbone resulted from the decreasing of exchange-repulsion between the peripheral aryl groups, we would expect a correlation between centroid-to-centroid distance and degree of backbone twist. In the end, however, no such correlation was detected. Having observed no trend relating the degree of backbone twist to electron deficiency of the peripheral aryl groups we next examined steric influences.

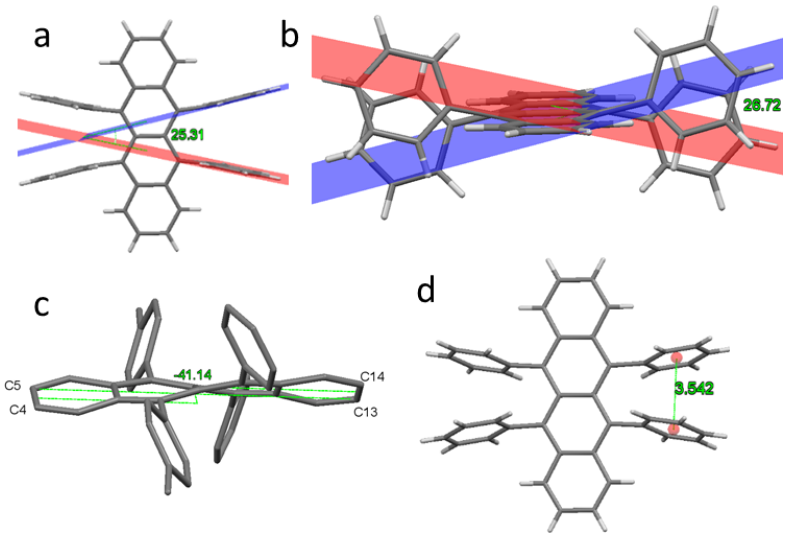

Figure 4.4: Example measurement of structural parameters: (a) splay angle, (b) slip angle, (c) backbone twist, (d) centroid-to-centroid distance. Note: Several of the rubrene derivatives, both flat and twisted, were found to have "puckering" along the tetracene backbone as well.[41]

To correlate the effect of intramolecular steric repulsion between the peripheral aryl groups with the observed twist, we first examined rubrene derivatives containing *para* substitutions. The introduction of CH_3 groups, as in **4.1b**, induced a high degree of twisting, 41.2°. However, upon substitution of the CH_3 with CF_3, **4.1e**, a planar backbone is observed. This suggests sterics at the *para* position are not a major contributor since the van der Waals volume of CH_3 is more than half that of CF_3, 16.8 and 42.6 $Å^3$ respectively.[42] Additionally, substituting the CH_3 group with a *t*-butyl group (**4.1i**, which displays a 2° backbone twist) or an isopropyl group (**4.1j**, a planar tetracene backbone) had minimal impact on planarity.

The effect of substitution at other positions was far more complex. The identity of the groups at the *meta* positions appeared to have a much more significant impact on the tetracene backbone conformation than at the *para* position. By comparing the crystal structures of **4.1g** and **4.1h**, we found that switching the position of CF_3 and CH_3 groups resulted in significant changes to the backbone conformation, planar (**4.1g**) to twisted (**4.1h**, 20.0°). Again, sterics could not explain the changes in backbone conformation observed upon replacing hydrogens with isosteric fluorines. For example, rubrenes **4.1e** and **4.1f** are both planar while **4.1l** and **4.1m** are both twisted, 28.9° and 28.4° respectively. Taken as a whole, we could not find any correlation between the planarity in the tetracene backbone and intramolecular interactions of the peripheral aryl groups. The computational studies of rubrene backbone conformations indicated that the twisted conformation was lower in energy, in the gas phase, by 1.7 to 3.5 kcal/mol.[41] Therefore, there must be solid-state interactions occurring which stabilize the higher energy planar conformation.

Aside from intramolecular steric and electronic factors, intermolecular interactions also impact each conformer's energy level within a crystal lattice. These additive intermolecular interactions have the potential of being more impactful to the conformation of rubrene during crystallization.[33] Furthermore, if intramolecular interaction of the peripheral aryl groups did dictate the conformation of the tetracene backbone in the solid-state, then one would not observe two symmetry independent conformers in the asymmetric unit, as is seen for compounds **4.1d** and **4.1k**. The crystal structures of **4.1d** and **4.1k** contain two molecules in the asymmetric unit, each molecule with differing amounts of twisting the tetracene core, 42.8° and 33.9°, 39.5° and 40.0° respectively. Additionally, Tokito and coworkers report a furan-containing rubrene derivative that has two molecules in the asymmetric unit, one twisted 35.8˚, and the other planar, with no π-overlap between the two conformations.[10] Therefore, to explain why some rubrene derivatives are planar while others are highly twisted, we examined the intermolecular interactions within each solved crystal structure.

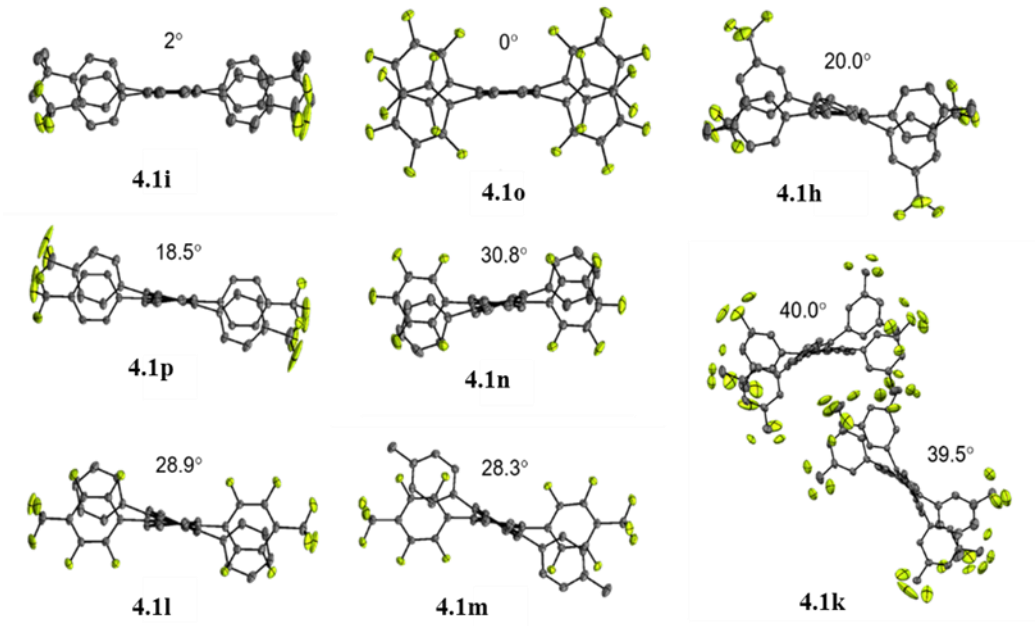

Figure 4.5: Thermal Ellipsoid plots of rubrene **4.1h-i**, **4.1k-o**, showing backbone twist angles. For **4.1k**, two twist angles are observed.[43]

4.3.2 Intermolecular interactions exert influence on solid state conformation:

In the solid-state, intermolecular C–F···X interactions quickly begin to dominate as the number of fluorine substitutions are increased in the rubrene derivatives. Our analysis of the data indicated that the backbone conformation and packing motifs observed in **4.1e-p** resulted from non-covalent intermolecular C–F···X interactions of CF_3 and/or aryl organofluorines (C–F) with functional groups of neighboring rubrene molecules. In addition to the C–F···X interactions that dominated in most of the prepared rubrenes derivatives, we also observed C–H···π, –1 to –3 kcal/mol, C–H···H, –0.4 kcal/mol, and π-π, –1 to –3 kcal/mol interactions.[44-47] Only intermolecular interactions within the van der Waals radii were used to examine the influence of interactions on molecular conformation and crystal packing, with all C–H bond distances being normalized to 1.083 Å.[48]

To gain a frame of reference for interactions that may be necessary to stabilize a planar core, we revisited the crystal structure of the parent rubrene, **4.1a**. [41] [49] The closest interactions within the π-dimer were symmetric C–H···H, 2.189 Å at 142.2°, occurring between a set of phenyl *ortho* hydrogens and the edge hydrogens of the tetracene core (**Figure 4.6a**). Across the interlayer (**Figure 4.6b**), neighboring *meta* hydrogens form short contacts, C–H···H 2.216 Å, with the peripheral aryl groups. The analysis of **4.1a** demonstrated that intermolecular C–H···H interactions between the intralayer dimers and across the interlayer (**Figure 4.6**) appear to stabilize crystal packing of the planar rubrene conformer. The symmetric interactions on both sides of a given rubrene molecule in the lattice indicated that counter-balancing intermolecular interactions were required to stabilize the otherwise higher energy planar conformation. This was supported by computations performed by the Brédas group which suggested that interactions within the intralayer significantly contribute to stabilization of planar π-stacking rubrenes.[33] The paper also concluded that interlayer interactions, between neighboring rubrene molecules, were more significant for stabilizing the *overall* crystal lattice. Based on these finding we then examined how the introduction of functional groups on the peripheral aryl rings enhanced and/or disrupted these key intermolecular interactions.

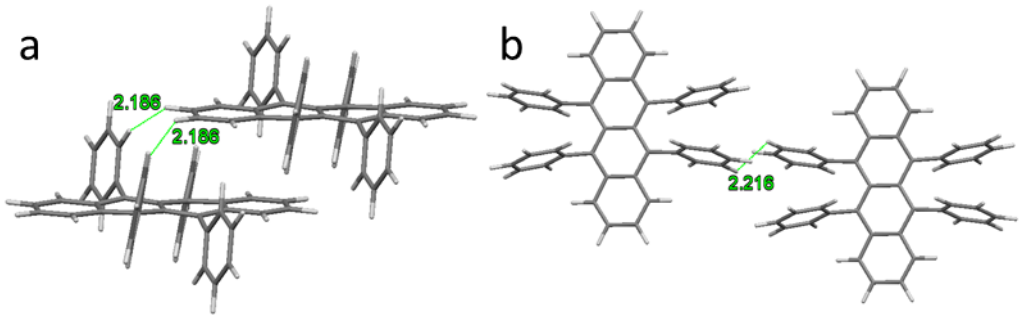

Figure 4.6: Intermolecular interactions of (a) intralayer dimers and (b) interlayer dimers in rubrene **4.1a**.

Starting with planar rubrenes **4.1e-g**, we worked to identify additional interactions which might influence the crystal packing. For compounds **4.1e** and **4.1f**, C–H···π interactions formed the closest short contacts with the core, however, the *ortho* hydrogens of the peripheral phenyl, or *para*-tolyl, groups were found to contact a nearby core in the herringbone dimer, as well as the π-dimer (**Figure 4.7**). Sassella and coworkers observed similar *ortho* C–H···π and C–H···H interactions in other planar rubrenes derivatives.[50] Yet while rubrene **4.1g** does contain a planar backbone, the *ortho* C–H···H interactions to the tetracene core in the π-stacked dimer are not the closest short contacts. In **4.1e-g**, groups at the *para* position forge the interlayer interactions, instead of the groups at the *meta* position (**4.1a**). Interlayer interactions for **4.1e** (**Figure 4.8**) are stabilized by symmetric C–F···H bonds between *para*-CF_3 and *para*-hydrogen at 2.417 Å. Rubrene **4.1f** displays C–F···H interactions of 2.585 and 2.559 Å as well as C–F···F interactions at 2.770 and 2.923 Å between the *para* substituents, due to rotational disorder of both the *para*-CF_3 and the *para*-methyl groups. Compound **4.1g** formed C–F···H interactions at 2.448 Å with the *para*-hydrogen and C–H···H interactions at 2.185 Å between *meta*-CH_3 groups. From the crystal

data we observed that *para*-CF_3 substituents form additional C–F···X interactions in the interlayer.

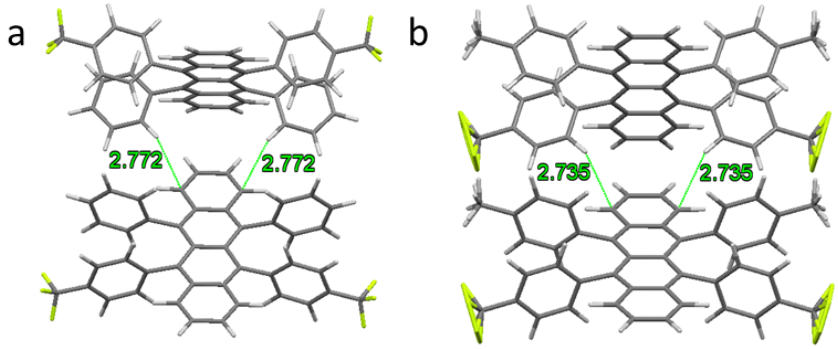

Figure 4.7: Intermolecular interactions between the herringbone dimers in a) **4.1e** and b) **4.1f**.

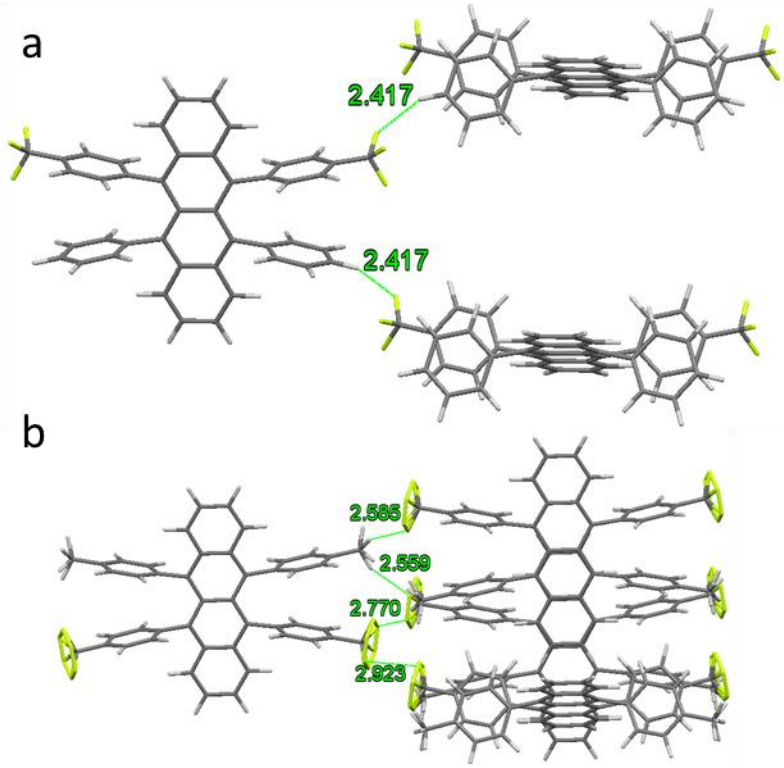

Figure 4.8: Interlayer interactions in a) **4.1e** and b) **4.1f**.

Comparatively we found that rubrenes **4.1b-d**, which have the exact same substitution pattern without the fluorines, all had twisted tetracene cores (41.2°, 30.3°, and 42.8°/33.9° respectively). In these derivatives, C–H···π interactions were found to dominate the close contacts. The absence of π-stacking in **4.1b-d** complicates direct comparison to **4.1e-f**, but some inferences could still be made. For example, rubrene **4.1b** (a structure analogous to **4.1e**) an *ortho*-hydrogen of an unsubstituted peripheral aryl group formed a C–H···π interaction at 2.692 Å with a methyl substituted peripheral aryl group rather that the tetracene core, as observed in **4.1e**. Rubrene **4.1b** also formed additional C–H···H interaction at 2.250 Å between an *ortho*-hydrogen of the peripheral tolyl group and a neighboring *para*-CH_3. In **4.1b**, a *meta*-hydrogen of the *para*-CH_3 peripheral aryl group formed a C–H···π interaction of 2.640 Å, C15-C14 centroid,[51] with the tetracene core and a C–H···H interaction of 2.346 Å. The distance from *meta*-hydrogen to centroid C15-C14,[52] as well as other centroid distances, represents a geometrically averaged interaction distance for atoms shown to have multiple interaction to other atoms on a neighboring rubrene. [41]

In single crystals of rubrene **4.1c**, the methyl groups at the *meta* positions formed close contacts with several regions of neighboring rubrene molecules. A methyl of a peripheral *meta*-xylyl group displayed C–H···π interactions with C9, C10, and C16 [53] of a neighboring tetracene core. In addition, each methyl substituent of the peripheral *meta*-xylyl group formed different close contacts to neighboring molecules. The analysis of compound **4.1d**, was complicated by the fact that the single-crystal structure contained two molecules in the asymmetric unit. From the XRD, we observed that C–H···π interactions dominate the close contacts interactions between the two molecules in the asymmetric unit;

the closest being 2.457 Å, C2-C3-C7 centroid [54] contact between neighboring tetracene cores. The majority of remaining short contacts involve the methyl substituents.[41] Overall, the introduction of methyl groups at either the *para* or *meta* positions favored interactions with the neighboring tetracene core rather than forming interactions across the interlayer with other peripheral aryl groups. Comparing the solid-state interactions of rubrenes **4.1a-g** indicated that stabilization of the planar conformation in the solid state requires the formation of symmetric intermolecular interactions about the rubrene molecule. To date, all planar rubrenes (**4.1a**, **4.1e-g**, and others [50]) have demonstrated a symmetric peripheral aryl group slip, via an *S*-like symmetry element, resulting from symmetric interlayer interactions.

The presence of additional CF_3 groups was found to have a dramatic effect on the crystal packing. Compound **4.1p**, which possesses *para*-CF_3 on all the peripheral aryl group, was found to have a monoclinic C2/*c* crystal structure with no π-stacking between neighboring rubrene molecules. Additionally, the core was twisted 18° and had slipped 1-D packing motif along the short axis. The slipped 1-D packing was found to contain C–H···π interactions between the *meta*-H and the tetracene core. Symmetric interactions are observed on the top and bottom face of the core, however, the intermolecular interaction were not equivalent along the tetracene backbone. On one end of the tetracene core a C–H···π interaction of 2.404 Å, C9-C9'-C10-C17 centroid, [55] was observed, while on the other end a longer C–H···π distance of 2.535 Å, C2-C2'-C1 centroid, was seen (**Figure 4.9**. See supporting information for additional diagrams of these contacts. [41]) Unlike the previous rubrenes, the *para* substituents of compound **4.1p** formed C–F···H interactions with the

tetracene core. On one end of the tetracene core, a fluorine formed a close contact with C2–H proton (2.478 Å) while on the other end the interaction was between the fluorine atom and C10–H proton (2.524 and 2.653 Å).[56] The fluorine was also found to form an interlayer interaction with a *meta*-carbon on the peripheral aryl group of a neighboring rubrene. The substitution of additional CF_3 groups appear to have disrupted interlayer interactions of the *para* substituents which were observed to align the tetracene backbones in rubrenes **4.1e-g**. When comparing rubrene **4.1e-g** to **4.1p**, we observed that the interlayer interactions of rubrenes **4.1e-g** aligned electron poor and electron rich peripheral aryl groups to form interactions which oriented the packing in the solid state, while the *para* the CF_3 groups of rubrene **4.1p** interacted with the electron-rich core dramatically altering solid state packing.

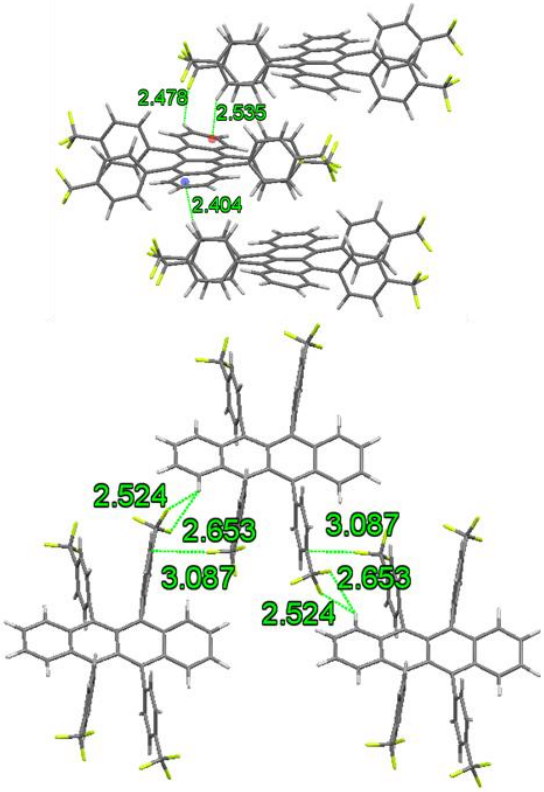

Figure 4.9: Intermolecular interactions in rubrene **4.1p**.

Extending the analysis of *para*-CF_3 rubrene derivatives rubrene **4.1i**, which also contained bulky *t*-butyl group at the *para* position, only had a slight twist of 2° and slipped π-stacking (**Figure 4.10**). Rather than the *ortho*-H···π interactions that were observed in rubrenes **4.1a** and **4.1e-f**, C–H···π interactions were observed between a *meta*-H of a *para*-CF_3 peripheral aryl group with the C3 carbon of the tetracene backbone (2.591 Å). Also, a *meta*-H of the *t*-butyl peripheral aryl group was observed to form a close contact with the C9 carbon (2.607 Å) [57] on the opposite side of the same tetracene core. Similar to **4.1e-g**, the electron-rich and electron-poor phenyl rings aligned across the interlayer. However, due to the bulkiness of the *t*-butyl group, a methyl of the *t*-butyl group was observed to interact with the *meta*-H on a *t*-butyl peripheral aryl group (2.742 Å), rather than CF_3. Overall, this is an interesting case where the nearly planar rubrene **4.1i** does not display any π-stacking. For rubrene **4.1j** the unit cell was determined to be primitive monoclinic with cell constants a = 15.2600(5) Å , b = 13.8935(4) Å, c = 18.1133(6) Å , β = 99.371(1) °, and V = 3789.0(2) $Å^3$, however, no suitable model could be obtained which refined the disorder to an appropriate degree to be considered a solved crystal structure.[41] Therefore, no detailed packing information could be obtained from the XRD experiments.

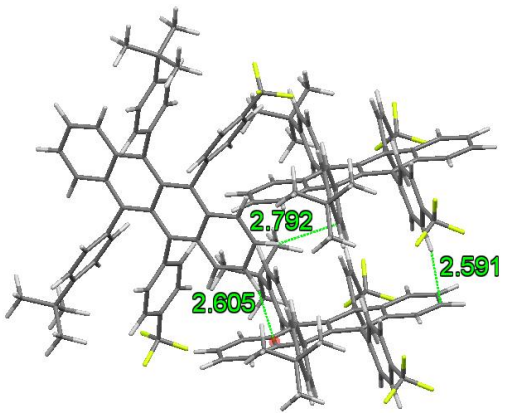

Figure 4.10: Intermolecular interactions in rubrene **4.1i**.

Introduction of CF_3 groups to *meta* positions, rubrenes **4.1h** and **4.1k**, resulted in twisted backbones, 20° and 40° respectively, and very different packing motifs, sandwich herringbone verses slipped 1D packing respectively. Examining rubrene **4.1h**, on one side of the tetracene unit, the π-stack dimers formed one C–H···H interaction between an *ortho* hydrogen on a *para*-tolyl peripheral aryl group and a neighboring tetracene core (2.138 Å *para*-CH_3, **Figure 4.11**). Additionally, an *ortho* hydrogen on a di-*meta*-CF_3 peripheral aryl group formed a rather acute C–H···H close contact to the same neighboring tetracene core (2.157 Å, *meta*-CF_3). On the opposite side of the same tetracene core, all the short contacts are between herringbone dimers. The *meta* CF_3 groups were observed to reach both the tetracene core and the peripheral aryl groups of a neighboring rubrene molecule, forming several C–F···H and C–F···F interactions. These different C–F···X interactions resulted in an imbalance of interactions on the rubrene molecule, disrupting both intra- and interlayer ordering. Consequently, the planar tetracene conformation is not achieved. Similar to **4.1j**, the high degree of disorder in **4.1k** only allowed for limited data analysis, therefore, while

the crystal structure was solved, a thorough analysis of intermolecular interactions could not be achieved.[41]

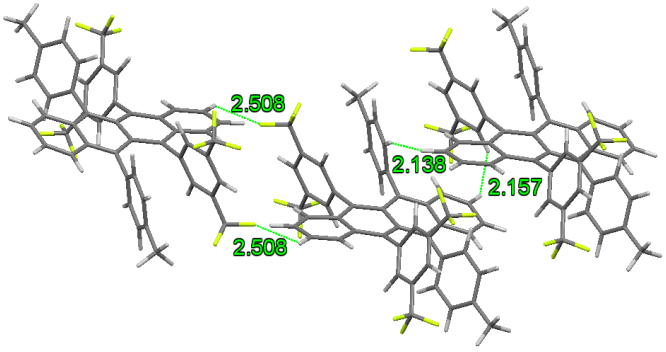

Figure 4.11: Intermolecular interactions in rubrene **4.1h**.

Perfluorination of the peripheral *para*-tolyl groups lead to a monoclinic C2/*c* crystal structure with 2-D brick packing for **4.1l** and a backbone twist of 28.9°. Examination of rubrene **4.1l** crystal demonstrated that the 2-D brick packing was a result of intermolecular interactions of both the *ortho* fluorines and *ortho* hydrogens on the peripheral aryl groups with the tetracene backbone of a neighboring molecule (**Figure 4.12**). The π-stack distances were slightly different at either end of the tetracene core, 3.622 and 3.525 Å. In rubrene **4.1l**, the closest intermolecular interactions were C–F···H occurring within the π-stacked dimers. The C–F···H interactions between tetracene C2–H and *ortho* fluorine atoms of a neighboring rubrene molecule occurred both above and below the plane of the tetracene backbone at 2.594 or 2.433 Å (**Figure 4.12b**). We also observed intralayer C–F···H interactions between *ortho* fluorine atoms and the C9–H of the tetracene backbone at 2.346 Å, again above and below the tetracene plane. Intralayer C–H···H interactions were also observed between *ortho* hydrogens and either C9–H or C10–H of the tetracene core. The interlayer once again demonstrated alternating electron-rich and electron-poor

peripheral aryl groups which interacted via the CF_3 group and the *meta* hydrogen forming C–F···H interactions at 2.573 Å and 2.555 Å, **Figure 4.12c**. The solved crystal structure of rubrene **4.1m** showed that both the *para*-CH_3 and the *meta* hydrogen of the tolyl group interacted with the CF_3 group which altered the packing motif. The *ortho* fluorine atoms of the peripheral aryl groups were seen to interact with the neighboring tetracene cores in an edge-to-edge manner (**Figure 4.13**). The *para*-CH_3 was also observed to form C–F···H interactions with *meta* fluorine atoms of a neighboring molecule. Overall, these observations lead to the conclusion that fluorine substituted rubrenes pack to maximize fluorine-based interactions. Also, comparing fluorine substituted rubrenes **4.1h**, **i**, and **m** to rubrenes **4.1.2.1e-g**, we observed that *meta*-fluorine substituents form C–F···X interactions that disrupted favorable intralayer and interlayer interactions necessary to produce planar rubrene conformers in the solid-state.

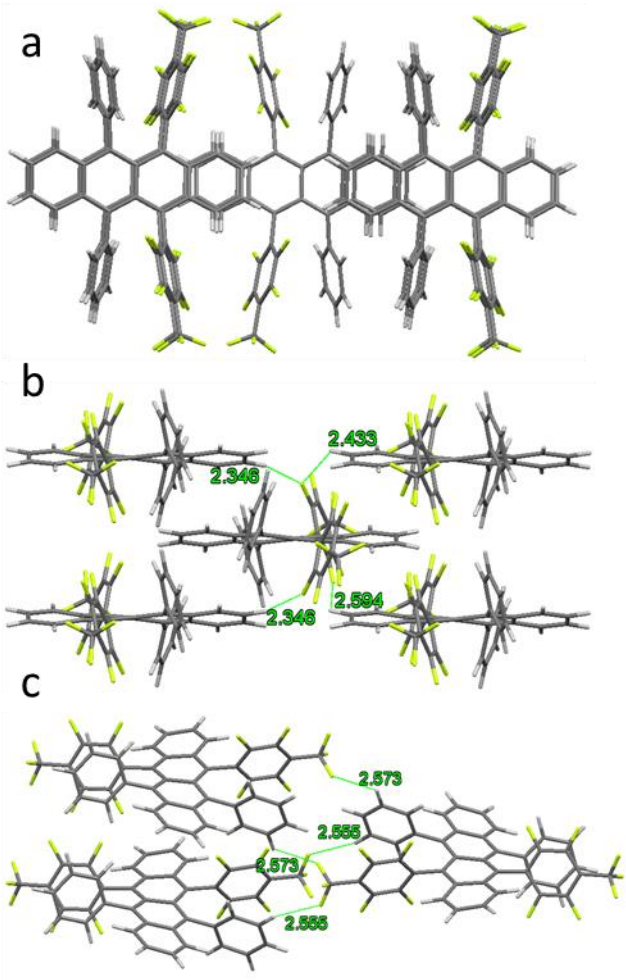

Figure 4.12: Crystal packing of rubrene **4.1l**, show a) the π-stacking of the 2-D brick b) intermolecular interactions between π-stack dimers c) intermolecular interactions of the interlayer.

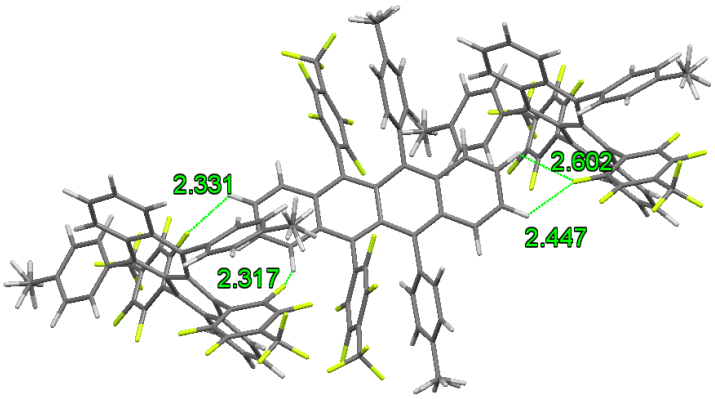

Figure 4.13: Intermolecular interactions in rubrene **4.1m**.

Rubrene **4.1n**, with both perfluoro and unsubstituted phenyls, twisted 30.8°, formed a triclinic Pī crystal system with a 2-D brick packing motif. Again, the *ortho* fluorine and *ortho* hydrogen atoms interacted with the tetracene core, orienting the π-stacked dimer (**Figure 4.14a**), manifesting in the 2-D brick packing. Similar to **4.1l**, the π-stacking distance of rubrene **4.1n** dimers were slightly different at either end of the tetracene core, 3.609 and 3.514 Å. C–F···H interactions between π-stacked rubrenes were found to form the tightest interactions (**Figure 4.14b**). As observed in rubrene **4.1l**, the interlayer dimers of **4.1n** aligned to allow the phenyl and perfluorophenyl groups of neighboring rubrenes to efficiently form C–F···H interactions (**Figure 4.14c**, 2.346–2.584 Å). The crystal structures of rubrene **4.1l** and **4.1n** are the first reported examples of rubrene derivatives obtaining this specific 2-D brick packing motif observed in the solid state. Computational models, as well as transport experiments, have demonstrated the improved charge transport of the 2-D brick packing motif verses the 1-D herringbone or π-stacked herringbone motifs. It has been reported that this improved transport is due to decreased charge transport anisotropy

in the single crystal.[58,59] These findings demonstrate a potential new crystal packing motif to target for crystal engineering of single crystal rubrenes: planar 2-D brick.

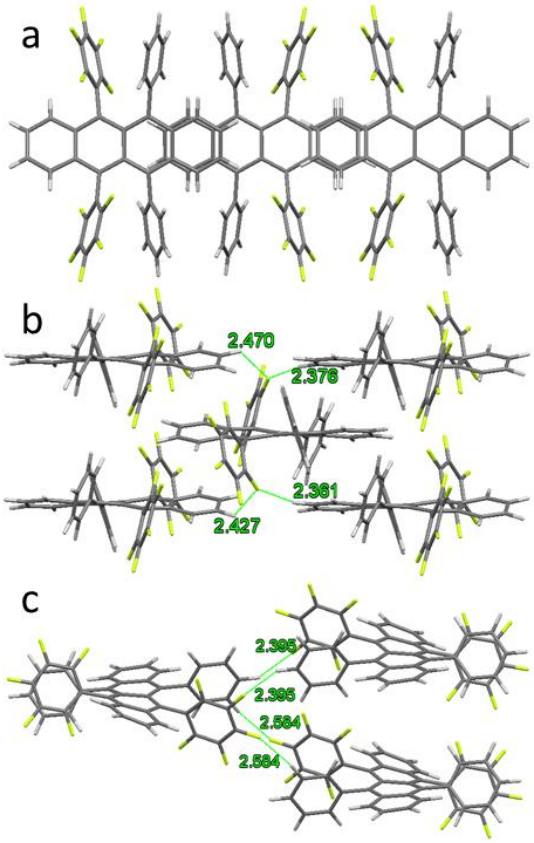

Figure 4.14: Crystal packing of rubrene **4.1n**, show a) the π-stacking of the 2-D brick b) intermolecular interactions between π-stack dimers c) intermolecular interactions of the interlayer.

Rubrene **4.1o** packed in a slipped herringbone motif with a planar tetracene backbone. Two molecules were observed in the asymmetric unit with two distinct π-stacking distances. The difference in π-dimer distance, 3.632 and 5.562 Å (**Figure 4.15**), were a result of a π-π_F interaction between neighboring herringbone dimers which pushed a neighboring set of π-dimers apart (**Figure 4.16**). Similar to **4.1l** and **4.1n**, the tightly

bound π-stacked dimers (3.632 Å) of rubrene **4.1o** formed three *ortho*-fluorine C–F···H interactions: C10–H (2.598 Å), C2–H (2.503 Å), and C9–H (2.413 Å). While a separate π-stacked dimer, formed C–F···π interactions between *ortho* fluorine and the tetracene core (3.024 Å, C2A-C1A centroid). Rubrenes **4.1e-n,** all contained the so-called type I C–F···F interactions, however, in **4.1o** we also observed the rarer type II C–F···F interactions between the herringbone dimers (**Figure 4.16**).[24,60,61] As with all planar rubrene derivatives we observed that the interactions along the tetracene backbone of rubrene **4.1o** contained an inversion symmetry element.

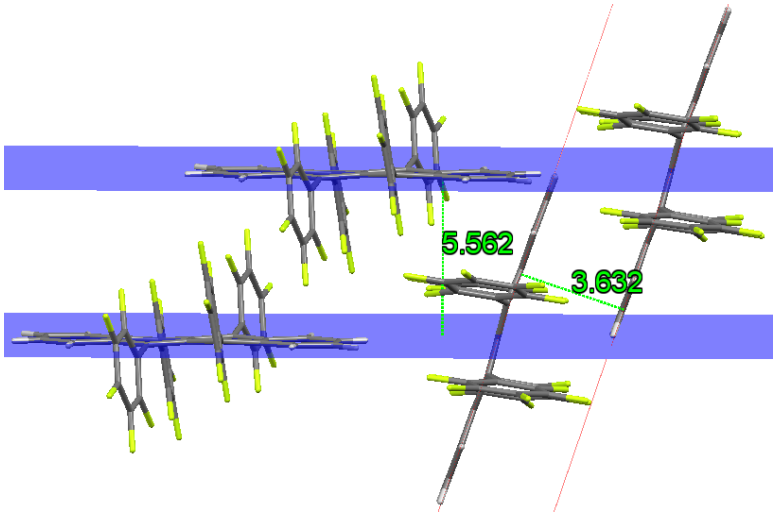

Figure 4.15: Rubrene **4.1o** π-stacked dimer distances.

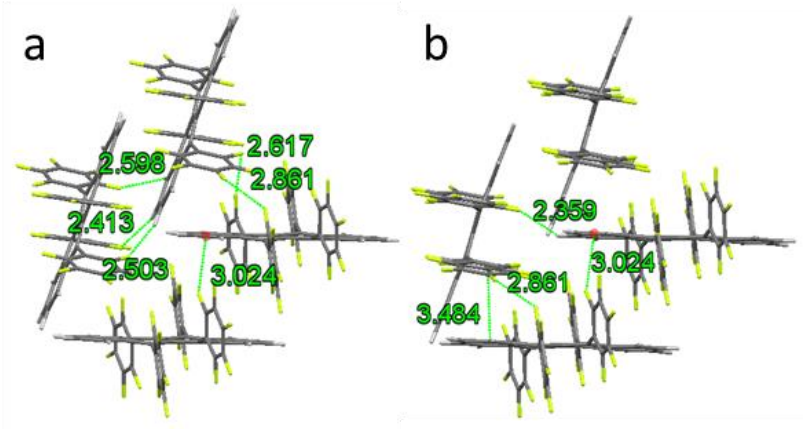

Figure 4.16: Packing arrangements and fluorine-based interactions in rubrene **4.1.2.1o**, a) intralayer close contacts are highlighted, b) shows additional intralayer close contacts including π-π_F and type II C–F···F interactions.

Our analysis of rubrenes **4.1a-p** demonstrated the importance of symmetric intermolecular interactions in stabilizing and crystallizing the planar rubrene conformations. We noted the need to consider all types of intermolecular interactions, even weak C–F···X interactions, when engineering rubrene derivatives for solid-state organic electronic devices. Also, through our analysis of the crystal structures compounds **4.1a-p**, we observed that intermolecular interactions between the *ortho* positions and the tetracene core oriented the π-stacking dimer as well as the herringbone dimers. We also observed that the intermolecular interaction of the peripheral aryl groups need to be symmetric to stabilize the higher energy planar conformation of rubrene derivatives. These symmetric interaction occurred in the interlayer between neighboring rubrene molecules via the *para* fluorine and *meta* or *para* hydrogens groups (**Table 4.2**).

Table 4.2: Position of key short contacts on peripheral aryl groups

	Rubrene	Intralayer	Interlayer	π-stacked dimer distance Å
Herringbone (planar)	**4.1a**	*ortho* H	*meta* H	3.66
	4.1e	*ortho* H	*para* H and *para* F	3.55
	4.1f	*ortho* H	*para* H and *para* F	3.51
	4.1g	*ortho* H	*para* H, *meta* H	3.63
	4.1o	*ortho* F, *meta* F	*para* F	3.63 and 5.56
Slipped 1D (slightly twisted)	**4.1i**	*meta* H	*para* F, *meta* H	NA
2D-brick (twisted)	**4.1l**	*ortho* H, *ortho* F	*para* F, *meta* H	3.62 and 3.53
	4.1n	*ortho* H, *ortho* F	*para* F, *meta* H	3.61 and 3.51
Other twisted	**4.1h**	*ortho* H, *meta* F	*para* H, *meta* F	NA
	4.1m	*para* H	*para* H, *para* F, *meta* H	
	4.1p	*para* F, *meta* H	*para* F	

4.3.3. Hirshfeld Surface analysis:

Hirshfeld analyses were performed on rubrenes **4.1a-p** to further examine the significance of the intermolecular interactions found during the geometric analysis of the solved crystal structure. The use of Hirshfeld surfaces to determine the shortest intermolecular interactions, and the significance of each interaction, has been used to analyze wide range of molecules, including rubrenes.[62-64]

Hirshfeld Surfaces (HS) and 2D fingerprint of all rubrene derivatives can be found in the Crystal Growth and Design paper.[41] All van der Waals and covalent radii were set manually, hydrogen 1.20 and 0.37 Å, fluorine 1.50 and 0.71 Å, carbon 1.50 and 0.77 Å. In Hirshfeld surface analysis color coding is used to indicate the closeness of individual contacts. Red represents close contacts inside the van der Waal radii, white represents close contacts near or at the van der Waals radii, and blue represents close contacts outside the van der Waals radii. 2D fingerprint analysis of Hirshfeld plots is used to indicate the

significance of each contact. Blue represents very little contribution of the close contact to the solid-state packing, while colors ranging from green to red represents a significant contribution of the close contacts to the solid-state packing.

The Hershfeld surface and 2D fingerprint of rubrene **4.1a** demonstrated that the closes contacts occurred between the *ortho* hydrogen and the hydrogens of the tetracene core in the π-stacked dimer.[64] The peripheral aryl groups showed close contacts that corresponded to interactions at the *meta* hydrogens of the peripheral aryl groups between the interlayers. Rubrene **4.1f** showed weaker close contacts at the *ortho* hydrogen and the tetracene core in the π-stacked dimer, compared to **4.1a** (**Figure 4.17a**). There are, however, significant close contact interactions between neighboring rubrenes across the interlayer at both the *para* CF_3 and *para* methyl groups. Examining the 2D fingerprint plot it was found that the C–F···X intermolecular interactions comprised a significant number of the interactions occurring in the **4.1f** crystal lattice, 30.5 % (**Figure 4.17b**).

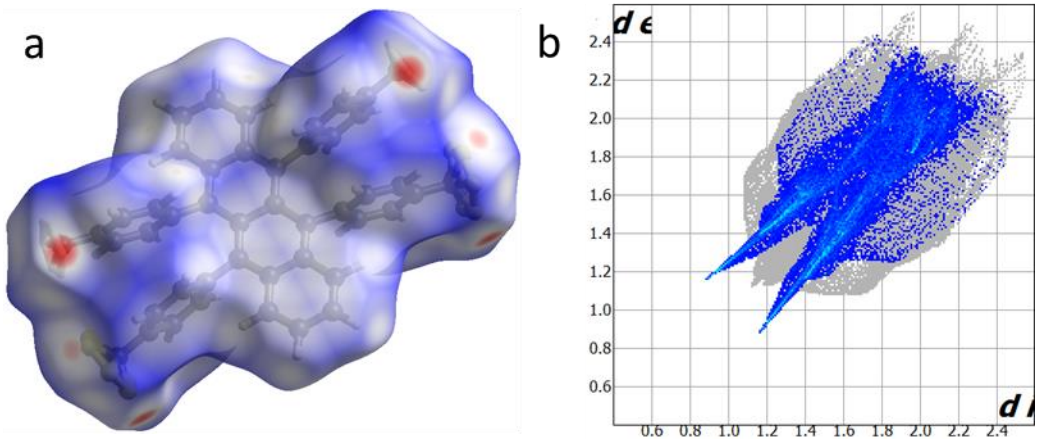

Figure 4.17: a) Hirshfeld surface b) C–F···H interactions 2D finger print plots of rubrene **4.1f**.

As was observed in our geometric analysis of close contacts, the HSs of rubrene **4.1p** plot showed close contacts that occurred between *meta* hydrogen of the peripheral aryl groups and the teracene core, **Figure 4.18a**. C–F···H close contacts were also seen at the *para* CF_3 and the tetracene core of a neighboring rubrene. The 2D plot again shows a significant contribution of C–F···X interactions, **Figure 4.18b**. In the single crystal of rubrene **4.1p** C–F···X interaction make up 55 % of all the close contacts occurring in the crystal lattice.

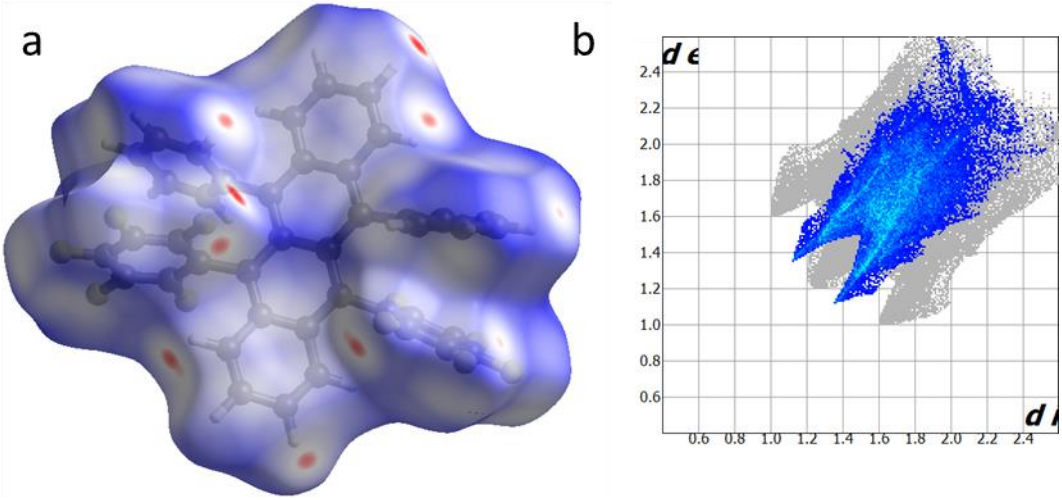

Figure 4.18: a) Hirshfeld surface b) C–F···H interactions 2D finger print plots of rubrene **4.1p**.

Rubrene **4.1n** showed similar close contacts. The crystal structure of rubrene **4.1n** formed close contacts at both the *ortho* hydrogen and *ortho* fluorine to the tetracene core in the π-stacked dimers, as well as between *meta* hydrogen and *meta* fluorine. The HS plot also showed the close contacts observed of *para* hydrogens and *para* fluorines in the interlayer (**Figure 4.19a**). From the 2D fingerprint plot we observed that C–F···X interactions now

accounted for 58 % of all the close contacts formed in the crystal lattice of rubrene **4.1p,** the vast majority of those being C–F···H interactions, 45 % (**Figure 4.19b**).

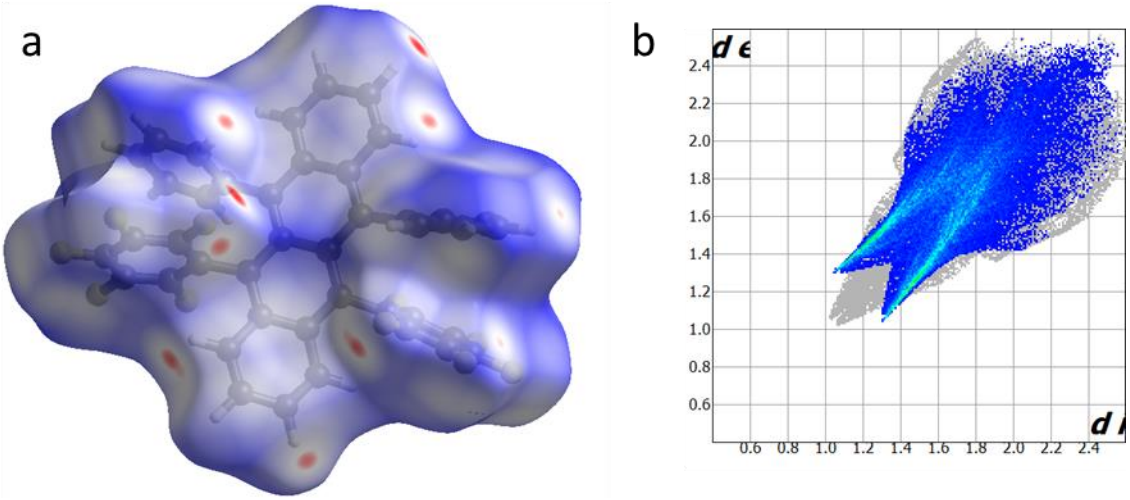

Figure 4.19: a) Hirshfeld surface b) C–F···H interactions 2D fingerprint plots of rubrene **4.1n**.

The Hirshfeld analysis of C–F···X interactions corroborates the single-crystal analysis of short contacts discussed above and the significates of the different intermolecular interactions that occur at the *ortho*, *meta*, and *para*, position of the peripheral aryl rings.

Although we originally targeted the packing motif that theory suggested was optimal for charge transport in single-crystal devices, i.e. slipped π-stacking in orthorhombic rubrene, our study of fluorinated rubrenes has led to a new packing motif not previously observed in other rubrene derivatives, 2-D brick. We observed that several of the rubrene derivative overlapped well with neighboring rubrene molecule. To probe the charge transport of these packing motifs we turned to chemical theory and computational modeling.

4.3.4 Charge transport properties of rubrene derivatives:

From the computational modeling of a select number of fluorinated rubrene derivatives we found that reorginization energies of the twisted conformation were lower, or equal to, the reorginization energies for the planar conformation for both hole and electron transport. Using the solved single-crystal structures and a dimer model to compute charge transport, the hole and electron transport integrals were found to be very similar for the fluorinated rubrene derivatives. A rather interesting result ocurred when the charge transport of **4.1l** and **4.1n** were examined. From the computational models we found that even in the twisted conformation, rubrenes **4.1l** and **4.1n** had a large transfer integral, 60 meV. This indicated that the 2-D brick packing could be a viable alternative packing motif to target when designing new rubrene derivatives.

Other charge transport properties were also calculated by Souman Gosh of the Gagliardi and Cramer groups, a complete analysis of which is publised in the Crystal Growth and Design paper.[41]

4.4 Conclusion and future work:

Analysis of the crystal structures of fluorinated rubrenes **4.1e-p** clearly showed that C–F···X intermolecular interactions play a major role in determining molecular conformation and crystal packing. Analysis of the solved crystal structures and computational results indicated symmetric intermolecular interactions in the crystal structures are needed to stabilize the higher energy planar rubrene conformation. Comparing the crystal structures of rubrene **4.1a-p**, it is clear that intermolecular interactions between the peripheral phenyl *ortho* positions and the tetracene core oriented

the π-stacking dimer. At the same time, interlayer interactions are necessary for stabilization of the planar rubrene conformation. When adding new functional groups to the peripheral aryl groups, consideration must be made for both new interactions formed as well as interactions that are disrupted. As more fluorines are added to rubrene molecules, C–F···X intermolecular interactions quickly dominate, disrupting π-stacking and planarity. Fluorines at the *ortho* position of the peripheral aryl groups of rubrenes **4.1l**, **4.1n**, and **4.1o** interacted strongly with the tetracene core orienting rubrene molecules in the intralayer helping to stabilize the π-stacking. Addition of fluorine groups to the *para* position appear to help stabilize the higher energy planar conformation of rubrene derivatives, **4.1e**-**g**, and **4.1o**. These stabilizing interactions were formed through the ordering of the interlayer, which paired electron rich and electron deficient peripheral aryl groups, allowing for favorable C–F···X interactions. However, substitutions at the *meta* position appear to disrupt these interactions preventing the planar conformation from crystallizing. We also observed fluorine substituents at the *meta* position forming new C–F···X interactions in the twisted conformation, leading to previously unseen 2-D brick crystal packing motifs.

Through our examination of intermolecular interactions, we demonstrated that when designing new rubrene derivatives, it is necessary to consider new intermolecular interactions that may occur, even weak C–F···X interaction. We have also observed, for the first time, a new packing motif for rubrenes: the 2-D brick, which theoretical calculations indicate could function efficiently as an organic semiconductor. This indicates that although planar rubrene remains ideal for maximal charge transport, planarity itself is not critical for efficient charge transport in rubrene-based single crystal

organic semiconductors. Our findings provide a better roadmap for crystal engineering of π-stacked rubrene derivatives for materials science and lead to increased development of improved organic semiconductors.

Future work on this project should include examination of the charge transport properties of rubrene **4.1l** and **n** which were found to pack in the 2-D brick packing motif. Also, the synthesis of new functionalized rubrenes, including functionalization off the tetracene core, should be attempted in order to find new rubrene packing motifs with unique charge transport properties.

4.5 Experimental:

6,11-bis(3,4,5-trimethylphenyl)tetracene-5,12-dione (**4.2.3**):

To a 2-neck round bottom flask, a 6:6:4 solution of benzene:dioxane:water (11.68:11.68:7.78 mL) was prepared and sparged with nitrogen for 10 minutes. At which point compound **4.2.1** (0.660 g, 2.017 mmol) was added to the solution, the round bottom flask was sealed, final purged the nitrogen 3 times, then the solution was then heated to 70 ˚C. Once the solution temperature had reached 70 ˚C PdCl(dppf) (0.148 g, 0.217 mmol), Cs_2CO_3 (2.629 g, 8.068 mmol), and compound **4.2.2** (1.489 g, 6.075 mmol) were all added. The reaction was stirred at 70 ˚C, under a nitrogen atmosphere, for 24 hours. After the 24 hours, the reaction was then allowed to cool to room temperature. The reaction was worked-up by pouring the crude reaction mixture into a 250 ml separatory funnel and diluted with 100 ml of water. The crude product **4.2.3** was then extracted from the aqueous layer using ethyl acetate (3 × 75 mL). The ethyl acetate was then dried over Mg SO_4, concentrated, and placed under high vacuum overnight. Pure compound **4.2.3** was obtained

by recrystallization from methylene chloride using methanol as the anti-solvent (0.716 g, 1.448 mmo, 72 %) ^{1}H NMR (500 MHz $CDCl_3$) δ 8.10 (dd, *J* = 5.8, 3.3 Hz, 2H), 7.65 (dd , *J* = 5.9, 3.3 Hz, 2H), 7.61 (dd, *J* = 6.5, 3.34Hz, 2H), 7.47 (dd, *J* = 6.6, 3.3 Hz, 2H), 6.93 (s, 4H), 2.39 (s, 12H), 2.34 (s, 6H);

5,12-bis(4-(trifluoromethyl)phenyl)-6,11-bis(3,4,5-trimethylphenyl)-5,12-dihydrotetracene-5,12-diol (**4.2.5**):

A 150 ml 3-neck flask was flamed dried and cooled to room temperature under vacuum. Compound **4.2.3** (0.716 g, 1.448 mmol) was then add to the 3-neck round bottom flask and the system was purged to nitrogen 3 time. 30 mL of freshly distilled THF was added to the 3-neck flask and gently heated to dissolve **4.2.3**. Once compound **4.2.3** was dissolved the solution was cooled to -77 ˚C. At the same time, a 50 ml 2-neck round bottom flask was flame dried then cooled to room temperature under vacuum. The 2-neck round bottom flask was then purged with nitrogen 3 time, freshly distilled THF was add, and then the system was cooled to -77 ˚C. Compound **4.2.4** (3.258 g, 14.48mmol) and n-butyl lithium (2.5 M in hexane, 5.212 mL, 0.835 g, 13.03 mmol) were add to the 2-neck round bottom flask and reacted at -77 ˚C for 30 minutes. After 30 minutes, the reaction was transferred to the 3-neck round bottom containing the solution of compound **4.2.3** at -77 ˚C via cannulation. The reaction was stirred at -77 ˚C for 2 hours and then allowed to warm up to room temperature. The reaction was stirred at room temperature for an addition 1 hour at which point, the reaction was quenched with 0.5 mL of NH_4Cl. The reaction was then concentrated under vacuum, placed under high vacuum overnight, and carried forward crude. %) ^{1}H NMR (500 MHz $CDCl_3$) δ 8.10 (dd, *J* = 5.8, 3.3 Hz, 2H), 7.65 (dd , *J* = 5.9,

3.3 Hz, 2H), 7.61 (dd, *J* = 6.5, 3.34Hz, 2H), 7.47 (dd, *J* = 6.6, 3.3 Hz, 2H), 6.93 (s, 4H), 2.39 (s, 12H), 2.34 (s, 6H);

5,12-bis(4-(trifluoromethyl)phenyl)-6,11-bis(3,4,5-trimethylphenyl)tetracene (**4.2.6**): Crude compound **4.2.5** was place in a 100 mL 2-neck round bottom flask and dissolved in 20 ml of acetone. The solution was sparged with nitrogen for 5 minutes, the round bottom flask seal, and the head space purged with nitrogen, the HI was added (57 % w/w, 1.91 mL, 1.852 g, 14.48 mmol) . The reaction was then heated to 75 ˚C and refluxed, under a nitrogen atmosphere. The reaction was monitored by TLC. Once all the starting material had been consumed the reaction was cooled to 0 ˚C in an ice bath and filtered. The crude product was washed 3 time with 50 mL of water then placed under high vacuum overnight. Crude **4.2.6** was purified by dissolving the product in dichloromethane and recrystallizing with methanol in the refrigerator overnight. After filtration of the recrystallization product pure compound **4.2.6** was obtained as orange solid (0.619 g, 0.823 mmol, 57 % over 2 steps). ^{1}H NMR (500 MHz $CDCl_3$) δ 7.54 (dd, *J* = 7.0, 3.3 Hz, 2H), 7.30 (d *J* = 8.0 Hz, 2H), 7.19 (dd , *J* = 7.1, 3.3 Hz, 2H), 7.16 (dd, *J* = 7.1, 3.2 Hz, 2H), 7.11 (dd, *J* = 7.2, 3.2 Hz, 2H), 7.00 (d *J* = 8.0 Hz, 2H), 6.53 (s, 4H), 2.15 (s, 12H), 2.12 (s, 6H);^{19}F NMR (379 MHz, CDCl3) δ 61.77;

Crystallography:

Rubrene derivatives were examined by single-crystal XRD using Bruker SMART Platform CCD diffractometer with graphite monochromater using CuKα radiation (λ=0.71073) at 123 K ω scans for **4.1.2.1h-o** and Bruker APEX II Platform CCD diffractometer with graphite monochromater using MoKα radiation (λ=1.54178) at 123 K

ω scans for **4.1.2.1p**. Reflections were integrated using SAINT program. Absorption correction was performed using SADABS program. Space group determination and data merge was performed using XPREP program. Structures solved using SHELTXL and SHELXLE. Hydrogen were initially assigned automatically by the structure solver program then allowed to relax to better fit the electron density. Fluorines were assigned via q-peaks. Fluorine conformational disorder was determined by examining residual q-peaks. Rotational disorder in CH_3 groups was modeled using AFIX constraints, while CF_3 disorder was modeled by creating multiple C–F bonds splitting them into parts and assigning fractional occupancy to each part. To correctly model fluorine conformational and rotational disorder some geometric and displacement restraint as well as constraints were needed.

4.6 References:

(1) Kang, I.; Yun, H. J.; Chung, D. S.; Kwon, S. K.; Kim, Y. H. *J. Am. Chem. Soc.* **2013**, *135*, 14896.

(2) Yassar, A. *Polym. Sci. Series C* **2014**, *56*, 4.

(3) Forrest, S. R. *Nature* **2004**, *428*, 911.

(4) Bao, Z.; Valente, C. *Organic Field-effect Transistors*; CRC Press: Boca Raton, 2007.

(5) West, R. A. *Basic Solid State Chemistry*; 2nd ed.; John Wiley & Sons: West Sussex, 1999.

(6) Coropceanu, V.; Cornil, J.; da Silva Filho, D. A.; Olivier, Y.; Silbey, R.; Bredas, J. L. *Chem. Rev.* **2007**, *107*, 926.

(7) Xie, W.; Prabhumirashi, P. L.; Nakayama, Y.; McGarry, K. A.; Geier, M. L.; Uragami, Y.; Mase, K.; Douglas, C. J.; Ishii, H.; Hersam, M. C.; Frisbie, C. D. *ACS Nano* **2013**, *7*, 10245.

(8) Mullenbach, T. K.; McGarry, K. A.; Luhman, W. A.; Douglas, C. J.; Holmes, R. J. *Adv. Mater.* **2013**, *25*, 3689.

(9) Podzorov, V.; Menard, E.; Borissov, A.; Kiryukhin, V.; Rogers, J. A.; Gershenson, M. E. *Phys. Rev. Lett.* **2004**, *93*, 086602.

(10) Mamada, M.; Katagiri, H.; Sakanoue, T.; Tokito, S. *Cryst. Growth Des.* **2014**, *15*, 442.

(11) Zhang, Z.; Ogden, W. A.; Young, V. G.; Douglas, C. J. *Chem. Commun. (Camb)* **2016**, *52*, 8127.

(12) McGarry, K. A.; Xie, W.; Sutton, C.; Risko, C.; Wu, Y.; Young, V. G.; Brédas, J.-L.; Frisbie, C. D.; Douglas, C. J. *Chem. Mater.* **2013**, *25*, 2254.

(13) Huang, L.; Liao, Q.; Shi, Q.; Fu, H.; Ma, J.; Yao, J. *J. Mater. Chem.* **2010**, *20*, 159.

(14) Desiraju, G. R. *J. Am. Chem. Soc.* **2013**, *135*, 9952.

(15) Anthony, J. E. *Chem Rev* **2006**, *106*, 5028.

(16) Anthony, J. E.; Brooks, J. S.; Eaton, D. L.; Parkin, S. R. *J. Am. Chem. Soc.* **2001**, *123*, 9482.

(17) Ryno, S. M.; Risko, C.; Bredas, J. L. *J. Am. Chem. Soc.* **2014**, *136*, 6421.

(18) Tang, M. L.; Reichardt, A. D.; Wei, P.; Bao, Z. *J. Am. Chem. Soc.* **2009**, *131*, 5264.

(19) Anthony, J. E.; Facchetti, A.; Heeney, M.; Marder, S. R.; Zhan, X. *Adv Mater* **2010**, *22*, 3876.

(20) Sherman, J. B.; Moncino, K.; Baruah, T.; Wu, G.; Parkin, S. R.; Purushothaman, B.; Zope, R.; Anthony, J.; Chabinyc, M. L. *J. Phys. Chem. C* **2015**, *119*, 20823.

(21) Black, H. T.; Perepichka, D. F. *Angew Chem Int Ed Engl* **2014**, *53*, 2138.

(22) Schwarzer, A.; Weber, E. *Cryst. Growth Des.* **2008**, *8*, 2862.

(23) Rybalova, T. V.; Bagryanskaya, I. Y. *J. Struct. Chem.* **2009**, *50*, 741.

(24) Chopra, D.; Row, T. N. G. *Cryst. Eng. Comm.* **2011**, *13*, 2175.

(25) Dou, J. H.; Zheng, Y. Q.; Yao, Z. F.; Yu, Z. A.; Lei, T.; Shen, X.; Luo, X. Y.; Sun, J.; Zhang, S. D.; Ding, Y. F.; Han, G.; Yi, Y.; Wang, J. Y.; Pei, J. *J. Am. Chem. Soc.* **2015**, *137*, 15947.

(26) Sakamoto, Y.; Suzuki, T.; Kobayashi, M.; Gao, Y.; Fukai, Y.; Inoue, Y.; Sato, F.; Tokito, S. *J. Am. Chem. Soc.* **2004**, *126*, 8138.

(27) Chopra, D. *Cryst. Growth Des.* **2012**, *12*, 541.

(28) Taylor, R. *Cryst. Growth Des.* **2016**, *16*, 4165.

(29) Taylor, R. *Cryst. Eng. Comm.* **2014**, *16*, 6852.

(30) Hunter, C. A. *Angew. Chem., Int. Ed.* **1993**, *32*, 1584.

(31) Cozzi, F.; Siegel, J. S. *Pure Appl. Chem.* **1995**, *67*, 683.

(32) Cozzi, F.; Ponzini, F.; Annunziata, R.; Cinquini, M.; Siegel, J. S. *Ang. Chem. Int.* **1995**, *34*, 1019.

(33) Sutton, C.; Marshall, M. S.; Sherrill, C. D.; Risko, C.; Bredas, J. L. *J. Am. Chem. Soc.* **2015**, *137*, 8775.

(34) Biehl, R.; Dinse, K.-P.; Mobius, K.; Plato, M.; Kurreck , H.; Mennenga, U. *Tetrahedron Lett.* **1793**, *29*, 363.

(35) Dodge, J. A.; Bain, J. D.; Chamberlin, A. R. *J. Org. Chem.* **1990**, *55*, 4190.

(36) Yagodkin, E.; McGarry, K. A.; Douglas, C. J. *Org. Prep. Proced. Int.* **2011**, *43*, 360.

(37) da Silva Filho, D. A.; Kim, E. G.; Brédas, J. L. *Adv. Mater.* **2005**, *17*, 1072.

(38) Huang, H.; Chen, Z.; Ponce Ortiz, R.; Newman, C.; Usta, H.; Lou, S.; Youn, J.; Noh, Y. Y.; Baeg, K. J.; Chen, L. X.; Facchetti, A.; Marks, T. J. *J. Am. Chem. Soc.* **2012**, *134*, 10966.

(39) Zhang, C.; Zang, Y.; Gann, E.; McNeill, C. R.; Zhu, X.; Di, C. A.; Zhu, D. *J. Am. Chem. Soc.* **2014**, *136*, 16176.

(40) Jackson, N. E.; Kohlstedt, K. L.; Savoie, B. M.; Olvera de la Cruz, M.; Schatz, G. C.; Chen, L. X.; Ratner, M. A. *J. Am. Chem. Soc.* **2015**, *137*, 6254.

(41) Ogden, W. A.; Ghosh, S.; Bruzek, M. J.; McGarry, K. A.; Balhorn, L.; Young, V.; Purvis, L. J.; Wegwerth, S. E.; Zhang, Z.; Serratore, N. A.; Cramer, C. J.; Gagliardi, L.; Douglas, C. J. *Cryst. Growth Des.* **2017**, *17*, 643.

(42) Seebach, D. *Angew. Chem., Int. Ed. Eng.* **1990**, *29*, 1320.

(43) To solve the crystal structure of 4.1k, both the CH_3 and CF_3 groups are to be refined in all meta positions with 50% occupancy at each side.

(44) Hunter, C. A.; Sanders, J. K. M. *J. Am. Chem. Soc.* **1990**, *112*, 5525.

(45) Takahashi, O.; Kohno, Y.; Nishio, M. *Chem. Rev.* **2010**, *110*, 6049.

(46) Nishio, M.; Umezawa, Y.; Honda, K.; Tsuboyama, S.; Suezawa, H. *Cryst. Eng. Comm.* **2009**, *11*, 1757.

(47) Kupcewicz, B.; Małecka, M. *Cryst. Growth Des.* **2015**, *15*, 3893.

(48) Rowland, R. S.; Taylor, R. *J. Phys. Chem.* **1996**, *100*.

(49) complete list of all intermolecular interactions for all rubrene derivatives can be found in the Supporting Information of the crystal growth and Design manusript Tables S4-S18 of paper

(50) Uttiya, S.; Miozzo, L.; Fumagalli, E. M.; Bergantin, S.; Ruffo, R.; Parravicini, M.; Papagni, A.; Moret, M.; Sassella, A. *J. Mater. Chem. C* **2014**, *2*, 4147.
(51) Atom numbering is based on the individual cif files
(52) Atom numbering is based on the individual cif files
(53) Atom numbering is based on the individual cif files
(54) Atom numbering is based on the individual cif files
(55) Atom numbering is based on the individual cif files
(56) Atom numbering is based on the individual cif files
(57) Atom numbering is based on the individual cif files
(58) Kirsch, P.; Tong, Q.; Untenecker, H. *Beil. J. Org. Chem.* **2013**, *9*, 2367.
(59) Wade, J.; Steiner, F.; Niedzialek, D.; James, D. T.; Jung, Y.; Yun, D.-J.; Bradley, D. D. C.; Nelson, J.; Kim, J.-S. *J. Mater. Chem. C* **2014**, *2*, 10110.
(60) Choudhury, A. R.; Guru Row, T. N. *Cryst. Growth Des.* **2004**, *4*, 47.
(61) Reichenbacher, K.; Suss, H. I.; Hulliger, J. *Chem. Soc. Rev.* **2005**, *34*, 22.
(62) Capozzi, M. A. M.; Capitelli, F.; Cardellicchio, C. *Cryst. Growth Des.* **2014**, *14*, 5442.
(63) Soman, R.; Sujatha, S.; Arunkumar, C. *J. Fluorine Chem.* **2014**, *163*, 16.
(64) Bergantin, S.; Moret, M. *Cryst. Growth Des.* **2012**, *12*, 6035.

Chapter 5: Synthesis of 5,6,11,12-tetraphenylnaphtho[2,3-*g*]quinoline

5.1. Introduction: N-substitution of acene organic semiconductors:

The incorporation of heteroatoms into a polycyclic aromatic ring system can have large effects on the electronic properties of a molecule. A very simple example of this are the differences between naphthalene (**5.1**) and quinoline (**5.2**) (**Figure 5.1**). By substituting a single nitrogen into the naphthalene π–system, λ_{max} decreases to 227 nm from 267 nm, the ionization energy increases, and the electron affinity goes from 0.14 eV to –0.60 eV.[1] There is also now a "forbidden" n–π* transition observed in the absorption spectra of quinoline at longer wavelengths, and the difference in Pualing electron negativity between carbon and nitrogen also results in the formation of a permanent dipole.[2]

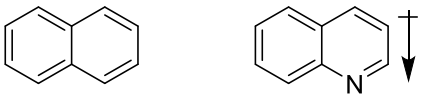

λ_{max} = 267nm
E_{HOMO}= 4.64eV
IE = 8.14eV
EA = +0.14eV

5.1

λ_{max} = 227nm
E_{HOMO} = 5.47eV
IE = 8.62eV
EA = -0.60eV
Dipole

5.2

Figure 5.1: Comparison of electronic properties of naphthalene and quinoline

The Miao group examined nitrogen substitution on TIPS-pentacene (**Figure 5.2**) and found that increasing the number of nitrogen atoms in the pentacene core, lowered both the HOMO and LUMO energies, and had a dramatic effect on the packing in the solid state. They also observed that moving the nitrogen atoms from the terminal rings (**5.3** and **5.4**), to the internal rings (**5.5** and **5.6**), had a more dramatic effect on the HOMO/LUMO energies.[3] Hole mobility of the N-substituted pentacene was examined, compounds **5.3** and **5.5** were found to function predominantly as p-type materials with **5.3** having the highest

hole mobility, 0.3-1.2 cm^2/Vs. When the mobility of the compounds **5.4** and **5.6** were examined it was found that the pentacene derivatives now performed as either ambipolar, **5.4**, or n-type, **5.6**, charge transport material. Substituting carbons 5, 7, 12 and 14, of the pentacene core with nitrogen, compound **5.6**, resulted in a complete reversal of the transport properties. All carbon pentacene is a p-type material with measured hole mobility of around 1 cm^2/Vs while compound **5.6** was found to be an n-type material with electron mobility's between 1.0 and 3.3 cm^2/Vs.

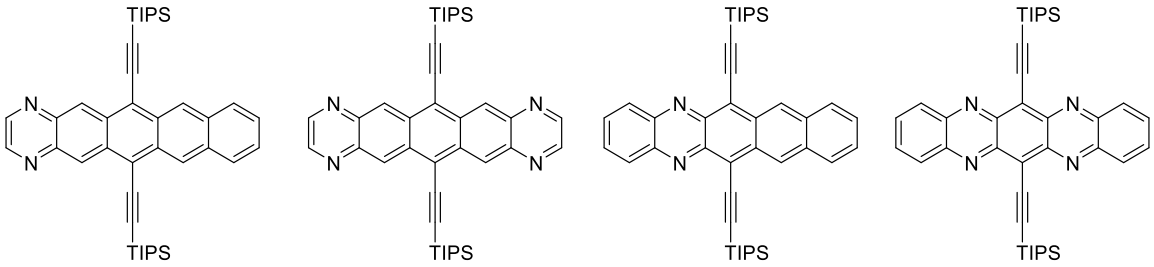

Figure 5.2: Nitrogen substituted TIPS-pentacene derivatives

From the single-crystal X-ray experiments compound **5.3** (**Figure 5.3b**) was found to pack in the 2-D brick motif with intermolecular π–π distance of from 3.36 to 3.39 Å. The substitution of two additional nitrogen atoms, compound **5.4**, resulted in a sandwich herring-bone packing motif and decreased overlap of the acene core while maintaining π-stacking, 3.38 Å (**Figure 5.3d)**. The single-crystal X-ray experiments indicated that changes in molecular packing, and the resulting charge transport, were due to increased intermolecular C-H···N interactions (**Figure 5.3c)**.

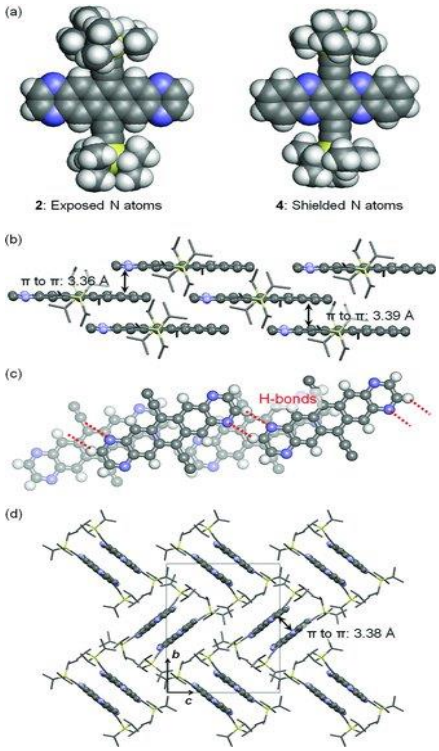

Figure 5.3: Packing of N-substituted TIPS-pentacene. Figure was taken from the paper published by the Miao group[44]

A meta-analysis performed by the Zhi-Gang group demonstrated the potential of further tuning of the HOMO/LUMO energies by substituting carbons in pentacene, with either N and/or N-H functional groups.[4] By performing the meta-analysis on several *N*-pentacene derivatives they found that *N*-substitutions lowered the LUMO energies more than the HOMO (**Figure 5.4**). Furthermore, they discovered that employing two imine and two amine groups in the molecule favored 1–D over 2–D brick packing due to increased intermolecular C–H--π interactions.

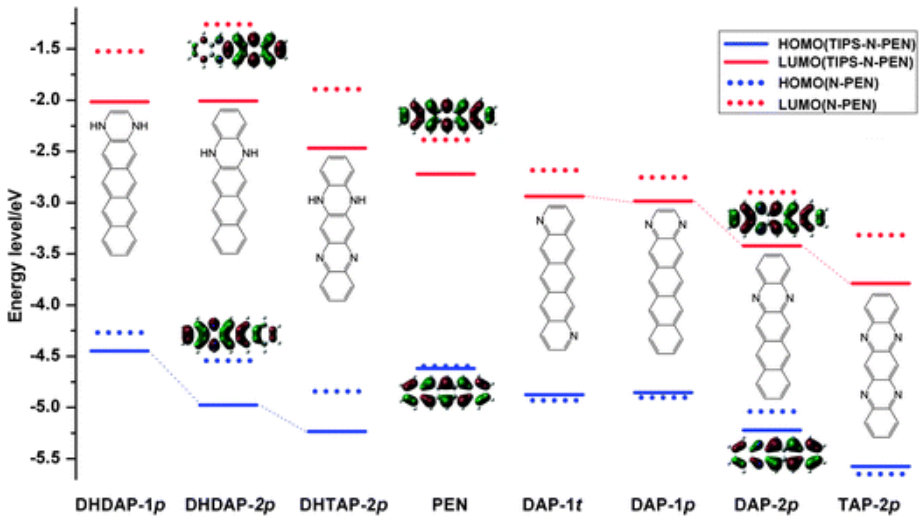

Figure 5.4: Compiled and calculated HOMO/LUMO energies of N-substituted pentacene systems. Figure taken from the paper published by the Zhi-Gang group.[45]

Given our previous work in rubrene crystal engineering, and others work with *N*–substituted acenes, we hypothesized that the addition of nitrogen atoms to the tetracene core of rubrene would allow us to tune solid-state packing and charge transport properties, in addition to potentially increase air stability and processability.

5.2 Retrosynthetic analysis:

The original retro synthetic strategy for the synthesis of *N*-substitued rubrene, azarubrene, was inspired by our group's prior synthesis of functionalized rubrenes (**Scheme 5.1**).[5 6] From compound **5.7**, 5,6,11,12-tetraphenylnaphtho[2,3-*g*]quinoline, the first disconnection of the aryl groups could be accomplished via an aryl-aryl Suzuki-Miyaura palladium cross-coupling producing compound **5.8**. From **5.8**, a reductive re-aromatization using NaI would produce 5,5,6,11,12,12-hexachloro-5,12-dihydronaphtho[2,3-*g*]quinoline, compound **5.10**. Halogenation using PCl_5 and $POCl_3$, would allow access to compound **5.11**. Breaking the bonds between both carbonyl groups

and the naphthol group via Freidel-Crafts acylation produces a pyridine di-acid chloride, compound **5.13**, and naphthalene-1,4-diol, compound **5.12**. Finally pyridine-2,3-dicarbonyl dichloride, compound **5.13**, could be converted into the di-acid via another halogenation from compound **5.15** and compound **5.12** can be accessed via reduction of 4a,8a-dihydronaphthalene-1,4-dione, compound **5.14**.

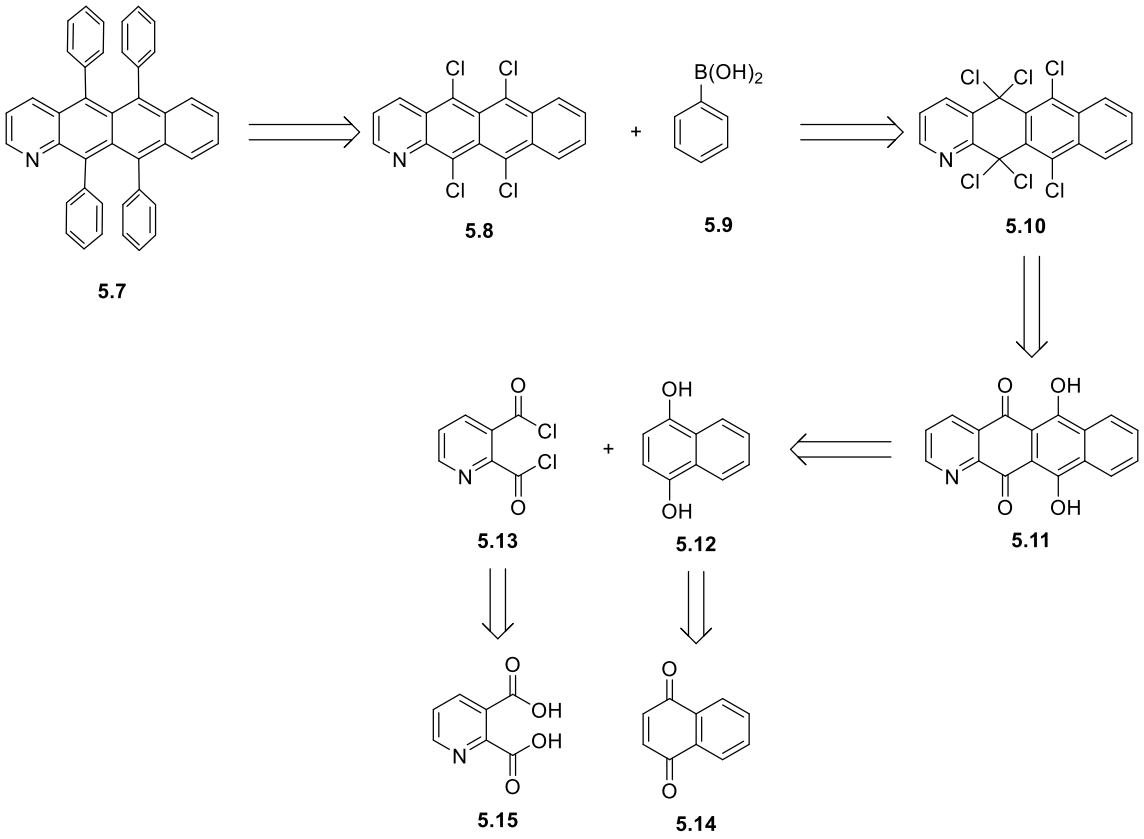

Scheme 5.1: Original retrosynthetic strategy for the synthesis of 5,6,11,12-tetraphenylnaphtho[2,3-*g*]quinoline (**5.7**)

Upon beginning the synthesis of azarubrene **5.7** the synthetic strategy need to be altered due to complication with halogenation of compound **5.11**. The modified retro synthetic strategy is shown in **Scheme 5.2**. From compound **5.7**, 5,6,11,12-tetraphenylnaphtho[2,3-g]quinoline, a reductive aromatization would allow to access to

compound **5.16**. Compound **5.17** can be obtained by nucleophilic attack of an aryllithium on compound **5.16**. Compound **5.19** can be reached from **5.17** via a Suzuki-Miyaura cross coupling. Using mild halogenation reagents we can access compound **5.11** from intermediate **5.21**. Compound **5.11** would be accessed as described in the previous retrosynthetic strategy (**Scheme 5.1**).

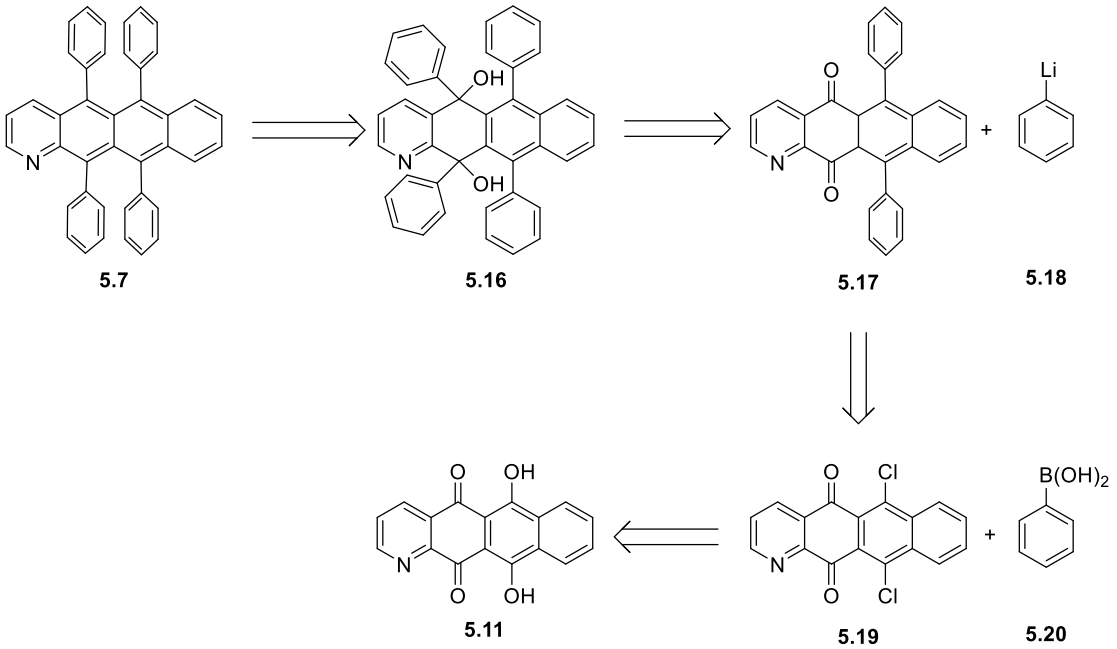

5.7 5.16 5.17 5.18

5.11 5.19 5.20

Scheme 5.2: Modified retrosynthetic strategy for the synthesis of 5,6,11,12-tetraphenylnaphtho[2,3-*g*]quinoline (**5.7**)

5.3 Synthetic progress:

The conversion of compound **5.15** to acid chloride **5.13** was accomplished following a previously reported procedure.[7] Reacting pyridine-2,3-dicarboxylic acid (**5.15**) with neat sulfonyl chloride gave a light yellow to white compound in 85 % yield. After aqueous work-up the crude reaction mixture was highly pure by H^1 NMR and required no further purification. Naphthlene-1,4-diol (**5.12**) was synthesized by reacting compound

5.14 with sodium hydrosulfite in a biphasic solution of water and diethyl ether at room temperature overnight to give a brown solid. By ^{1}H NMR the unpurified product was highly pure and required no further purification after aqueous work-up, though residual water was always present in the product. The persistent presence of water in the final product resulted in yields that were always 100 % or higher. Several different reaction conditions were tested to generate 6,11-dihydroxynaphtho[2,3-*g*]quinoline-5,12-dione (**5.11**) in sufficient yields. The Friedel-Crafts acylation was first attempted using $AlCl_3$ in nitrobenzene but no product was isolated (**Table 5.1**). The reaction appeared to be working due to the formation of a red color, however, the presence of aluminum byproducts in the crude reaction mixture made isolating compound **5.11** from the aqueous layer extremely difficult. Therefore, an alternative Lewis acid was required. In the literature several Friedel–Crafts acylations had been successfully performed using $BF_3{\cdot}OEt_2$. Exploring both neat and solution reaction conditions, it was found that reacting compound **5.11** with $BF_3{\cdot}OEt_2$, neat, at 90 ˚C overnight produce **5.11** in the best yield, 56 % (**Scheme 5.3**). To achieve good yields of isolated product all the $BF_3{\cdot}OEt_2$ needed be removed prior to aqueous work-up. This was accomplished by placing the cooled crude reaction mixture under vacuum and slowly heating until solids formed. The evaporated $BF_3{\cdot}OEt_2$ was quenched by bubbling the vapor through a saturated sodium carbonate solution. To remove any remaining $BF_3{\cdot}OEt_2$ the reaction was quenched with water. To extract compound **5.11** into the organic phase, the aqueous layer needed to be kept acidic. At pH > 5 compound **5.11** turns from a bright red to a dark blue/green color and becomes highly soluble in the aqueous layer.

Table 5.1: Friedel-Craft acylation conditions

Trial	Lewis acid	Solvent	Time	Temp	Product yield
1	$AlCl_3$	$PhNO_2$	4 hours	60 ˚C	none
2	$BF_3{\cdot}OEt_2$	$PhNO_2$	4 hours	90 ˚C	minimal
3	$BF_3{\cdot}OEt_2$	$EtCl_2$	4 hours	85 ˚C	none
4	$BF_3{\cdot}OEt_2$	none	overnight	90 ˚C	56%

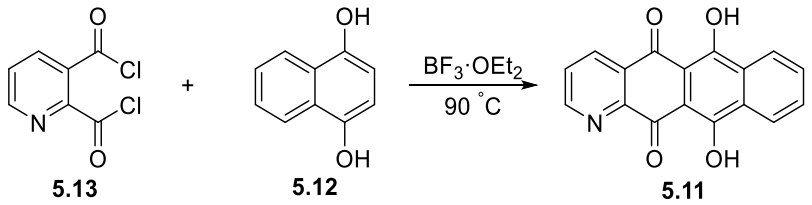

Scheme 5.3: Synthesis of 6,11-dihydroxynaphtho[2,3-*g*]quinoline-5,12-dione, compound **5.11**

Recrystallization of compound **5.1** via slow evaporation of methylene chloride produced single crystals of high enough quality to perform single-crystal X-ray experiments. From the solved crystal structure, compound **5.11** was found to pack in a monoclinic $P2_1/n$ crystal system with intermolecular π-π distance of 3.39 Å (**Figure 5.5**). It should be noted that solved crystal system was highly disordered. To adequately refine the X-ray both the nitrogen and carbon groups had to be placed at positions 1, 4, 7, and 10 with 50 % occupancy. Also, it was found that the hydrogen of the alcohol was at an intermediate distance between the two oxygen functional groups. Measuring the length of the C-O bond in compound **5.11** we found that both carbonyl groups had a mixed single and double bond character. The measured C-O bond length was 1.29 Å, in between double and single bonded lengths.

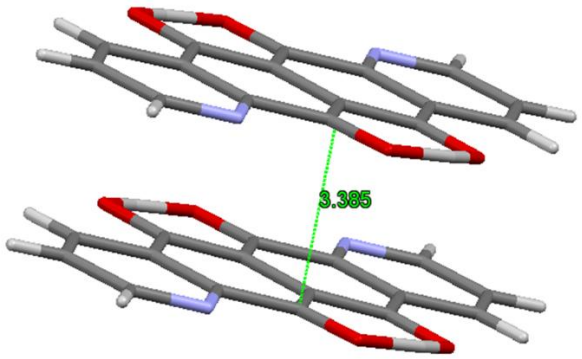

Figure 5.5: Shows the π-π stacking distance as well as the modeled disorder.

The partial double bond character for all C-O bonds in compound **5.11**, seen in the X-ray structure, was also observed by ^{1}H-NMR and IR. In the IR spectra we saw no signal corresponding to the O-H stretch of an alcohol between 3500 and 3300 cm^{-1}, and that the signal associated with the carbonyl stretch was shifted to lower wavenumber, 1625 cm^{-1}. By ^{1}H-NMR we observed a very strong signal at 14.9 ppm indicating the presence of a highly deshielded, acidic, proton. This confirmed the delocalized nature of the carbonyl double bond and alcohol protons of compound **5.11**.

The original conditions for the chlorination of compound **5.11** were taken from our previous reported synthesis of asymmetrically functionalized rubrene derivatives.[6] The original conversion of compound **5.11** to compound **5.10** was attempted using PCl_5 and $POCl_3$. To achieved reasonable consumption of starting material the reaction needed to be heated to 110 ˚C for 2 days. After aqueous workup and purification by silica gel column chromatography the isolated compound was determined to be 6,11-dichloronaphtho[2,3-*g*]quinoline-5,12-dione (**5.19**) (**Scheme 5.4**) rather than compound **5.10**. While compound **5.19** was not the intended product the ability to access compound **5.19** directly allowed for a modification of the synthesis. Also, the use of PCl_5 and $POCl_3$ to produce compound **5.19**

required high heat, long reaction time, and resulted in only impure isolated product. Taking advantage of the highly acidic nature of alcohol proton in compound **5.11**, reaction conditions were modified to use neat thionyl chloride. Under the new reaction conditions, compound **5.11** was refluxed in neat thionyl chloride for 16 hour to produce compound **5.19** in 58 % yield (**Scheme 5.5**). The reaction produced two regioisomers, compounds **5.19** and **5.21**, though this should be expected due to the partial double bond character of all the C-O bonds. Since the current planned synthesis involved only symmetrically substitution around the tetracene core intermediates **5.19** and **5.21** could be taken on as a mixture. Separation of the regioisomers was accomplished by recrystallization from methylene chloride with ethanol in the refrigerator overnight. From the recrystallization a major and a minor product was obtained. The regioisomers were tentatively assigned by ^{1}H and ^{13}C NMR. The ^{1}H and ^{13}C-NMR for both compounds **5.19** and **5.21** can be found in the **Figures 5.6** through **5.9**. Comparing the ^{1}H-NMR chemical shift of the C1 protons, we observed that in the major product the C1 proton had a chemical shift of 9.1 ppm while in the minor product the C1 proton chemical shift was 9.3 ppm (**Figures 5.6** and **5.7**). This suggested that the major product contained a pyridine group, as in **5.19**, while the minor product contained a quinoline, as in **5.21**. Comparing the ^{13}C-NMR chemical shift of the carbonyl groups allowed for a more definitive assignment of each product. For the major product we observed two distinct carbonyl signals at 181.4 and 181.9 ppm, while in the minor product the two carbonyl signals were almost the same, 182.2 and 182.3 ppm (**Figures 5.8** and **5.89**). This indicated that two carbonyl groups in the major product were in two different environments, as in **5.19**, compared to the minor product, **5.21**. This allowed us to assign the major product to compound **5.19** and the minor product to

compound **5.21**. From the crude reaction mixture pure compound **5.19** was obtained in 73 % yield. Pure compound **5.21** was never obtained, as can be seen by the ^{1}H-NMR (**Figure 5.7**). Attempts to grow single crystals of single crystal X-ray experiments are still on going.

To date only a small number of reaction condition have been test to perform the arylation of compound **5.19**, however, none have resulted in the production of pure product. The standard reaction conditions for both Suzuki-Miyaura and Kumada aryl-aryl cross coupling resulted in formation of the desired products, by mass spectroscopy, however the reactions were always incomplete and the desired product was not separable.

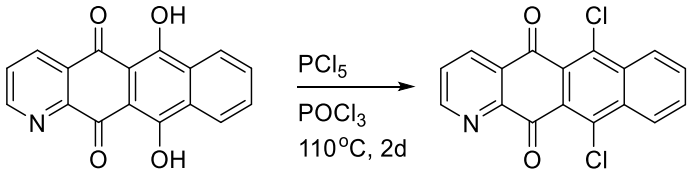

5.11 **5.19**

Scheme 5.4: Synthesis of 6,11-dichloronaphtho[2,3-*g*]quinoline-5,12-dione (**5.19**) using PCl_5 and $POCl_3$

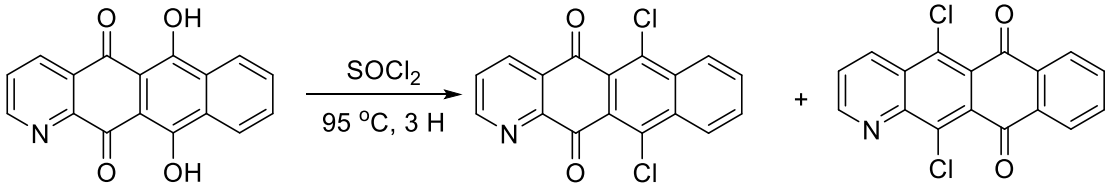

5.11 **5.19** **5.21**

Scheme 5.5: Synthesis of 6,11-dichloronaphtho[2,3-*g*]quinoline-5,12-dione (**5.19**) using $SOCl_2$

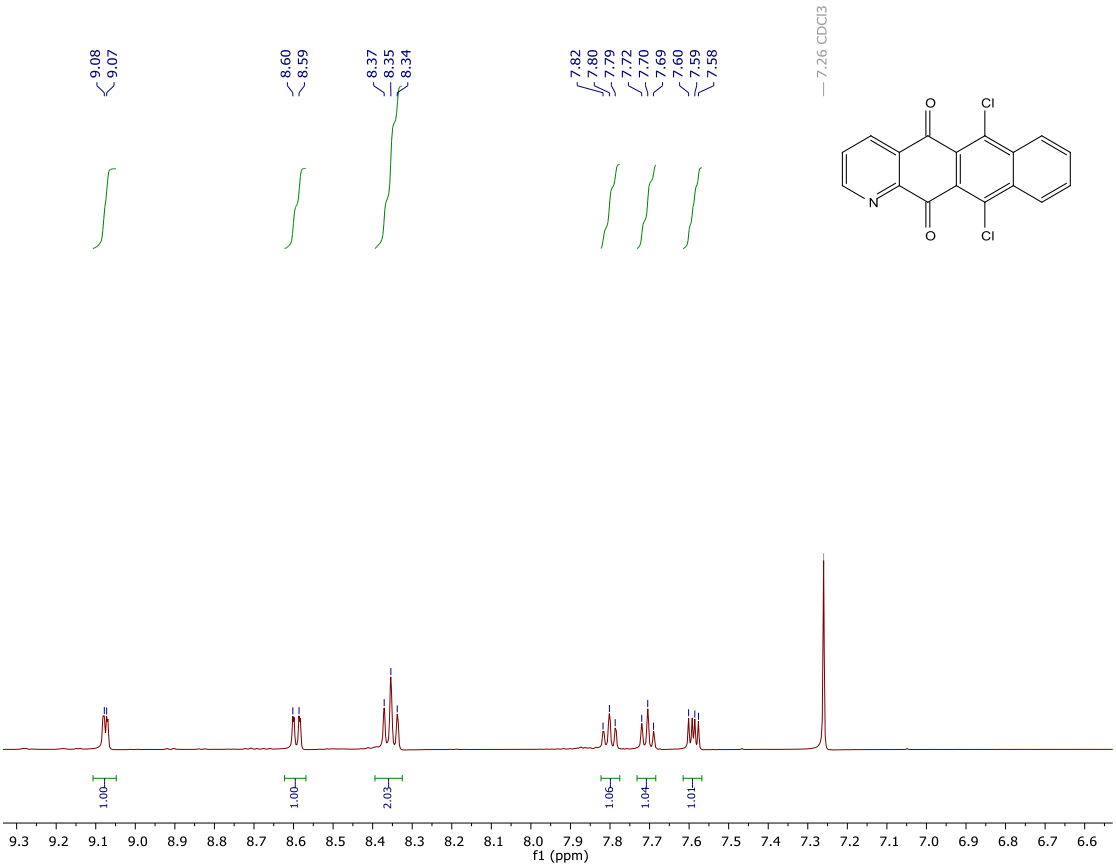

Figure 5.6 ^{1}H-NMR spectra of 6,11-dichloronaphtho[2,3-*g*]quinoline-5,12-dione (**5.19**)

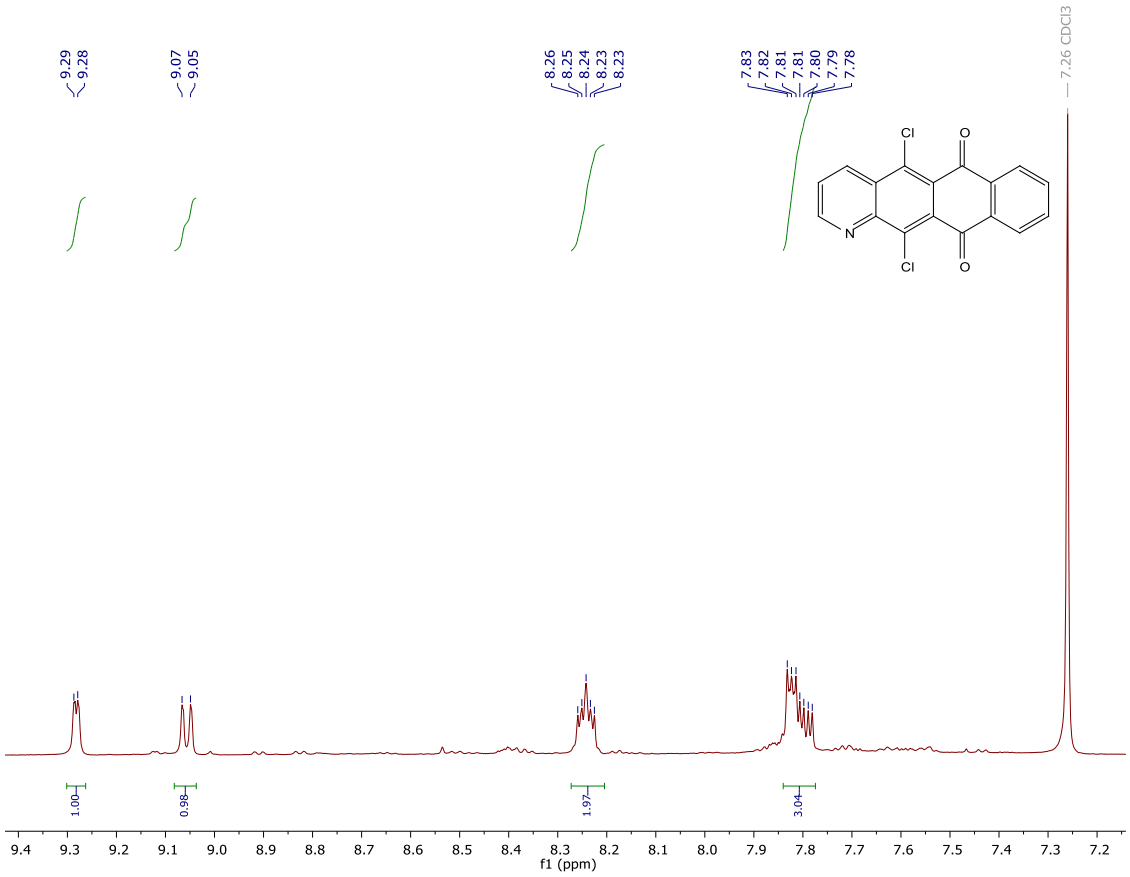

Figure 5.7 ^{1}H-NMR spectra of 5,12-dichloronaphtho[2,3-*g*]quinoline-6,11-dione (**5.21**)

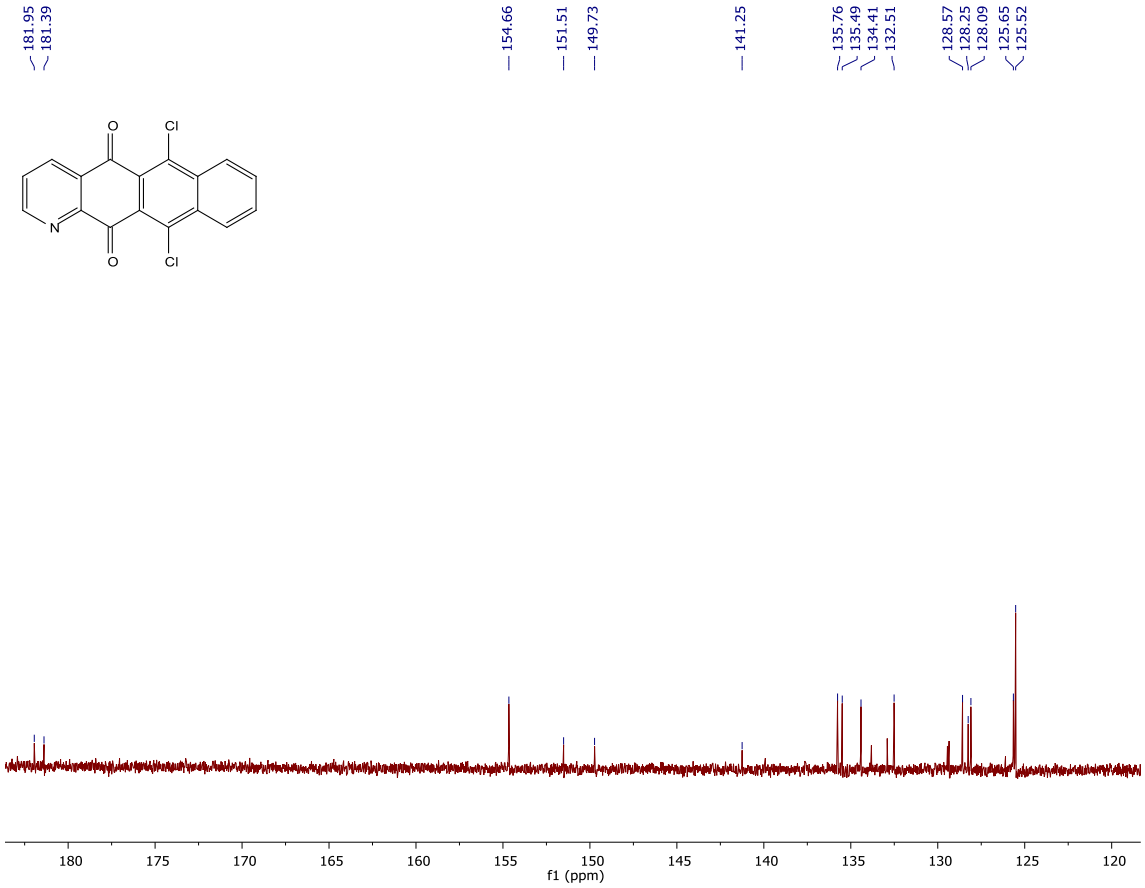

Figure 5.8 ^{13}C -NMR spectra of 6,11-dichloronaphtho[2,3-*g*]quinoline-5,12-dione (**5.19**)

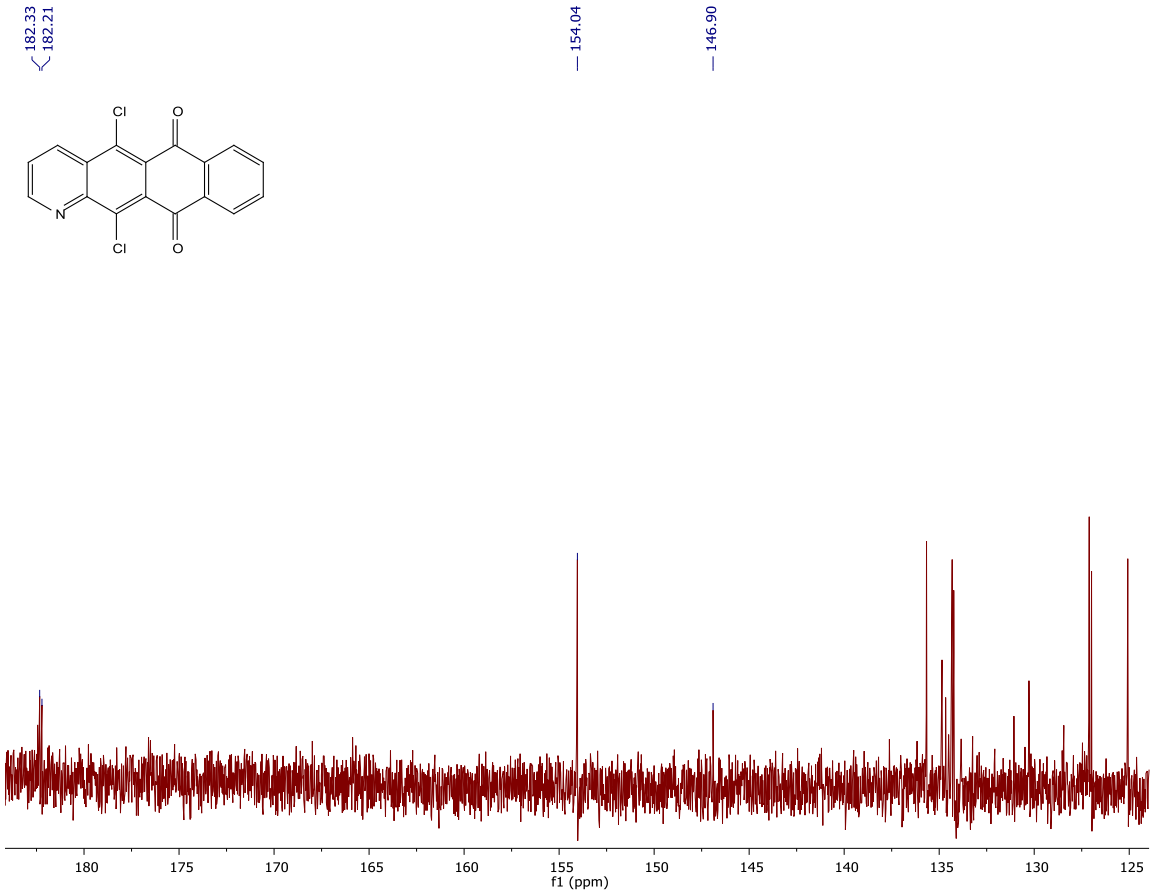

Figure 5.9^{13}C -NMR spectra of 5,12-dichloronaphtho[2,3-*g*]quinoline-6,11-dione (**5.21**)

5.4 Conclusion and Future Work:

To date good progress has been made in the synthesis of 5,6,11,12-tetraphenylnaphtho[2,3-*g*]quinoline (**5.7**). From compound **5.19** conditions need to be developed to efficiently perform the arylation. Once sufficient quantities have been prepared then physical and electronic properties of 5,6,11,12-tetraphenylnaphtho[2,3-*g*]quinoline (**5.7**) can be determined. If the physical and electronic properties of **5.7** prove interesting then examining the different derivatives of azarubrene and solid-state packing,

as performed on rubrene derivatives in chapter 4, could produce molecules with improved charge transport properties.

5.5 Experimental:

Pyridine-2,3-dicarbonyl dichloride (5.13):

Pyridine-2,3-dicarbonyl dichloride (**5.13)** was prepared by refluxing pyridine-2,3-dicarboxylic acid (**5.15)** (2.003 g, 11.97 mmol) in thionyl chloride (12.70 mL, 55.08 mmol) for 2 hours. The reaction was then cooled to room temperature, placed under vacuum, then heated to 85 ˚C to remove excess sulfonyl chloride. The removed thionyl chloride was neutralized by bubbling the vapors through a saturated sodium bicarbonate solution. Once the reaction was dry it was placed under vacuum overnight to give a light yellow solid. (1.731 g, 71 % yield): ^{1}H NMR (500 MHz, DMSO-d_6) δ 9.14 (dd, J = 4.8, 1.4 Hz, 1 H), 8.53 (dd, J = 7.8, 1.4 Hz, 1 H), 7.94 (dd, J = 7.8, 4.9 Hz, 1 H); ^{1}H NMR (500 MHz $CDCl_3$) δ 9.18 (dd, J = 4.8, 1.4 Hz, 1 H), 8.38 (dd, J = 7.8, 1.5 Hz, 1 H), 7.83 (dd, J = 7.8, 4.8 Hz, 1 H); ^{13}C NMR (126 MHz, DMSO-d_6) δ 162.2, 162.0, 157.41, 151.3, 134.1, 129.6, 127.8; IR (KBr) 3629, 3116,1861, 1777, 1609, 1583 cm^{-1}; mp 136-137 ˚C

Naphthalene-1,4-diol (**5.12**):

Naphthalene-1,4-diol (**5.12**) was synthesized by stirring 4,8-dihydronaphthalene-1,4-dione (**5.14**) (2.002 g, 12.6 mmol) with sodium hydrosulfite (10.128 g, 58.2 mmol) in a nitrogen degassed biphasic solution of water and diethyl ether (76 mL/ 64 mL) at room temperature for overnight. The reaction was worked up by pouring the solution in to a separatory funnel, extracting of the organic layer, washing the aqueous layer 2 × 30 ml with diethyl ether, combing all the extracted diethyl ether layers, drying over sodium sulfate, and concentrated

under reduced pressure. The brown solid, **5.12**, was placed under high vacuum overnight. (2.124 g, ≥100 % yield by mass, carried through crude): ^{1}H NMR (500 MHz, DMSO-d_6) δ 9.28 (s, 2 H), 8.04 (dd, *J* = 6.4, 3.3 Hz, 2 H), 7.42 (dd, *J* = 6.4, 3.3 Hz, 2 H), 6.66 (s, 2 H); ^{1}H NMR (500 MHz, $CDCl_3$) δ 8.16 (dd, *J* = 6.5, 3.3 Hz, 2 H), 7.55 (dd, *J* = 6.5, 3.3 Hz, 2 H), 6.70 (s, 2 H), 4.90 (s, 2 H); ^{13}C NMR (126 MHz, DMSO-d_6) δ 145.8, 125.8, 125.1, 122.3, 108.3; IR (KBr Pellet) 3284, 3061, 1642, 1598 cm^{-1}; LRMS (MeOH) *m*/*z* 159.0 $(M–H)^{–}$; mp, broad melt 182-184 ˚C, compound decomposed becoming a black tar.

6,11-dihydroxynaphtho[2,3-*g*]quinoline-5,12-dione (5.11):

6,11-dihydroxynaphtho[2,3-*g*]quinoline-5,12-dione (**5.11**) was prepared by reacting intermediates (**5.13**) (0.500 g, 2.46 mmol) and (**5.12**) (0.434 g, 2.71 mmol) in a flame dried 25 mL three-neck round bottom flask that was purged with N_2 and vacuum 3 times. The reaction was heated to 90 ˚C at which point $BF_3{\cdot}OEt_2$ (3.041 mL, 24.64 mmol) was added. The reaction was stirred at 90 ˚C for 16 h. After 16 h the reaction was cooled to room temperature placed under vacuum the slowly heated to remove the $BF_3{\cdot}OEt_2$. The BF_3 gas was quenched by bubbling the vapor through a saturated sodium bicarbonate solution. Once all the $BF_3{\cdot}OEt_2$ had been removed the reaction was dissolved in a 75:25 mixture of DCM and TEA and evaporated 3 × 60 ml. Next the reaction was dissolved and evaporated in EtAc 2 × 30 ml. The third time ethyl acetate was added a blue solid was filtered off. The product was obtained by dissolving the blue solid in a mixture of DCM and TFA, evaporating, and then dissolving in a mixture of ethyl acetate and trifluoroacetic acid and washed with pH 5 water in a separatory funnel. The organic layer was then evaporated, the desired product **5.11**, a red solid, was precipitated (0.405 g, 56 % yield). ^{1}H NMR (500 MHz, $CDCl_3$) δ 14.88 (s, 2 H), , 9.20 (dd, *J* = 4.1, 1.5 Hz, 1 H), 8.84 (dd, *J* = 8.2, 1.4 Hz,

1 H), 8.52 – 8.47 (m, 2 H), 7.92 – 7.88 (m, 1 H), 7.75 (dd, *J* = 8.2, 4.3 Hz, 1 H); ^{13}C NMR (126 MHz, $CDCl_3$) δ 181.81, 181.2, 162.9, 162.7, 154.0, 145.8, 134.1, 133.7, 133.4, 133.4, 127.4, 127.0, 126.9, 125.5, 109, 107.1, 100; IR (KBr pellet) 1625, 1582, 1499 cm^{-1}; HRMS (ESI) m/z: $[M]^+$ Calcd for $C_{17}H_9NO_4$, 291.0532 Found 292.0595; mp: no melt observed, sublimation above 330 ˚C.

6,11-dichloronaphtho[2,3-*g*]quinoline-5,12-dione (5.19):

Compound **5.11** (0.259 g, 0.854 mmol) and thionyl chloride (1.55 mL, 2.538 g, 21.35 mmol) were added to a 50 mL round bottom flask purged 3 times with nitrogen then heated to 95 ˚C. The reaction was run under inert atmosphere at 95 ˚C overnight. The reaction was monitored by thin layer chromatography. Once all the starting material had been consumed the reaction was allowed to cool to room temperature. The reaction was worked-up by adding the crude reaction mixture on to solid Na_2CO_3. The remaining solid Na_2CO_3 was dissolved in water and the organic solid was dissolved in $CHCl_3$, 100 mL. The aqueous layer was washed two times with 25 mL of $CHCl_3$ to extract any remaining product. The combined $CHCl_3$ organic phase was then washed with water (3 × 50 mL), once with 1N TFA in water, once with a brine solution, dried over $MgSO_4$, concentrated, and placed under high vacuum overnight. Pure **5.19** was obtained by dissolving the crude product in methylene chloride then precipitating with ethanol in the refrigerator overnight. Pure **5.19** was collected by vacuum filtration as a orange/red solid (0.792 g, 0.241 mmol, 30 % yield); ^{1}H NMR (500 MHz, $CDCl_3$) δ 9.09 (dd, *J* = 3.1, 1.4 Hz, 1H), 8.60 (dd, *J* = 6.3, 1 1.4 Hz, 1H), 8.35 (dd, *J* = 12.1, 8.4 Hz, 2H) 7.85 – 7.76 (m, 1H), 7.76 – 7.67 (m, 1H), 7.61 (dd, *J* = 7.8, 4.6 Hz, 1H). ; HRMS (GC-QTOF) m/z: $[M]^+$ Calcd for $C_{17}H_7Cl_2NO_2$ 326.9854; found 327.0020

5.6 References:

(1) National Institute of Standards and Technology

(2) Anslyn, V. E.; Dougherty, A. D. *Modern Physical Organic Chemistry*; University Science Books: Sausalito, 2006.

(3) Liang, Z.; Tang, Q.; Mao, R.; Liu, D.; Xu, J.; Miao, Q. *Adv. Mater.* **2011**, *23*, 5514.

(4) Tang, X.-D.; Liao, Y.; Geng, H.; Shuai, Z.-G. *J. Mater. Chem.* **2012**, *22*, 18181.

(5) Ogden, W. A.; Ghosh, S.; Bruzek, M. J.; McGarry, K. A.; Balhorn, L.; Young, V.; Purvis, L. J.; Wegwerth, S. E.; Zhang, Z.; Serratore, N. A.; Cramer, C. J.; Gagliardi, L.; Douglas, C. J. *Cryst. Growth Des.* **2017**, *17*, 643.

(6) McGarry, K. A.; Xie, W.; Sutton, C.; Risko, C.; Wu, Y.; Young, V. G.; Brédas, J.-L.; Frisbie, C. D.; Douglas, C. J. *Chem. Mater.* **2013**, *25*, 2254.

(7) Barczyński, P.; Szafran, M.; Ratajczak-Sitarz, M.; Nowaczyk, Ł.; Dega-Szafran, Z.; Katrusiak, A. *J. Mol. Struct.* **2012**, *1018*, 21.

Chapter 6: Examination of Asymmetrically Substituted Indenotetracenes as the Electron Accepting Molecules in Organic Photovoltaics:

6.1 Introduction:

6.1.1 General background:

By 2040 global energy consumption is expected to increase by 48 %.[1] During this time renewable energy production is expected to increase by 2.6 % per year. Currently, the United States produces approximately just 1 % of its annual energy from via solar power. This number is expected to continually increase as energy production from photovoltaics becomes more efficient and cheaper.

The ability to produce power by converting solar energy into electricity was first reported in 1956. Chaplin and co-workers were able to achieve a 6% power conversion efficiency from a silicon *p*-*n* junction solar cells.[2] Since this original report, the efficiency of silicon-based solar cells has increased substantially reaching 20% efficiency. The development of new materials, for example CIGS and CdTe, and new device architectures, multi-junction solar cells, has further increased photovoltaics PCE to as high as 44 % (**Figure 6.1)**.[3] One major issues preventing the broader application of solar energy production is cost. Currently energy produced from solar cells cost $ 3.22 per AC watt.[4] This is predominately due to solar cell production costs and life times. Organic photovoltaics are seen as a viable way to decrease solar cell cost, via high through-put roll-to-roll processing, which would dramatically decrease photovoltaic production cost.[5] However, there is still a considerable amount of research needed in order to achieve the efficiencies required for OPV to become commercially viable.

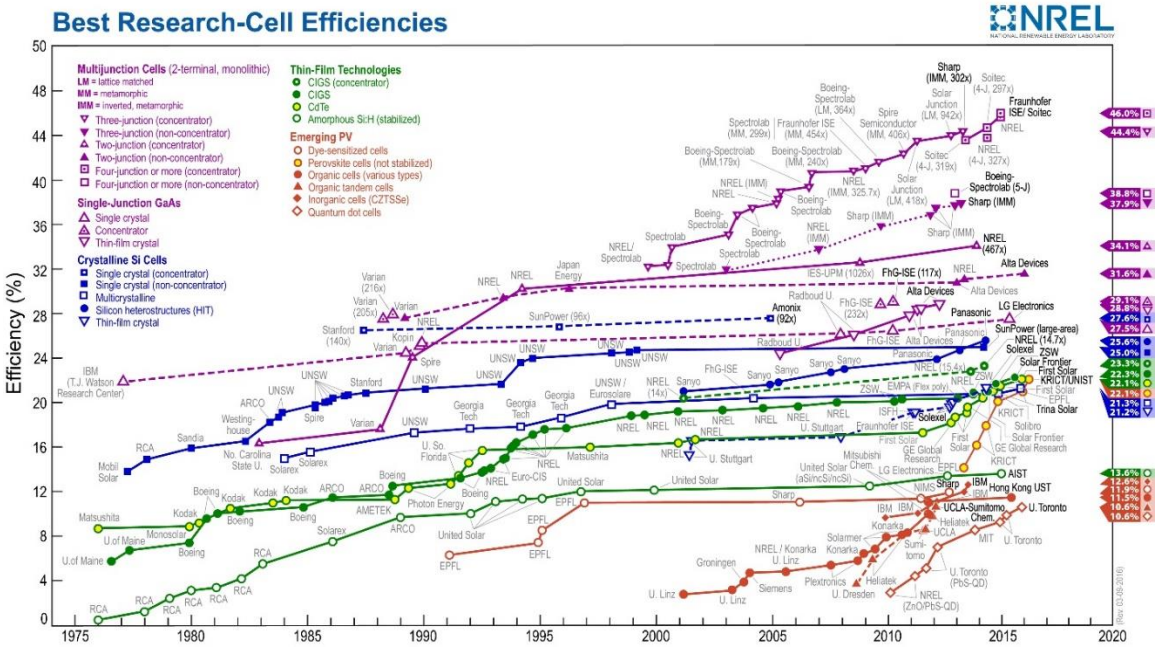

Figure 6.1: Taken from National Renewable Energy Lab showing the best performing solar cells and solar cell type.

6.1.2 Energy production and charge transport in organic photovoltaics:

The ability to create molecules with specific electronic and physical properties is a major advantage of organic semiconductors. The ability to tune the properties of OSC allows them to be used in wide variety of device architectures, prepared from vastly different processing methods. In photovoltaics, energy is generated when the molecules in the active lay absorb a photon resulting in an excited charge carrying species, an exciton.[6] For inorganic photovoltaics the excitons generated are weakly bound electron–hole pairs that have work functions less than kT, kT = 0.026 eV, called Wannier exciton.[7] As a result the excitons are easily separated into free electron and hole charge carriers which can then generate power. In contrast, organic materials generate tightly bound electron-hole pair

with work functions greater than kT, and usually greater than 0.1 eV known as Frenkel excitons.[8] These tightly bound electron–hole pairs result in a much smaller Bohr radii requiring additional energy to separate the excitons into free electron and hole charge carries, due the weak van der Waals interactions between of OSCs. Also, there is a much larger coulombic interaction between the OSC and the generated excitons due to the small dielectric constant of organic molecules decreasing exciton lifetime and diffusion length, 5–10 nm.[9] [10] Because of the very short lifetime and larger work function of excitons in OSC, organic photovoltaics need to be designed with an energy gradient to separate the exciton into free charge carriers as quickly as possible. To accomplish this organic photovoltaics use a donor/acceptor system which allows for rapid and efficient exciton dissociation.

In OPVs, exciton dissociation only occurs at the donor-acceptor interface. This means that any exciton not generated at the interface must travel to an interface in order to be dissociated into free charge carriers. For this to occur, both the donor and acceptor molecules need to be able to rapidly transport charge. If this does not occur the excited electron–hole pair simply recombine resulting in energy loss and decreased OPV efficiency. In small molecule OSC, donor hole mobilities as high as 15-40 cm^2/Vs have been measured in organic single crystal of rubrenes, while electron mobilities up to 400 cm^2/Vs have been measured in fullerenes.[11] [12] **Figure 6.2** shows two fullerene molecules commonly used as electron acceptors in organic photovoltaics, C_{60} and Phenyl-C61-butyric acid methyl ester, PCBM.

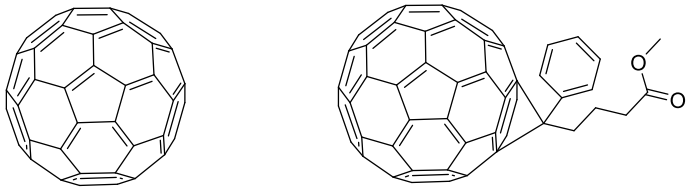

C_{60} **6.1** PCBM **6.2**

Figure 6.2: Two example of fullerenes commonly used as electron acceptors in organic photovoltaics, C_{60} and PCBM.

Once at the donor/acceptor interface, for exciton dissociation to occur, the HOMO/LUMO energies of the donor and acceptor must be aligned to promote exciton dissociation (**Figure 6.3**). Donor materials are designed to promote electron transfer into the low-lying LUMO of the acceptor material while the acceptor molecules are designed to promote hole transfer into the HOMO of the donor material. A difference of approximately 0.3 eV between the LUMO of the donor and the LUMO the acceptor has been postulated as ideal for exciton dissociation to occur.[13] In designing new electron accepting materials for OPVs HOMO/LUMO energies are of critical importance. This is because, the LUMO of the acceptor molecule needs to be low enough to favor electron accepting, less than -3.5 eV, while not so low as to decrease open-circuit voltage in the OPV, as explained in chapter 3. As shown previously, all the ASI derivatives have LUMO levels around -4 eV and HOMO levels around -5.5 eV, which are comparable to C_{60}.[14] In the following study three different ASI molecules are used as the electron accepting material, **2.4b-d**, while two small molecule donor, 5,5′′′′-Dihexyl-2,2′:5′,2′′:5′′,2′′′:5′′′,2′′′′:5′′′′,2′′′′′-sexithiophene (DH6T), Bis[4-(N,N-diisobutylamino)-2,6-dihydroxyphenyl] squaraine (Sq), and two polymers donors, PTB7-Th and PiI-2T-

PS10. All the donor materials used had similar HOMO energies, between -5.1 and -5.4 eV and LUMO energies, -2.9 to -3.4 eV. The LUMO energies determined for the ASI derivatives should allow them to perform as electron accepting materials in OPVs while the donor energies should allow for charge transfer between the electron donating and electron accepting materials.

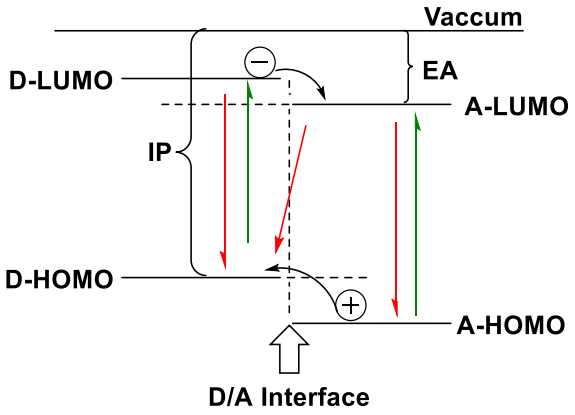

Figure 6.3: Diagrams photo induced charge separation and recombination at the donor/acceptor interface. Half headed arrows indicate electron movement in the donor or acceptor material, and full headed arrow indicate electron movement between the donor and acceptor material. EA is the electron affinity of the acceptor and IP in the ionization potential of the donor molecule

6.1.3 Organic photovoltaics device architectures:

While the development of new materials with improved physical and electronic properties has resulted in improved OPV power conversion efficiencies, the continual improvement of organic photovoltaics device architecture has also greatly improved OPV power conversion efficiencies. The first OPVs developed were the single layer device containing only one light absorbing material between the cathode and anode which resulted

in poor device performance. The poor OPV performance of the single layer devices occurred because exciton dissociation only occurred at the anode and cathode resulting in a large amount of recombination, due to the short exciton diffusion length. The more efficient bilayer device architecture utilized two semiconducting materials to create a layered device increasing donor/acceptor interface (**Figure 6.4**).[15] The bilayer device improved efficiency by increasing the rate of exciton dissociation by creating a large interface between the donor and acceptor materials closer to the site of exciton generation. A further mixing of the donor and acceptor molecules resulted in the bulk heterojunctions OPV architectures. These devices contained large contact surface area between the donor and acceptor material which allowed for enhanced exciton dissociation further improving device efficiency. Other more exotic device active layer morphologies have been studied, such as using nanorods, to further increase donor/acceptor contact surface area to improve exciton dissociations and improve OPV performance.[16]

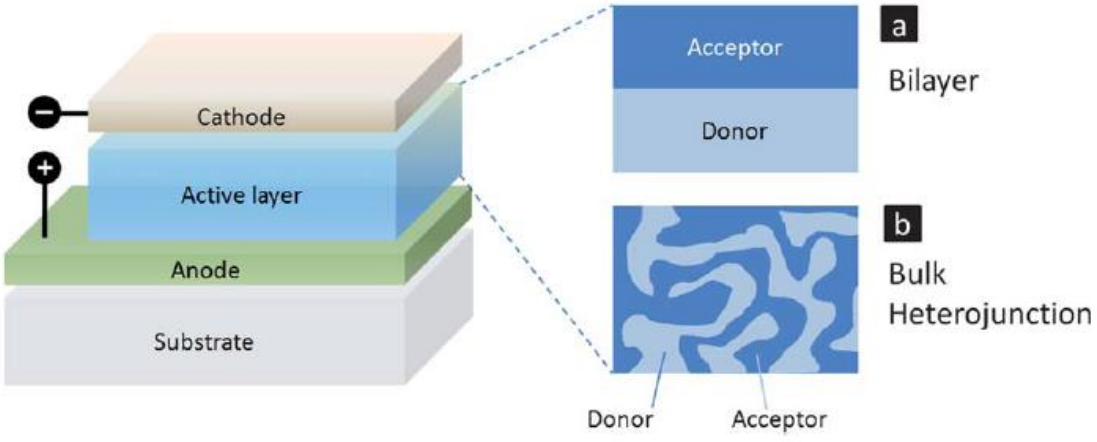

Figure 6.4: Schematic diagram of OPV architectures a) bilayer acceptor/donor b) blended acceptor/donor bulk heterojunction.[17]

Solar cells can also be fabricated in either a standard or inverted architecture (**Figure 6.5**). In the standard architecture indiumtinoxide (ITO) functions as the anode while low-work-function metals such as aluminum functions as the cathode. In the inverted architecture, the ITO functions as the cathode and a high-work-function metal (HWF), such as silver, functions as the anode, reversing the direction of current flow in the solar cell. One advantage to the inverted architecture is the increased stability of the HWF electrode, however, this can also result in decreased efficiency due to energy mismatch with the HWF metal and the active layer.[18] All the OPV devices prepared for the following experiments were fabricated in the inverted architecture, ITO/ZnO/**BHJ**/MoO_3/Ag.

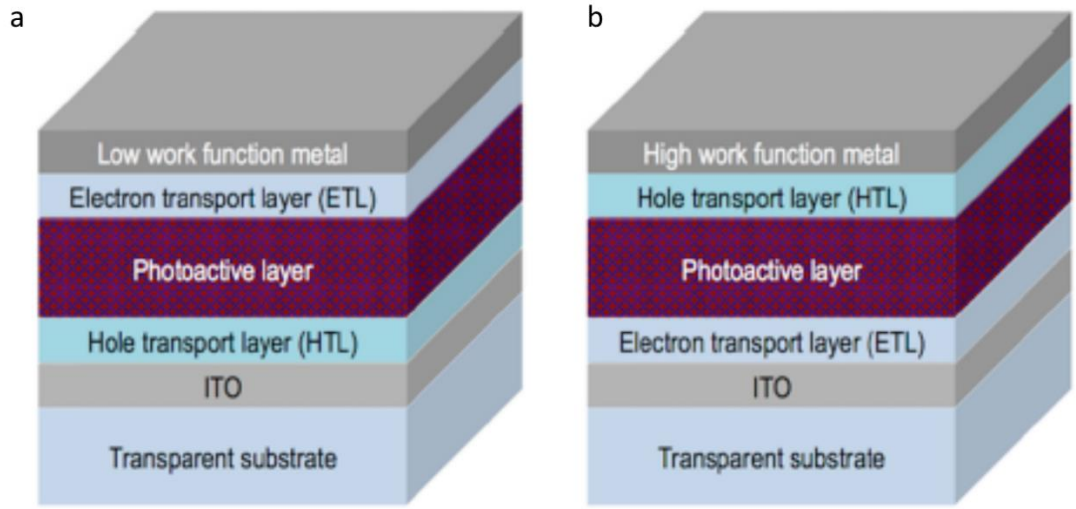

Figure 6.5: Schematic diagrams of the layered structure of OPVs; a) standard device architecture b) inverted device architecture.[19]

6.1.4. Evaluating organic photovoltaic performance:

All solar cells were evaluated by measuring the current (I)-voltage (V) characteristics of each OPV device. The solar cells were evaluated by examining the V_{oc}, J_{sc}, and FF. A detailed explanation of solar cell data analysis was presented in chapter 3

With previous characterization data indicating that ASIs should function as a new small molecule electron acceptor, we prepared thin films and fabricated OPVs to evaluate ASIs' performance as an electron acceptor in organic solar cell. OPVs and thin films were fabricated with three different ASI derivatives, **2.4b-d**, and either a small molecule or a polymer electron donor. The fluorescence and OPV performance data indicated that ASIs do function as electron acceptors for commonly used donor molecules in OPVs, however, either the OPV design and/or ASI electron and physical properties were not ideal for high performing OPVs to be fabricated..

6.2. Results and discussion:

To test ASIs as a potential new n-type semiconductor in OPVs devices were fabricated in an inverted architecture. In which Indium Tin Oxide (ITO) served as the cathode, ZnO was used as the electron acceptor layer, mixed ASI:donor thin film BHJ was the active layer, MoO was the hole accepting layer, and, silver served as the anode.[6] The small molecule donors used for this experiment were; 5,5′′′′-Dihexyl-2,2′:5′,2′′:5′′,2′′′:5′′′,2′′′′:5′′′′,2′′′′′-sexithiophene (DH6T), Bis[4-(N,N-diisobutylamino)-2,6-dihydroxyphenyl] squaraine (Sq), and polymers donors used were PTB7-Th and PiI-2T-PS10 (**Figure 6.6**).[20] [21] All the small molecule Bulk heterojunction thin films were prepared via spin-coating from either (2:3) $CHCl_3$:ODCB or (2:3) MeTHF:Toluene. The BHJ active layers for the ASI:Polymer OPVs were prepared from chlorobenzene.

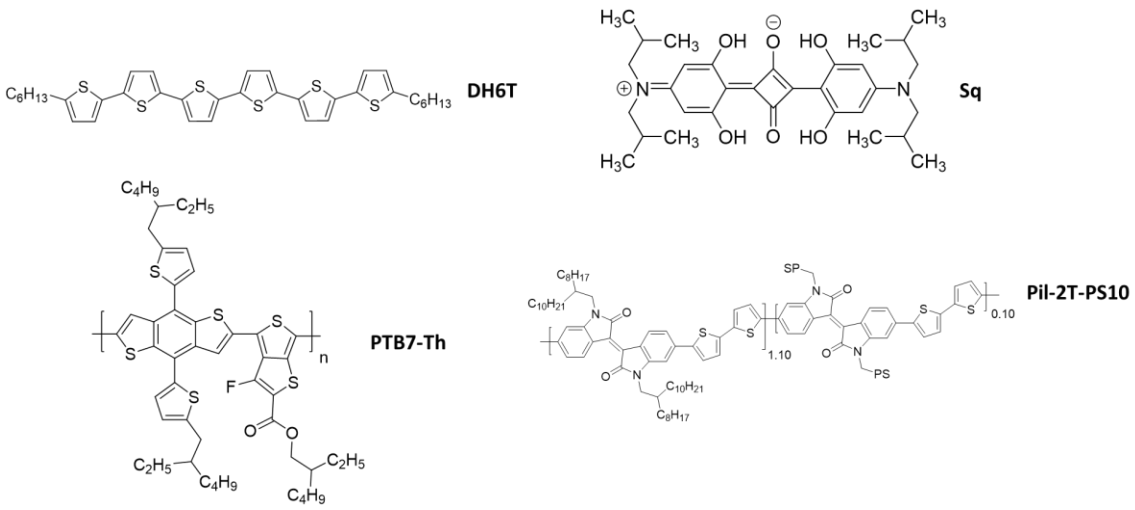

Figure 6.6: Structures of small molecule donors DH6T and Sq and polymer donor PTB7-Th and Pil-2T-PS10.

6.2.1 All small molecule organic photovoltaics:

All the small molecule donors chosen had previously been used as electron donating materials in several other OPVs, allowing for the direct comparison of OPV performance using ASIs as the electron acceptors. DH6T was originally chosen because of its good alignment with the maximum absorbance energies of the ASIs derivatives.[14] For ASI molecules, λ_{max} occurred around 550 nm corresponding to the energy of the second electron addition by CV, around -3.3 eV.[14] The LUMO of DH6T is -2.9 eV, which results in a difference of 0.4 eV between the LUMO of the ASIs and the LUMO of DH6T which should favor electron transfer from DH6T to the ASI.[22] The Sq donor was chosen because it had previously been shown to be a highly efficient p-type small molecule in several OPVs.[23]

6.2.1.1 Electronic properties of neat ASI thin films:

As previously reported the molar attenuation coefficients for the ASI molecules in solution was found to be between 10^4 and 10^5 M^{-1} cm^{-1} in solution.[14] For compounds **2.4a-d**, the thin film absorption coefficient was calculated using **equation 6.1**,

$$\alpha = \frac{\ln(A)}{t} \quad (\mathbf{6.1})$$

where α is the absorption coefficient, A is the thin film absorbance, and t in the film thickness. For thin films of compound **2.4a-d**, α was found to be between 5 x 10^4 and 8 x 10^4 cm^{-1}. When thin film absorbance spectra were compared to solution spectra, the thin film absorbance spectra were found to be slightly red shifted. This bathochromatic shift in thin film absorption spectra is indicative of tighter π-π stacking in the solid state.[24] **Figure 6.7** shows the comparison of the solution and thin film absorbance spectra of compounds **2.4a-d**. The absorbance spectra of compound **2.4c**, also showed that increasing annealing temperatures resulted in an increased absorbance at 597 nm (**Figure 6.8**). This increase in absorbance at 597 nm indicated that, as annealing temperatures increased the π-π stacking distance in the solid state decreased which could lead to improved charge transport through the thin films.

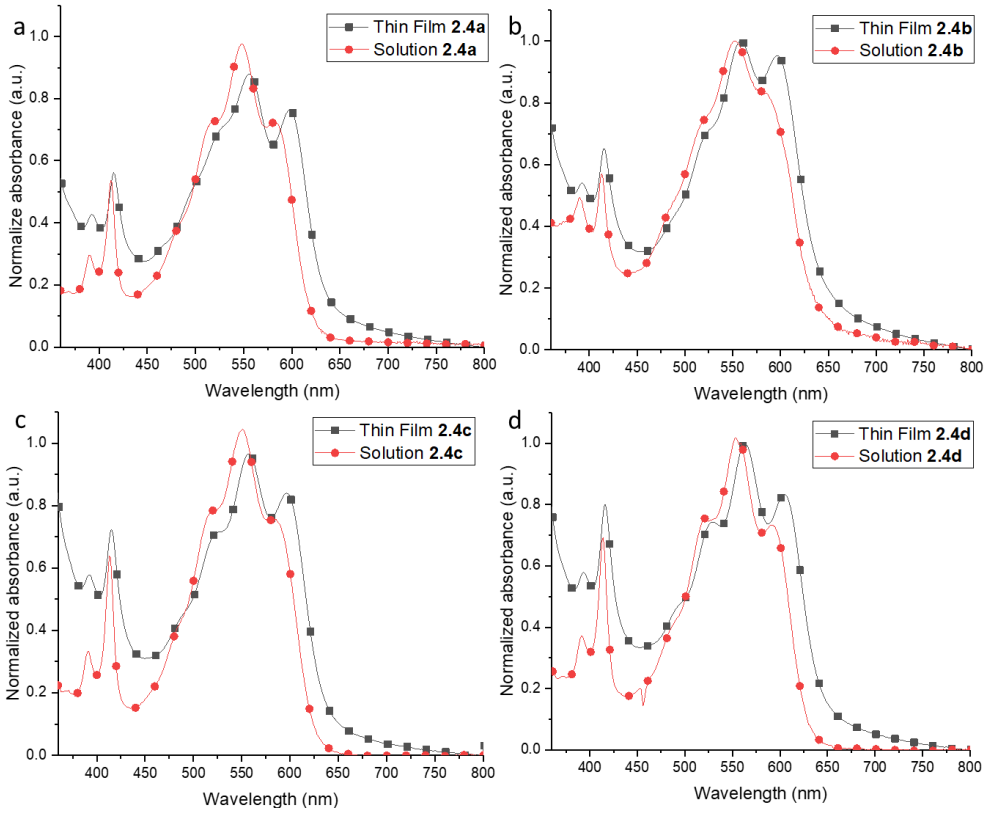

Figure 6.7: Absorption spectra of compound **2.4a-d**, the solution absorption spectra is shown witrh circles and the thin film absorption spectra is shown with squares.

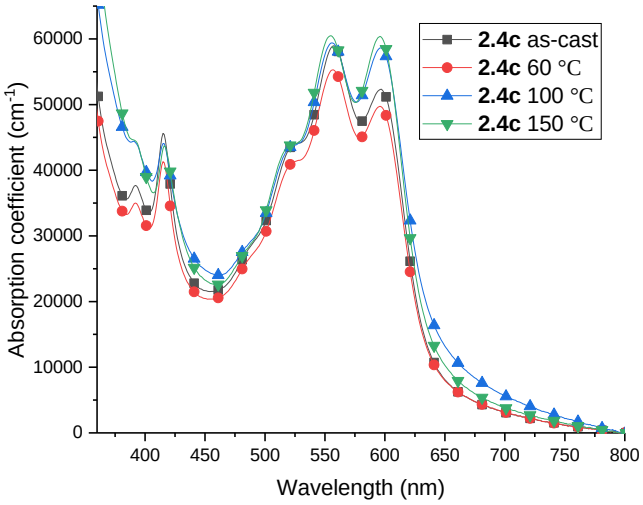

Figure 6.8: The absorption spectra of compound **2.4c** comparing the as-cast, and annealed thin films, 60 ˚C, 100 ˚C, and 150 ˚C

The measured relative fluorescence intensities of thin films of ASI derivatives **2.4a-d** varied greatly (**Figure 6.9**). While compounds **2.4a** and **d** demonstrated some fluorescence when excited at 563 nm, both compounds **2.4b** and **c** showed only very weak fluorescence. Comparing the emission spectra of the solution and thin films, we again observed a bathochromatic of the emission spectra, form a λ_{max} of 618 nm in solution to 628 nm in the thin film.[14]

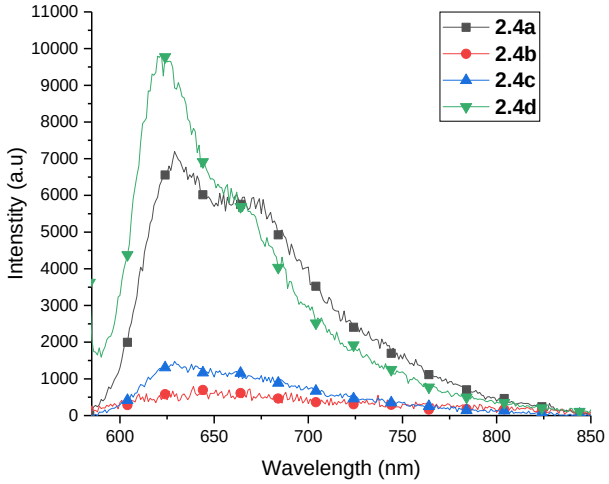

Figure 6.9: The fluorescent spectra of the as-cast thin films of compounds **2.4a-d**.

6.2.1.2 OPV performance:

6.2.1.2.1 Bulk heterojunction ASI:DH6T:

To determine whether ASI derivatives could function as an electron acceptor for DH6T, UV/visible light absorption and fluorescence spectroscopy measurements were performed on mixed thin films of ASI and DH6T. UV/Vis experiments were used to study molecular mixing and fluorescence experiments were used to examine charge transfer between ASI derivatives and DH6T. To examine mixing of the ASI derivatives and DH6T thin film absorption experiments were done on neat thin films of both ASI derivative **2.4a-**

d and DH6T as well as 1:1 mixtures of **2.4a-d** and DH6T. All absorbance spectra can be found in the appendix **Figures A53-55**.

Comparing the absorbance spectra of both the neat and mixed thin films of DH6T and **2.4c**, we observed very little mixing of DH6T and **2.4c** in the thin film (**Figure 6.10**). The absorbance of (1:1) **2.4c**:DH6T mixed thin film showed no change in the λ_{max} compared to the neat films, while the attenuation coefficient decreased by half due increased thin film thickness. The fact that the absorbance spectra of the mixed thin film was simply a linear combination of the two neat absorbance spectra, demonstrated that there was limited mixing, and π-stacking, of the donor DH6T and **2.4c** in the thin film. This is similar to what was seen in the mixed thin films with the other ASI derivatives, however, the thickness of the mixed thin film using **2.4a**, **b**, and **d** was not obtained so the absorption coefficients could not be determined.

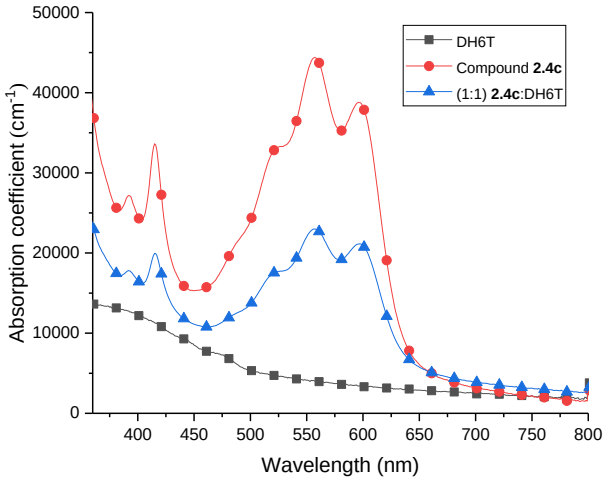

Figure 6.10: Absorption spectra of thin films neat DH6T, neat **2.4c**, and mixed (1:1) **2.4c**:DH6T

Examining donor:acceptor charge transfer of the ASI:DH6T mixed thin films, we observed a large ASI substrate dependence (Appendix **Figure A49-52**). All thin films were prepared from the same initial concentrations normalized to the maximum intensity observed between the three films. **Figure 6.11** shows the fluorescence spectra the (1:1) **2.4c**:DH6T mixed thin film. From the fluorescence spectra of the mixed thin film we observed incomplete quenching of the DH6T donor. When the neat DH6T thin film is stimulated at 420 nm we observed a maximum emission signal at 523 nm. In the mixed thin film the partial quenching of the DH6T was seen by the decreased emission signal maximum at 523 nm. However, the charge transfer from the DH6T to compound **2.4c** was inefficient, as indicated by the large fluorescence intensity below 550 nm for the mixed thin film. The amount of DH6T fluorescence quenching observed was dependent on the ASI acceptor used. Compounds **2.4a**,**b**, and **d** all showed improved fluorescence quenching compared to **2.4c**. The percent quenching of the DH6T was calculated by comparing the area under the curve of the neat films to the mixed between 475 to 580 nm. **Table 6.1** shows that the least efficient acceptor for DH6T was compound **2.4c** while the best was **2.4d**.

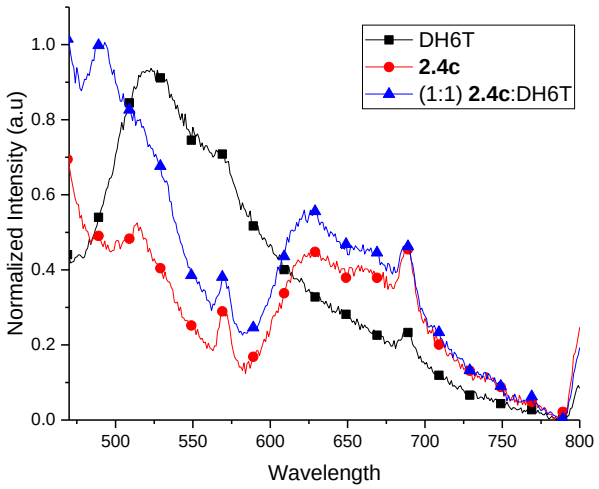

Figure 6.11: Fluorescence spectra of thin films neat DH6T, neat **2.4c**, and mixed (1:1) **2.3.10c**:DH6T.

Table 6.1: The calculated percent quenching of DH6T by the ASI derivatives in the (1:1) mixed thin films.

Thin Film Composition	Percent DH6T quenching
(1:1) **2.4a**:DH6T	78 %
(1:1) **2.4b**:DH6T	71 %
(1:1) **2.4c**:DH6T	63 %
(1:1) **2.4d**:DH6T	98 %

6.2.1.2.2 ASI:DH6T mixed thin film OPVs:

Since all the ASI derivatives tested demonstrated some quenching of DH6T, OPVs were fabricated using an ASI:DH6T BHJ active layer. As previously stated the OPVs were prepared using the inverted architecture and a bulk heterojunction active layer. OPVs were prepared via spin-coating from either the (2:3) $CHCl_3$:ODCB or MeTHF:Toluene solvent systems. OPV performance was examined by generating I-V curves of each solar cell.

Table 6.2 shows the performance of the **2.4c**:DH6T BHJ prepared from (2:3) $CHCl_3$:ODCB. From the I-V curves we saw no rectification behavior of any of the OPVs using the **2.4c**:DH6T BHJ active layer. Increasing the percentage of the stronger absorbing ASI derivative had no effect on OPV performance.

Table 6.2: Table showing the OPV performance of ITO/ZnO/**2.4c**:DH6T/MoO_3/Ag where the **2.4c**:DH6T active layer was deposited via spin-coating from the (2:3) $CHCl_3$:ODCB solvent system. J_{sc} (mA/cm^2) is the short-circuit current, V_{oc} (V) s the open-circuit voltage, and P_{max} (mW/cm^2) is the maximum power output

Composition	J_{sc} (mA/cm^2)	V_{oc} (V)	P_{max} (mW/cm^2)	Fill Factor
2.4c:DH6T (1:1) as-cast	-2.08E^{-02}	0.002	0.00	0.000
2.4c:DH6T (3:1) as-cast	-1.39E^{-02}	0.006	0.00	0.000
2.4c:DH6T (6:1) as-cast	-5.43E^{-03}	0.000	0.00	0.000

Changing the solvent system to (2:3) MeTHF:Toluene, in an attempt to alter molecular mixing and BHJ morphology, also resulted in no rectification behavior in the fabricated OPVs (**Table 6.3**). I-V curves comparing (1:1), (3:1), and (6:1) as-cast **2.4c**:DH6T OPVs can be found in the appendix **Figure A53**.

Table 6.3: Table showing the OPV performance of ITO/ZnO/**2.4c**:DH6T/MoO_3/Ag where the **2.4c**:DH6T active layer was deposited via spin-coating from the (2:3) MeTHF:Toluene solvent system. J_{sc} (mA/cm^2) is the short-circuit current, V_{oc} (V) s the open-circuit voltage, and P_{max} (mW/cm^2) is the maximum power output

Composition	J_{sc} (mA/cm^2)	V_{oc} (V)	P_{max} (mW/cm^2)	Fill Factor
2.4c:DH6T (1:1) as-cast	-5.63E^{-03}	0.000	0.00	0.000
2.4c:DH6T (3:1) as-cast	-1.91E^{-02}	0.000	0.00	0.000
2.4c:DH6T (6:1) as-cast	-6.51E^{-03}	0.003	0.00	0.000

We then switched to using **2.4b** and **d**, which were shown to be more efficient electron acceptors for DH6T, as the n-type material in BHJ and annealed the films at 60 ˚C. However, this again resulted in no OPV performance (**Table 6.4**). I-V curves comparing 60 ºC annealed (6:1) **2.4b**:DH6T and **2.4d**:DH6T OPVs can be found in the appendix **Figure A54**.

Table 6.4: OPV performance of ITO/ZnO/**2.4b** or **2.4d**:DH6T/MoO_3/Ag where the BHJ active layer was deposited via spin-coating from the (2:3) MeTHF:toluene solvent system. J_{sc} (mA/cm^2) is the short-circuit current, V_{oc} (V) s the open-circuit voltage, and P_{max} (mW/cm^2) is the maximum power output

Composition	J_{sc} (mA/cm^2)	V_{oc} (V)	P_{max} (mW/cm^2)	Fill Factor
2.4b:DH6T (6:1) 60 ˚C	-7.74E^{-04}	0.002	0.00	0.000
2.4d:DH6T (6:1) 60 ˚C	-2.86E^{-03}	0.012	-8.11E^{-06}	0.241

6.2.1.2.3 Solid-state characterization BHJ 2.4b and c:DH6T OPVs:

To better understand why no rectification behavior was observed for any of the prepared OPVs, despite the fact that ASI's were found to quench DH6T in the mixed thin films, solid-state characterization was performed using both atomic force microscopy (AFM) and grazing incident wide-angle X-ray scattering (GIWAXS). Thin film of the mixed **2.4b** and **c**:DH6T active layer were prepared via spin-coating on Si/SiO_2 substrate using (2:3) $CHCl_3$:ODCB solvent system. In the AFM images of (1:1) **2.4c**:DH6T mixed thin films, the rough part of the film is the **2.4c** and the smooth part of the film is the DH6T (**Figure 6.12**). From the AFM images we observed a large amount of segregation between **2.4c** and DH6T resulting in two distinct phases in the thin film. The large amount of phase separation also resulted in very large domains in the (1:1) **2.4c**:DH6T mixed thin films. When (1:1) **2.4b**:DH6T mixed thin films were examined by AFM, we again observed the same bi-phasic thin film morphology (**Figure 6.13**). The thin film morphology observed by AFM explained the lack of OPV performance observed with this material. The large number of grain boundaries and rough texturing observed in the thin films, would result in increased charge recombination and decreased OPV performance. Also, the large grain sizes in the thin film would decrease OPV efficiency due to decreased exciton dissociation. As stated previously exciton dissociation only occurs at the p-n junction interface, and given the short exciton lifetime and diffusion length, approximately 10 nm, the large domains observed in the thin film, greater than 1 μm, would result in a significant amount of exciton recombination decreasing OPV performance.

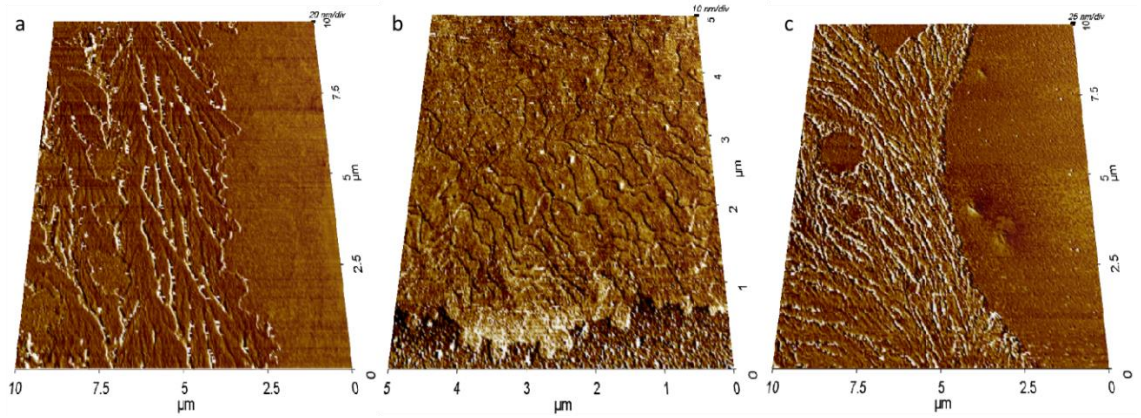

Figure 6.12: The AFM images of **2.4c**:DH6T mixed in the as-cast thin films prepared from (2:3) $CHCl_3$:ODCB solvent system, a) (1:1) **2.4c**:DH6T, b) (3:1) **2.4c**:DH6T, and c) (6:1) **2.4c**:DH6T

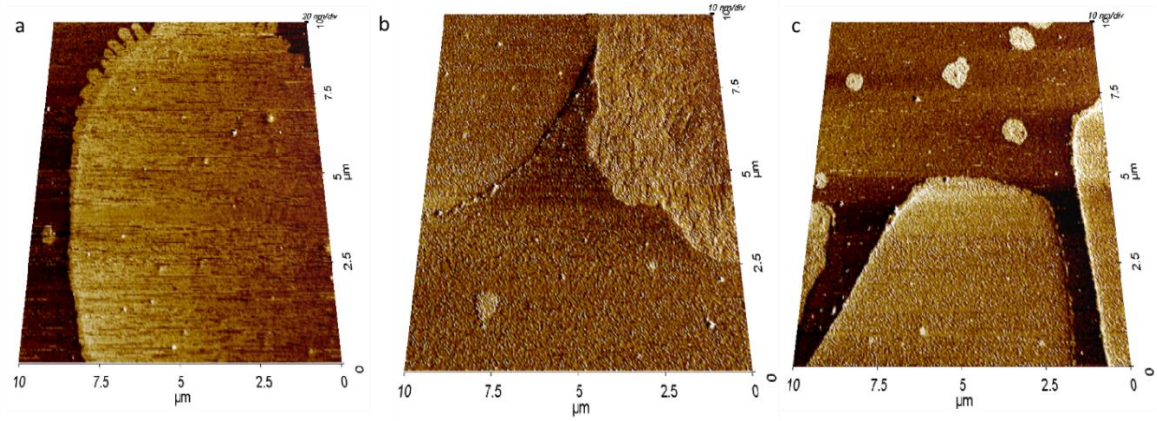

Figure 6.13: The AFM images of **2.4b**:DH6T mixed in the as-cast thin films prepared from (2:3) $CHCl_3$:ODCB solvent system, a) (1:1) **2.4b**:DH6T, b) (3:1) **2.4b**:DH6T, and c) (6:1) **2.4b**:DH6T

Examining the thin film morphology via X-ray spectroscopy, GIWAXS experiments showed little to no mixing of **2.4c** and DH6T throughout the bulk. The 2-D diffraction pattern of neat **2.4c** annealed at 150 ˚C showed a high level of ordering and good π-stacking discussed previously in chapter 2 (**Figure 6.14a**). Comparing the neat thin

film morphology, **Figure 6.14a**, to the mixed thin film, **Figure 6.14b**, we clearly observed two distinct phases in the thin film. In **Figure 6.14b** the diffraction from **2.4c** indicated an increase in the polycrystalline nature of the thin film, as indicated by the diffraction signal extending from χ = -90 to 90˚. Also, from the increased diffraction signal of **2.4c**, in the mixed thin film, we concluded that the crystallinity and molecular ordering of **2.4c** had increased compared to the neat thin film. In the mixed thin film we also observed a clear signal for DH6T packing, the vertical diffraction signals observed around qxy = 1.5 $Å^{-1}$. In fact the DH6T molecules were so well ordered in the (1:1) **2.4c**:DH6T mixed thin film that, from the GIWAXS diffraction signal, we were able to orient the DH6T as standing on the hexyl side-chains relative to the Si/SiO_2 substrate. The GIWAXS data of the (1:1) **2.4c**:DH6T thin film corroborated what was observed by AFM, that there was extremely poor mixing of ASI derivatives and DH6T in the solid state.[25,26]

From the solid-state characterization of the mixed ASI:DH6T thin film morphologies, we concluded that the lack of OPV performance form the ASI:DH6T BHJ active layer was due to the poor mixing, and large domain sizes in the active layer, which resulted in poor charge transport and extraction.

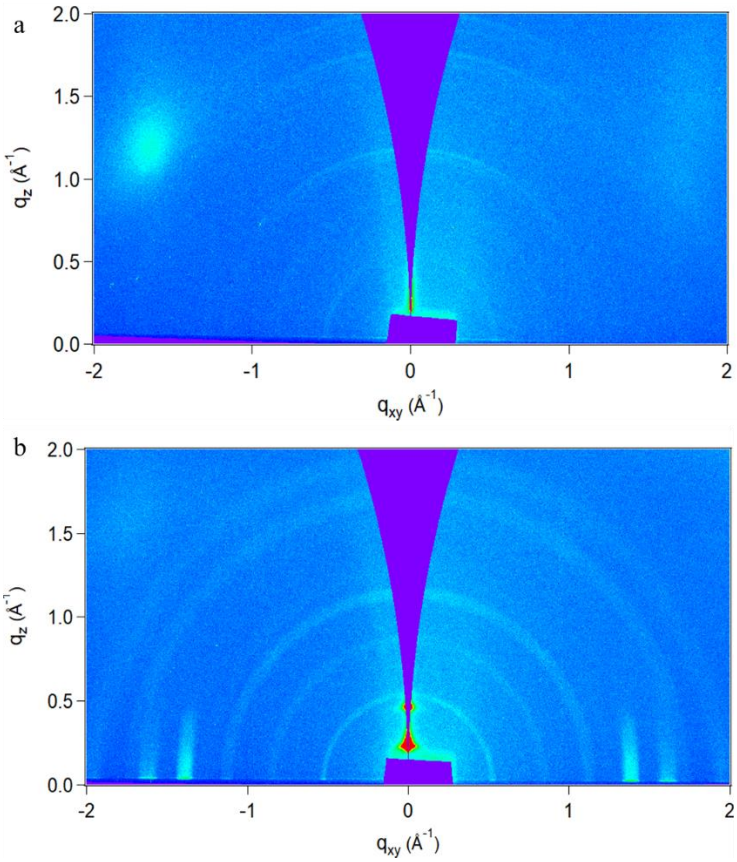

Figure 6.14: Showing the experimentally observed 2-D diffraction patterns; a) neat **2.4c**, b) (1:1) **2.4c**:DH6T thin films prepared from (2:3) $CHCl_3$:ODCB solvent system

6.2.1.2.4 Bulk heterojunction ASI:Sq:

Switching the donor to Bis[4-(N,N-diisobutylamino)-2,6-dihydroxyphenyl] squaraine (Sq), we again first examined molecular mixing and charge transfer between ASI derivatives and Sq via UV/visible light absorption and fluorescence spectroscopy. From the absorption spectra comparing the neat and mixed thin films, we saw evidence of good molecular mixing in the solid state (**Figure 6.15**). From the UV/Vis data, we observed a shift in the λ_{max} from 706 nm of the neat Sq thin film to 678 and 682 nm of both (1:1) **2.4b**:Sq and (1:1) **2.4c**:Sq, respectively. The shift in the λ_{max} of both (1:1) **2.4b**:Sq and (1:1)

2.4c:Sq thin films indicated that new π-π interactions were occurring in the mixed thin films which did not exist in either of the neat thin films suggesting improved solid-state molecular mixing, compared to **2.4a-d**:DH6T mixed thin films.

The efficiency of charge transfer from the Sq donor to the ASI acceptor was determine by measuring the fluorescence quenching of Sq in the (1:1) **2.c**:Sq mixed thin films (**Figure 6.16**). Again, by comparing the relative fluorescence intensities of the neat **2.4c** and Sq thin films to the (1:1) **2.4c**:Sq mixed thin film, we determined the percent quenching of Sq in the mixed thin film. We observed, from the fluorescence experiments, that **2.4c** quenched the Sq donor with 93 % efficiency. This indicated highly efficient charge transfer between ASI acceptors and the Sq donor and improved charge transfer efficiency in the (1:1) **2.4c**:Sq thin films verses (1:1) **2.4c**:DH6T thin films. The improvrd charge transfer could be attributed to the difference in the HOMO/LUMO energies between DH6T and Sq. The difference in the HOMO/LUMO energies between DH6T and Sq are, -5.2 and -2.9 eV for DH6T and -5.3 and -3.4 eV for Sq. The lower LUMO of the Sq molecule could make charge transfer in to the LUMO of the ASI molecule, -4.1 eV, much more efficient potentially improving charge transfer. Alternatively, the improved charge transfer could simply be due to improved molecular mixing and thin film morphology.

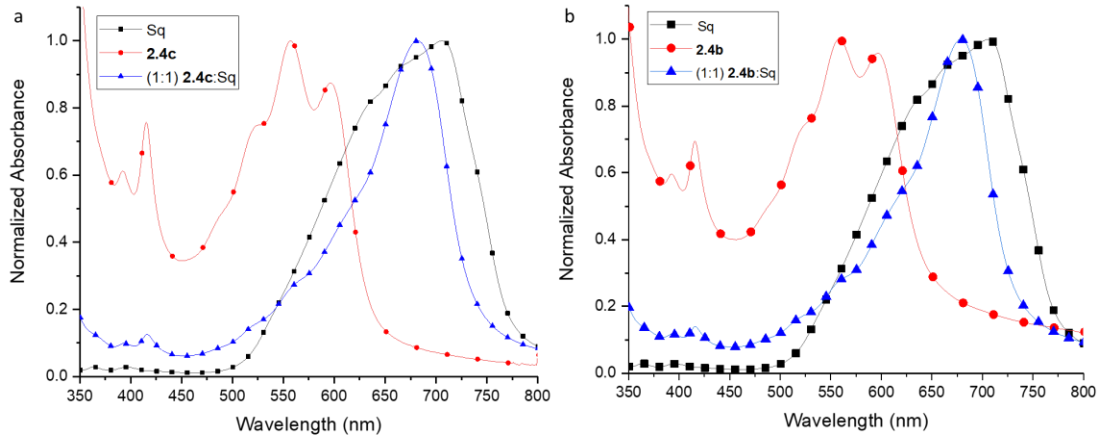

Figure 6.15: Absorption spectra of thin films prepare form (2:3) $CHCl_3$:ODCB a) neat DH6T, neat **2.4c**, and mixed (1:1) **2.4c**:Sq b) neat DH6T, neat **2.4b**, and mixed (1:1) **2.4b**:Sq

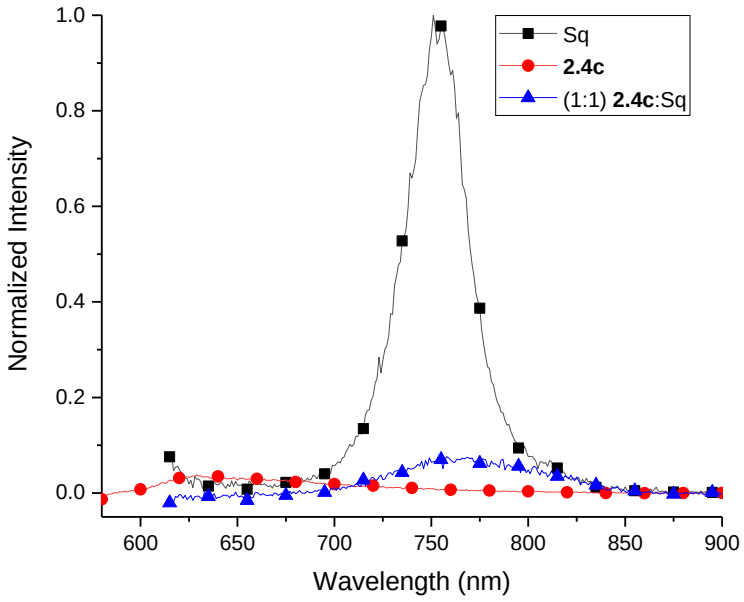

Figure 6.16: Fluorescence spectra of thin films prepare form (2:3) $CHCl_3$:ODCB; neat DH6T, neat **2.4c**, and mixed (1:1) **2.4c**:Sq

6.2.1.2.5 ASI:Sq mixed thin film OPV:

When OPVs were fabricated using ASI:Sq bulk heterojunctions as the active layer, we observed OPV performance and rectification behavior (**Table 6.5**). I-V curves comparing as-cast (6:1) **2.4b**:Sq, 60 ºC annealed (6:1) **2.4b**:Sq, and **2.4d**:Sq OPVs are shown in **Figure 6.17**.

In all cases the J_{sc} was very low however there was a marked improvement in the V_{oc}. The V_{oc} observed in the **2.4d**:Sq OPVs is comparable to a-Si which has a commercial operating V_{oc} of 0.600 V.[5] The improved V_{oc} is most likely due to better charge extraction from the active layer due to improved thin film morphology. However, no thin film characterization has yet been performed on these films. The very low J_{sc} in these films could be due to either poor charge transport, in the thin films, or poor energy match with the charge extraction layers, which also resulted in a high series resist, R_S, for these OPVs.

Table 6.5: OPV performance of ITO/ZnO/**2.4b** or **2.4d**:Sq/MoO_3/Ag where the BHJ active layer was deposited via spin-coating from the (2:3) MeTHF:toluene solvent system. J_{sc} (mA/cm^2) is the short-circuit current, V_{oc} (V) s the open-circuit voltage, and P_{max} (mW/cm^2) is the maximum power output.

Composition	J_{sc} (mA/cm^2)	V_{oc} (V)	P_{max} (mW/cm^2)	Fill Factor
2.4b:Sq (6:1) rt	$-1.30E^{-03}$	0.243	$9.26E^{-05}$	0.290
2.4b:Sq (6:1) 60 ˚C	$-1.52E^{-03}$	0.213	$8.77E^{-05}$	0.294
2.4d:Sq (6:1) 60 ˚C	$-6.62E^{-04}$	0.460	$9.66E^{-05}$	0.318

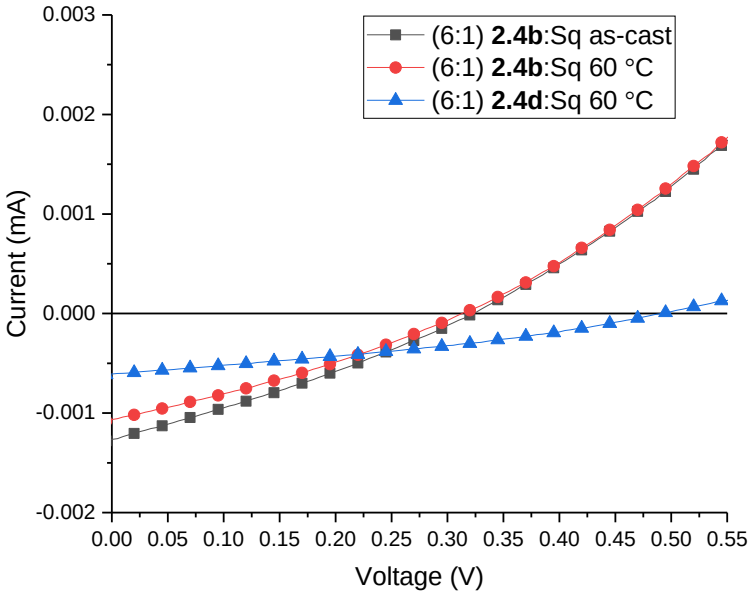

Figure 6.17: I-V curves for BHJ small molecule organic solar using **2.4b** or **d** as the electron acceptor and Sq as the electron donor, ITO/ZnO/**2.4b** or **2.4d**:Sq/MoO_3/Ag.

6.2.2 ASI:polymer OPVs:

Kevin Gu of the Bao group also fabricated and tested OPVs utilizing ASI acceptors and polymer donors PTB7-Th and Pil-2T-PS10 (**Figure 6.6**). (**Table 6.6**). For ASI **2.4c** very high open-circuit voltages of around 1 V were measured while **2.4b** had a maximum V_{oc} of 0.7 V with the PiI-2T-PS10 polymer. Switching from the small molecule donor to the polymer donor, we observed a 10-fold increase in the short-circuit current, though it was still extremely low, and again a high R_S was measured for all solar cells. I-V curves for the ASI:Polymer solar cells can be found in the appendix **Figure A55**.

Table 6.6: Shows the short-circuit current, open-circuit voltage, maximum power, and Fill Factor for a few of the OPVs fabricated using polymer donors PTB7-Th or PiI-2T-PS10 and ASI acceptors.

	J_{sc} (mA/cm^2)	V_{oc} (V)	P_{max} (mW/cm^2)	Fill Factor
(1:1) PTB7-Th / **2.4c**	-5.01E-02	1.17	-1.20E-02	0.242
(1:1) PTB7-Th / **2.4b**	-3.38E-02	0.25	-2.23E-03	0.262
(1:1) PiI-2T-PS10 / **2.4c**	-3.41E-03	1.03	-8.94E-04	0.257
(1:1) PiI-2T-PS10 / **2.4b**	-5.39E-03	0.70	-1.04E-03	0.276
(1:3) PTB7-Th / **2.4c**	-3.75E-02	0.47	-6.50E-03	0.364
(1:3) PTB7-Th / **2.4b**	-2.36E-02	0.22	-1.34E-03	0.264
(1:3) PiI-2T-PS10 / **2.4c**	-1.27E-02	0.06	-2.14E-04	0.257
(1:3) PiI-2T-PS10 / **2.4b**	-5.21E-03	0.07	-9.32E-05	0.252

6.3 Conclusion and future work:

From the fluorescence experiments we observed that ASI derivatives **2.4a-d** do quench DH6T indicating that these molecules do function as electron acceptors for the DH6T donors. However, when OPVs containing **2.4b-d**:DH6T BHJs were tested we saw little to no rectification behavior in the devices. After solid state characterization, it was observed that very poor mixing of the ASI molecules and DH6T occurred in thin films. The rough texture and large domain size observed by AFM, as well as the large degree of phase segregation observed by GWAXS, would result in inefficient charge transfer through the active layer and poor charge extraction at the interface, explaining the lack of OPV performance observed in the **2.4b-d**:DH6T BHJ devices. Switching to a more efficient donor molecule Sq, we observed improved charge transfer via fluorescence as well as rectification behavior form the completed OPVs. It was also observed that OPVs utilizing ASI acceptors and polymer donors, PTB7-Th and Pil-2T-PS10, resulted in improved V_{oc},

though the FF remained low do to the poor J_{sc}. The poor FF and J_{sc} observed for all OPVs was attributed to the very high series resist observed. Although the data analysis is in complete, we can conclude that ASIs do function as electron acceptors in OPVs, however, significant improvement are need to either via optimization of the OPVs and/or synthetic modification of the ASI molecules to improve charge transport.

Future work in this project will initially focus on completing the analysis of the OPV data and publishing the results. For device improvements, the major problem with the ASI acceptor OPVs was the poor short-circuit current and the high series resist. To improve both the J_{sc} and the R_s, the new ASI derivatives proposed in chapter 2 should be examined for improved transport through the BHJ. Also, one could examine different hole and electron transport layers, such as graphene, in an attempt to decrease resistance at the at the metal:BHJ interface.

6.4. Experimental:

Thin films of neat compounds **2.4a-d**, DH6T, Sq and mixed thin films of **2.4a**, **b**, **c**, or **d**:DH6T and (1:1) **2.4c**:Sq or **2.4b**:Sq were fabricated from a mixed solvent system of (2:3) chloroform ($CHCl_3$):orthodichlorobenzene (ODCB) or (2:3) 2-Methyltetrahydrofuran (MeTHF):toluene in a nitrogen-filled glovebox. Solutions were prepared by dissolving 15 mg of the compounds in either ODCB or toluene. The suspensions were then heated to 80 ˚C and stirred for 5 minutes in a sealed 2 mL screw top vial. The suspensions were then cooled to 55 ˚C, chloroform or MeTHF was added, and the solutions were stirred for an additional 5 minutes at 55 ˚C. The solutions were then

removed from heat, allowed to cool to room temperature, and filtered through a 0.45 μm PTFE filter. Using this procedure 10 mg/mL and 20 mg/mL solutions of compounds **2.4a-d** were prepared.

Thin films of neat compounds **2.4a-d**, DH6T, Sq and mixed thin films of **2.4a**, **b**, **c**, or **d**:DH6T and (1:1) **2.4c**:Sq or **2.4b**:Sq were prepared on either glass, Si with a native oxide layer, or ITO on glass covered with zinc oxide nanoparticles (ITO/ZnO). ITO/glass substrates were cleaned by sequentially sonicating in detergent, deionized water, acetone, and isopropyl alcohol for 10 minutes each. The substrates were blown dry with N_2 and cleaned with UV/ozone for 20 minutes. ZnO nanoparticles were immediately applied to the cleaned ITO surface from a 2.8 wt% solution in acetone. A 50 μL drop of the ZnO solution was placed on the cleaned substrate and then spun at 7000 rpm for 30 seconds to give a ZnO layer 30 to 40 nm thick. The ITO/ZnO substrate was then transferred to the glovebox and used immediately. The Si and glass substrates were cleaned by sonication in acetone for 15 minutes followed by sonication in isopropyl alcohol for 15 minutes, blown dry with N_2, and finally cleaned with UV/ozone for 20 minutes. The cleaned substrates were directly transferred to the glove box and used immediately.

Thin films were prepared in an oxygen free and moisture free nitrogen glovebox. A 50 μl drop of the prepared ASI solution was spread over the substrate to assure even coverage. The substrate was then spin cast at 1000 rpm for 45 s. Thin films of neat compound **2.4a-d**, DH6T, and Sq were prepared from a 10 mg/ml solution and mixed thin film, (1:1), of **2.4a**, **b**, **c**, or **d**:DH6T and (1:1) **2.4c**:Sq or **2.4b**:Sq were prepared from a 20 mg/ml solution, (10 mg/ml ASI: 10 mg/ml DH6T) for UV/Visible light absorption

spectroscopy (UV/Vis), and fluorescence spectroscopy experiments to give films between 20 to 40 nm thick. Thin films of neat compound **2.4c**, and (1:1) **2.4c**:DH6T for Grazing incidence wide-angle X-ray scattering (GIWAXS), atomic force microscopy (AFM) experiments were prepared from either 10 or 20 mg/ml solutions. Compound **2.4c** was prepared from a 10 mg/ml solution, to give films between 20 and 30 nm thick, for all experiments. Thin films of compounds **2.4a-d**, DH6T, and Sq and mixed **2.4a**, **b**, **c**, or **d**:DH6T and (1:1) **2.4c**:Sq or **2.4b**:Sq, were prepared on Si/SiO_2 for GIWAXS, and AFM experiments, and glass for UV/Vis and fluorescence experiments. To study thin film properties at variable temperatures four samples were prepared. One was left as-cast, while the remaining three samples were annealed at 60, 100 or 150 ˚C for 2 minutes in a nitrogen-filled glovebox and then quenched by removal from heat.

Thin film mixing and molecular orientation were determined via GIWAXS experiments performed on beamline 11-3 at the Stanford Synchrotron Radiation Lightsource (SSRL) using an X-ray energy of 12.7 keV and a 2-D MACCD detector at a sample-detector distance of 250 mm. The samples were placed in a chamber with flowing He at an incident angle of either 0.16˚ for samples on Si/SiO_2. Samples were calibrated using a LaB_6 standard.[27] To minimize beam damage samples were exposed to X-rays in five 60 second increments in the same place. The images were then averaged to produce the raw diffraction pattern. The grazing incident geometry results in distortion of reciprocal space in the raw diffraction pattern.[28] [29] Using the WAXStools program, χ and polarization corrections were applied and the intensity versus scattering vector component, qz and qxy, were plotted.[30] No absorbance intensity correction was performed because only peak

location and relative intensities within a given scan were of interest. Line scans were produced by integrating 2-D GIWAXS data over a given polar angle. I vs q curves were modeled by first performing a baseline correction then fitting each peak to a Gaussian curve. Baseline correction and peak fitting of I vs q was performed using Origin data analysis software. I vs q graphs obtained from the 2-D GIWAXS were compared to theoretical I vs q powder diffraction patterns generated from the CrystalDiffract software. SimDiffraction program was used to model 2-D GIWAXS diffraction patterns.[31] Mercury software was used to determine intermolecular distances, angle of crystallographic planes, and molecular orientation.[32]

To characterize thin film morphology and thickness, AFM images in non-contact mode were obtained at the Stanford Nano Shared Facilities: Soft & Hybrid Material Facility using Park NX-10. Image analysis was performed using Park systems XEI.

Fluorescence spectroscopy was used to determine charge transfer from the donor molecules to the ASI acceptor molecules by examining changes between neat donor and mixed (donor:ASI) thin film fluorescence. Fluorescence experiments were performed at the Stanford Nano Shared Facilities: Soft & Hybrid Material Facility using the Horiba FluoroLog-3 Fluorimeter.

To determine thin film thickness profilometry measurements were performed at the Stanford Nano Shared Facilities: Soft & Hybrid Material Facility using the Bruker Dektak XT Profilometer.

UV/Visible light spectroscopy (UV/Vis) was used to determine changes in π-stacking in the thin films. UV/Vis experiments were done at the Stanford Nano Shared

Facilities: Soft & Hybrid Material Facility using the Agilent Cary 6000i UV/Vis/NIR spectrophotometer. Absorbance measurements were performed on thin films of compound 1 and 2 on glass scanning from 1200 to 200 nm. Data was analyzed using Origin data analysis software.

Organic Photovoltaic fabrication

Organic photovoltaic (OPV) devices were prepared with an inverted architecture, ITO/ZnO/ASI:Donor/MoO_3/Ag. OPV active layers were prepared from 20 mg/ml solutions of compounds **2.4a-d** mixed with either DH6T or Sq. A 50 μl drop of the desired ASI solution was spread over the substrate to assure even coverage. The substrate was then spin cast at 1000 rpm for 45 s. The effects of annealing temperatures on OPV performance were studied by preparing four separate devices. One left as-cast, while the remaining three samples were annealed at either 60, 100 or 150 ˚C for 2 minutes in a Nitrogen-filled glovebox and then quenched by removal from heat. Electron transport layer and anode were deposited via thermal evaporation, 10 nm thick MoO_3 and 100 nm thick silver respectively, under high vacuum at 10^{-6} torr. Solar cell devices were illuminated under a simulated AM 1.5G solar spectrum (Newport Solar Simulator 94021A) calibrated to a KG5 Si photodiode, and current-voltage curves were collected by a Keithley 2400 analyzer.

6.5 References:

(1) “International Energy Outlook,” United Stated Energy Infromation Administration, **2016**.

(2) Chapin, D. M.; Fuller, C. S.; Pearson, G. L. *J. Appl. Phys.* **1954**, *25*, 676.

(3) Research-cell-efficiency-records, Ed. National Renewable Energy Laboratory - National Center for Photovoltaics.

(4) Fu, R.; Feldman, D.; Margolis, R.; Woodhouse, M.; Ardani, K. “U.S. Solar Photovoltaic System Cost Benchmark,” National Renewable Energy Laboratory, 2017.

(5) “BASIC RESEARCH NEEDS FOR SOLAR ENERGY UTILIZATION,” **2005**.

(6) *Organic Solar Cells: Fundamentals, Devices, and Upscaling.*; CRC Press: Boca Raton, Fl, **2014**.

(7) Kazmerski, L. L. *J. Elect. Spect. Rel. Phenom.* **2006**, *150*, 105.

(8) Sun, S.-S. *Mater. Sci. Eng., B* **2005**, *116*, 251.

(9) Forrest, S. R. *Nature* **2004**, *428*, 911.

(10) Riede, M.; Mueller, T.; Tress, W.; Schueppel, R.; Leo, K. *Nanotechnology* **2008**, *19*, 424001.

(11) Yassar, A. *Polym. Sci. Series C* **2014**, *56*, 4.

(12) Mihailetchi, V. D.; Wildeman, J.; Blom, P. W. *Phys. Rev. Lett.* **2005**, *94*, 126602.

(13) Eftaiha, A. F.; Sun, J. P.; Hill, I. G.; Welch, G. C. *J. Mater. Chem. A* **2014**, *2*, 1201.

(14) Purvis, L. J.; Gu, X.; Ghosh, S.; Zhang, Z.; Cramer, C. J.; Douglas, C. J. *J. Org. Chem.* **2018**, *83*, 1828.

(15) Peumans, P.; Yakimov, A.; Forrest, S. R. *J. Appl. Phys.* **2003**, *93*, 3693.

(16) Hsiao, Y. S.; Whang, W. T.; Suen, S. C.; Shiu, J. Y.; Chen, C. P. *Nanotechnology* **2008**, *19*, 415603.

(17) Sonar, P.; Fong Lim, J. P.; Chan, K. L. *Energy Environ. Sci.* **2011**, *4*, 1558.

(18) Savva, A.; Burgues-Ceballos, I.; Papazoglou, G.; Choulis, S. A. *ACS Appl. Mater. Interfaces* **2015**, *7*, 24608.

(19) Alaman, J.; Alicante, R.; Pena, J. I.; Sanchez-Somolinos, C. *Materials* **2016**, *9*, 910.

(20) Zhou, Y.; Gu, K. L.; Gu, X.; Kurosawa, T.; Yan, H.; Guo, Y.; Koleilat, G. I.; Zhao, D.; Toney, M. F.; Bao, Z. *Chem. Mater.* **2016**, *28*, 5037.

(21) Li, X.; Liu, X.; Sun, P.; Feng, Y.; Shan, H.; Wu, X.; Xu, J.; Huang, C.; Chen, Z.-K.; Xu, Z.-X. *RSC Adv.* **2017**, *7*, 17076.

(22) Muhammad, F. F.; Sulaiman, K. *Thin Solid Films* **2011**, *519*, 5230.

(23) Chen, G.; Sasabe, H.; Wang, Z.; Wang, X. F.; Hong, Z.; Yang, Y.; Kido, J. *Adv Mater* **2012**, *24*, 2768.

(24) Zhang, J.; Singh, S.; Hwang, D. K.; Barlow, S.; Kippelen, B.; Marder, S. R. *J. Mater. Chem. C* **2013**, *1*, 5093.

(25) Birkholz, M. *Thin Film Analysis by X-ray Scattering*; Wiley-VCH: Weinheim, 2006.

(26) Rivnay, J.; Mannsfeld, S. C.; Miller, C. E.; Salleo, A.; Toney, M. F. *Chem. Rev.* **2012**, *112*, 5488.

(27) Ilavsky, J. *J. Appl. Crystallogr.* **2012**, *45*, 324.

(28) Smilgies, D.-M. *Rev. Sci. Instrum.* **2002**, *73*, 1706.

(29) Baker, J. L.; Jimison, L. H.; Mannsfeld, S.; Volkman, S.; Yin, S.; Subramanian, V.; Salleo, A.; Alivisatos, A. P.; Toney, M. F. *Langmuir* **2010**, *26*, 9146.

(30) Oosterhout, S. D.; Savikhin, V.; Zhang, J.; Zhang, Y.; Burgers, M. A.; Marder, S. R.; Bazan, G. C.; Toney, M. F. *Chem. Mater.* **2017**, *29*, 3062.

(31) Breiby, D. W.; Bunk, O.; Andreasen, J. W.; Lemke, H. T.; Nielsen, M. M. *J. Appl. Crystallogr.* **2008**, *41*, 262.

(32) Macrae, C. F.; Bruno, I. J.; Chisholm, J. A.; Edgington, P. R.; McCabe, P.; Pidcock, E.; Rodriguez-Monge, L.; Taylor, R.; van de Streek, J.; Wood, P. A. *J. Appl. Crystallogr.* **2008**, *41*, 466.

References:

Chapter 1:

(1) Tsumura, A.; Koezuka, H.; Ando, T. *Appl. Phys. Lett.* **1986**, *49*, 1210.

(2) *Org. Elect., Mater., Manufac., and Appl.*; Klauk, H., Ed.; Weinheim : Wiley-VCH: Germany, 2006.

(3) Forrest, S. R. *Nature* **2004**, *428*, 911.

(4) de Mello, J.; Anthony, J.; Lee, S. *Chem. Phys. Chem.* **2015**, *16*, 1099.

(5) Anthony, J. E. *Chem Rev* **2006**, *106*, 5028.

(6) Coropceanu, V.; Cornil, J.; da Silva Filho, D. A.; Olivier, Y.; Silbey, R.; Bredas, J. L. *Chem. Rev.* **2007**, *107*, 926.

(7) Rivnay, J.; Jimison, L. H.; Northrup, J. E.; Toney, M. F.; Noriega, R.; Lu, S.; Marks, T. J.; Facchetti, A.; Salleo, A. *Nat. Mater.* **2009**, *8*, 952.

(8) Dobler, C.; Tönshoff, C.; Bettinger, H. F.; Chassé, T.; Casu, M. B. *J. Phys. Chem. C* **2017**, *121*, 13660.

(9) Wasikiewicz, J. M.; Abu-Sen, L.; Horn, A. B.; Koelewijn, J. M.; Parry, A. V. S.; Morrison, J. J.; Yeates, S. G. *J. Mater. Chem. C* **2016**, *4*, 7309.

(10) Gundlach, D. J.; Lin, Y. Y.; Jackson, T. N.; Nelson, S. F.; Schlom, D. G. *IEEE Electron Device Lett.* **1997**, *18*, 87.

(11) Miao, Q.; Nguyen, T. Q.; Someya, T.; Blanchet, G. B.; Nuckolls, C. *J. Am. Chem. Soc.* **2003**, *125*, 10284.

(12) Tang, Q.; Zhang, D.; Wang, S.; Ke, N.; Xu, J.; Yu, J. C.; Miao, Q. *Chem. Mater.* **2009**, *21*, 1400.

(13) Anthony, J. E.; Brooks, J. S.; Eaton, D. L.; Parkin, S. R. *J. Am. Chem. Soc.* **2001**, *123*, 9482.

(14) Park, S. K.; Jackson, T. N.; Anthony, J. E.; Mourey, D. A. *Appl. Phys. Lett.* **2007**, *91*, 063514.

(15) Nabok, D.; Puschnig, P.; Ambrosch-Draxl, C.; Werzer, O.; Resel, R.; Smilgies, D.-M. *Phys. Rev. B* **2007**, *76*.

(16) Giri, G.; Verploegen, E.; Mannsfeld, S. C.; Atahan-Evrenk, S.; Kim, D. H.; Lee, S. Y.; Becerril, H. A.; Aspuru-Guzik, A.; Toney, M. F.; Bao, Z. *Nature* **2011**, *480*, 504.

(17) Sheraw, C. D.; Jackson, T. N.; Eaton, D. L.; Anthony, J. E. *Adv. Mater.* **2003**, *15*, 2009.

(18) James, D. T.; Frost, J. M.; Wade, J.; Nelson, J.; Kim, J. S. *ACS Nano* **2013**, *7*, 7983.

(19) Payne, M. M.; Parkin, S. R.; Anthony, J. E.; Kuo, C. C.; Jackson, T. N. *J. Am. Chem. Soc.* **2005**, *127*, 4986.

(20) Payne, M. M.; Delcamp, J. H.; Parkin, S. R.; Anthony, J. E. *Org. Lett.* **2004**, *6*, 1609.

(21) Griffith, O. L.; Anthony, J. E.; Jones, A. G.; Shu, Y.; Lichtenberger, D. L. *J. Am. Chem. Soc.* **2012**, *134*, 14185.

(22) Lane, P. A.; Palilis, L. C.; Kushto, G. P.; Kafafi, Z. H.; Purushothaman, B.; Anthony, J. E. *Proc. of SPIE* **2008**, *7052*, 70521J.

(23) Swartz, C. R.; Parkin, S. R.; Bullock, J. E.; Anthony, J. E.; Mayer, A. C.; Malliaras, G. G. *Org. Lett.* **2005**, *7*, 3163.

(24) Sherman, J. B.; Moncino, K.; Baruah, T.; Wu, G.; Parkin, S. R.; Purushothaman, B.; Zope, R.; Anthony, J.; Chabinyc, M. L. *J. Phys. Chem. C* **2015**, *119*, 20823.

(25) Lim, Y.-F.; Shu, Y.; Parkin, S. R.; Anthony, J. E.; Malliaras, G. G. *J. Mater. Chem.* **2009**, *19*, 3049.

(26) Sherman, J. B.; Purushothaman, B.; Parkin, S. R.; Kim, C.; Collins, S.; Anthony, J.; Nguyen, T.-Q.; Chabinyc, M. L. *J. Mater. Chem. A* **2015**, *3*, 9989.

Chapter 2:

(1) Zhou, Y.; Ding, L.; Shi, K.; Dai, Y. Z.; Ai, N.; Wang, J.; Pei, J. *Adv. Mater.* **2012**, *24*, 957.

(2) Zhang, J.; Li, C. Z.; Williams, S. T.; Liu, S.; Zhao, T.; Jen, A. K. *J. Am. Chem. Soc.* **2015**, *137*, 2167.

(3) Kim, Y.; Park, G.; Choi, S.; Lee, D.; Cho, M.; Choi, D. *J. Mater. Chem. C* **2017**, *5*, 7182.

(4) Hwang, Y. J.; Li, H.; Courtright, B. A.; Subramaniyan, S.; Jenekhe, S. A. *Adv. Mater.* **2016**, *28*, 124.

(5) Meng, D.; Sun, D.; Zhong, C.; Liu, T.; Fan, B.; Huo, L.; Li, Y.; Jiang, W.; Choi, H.; Kim, T.; Kim, J. Y.; Sun, Y.; Wang, Z.; Heeger, A. J. *J. Am. Chem. Soc.* **2016**, *138*, 375.

(6) Hendsbee, A. D.; Sun, J. P.; Rutledge, L. R.; Hill, I. G.; Welch, G. C. *J. Mater. Chem. A* **2014**, *2*, 4198.

(7) Jones, B. A.; Ahrens, M. J.; Yoon, M. H.; Facchetti, A.; Marks, T. J.; Wasielewski, M. R. *Angew. Chem., Int. Ed.* **2004**, *43*, 6363.

(8) Chase, D. T.; Fix, A. G.; Rose, B. D.; Weber, C. D.; Nobusue, S.; Stockwell, C. E.; Zakharov, L. N.; Lonergan, M. C.; Haley, M. M. *Angew. Chem. Int. Ed.* **2011**, *50*, 11103.

(9) Li, M. M.; Liu, Y. T.; Ni, W.; Liu, F.; Feng, H. R.; Zhang, Y. M.; Liu, T. T.; Zhang, H. T.; Wan, X. J.; Kan, B.; Zhang, Q.; Russell, T. P.; Chen, Y. S. *J. Mater. Chem. A* **2016**, *4*, 10409.

(10) Rananaware, A.; Gupta, A.; Kadam, G.; Duc La, D.; Bilic, A.; Xiang, W.; Evans, R., A.; Bhosale, S., V. *Mater. Chem. Front.* **2017**, *1*, 2511.

(11) Gupta, A.; Rananaware, A.; Srinivasa Rao, P.; Duc La, D.; Bilic, A.; Xiang, W.; Li, J.; Evans, R., A.; Bhosale, S., V.; Bhosale, S., V. *Mater. Chem. Front.* **2017**, *1*, 1600.

(12) Liu, F.; Zhou, Z.; Zhang, C.; Vergote, T.; Fan, H.; Liu, F.; Zhu, X. *J. Am. Chem. Soc.* **2016**, *138*, 15523.

(13) Li, M.; Liu, Y.; Ni, W.; Liu, F.; Feng, H.; Zhang, Y.; Liu, T.; Zhang, H.; Wan, X.; Kan, B.; Zhang, Q.; Russell, T. P.; Chen, Y. *J. Mater. Chem. A* **2016**, *4*, 10409.

(14) Zhao, W.; Li, S.; Yao, H.; Zhang, S.; Zhang, Y.; Yang, B.; Hou, J. *J. Am. Chem. Soc.* **2017**, *139*, 7148.

(15) Diao, Y.; Shaw, L.; Bao, Z.; Mannsfeld, S. C. B. *Energy Environ. Sci.* **2014**, *7*, 2145.

(16) Eftaiha, A. F.; Sun, J. P.; Hill, I. G.; Welch, G. C. *J. Mater. Chem. A* **2014**, *2*, 1201.

(17) Kondratenko, M.; Moiseev, A. G.; Perepichka, D. F. *J. Mater. Chem.* **2011**, *21*, 1470.

(18) Li, S. X.; Yan, J. L.; Li, C. Z.; Liu, F.; Shi, M. M.; Chen, H. Z.; Russell, T. P. *J. Mater. Chem. A* **2016**, *4*, 3777.

(19) Shen, Z.; Xu, B.; Liu, P.; Hu, Y.; Yu, Y.; Ding, H.; Kloo, L.; Hua, J.; Sun, L.; Tian, H. *J. Mater. Chem. A* **2017**, *5*, 1242.

(20) Jiang, H.; Ferrara, G.; Zhang, X.; Oniwa, K.; Islam, A.; Han, L.; Sun, Y. J.; Bao, M.; Asao, N.; Yamamoto, Y.; Jin, T. *Chemistry* **2015**, *21*, 4065.

(21) Deng, Y.; Xu, B.; Castro, E.; Fernandez-Delgado, O.; Echegoyen, L.; Baldridge, K., K.; Siegel, J., S. *Euro. J. Org. Chem.* **2017**, *2017*, 4338.

(22) Lee, C. H.; Plunkett, K. N. *Org. Lett.* **2013**, *15*, 1202.

(23) Zhu, X. J.; Bheemireddy, S. R.; Sambasivarao, S. V.; Rose, P. W.; Guzman, R. T.; Walther, A. G.; DuBay, K. H.; Plunkett, K. N. *Macromolecules* **2016**, *49*, 127.

(24) Lu, R. Q.; Zheng, Y. Q.; Zhou, Y. N.; Yan, X. Y.; Lei, T.; Shi, K.; Zhou, Y.; Pei, J.; Zoppi, L.; Baldridge, K. K.; Siegel, J. S.; Cao, X. Y. *J. Mater. Chem. A* **2014**, *2*, 20515.

(25) Chen, H.-Y.; Golder, J.; Yeh, S.-C.; Lin, C.-W.; Chen, C.-T.; Chen, C.-T. *RSC Advances* **2015**, *5*, 3381.

(26) Gu, X.; Luhman, W. A.; Yagodkin, E.; Holmes, R. J.; Douglas, C. J. *Org. Lett.* **2012**, *14*, 1390.

(27) Zhai, L.; Shukla, R.; Rathore, R. *Org. Lett.* **2009**, *11*, 3474.

(28) Zhai, L.; Shukla, R.; Wadumethrige, S. H.; Rathore, R. *J. Org. Chem.* **2010**, *75*, 4748.

(29) Grzybowski, M.; Skonieczny, K.; Butenschon, H.; Gryko, D. T. *Angew. Chem. Int. Ed. Engl.* **2013**, *52*, 9900.

(30) Rempala, P.; Kroulik, J.; King, B. T. *J. Am. Chem. Soc.* **2004**, *126*, 15002.

(31) Smet, M.; Van Dijk, J.; Dehaen, W. *Syn. Lett.* **1999**, *4*, 495.

(32) Eversloh, C., L. ; Avlasevich, Y.; Li, C.; Mullen, K. *Chemistry* **2011**, *17*, 12756.

(33) Lakshminarayana, A., N.; Chang, J.; Luo, J.; Zheng, B.; Huang, K. W.; Chi, C. *Chem. Commun.* **2015**, *51*, 3604.

(34) Wu, J.; Pisula, W.; Mullen, K. *Chem. Rev.* **2007**, *107*, 718.

(35) Buchholtz, F.; Zelichenok, A.; Krongauz, V. *Macromolecules* **1993**, *26*, 906.

(36) It must be noted, to remove all the inorganic tin from the product the reaction has to be made basic, filtered over diatomaceous earth and further purified via recrystallization from hot chloroform with methonal

(37) Miao, Q.; Chi, X.; Xiao, S.; Zeis, R.; Lefenfeld, M.; Siegrist, T.; Steigerwald, M. L.; Nuckolls, C. *J. Am. Chem. Soc.* **2006**, *128*, 1340.

(38) Purvis, L. J.; Gu, X.; Ghosh, S.; Zhang, Z.; Cramer, C. J.; Douglas, C. J. *J. Org. Chem.* **2018**, *83*, 1828.

(39) Yagodkin, E.; Douglas, C. J. *Tet. Lett.* **2010**, *51*, 3037.

(40) O'Brien, C. J.; Kantchev, E. A.; Valente, C.; Hadei, N.; Chass, G. A.; Lough, A.; Hopkinson, A. C.; Organ, M. G. *Chem. Eur. J.* **2006**, *12*, 4743.

(41) Compounds **2.4d-e** were chraterized by ^{1}H, ^{13}C, ^{19}F NMR and IR. HRMS was done via QTOF and ESI. Single-crystal X-ray structures were obtain for compounds 2.4d-e, f.

(42) Dexter, D., L., *J. Chem. Phys.* **1953**, *21*, 836.

(43) CIFs found in the supporting information of JOC paper.

(44) The degree of indenotetracene core overlap and pi-stacking distance were measured form the solved crystal structures.

(45) Coropceanu, V.; Cornil, J.; da Silva Filho, D. A.; Olivier, Y.; Silbey, R.; Bredas, J. L. *Chem. Rev.* **2007**, *107*, 926.

(46) Sonar, P.; Williams, E. L.; Singh, S. P.; Manzhos, S.; Dodabalapur, A. *Phys. Chem. Chem. Phys.* **2013**, *15*, 17064.

(47) Lan, L. Y.; Chen, Z. M.; Ying, L.; Huang, F.; Cao, Y. *Org. Elect.* **2016**, *30*, 176.

(48) Valenti, G.; Bruno, C.; Rapino, S.; Fiorani, A.; Jackson, E. A.; Scott, L. T.; Paolucci, F.; Marcaccio, M. *J. Phys. Chem. C* **2010**, *114*, 19467.

(49) Zhu, X. J.; Yuan, B. X.; Plunkett, K. N. *Tet. Lett.* **2015**, *56*, 7105.

(50) Bheemireddy, S. R.; Ubaldo, P. C.; Rose, P. W.; Finke, A. D.; Zhuang, J.; Wang, L.; Plunkett, K. N. *Angew. Chem. Int. Ed.* **2015**, *54*, 15762.

(51) Zhou, K.; Dong, H.; Zhang, H. L.; Hu, W. *Phys. Chem. Chem. Phys.* **2014**, *16*, 22448.

(52) Li, H. Y.; Earmme, T.; Subramaniyan, S.; Jenekhe, S. A. *Adv. Eng. Mater.* **2015**, *5*, 1402041.

(53) Zhou, F.; Jehoulet, C.; Bard, A. J. *J. Am. Chem. Soc.* **1992**, *114*, 11004.

(54) Kulshreshtha, C.; Kim, W., G.; Lampande, R.; Huh, H., D.; Chae, M.; Kwon, H., J. *J. Mater. Chemi. A* **2013**, *1*, 4077.

(55) Zhao, Y.; Truhlar, D. *Theor. Chem. Account.* **2007**, *120*, 215.

(56) Kwon, O. K.; Park, J. H.; Kim, D. W.; Park, S. K.; Park, S. Y. *Adv. Mater.* **2015**, *27*, 1951.

(57) Shi, X.; Liu, S.; Liu, C.; Hu, Y.; Shi, S.; Fu, N.; Zhao, B.; Wang, Z.; Huang, W. *Chem. Asian J.* **2016**, *11*, 2188.

(58) Lu, X.; Fan, S.; Wu, J.; Jia, X.; Wang, Z. S.; Zhou, G. *J. Org. Chem.* **2014**, *79*, 6480.

(59) Frischmann, P. D.; Mahata, K.; Wurthner, F. *Chem. Soc. Rev.* **2013**, *42*, 1847.

(60) Huss, A. S.; Pappenfus, T.; Bohnsack, J.; Burand, M.; Mann, K. R.; Blank, D. A. *J. Phys. Chem. A* **2009**, *113*, 10202.

(61) Li, C.; Liu, M.; Pschirer, N. G.; Baumgarten, M.; Mullen, K. *Chem. Rev.* **2010**, *110*, 6817.

(62) Vura-Weis, J.; Ratner, M. A.; Wasielewski, M. R. *J. Am. Chem. Soc.* **2010**, *132*, 1738.

(63) Ide, J.; Mereau, R.; Ducasse, L.; Castet, F.; Olivier, Y.; Martinelli, N.; Cornil, J.; Beljonne, D. *J. Phys. Chem. B* **2011**, *115*, 5593.

(64) Adamo, C.; Barone, V. *J. Chem. Phy.* **1999**, *110*, 6158.

(65) Arbeloa, F. L.; Ojeda, R. P.; Arbeloa, L. I. *J. Lumin.* **1989**, *44*, 105—112.

(66) Grabolle, M.; Spieles, M.; Lesnyak, V.; Gaponik, N.; Eychmuller, A.; Resch-Genger, U. *Anal. Chem.* **2009**, *81*, 6285.

Chapter 3:

(1) Liao, H.-C.; Ho, C.-C.; Chang, C.-Y.; Jao, M.-H.; Darling, S. B.; Su, W.-F. *Mater. Tod.* **2013**, *16*, 326.

(2) Diao, Y.; Shaw, L.; Bao, Z.; Mannsfeld, S. C. B. *Energy Environ. Sci.* **2014**, *7*, 2145.

(3) Yuan, D.; Huang, D.; Zhang, C.; Zou, Y.; Di, C. A.; Zhu, X.; Zhu, D. *ACS Appl. Mater. Interfaces* **2017**, *9*, 28795.

(4) Zhou, N.; Vegiraju, S.; Yu, X.; Manley, E. F.; Butler, M. R.; Leonardi, M. J.; Guo, P.; Zhao, W.; Hu, Y.; Prabakaran, K.; Chang, R. P. H.; Ratner, M. A.; Chen, L. X.; Facchetti, A.; Chen, M.-C.; Marks, T. J. *J. Mater. Chem. C* **2015**, *3*, 8932.

(5) James, D. T.; Kjellander, B. K.; Smaal, W. T.; Gelinck, G. H.; Combe, C.; McCulloch, I.; Wilson, R.; Burroughes, J. H.; Bradley, D. D.; Kim, J. S. *ACS Nano* **2011**, *5*, 9824.

(6) Park, S. K.; Jackson, T. N.; Anthony, J. E.; Mourey, D. A. *Appl. Phys. Lett.* **2007**, *91*, 063514.

(7) Wasikiewicz, J. M.; Abu-Sen, L.; Horn, A. B.; Koelewijn, J., M.; Parry, A., V. S.; Morrison, J. J.; Yeates, S. G. *J. Mater. Chem. C* **2016**, *4*, 7309.

(8) Dou, J. H.; Zheng, Y. Q.; Yao, Z. F.; Yu, Z. A.; Lei, T.; Shen, X.; Luo, X. Y.; Sun, J.; Zhang, S. D.; Ding, Y. F.; Han, G.; Yi, Y.; Wang, J. Y.; Pei, J. *J. Am. Chem. Soc.* **2015**, *137*, 15947.

(9) McGarry, K. A.; Xie, W.; Sutton, C.; Risko, C.; Wu, Y.; Young, V. G.; Brédas, J.-L.; Frisbie, C. D.; Douglas, C. J. *Chem. Mater.* **2013**, *25*, 2254.

(10) Ogden, W. A.; Ghosh, S.; Bruzek, M. J.; McGarry, K. A.; Balhorn, L.; Young, V.; Purvis, L. J.; Wegwerth, S. E.; Zhang, Z.; Serratore, N. A.; Cramer, C. J.; Gagliardi, L.; Douglas, C. J. *Cryst. Growth Des.* **2017**, *17*, 643.

(11) Yadav, H. R.; Choudhury, A. R. *J. Molec. Struc.* **2017**, *1150*, 469.

(12) Osuna, R. M.; Hernández, V.; Navarrete, J. T. L.; D'Oria, E.; Novoa, J. J. *Theor. Chem. Acc.* **2010**, *128*, 541.

(13) Panini, P.; Chopra, D. *Cryst. Eng. Comm* **2013**, *15*, 3711.

(14) Jiang, H.; Ye, J.; Hu, P.; Wei, F.; Du, K.; Wang, N.; Ba, T.; Feng, S.; Kloc, C. *Sci. Rep.* **2014**, *4*, 7573.

(15) Rivnay, J.; Jimison, L. H.; Northrup, J. E.; Toney, M. F.; Noriega, R.; Lu, S.; Marks, T. J.; Facchetti, A.; Salleo, A. *Nat. Mater.* **2009**, *8*, 952.

(16) Marks, M.; Schmidt, C.; Schwalb, C. H.; Breuer, T.; Witte, G.; Höfer, U. *J. Phys. Chem. C* **2012**, *116*, 1904.

(17) Parkhomenko, R. G.; Sukhikh, A. S.; Klyamer, D. D.; Krasnov, P. O.; Gromilov, S.; Kadem, B.; Hassan, A. K.; Basova, T. V. *J. Phys. Chem. C* **2017**, *121*, 1200.

(18) Breuer, T., Witte, G., *Phys. Rev. B* **2011**, *83*, 155428.

(19) Wong, S. L.; Huang, H.; Huang, Y. L.; Wang, Y. Z.; Gao, X. Y.; Suzuki, T.; Chen, W.; Wee, A. T. S. *J. Phys. Chem. C* **2010**, *114*, 9356.

(20) Breuer, T.; Klues, M.; Liesfeld, P.; Viertel, A.; Conrad, M.; Hecht, S.; Witte, G. *Phys. Chem. Chem. Phys.* **2016**, *18*, 33344.

(21) Klues, M.; Jerabek, P.; Breuer, T.; Oehzelt, M.; Hermann, K.; Berger, R.; Witte, G. *J. Phys. Chem. C* **2016**, *120*, 12693.

(22) Kim, C. H.; Hlaing, H.; Payne, M. M.; Parkin, S. R.; Anthony, J. E.; Kymissis, I. *Chem. phys. chem.* **2015**, *16*, 1251.

(23) Sherman, J. B.; Moncino, K.; Baruah, T.; Wu, G.; Parkin, S. R.; Purushothaman, B.; Zope, R.; Anthony, J.; Chabinyc, M. L. *J. Phys. Chem. C* **2015**, *119*, 20823.

(24) Kline, R. J.; Hudson, S. D.; Zhang, X.; Gundlach, D. J.; Moad, A. J.; Jurchescu, O. D.; Jackson, T. N.; Subramanian, S.; Anthony, J. E.; Toney, M. F.; Richter, L. J. *Chem. Mater.* **2011**, *23*, 1194.

(25) Birkholz, M. *Thin Film Analysis by X-ray Scattering*; Wiley-VCH: Weinheim, 2006.

(26) Smilgies, D.-M. *Rev. Sci. Instrum.* **2002**, *73*, 1706.

(27) Baker, J. L.; Jimison, L. H.; Mannsfeld, S.; Volkman, S.; Yin, S.; Subramanian, V.; Salleo, A.; Alivisatos, A. P.; Toney, M. F. *Langmuir* **2010**, *26*, 9146.

(28) Oosterhout, S. D.; Savikhin, V.; Zhang, J.; Zhang, Y.; Burgers, M. A.; Marder, S. R.; Bazan, G. C.; Toney, M. F. *Chem. Mater.* **2017**, *29*, 3062.

(29) Rivnay, J.; Mannsfeld, S. C.; Miller, C. E.; Salleo, A.; Toney, M. F. *Chem. Rev.* **2012**, *112*, 5488.

(30) Stöhr, J. *NEXAFS Spectroscopy*; Springer-Verlag: New York, 1992.

(31) Stöhr, J.; Baberschke, K.; Jaeger, R.; Treichler, R.; Brennan, S. *Phys. Rev. Lett.* **1981**, *47*, 381.

(32) Dobler, C.; Tönshoff, C.; Bettinger, H. F.; Chassé, T.; Casu, M. B. *J. Phys. Chem. C* **2017**, *121*, 13660.

(33) McNeill, C. R.; Watts, B.; Swaraj, S.; Ade, H.; Thomsen, L.; Belcher, W.; Dastoor, P. C. *Nanotechnology* **2008**, *19*, 424015.

(34) Massa, W. *Crystal Structure Determination*; Springer: New York, 2004.

(35) Witte, G.; Wöll, C. *Phys. Status Solidi A* **2008**, *205*, 497.

(36) Dickey, K. C.; Anthony, J. E.; Loo, Y. L. *Adv. Mater.* **2006**, *18*, 1721.

(37) Hu, S.; Dyck, O.; Chen, H.; Hsiao, Y.-c.; Hu, B.; Duscher, G.; Dadmun, M.; Khomami, B. *RSC Adv.* **2014**, *4*, 27931.

(38) Ilavsky, J. *J. Appl. Crystallogr.* **2012**, *45*, 324.

(39) Breiby, D. W.; Bunk, O.; Andreasen, J. W.; Lemke, H. T.; Nielsen, M. M. *J. Appl. Crystallogr.* **2008**, *41*, 262.

(40) Macrae, C. F.; Bruno, I. J.; Chisholm, J. A.; Edgington, P. R.; McCabe, P.; Pidcock, E.; Rodriguez-Monge, L.; Taylor, R.; van de Streek, J.; Wood, P. A. *J. Appl. Crystallogr.* **2008**, *41*, 466.

(41) Ravel, B.; Newville, M. *J. Synch. Radiat.* **2005**, *12*, 537.

Chapter 4:

(1) Kang, I.; Yun, H. J.; Chung, D. S.; Kwon, S. K.; Kim, Y. H. *J. Am. Chem. Soc.* **2013**, *135*, 14896.

(2) Yassar, A. *Polym. Sci. Series C* **2014**, *56*, 4.

(3) Forrest, S. R. *Nature* **2004**, *428*, 911.

(4) Bao, Z.; Valente, C. *Organic Field-effect Transistors*; CRC Press: Boca Raton, 2007.

(5) West, R. A. *Basic Solid State Chemistry*; 2nd ed.; John Wiley & Sons: West Sussex, 1999.

(6) Coropceanu, V.; Cornil, J.; da Silva Filho, D. A.; Olivier, Y.; Silbey, R.; Bredas, J. L. *Chem. Rev.* **2007**, *107*, 926.

(7) Xie, W.; Prabhumirashi, P. L.; Nakayama, Y.; McGarry, K. A.; Geier, M. L.; Uragami, Y.; Mase, K.; Douglas, C. J.; Ishii, H.; Hersam, M. C.; Frisbie, C. D. *ACS Nano* **2013**, *7*, 10245.

(8) Mullenbach, T. K.; McGarry, K. A.; Luhman, W. A.; Douglas, C. J.; Holmes, R. J. *Adv. Mater.* **2013**, *25*, 3689.

(9) Podzorov, V.; Menard, E.; Borissov, A.; Kiryukhin, V.; Rogers, J. A.; Gershenson, M. E. *Phys. Rev. Lett.* **2004**, *93*, 086602.

(10) Mamada, M.; Katagiri, H.; Sakanoue, T.; Tokito, S. *Cryst. Growth Des.* **2014**, *15*, 442.

(11) Zhang, Z.; Ogden, W. A.; Young, V. G.; Douglas, C. J. *Chem. Commun. (Camb)* **2016**, *52*, 8127.

(12) McGarry, K. A.; Xie, W.; Sutton, C.; Risko, C.; Wu, Y.; Young, V. G.; Brédas, J.-L.; Frisbie, C. D.; Douglas, C. J. *Chem. Mater.* **2013**, *25*, 2254.

(13) Huang, L.; Liao, Q.; Shi, Q.; Fu, H.; Ma, J.; Yao, J. *J. Mater. Chem.* **2010**, *20*, 159.

(14) Desiraju, G. R. *J. Am. Chem. Soc.* **2013**, *135*, 9952.

(15) Anthony, J. E. *Chem Rev* **2006**, *106*, 5028.

(16) Anthony, J. E.; Brooks, J. S.; Eaton, D. L.; Parkin, S. R. *J. Am. Chem. Soc.* **2001**, *123*, 9482.

(17) Ryno, S. M.; Risko, C.; Bredas, J. L. *J. Am. Chem. Soc.* **2014**, *136*, 6421.

(18) Tang, M. L.; Reichardt, A. D.; Wei, P.; Bao, Z. *J. Am. Chem. Soc.* **2009**, *131*, 5264.

(19) Anthony, J. E.; Facchetti, A.; Heeney, M.; Marder, S. R.; Zhan, X. *Adv Mater* **2010**, *22*, 3876.

(20) Sherman, J. B.; Moncino, K.; Baruah, T.; Wu, G.; Parkin, S. R.; Purushothaman, B.; Zope, R.; Anthony, J.; Chabinyc, M. L. *J. Phys. Chem. C* **2015**, *119*, 20823.

(21) Black, H. T.; Perepichka, D. F. *Angew Chem Int Ed Engl* **2014**, *53*, 2138.
(22) Schwarzer, A.; Weber, E. *Cryst. Growth Des.* **2008**, *8*, 2862.
(23) Rybalova, T. V.; Bagryanskaya, I. Y. *J. Struct. Chem.* **2009**, *50*, 741.
(24) Chopra, D.; Row, T. N. G. *Cryst. Eng. Comm.* **2011**, *13*, 2175.
(25) Dou, J. H.; Zheng, Y. Q.; Yao, Z. F.; Yu, Z. A.; Lei, T.; Shen, X.; Luo, X. Y.; Sun, J.; Zhang, S. D.; Ding, Y. F.; Han, G.; Yi, Y.; Wang, J. Y.; Pei, J. *J. Am. Chem. Soc.* **2015**, *137*, 15947.
(26) Sakamoto, Y.; Suzuki, T.; Kobayashi, M.; Gao, Y.; Fukai, Y.; Inoue, Y.; Sato, F.; Tokito, S. *J. Am. Chem. Soc.* **2004**, *126*, 8138.
(27) Chopra, D. *Cryst. Growth Des.* **2012**, *12*, 541.
(28) Taylor, R. *Cryst. Growth Des.* **2016**, *16*, 4165.
(29) Taylor, R. *Cryst. Eng. Comm.* **2014**, *16*, 6852.
(30) Hunter, C. A. *Angew. Chem., Int. Ed.* **1993**, *32*, 1584.
(31) Cozzi, F.; Siegel, J. S. *Pure Appl. Chem.* **1995**, *67*, 683.
(32) Cozzi, F.; Ponzini, F.; Annunziata, R.; Cinquini, M.; Siegel, J. S. *Ang. Chem. Int.* **1995**, *34*, 1019.
(33) Sutton, C.; Marshall, M. S.; Sherrill, C. D.; Risko, C.; Bredas, J. L. *J. Am. Chem. Soc.* **2015**, *137*, 8775.
(34) Biehl, R.; Dinse, K.-P.; Mobius, K.; Plato, M.; Kurreck , H.; Mennenga, U. *Tetrahedron Lett.* **1793**, *29*, 363.
(35) Dodge, J. A.; Bain, J. D.; Chamberlin, A. R. *J. Org. Chem.* **1990**, *55*, 4190.
(36) Yagodkin, E.; McGarry, K. A.; Douglas, C. J. *Org. Prep. Proced. Int.* **2011**, *43*, 360.
(37) da Silva Filho, D. A.; Kim, E. G.; Brédas, J. L. *Adv. Mater.* **2005**, *17*, 1072.
(38) Huang, H.; Chen, Z.; Ponce Ortiz, R.; Newman, C.; Usta, H.; Lou, S.; Youn, J.; Noh, Y. Y.; Baeg, K. J.; Chen, L. X.; Facchetti, A.; Marks, T. J. *J. Am. Chem. Soc.* **2012**, *134*, 10966.
(39) Zhang, C.; Zang, Y.; Gann, E.; McNeill, C. R.; Zhu, X.; Di, C. A.; Zhu, D. *J. Am. Chem. Soc.* **2014**, *136*, 16176.
(40) Jackson, N. E.; Kohlstedt, K. L.; Savoie, B. M.; Olvera de la Cruz, M.; Schatz, G. C.; Chen, L. X.; Ratner, M. A. *J. Am. Chem. Soc.* **2015**, *137*, 6254.
(41) Ogden, W. A.; Ghosh, S.; Bruzek, M. J.; McGarry, K. A.; Balhorn, L.; Young, V.; Purvis, L. J.; Wegwerth, S. E.; Zhang, Z.; Serratore, N. A.; Cramer, C. J.; Gagliardi, L.; Douglas, C. J. *Cryst. Growth Des.* **2017**, *17*, 643.
(42) Seebach, D. *Angew. Chem., Int. Ed. Eng.* **1990**, *29*, 1320.
(43) To solve the crystal structure of 4.1k, both the CH_3 and CF_3 groups are to be refined in all meta positions with 50% occupancy at each side.
(44) Hunter, C. A.; Sanders, J. K. M. *J. Am. Chem. Soc.* **1990**, *112*, 5525.
(45) Takahashi, O.; Kohno, Y.; Nishio, M. *Chem. Rev.* **2010**, *110*, 6049.
(46) Nishio, M.; Umezawa, Y.; Honda, K.; Tsuboyama, S.; Suezawa, H. *Cryst. Eng. Comm.* **2009**, *11*, 1757.
(47) Kupcewicz, B.; Małecka, M. *Cryst. Growth Des.* **2015**, *15*, 3893.
(48) Rowland, R. S.; Taylor, R. *J. Phys. Chem.* **1996**, *100*.

(49) complete list of all intermolecular interactions for all rubrene derivatives can be found in the Supporting Information of the crystal growth and Design manusript Tables S4-S18 of paper

(50) Uttiya, S.; Miozzo, L.; Fumagalli, E. M.; Bergantin, S.; Ruffo, R.; Parravicini, M.; Papagni, A.; Moret, M.; Sassella, A. *J. Mater. Chem. C* **2014**, *2*, 4147.

(51) Atom numbering is based on the individual cif files

(52) Atom numbering is based on the individual cif files

(53) Atom numbering is based on the individual cif files

(54) Atom numbering is based on the individual cif files

(55) Atom numbering is based on the individual cif files

(56) Atom numbering is based on the individual cif files

(57) Atom numbering is based on the individual cif files

(58) Kirsch, P.; Tong, Q.; Untenecker, H. *Beil. J. Org. Chem.* **2013**, *9*, 2367.

(59) Wade, J.; Steiner, F.; Niedzialek, D.; James, D. T.; Jung, Y.; Yun, D.-J.; Bradley, D. D. C.; Nelson, J.; Kim, J.-S. *J. Mater. Chem. C* **2014**, *2*, 10110.

(60) Choudhury, A. R.; Guru Row, T. N. *Cryst. Growth Des.* **2004**, *4*, 47.

(61) Reichenbacher, K.; Suss, H. I.; Hulliger, J. *Chem. Soc. Rev.* **2005**, *34*, 22.

(62) Capozzi, M. A. M.; Capitelli, F.; Cardellicchio, C. *Cryst. Growth Des.* **2014**, *14*, 5442.

(63) Soman, R.; Sujatha, S.; Arunkumar, C. *J. Fluorine Chem.* **2014**, *163*, 16.

(64) Bergantin, S.; Moret, M. *Cryst. Growth Des.* **2012**, *12*, 6035.

Chapter 5:

(1) National Institute of Standards and Technology

(2) Anslyn, V. E.; Dougherty, A. D. *Modern Physical Organic Chemistry*; University Science Books: Sausalito, 2006.

(3) Liang, Z.; Tang, Q.; Mao, R.; Liu, D.; Xu, J.; Miao, Q. *Adv. Mater.* **2011**, *23*, 5514.

(4) Tang, X.-D.; Liao, Y.; Geng, H.; Shuai, Z.-G. *J. Mater. Chem.* **2012**, *22*, 18181.

(5) Ogden, W. A.; Ghosh, S.; Bruzek, M. J.; McGarry, K. A.; Balhorn, L.; Young, V.; Purvis, L. J.; Wegwerth, S. E.; Zhang, Z.; Serratore, N. A.; Cramer, C. J.; Gagliardi, L.; Douglas, C. J. *Cryst. Growth Des.* **2017**, *17*, 643.

(6) McGarry, K. A.; Xie, W.; Sutton, C.; Risko, C.; Wu, Y.; Young, V. G.; Brédas, J.-L.; Frisbie, C. D.; Douglas, C. J. *Chem. Mater.* **2013**, *25*, 2254.

(7) Barczyński, P.; Szafran, M.; Ratajczak-Sitarz, M.; Nowaczyk, Ł.; Dega-Szafran, Z.; Katrusiak, A. *J. Mol. Struct.* **2012**, *1018*, 21.

Chapter 6:

(1) “International Energy Outlook,” United Stated Energy Infromation Administration, **2016**.

(2) Chapin, D. M.; Fuller, C. S.; Pearson, G. L. *J. Appl. Phys.* **1954**, *25*, 676.

(3) Research-cell-efficiency-records, Ed. National Renewable Energy Laboratory - National Center for Photovoltaics.

(4) Fu, R.; Feldman, D.; Margolis, R.; Woodhouse, M.; Ardani, K. “U.S. Solar Photovoltaic System Cost Benchmark,” National Renewable Energy Laboratory, 2017.

(5) “BASIC RESEARCH NEEDS FOR SOLAR ENERGY UTILIZATION,” **2005**.

(6) *Organic Solar Cells: Fundamentals, Devices, and Upscaling.*; CRC Press: Boca Raton, Fl, **2014**.

(7) Kazmerski, L. L. *J. Elect. Spect. Rel. Phenom.* **2006**, *150*, 105.

(8) Sun, S.-S. *Mater. Sci. Eng., B* **2005**, *116*, 251.

(9) Forrest, S. R. *Nature* **2004**, *428*, 911.

(10) Riede, M.; Mueller, T.; Tress, W.; Schueppel, R.; Leo, K. *Nanotechnology* **2008**, *19*, 424001.

(11) Yassar, A. *Polym. Sci. Series C* **2014**, *56*, 4.

(12) Mihailetchi, V. D.; Wildeman, J.; Blom, P. W. *Phys. Rev. Lett.* **2005**, *94*, 126602.

(13) Eftaiha, A. F.; Sun, J. P.; Hill, I. G.; Welch, G. C. *J. Mater. Chem. A* **2014**, *2*, 1201.

(14) Purvis, L. J.; Gu, X.; Ghosh, S.; Zhang, Z.; Cramer, C. J.; Douglas, C. J. *J. Org. Chem.* **2018**, *83*, 1828.

(15) Peumans, P.; Yakimov, A.; Forrest, S. R. *J. Appl. Phys.* **2003**, *93*, 3693.

(16) Hsiao, Y. S.; Whang, W. T.; Suen, S. C.; Shiu, J. Y.; Chen, C. P. *Nanotechnology* **2008**, *19*, 415603.

(17) Sonar, P.; Fong Lim, J. P.; Chan, K. L. *Energy Environ. Sci.* **2011**, *4*, 1558.

(18) Savva, A.; Burgues-Ceballos, I.; Papazoglou, G.; Choulis, S. A. *ACS Appl. Mater. Interfaces* **2015**, *7*, 24608.

(19) Alaman, J.; Alicante, R.; Pena, J. I.; Sanchez-Somolinos, C. *Materials* **2016**, *9*, 910.

(20) Zhou, Y.; Gu, K. L.; Gu, X.; Kurosawa, T.; Yan, H.; Guo, Y.; Koleilat, G. I.; Zhao, D.; Toney, M. F.; Bao, Z. *Chem. Mater.* **2016**, *28*, 5037.

(21) Li, X.; Liu, X.; Sun, P.; Feng, Y.; Shan, H.; Wu, X.; Xu, J.; Huang, C.; Chen, Z.-K.; Xu, Z.-X. *RSC Adv.* **2017**, *7*, 17076.

(22) Muhammad, F. F.; Sulaiman, K. *Thin Solid Films* **2011**, *519*, 5230.

(23) Chen, G.; Sasabe, H.; Wang, Z.; Wang, X. F.; Hong, Z.; Yang, Y.; Kido, J. *Adv Mater* **2012**, *24*, 2768.

(24) Zhang, J.; Singh, S.; Hwang, D. K.; Barlow, S.; Kippelen, B.; Marder, S. R. *J. Mater. Chem. C* **2013**, *1*, 5093.

(25) Birkholz, M. *Thin Film Analysis by X-ray Scattering*; Wiley-VCH: Weinheim, 2006.

Appendix:

6-chloro-5,12-diphenyl-5,12-dihydrotetracene-5,12-diol (2.7a):

^{1}H NMR Spectrum

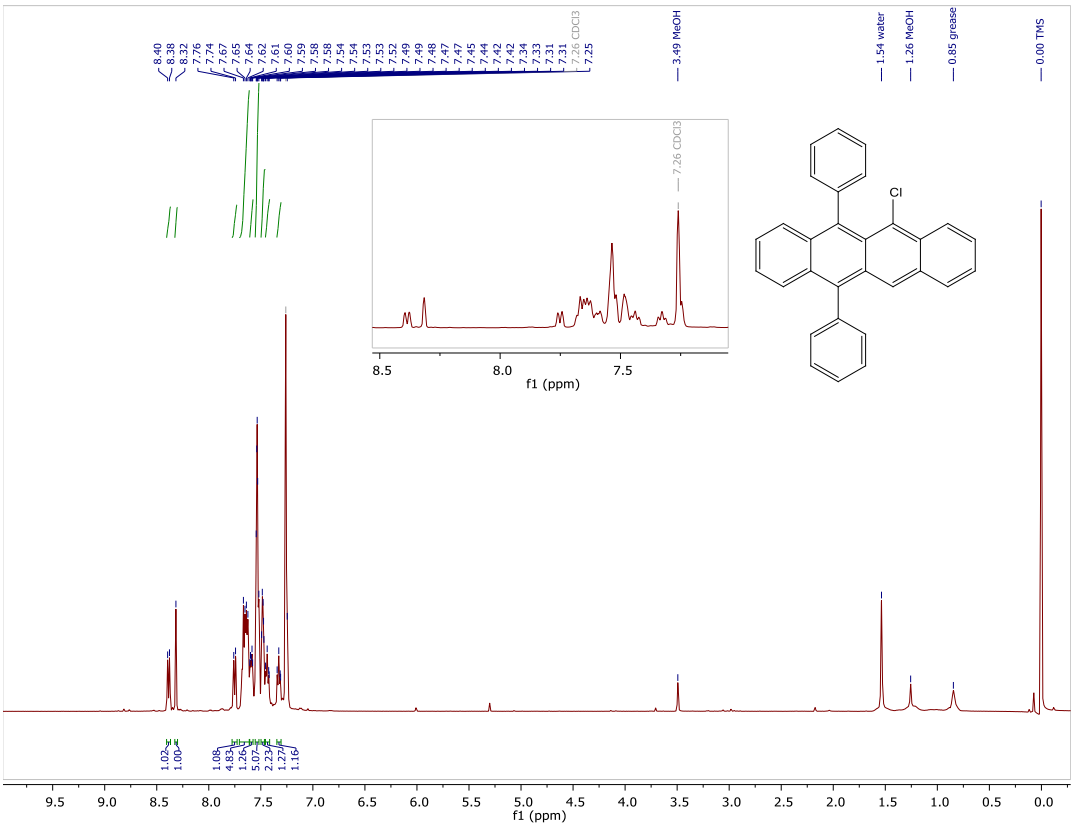

9-chloro-10-phenylindeno[1,2,3-*fg*]tetracene (2.5a):

^{1}H NMR Spectrum

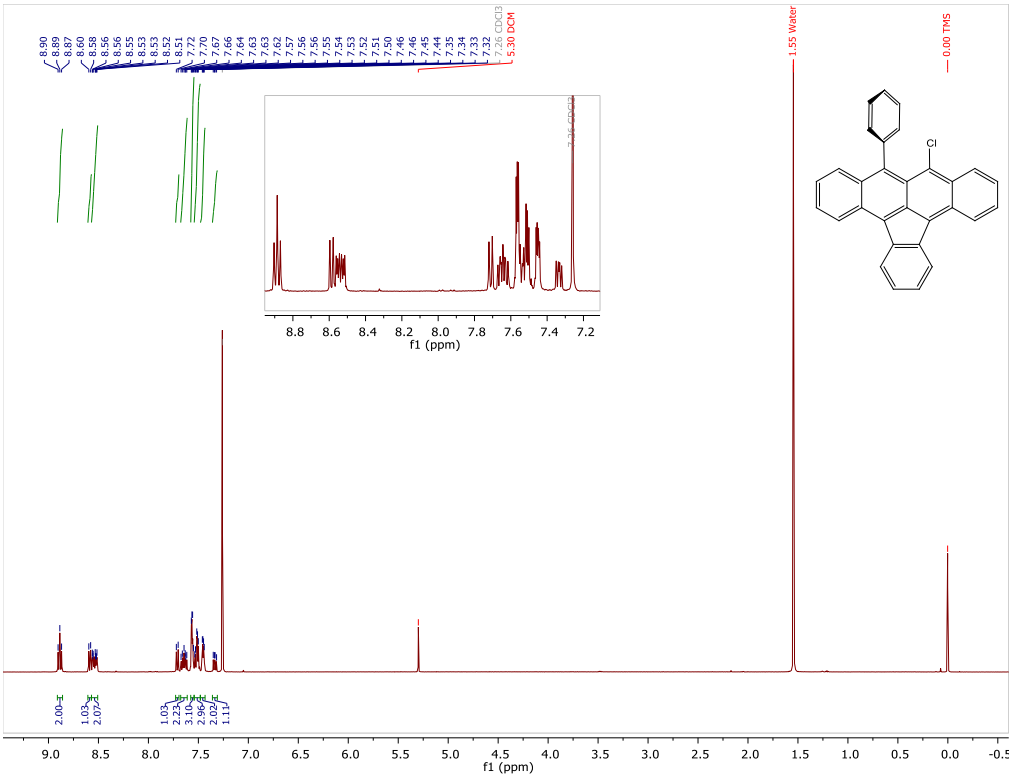

9,10-diphenylindeno[1,2,3-*fg*]tetracene (2.4a)

^{1}H NMR Spectrum

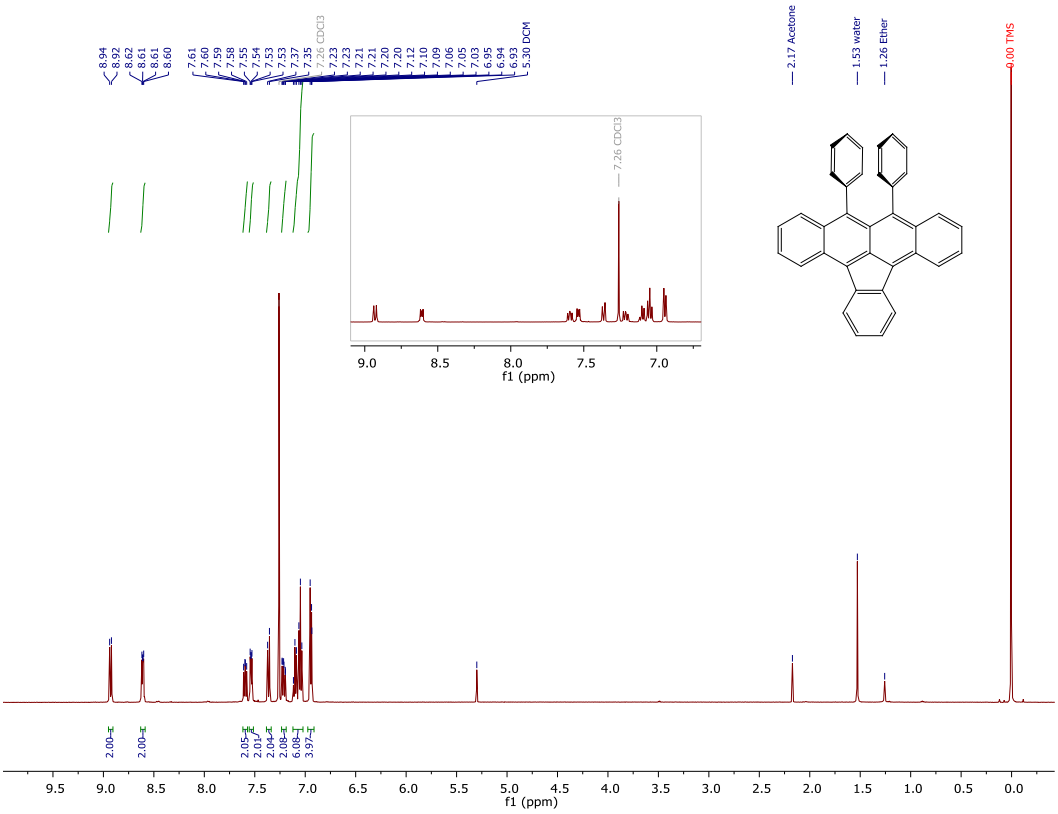

5-chloro-6,11-di-p-tolyltetracene (2.7b)

^{1}H NMR Spectrum

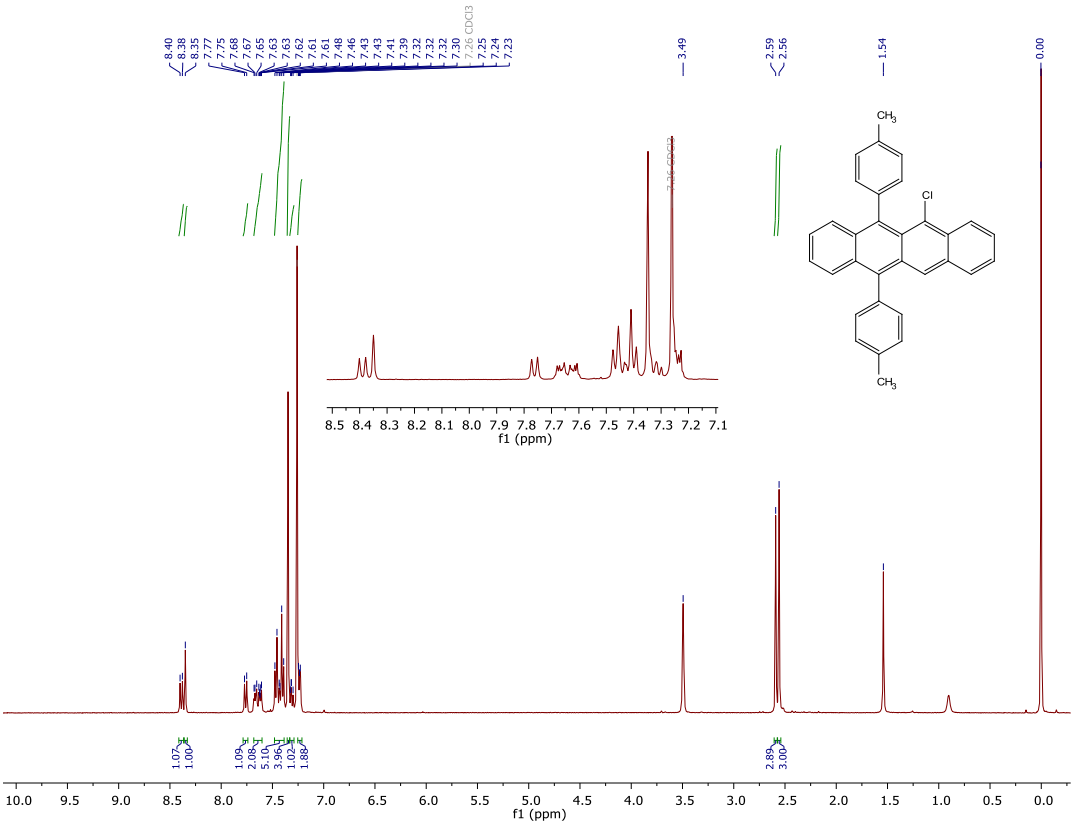

10-chloro-2-methyl-9-(p-tolyl)indeno[1,2,3-*fg*]tetracene (2.5b)

^{1}H NMR Spectrum

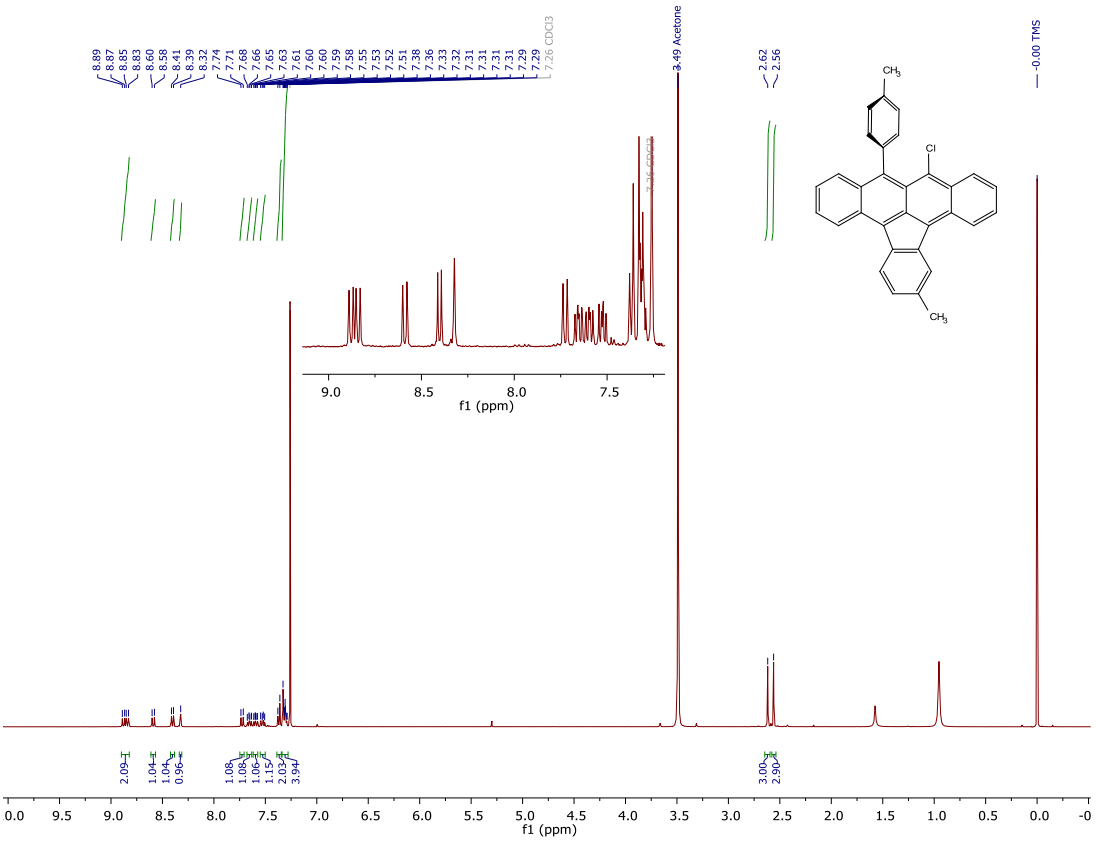

2-methyl-10-phenyl-9-(*p*-tolyl)indeno[1,2,3-*fg*]tetracene (2.4b)

^{1}H NMR Spectrum

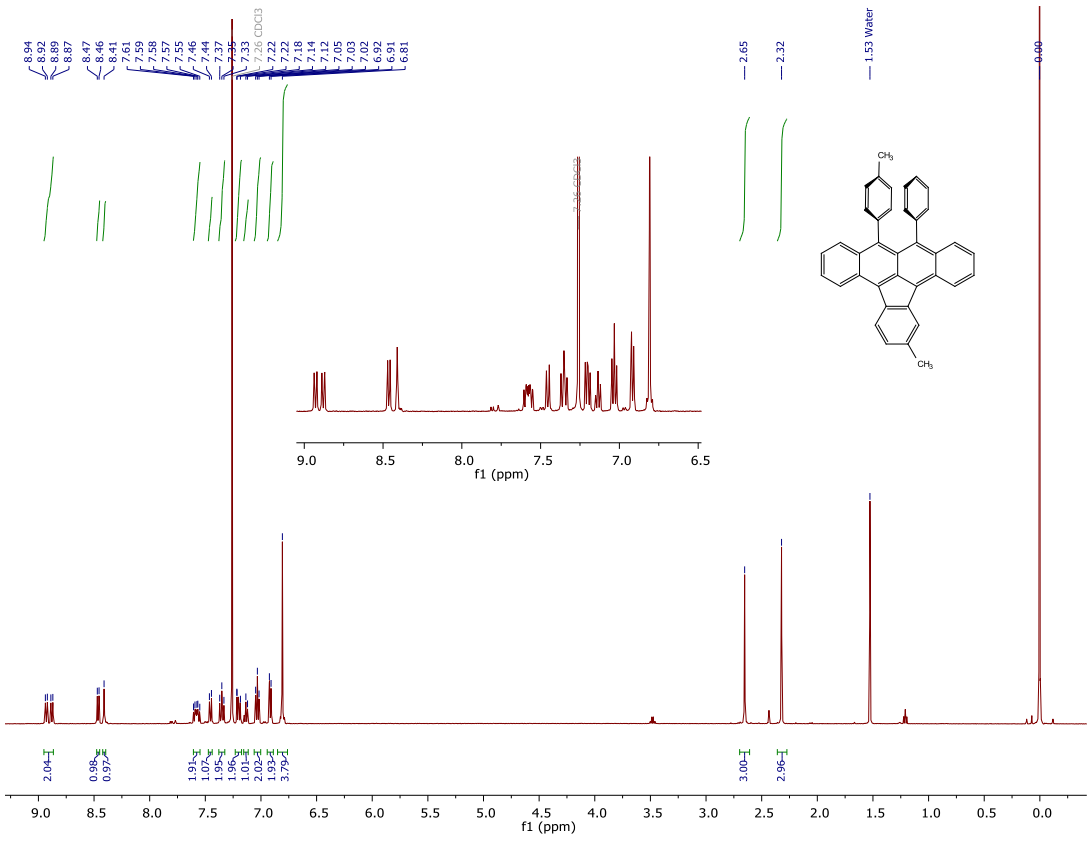

6,11-bis(3,4,5-trimethylphenyl)tetracene-5,12-dione (**4.4**):

^{1}H NMR Spectrum

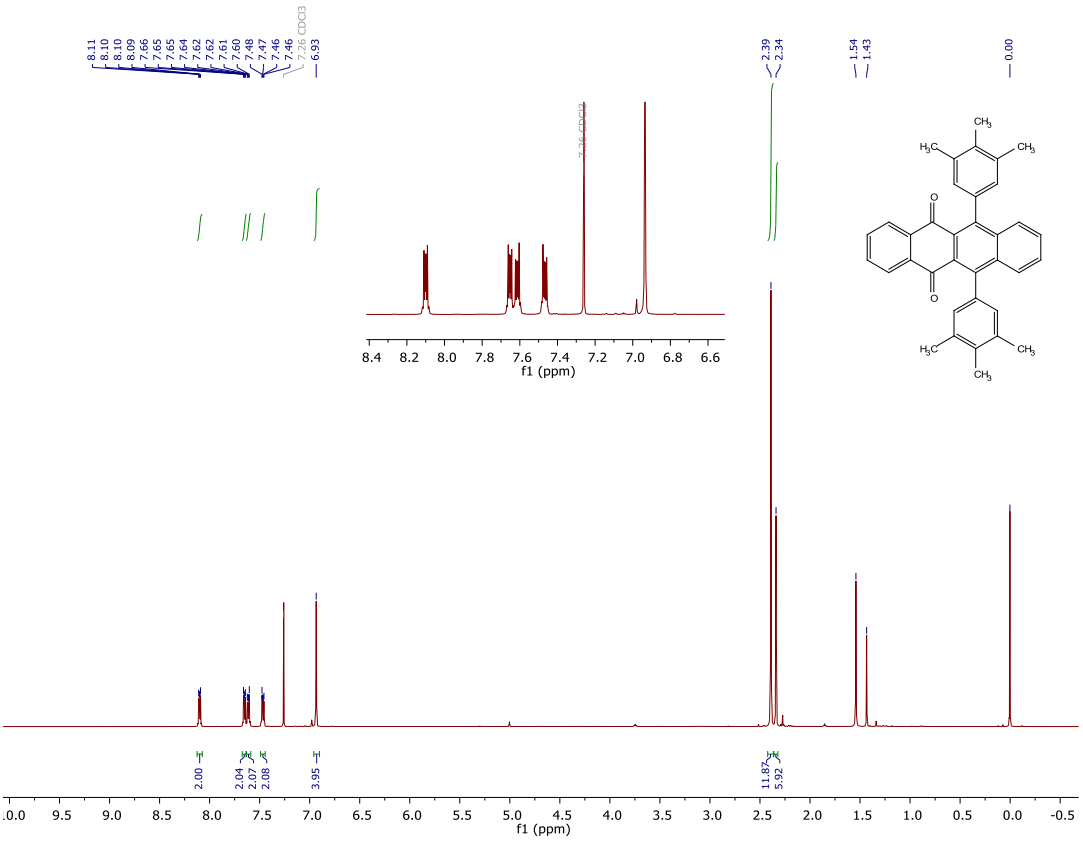

5,12-bis(4-(trifluoromethyl)phenyl)-6,11-bis(3,4,5-trimethylphenyl)tetracene (**4.7**):

^{1}H NMR Spectrum

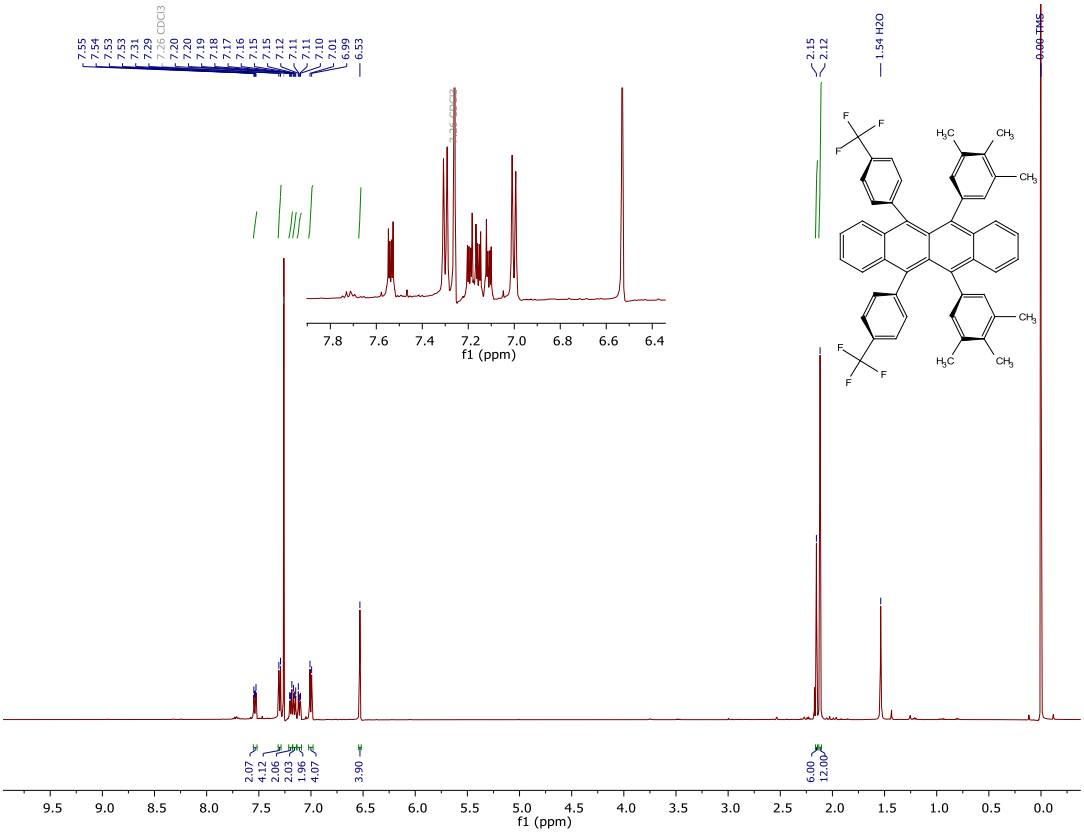

^{19}F NMR Spectrum

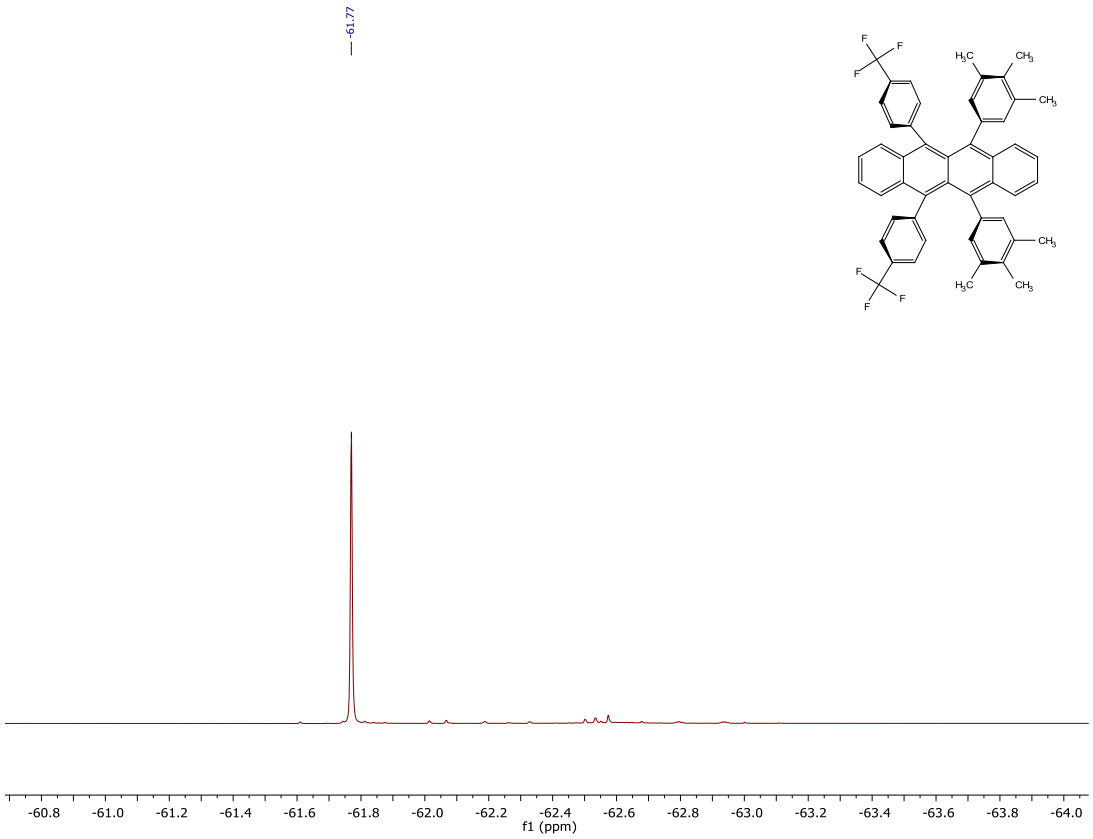

Pyridine-2,3-dicarbonyl dichloride (5.13):

^{1}H NMR Spectrum

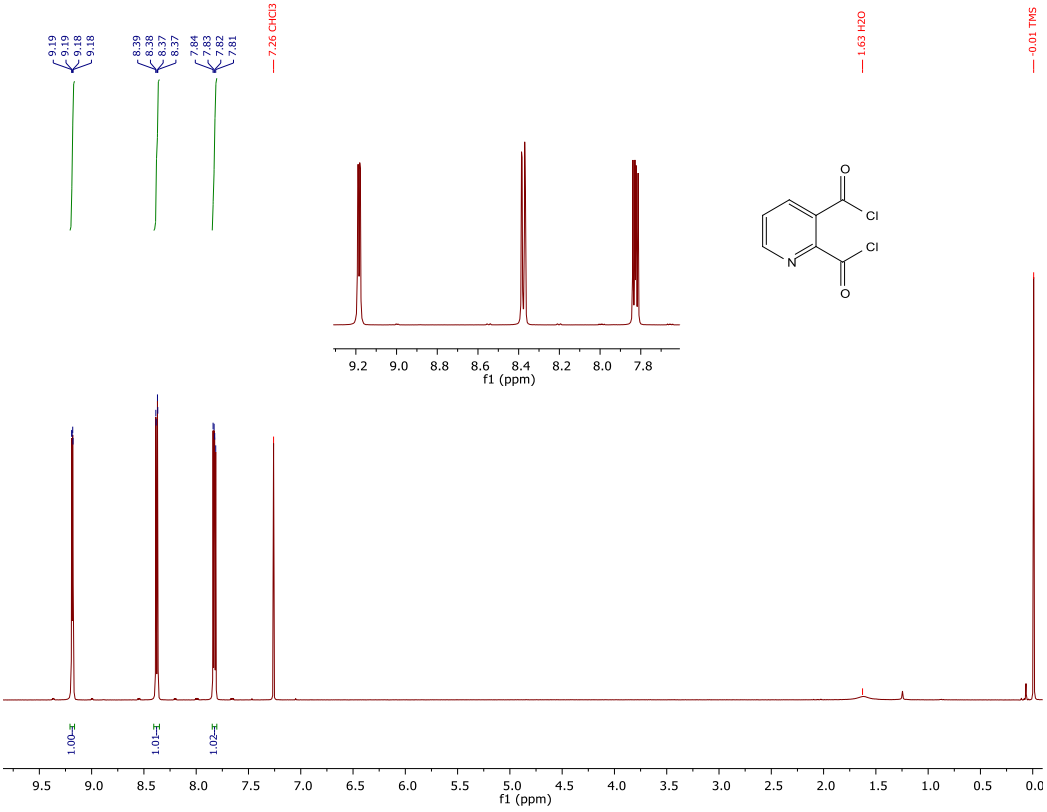

^{1}H NMR Spectrum DMSO-*d*6

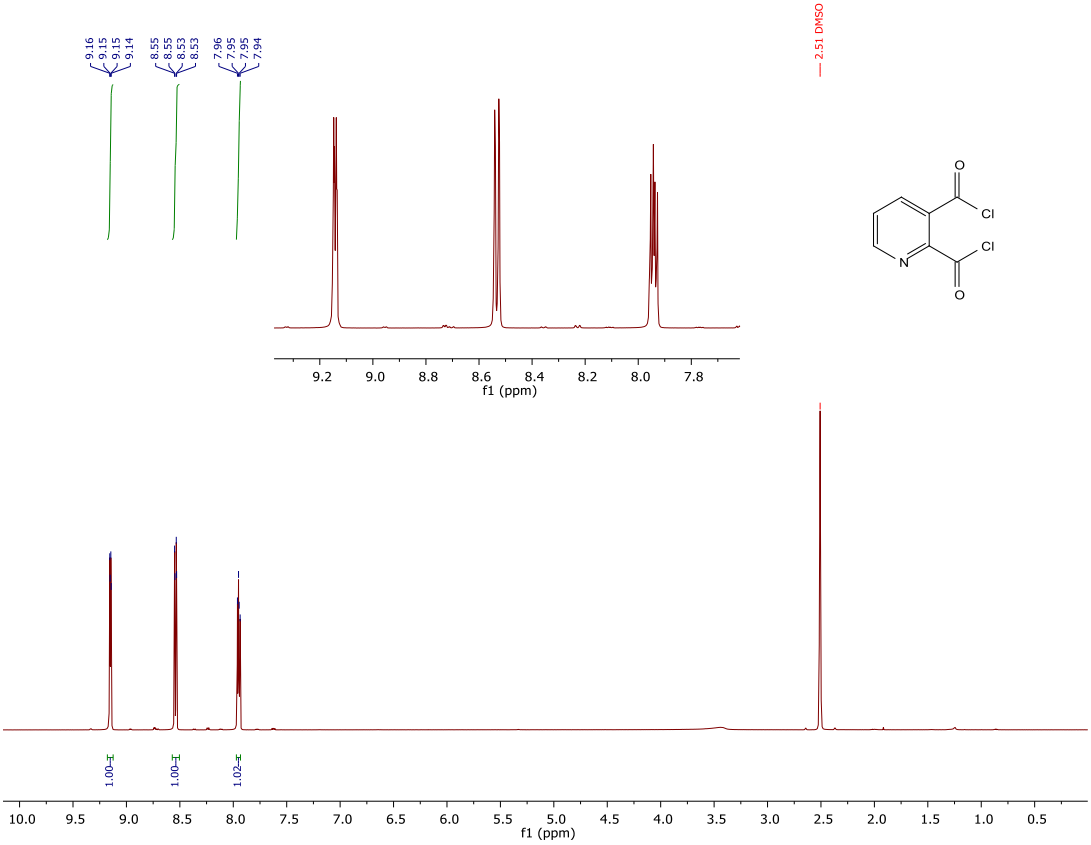

^{13}C NMR Spectrum DMSO-*d*6

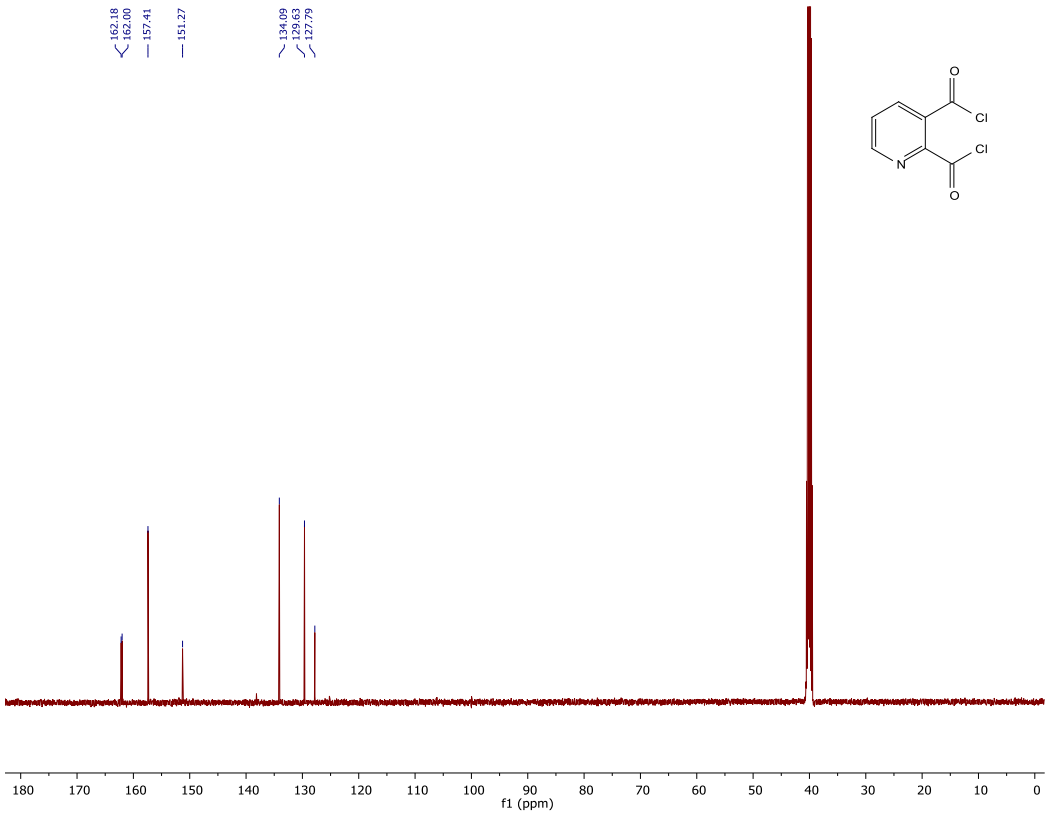

Naphthalene-1,4-diol (5.12):

^{1}H NMR Spectrum DMSO-*d*6

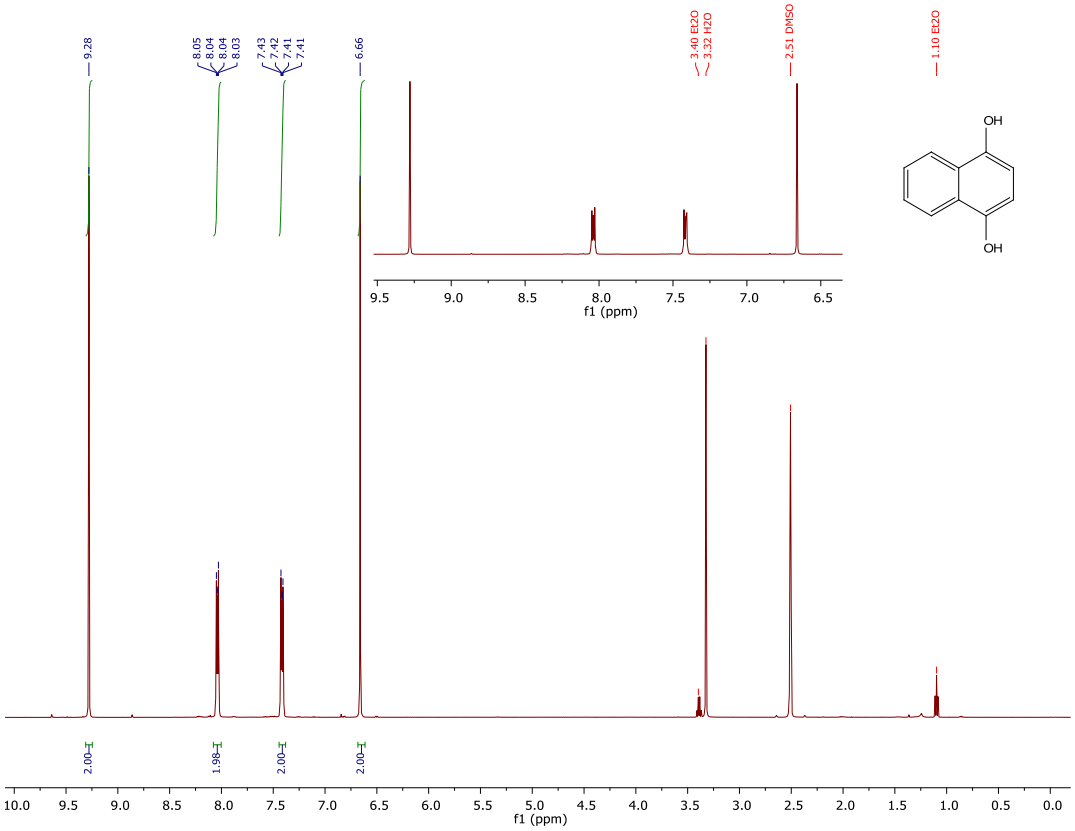

^{13}C NMR Spectrum DMSO-*d*6

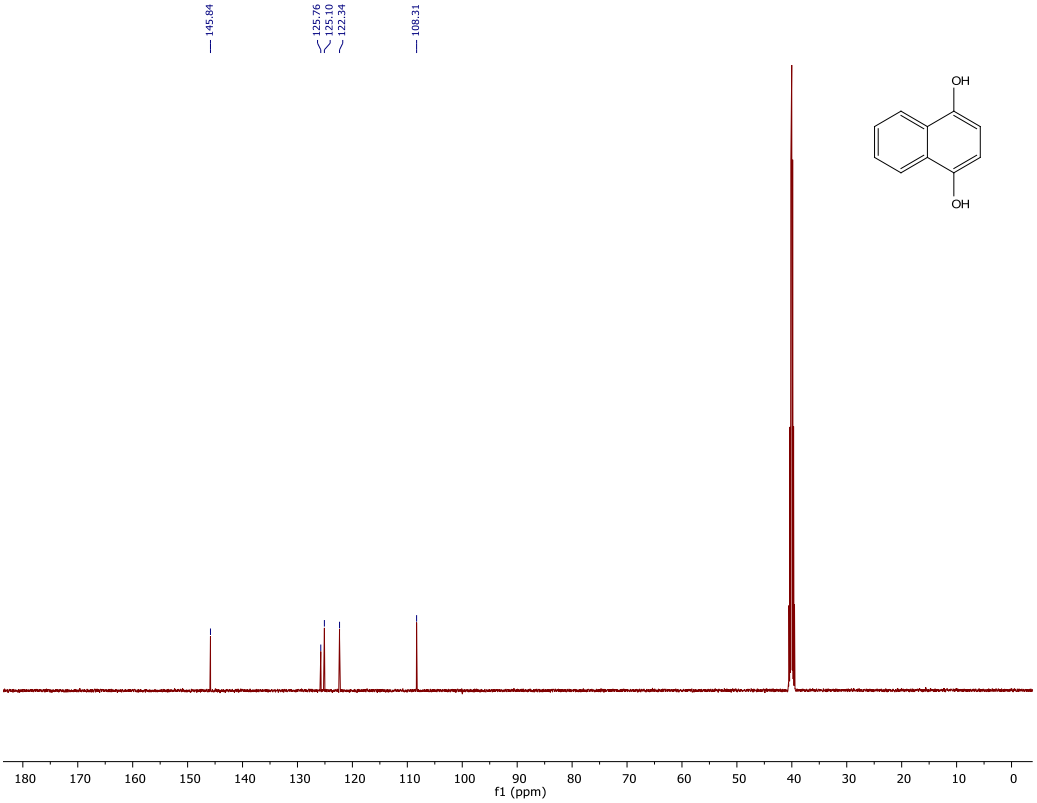

6,11-dihydroxynaphtho[2,3-*g*]quinoline-5,12-dione (5.11)

^{1}H NMR Spectrum

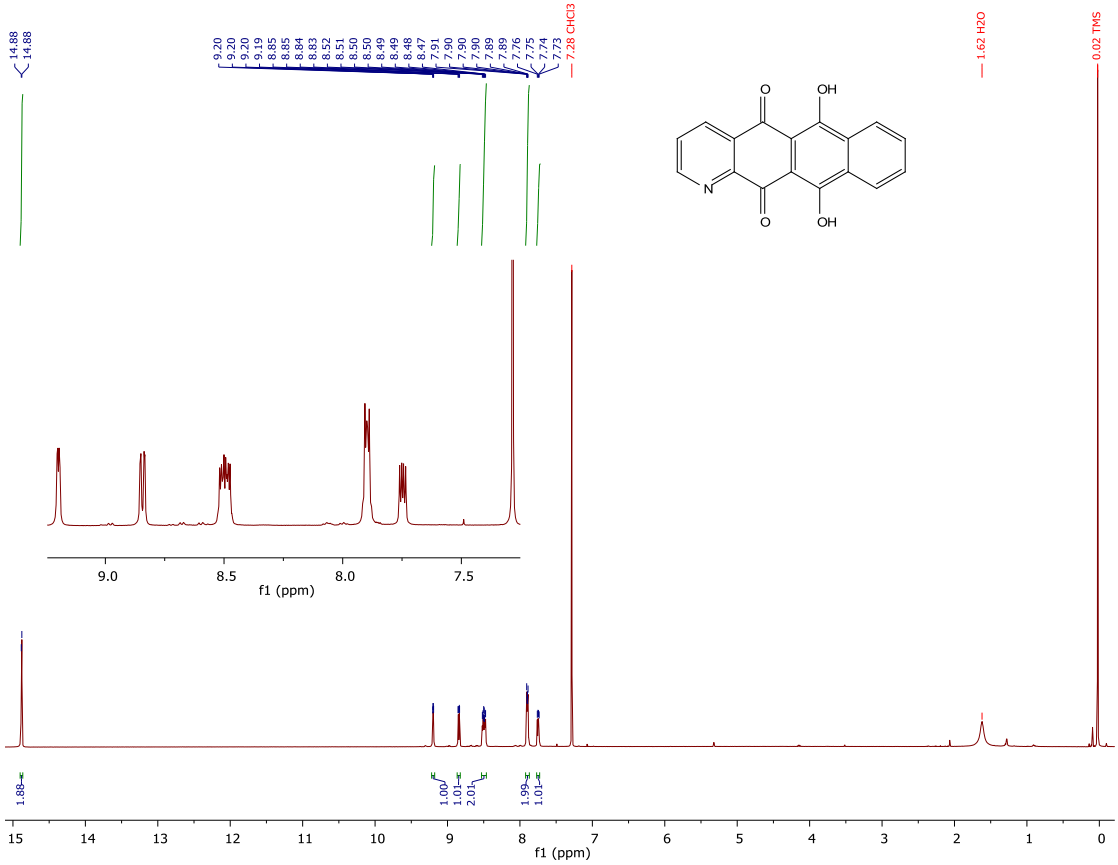

^{13}C NMR Spectrum

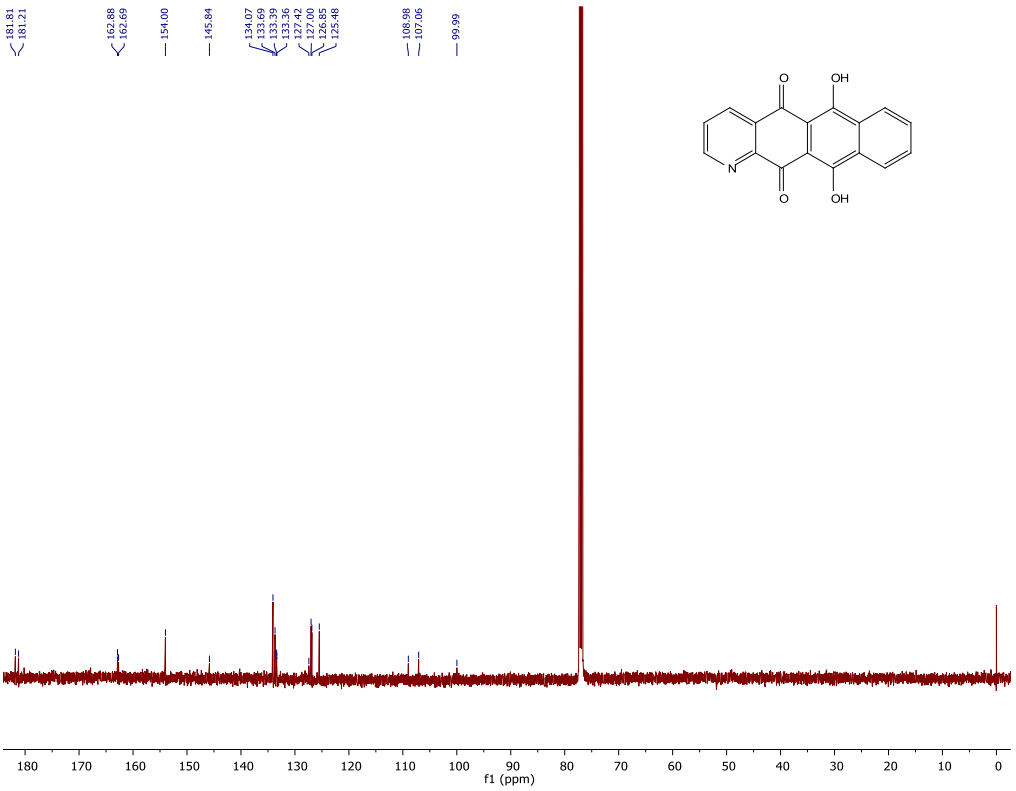

6,11-dichloronaphtho[2,3-*g*]quinoline-5,12-dione (5.19):

^{1}H NMR Spectrum

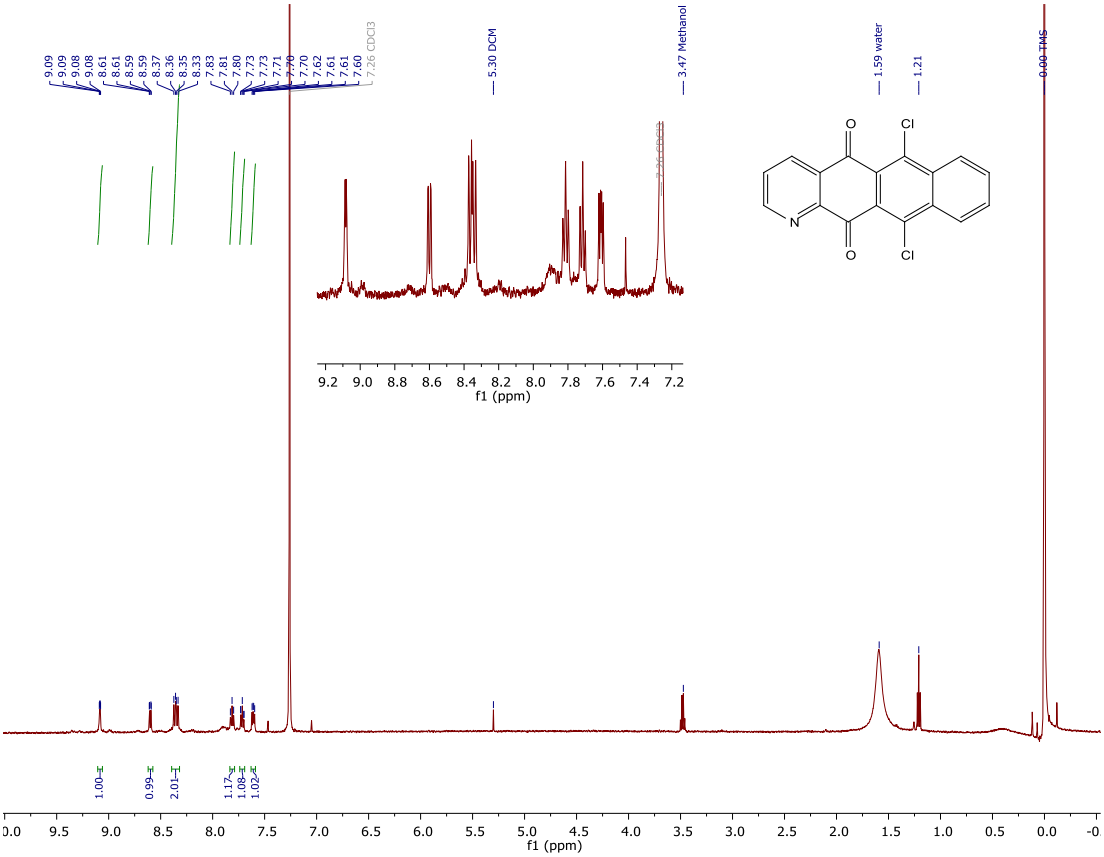

Pyridine-2,3-dicarbonyl dichloride (5.13):

Infrared absorption spectrum (KBr)

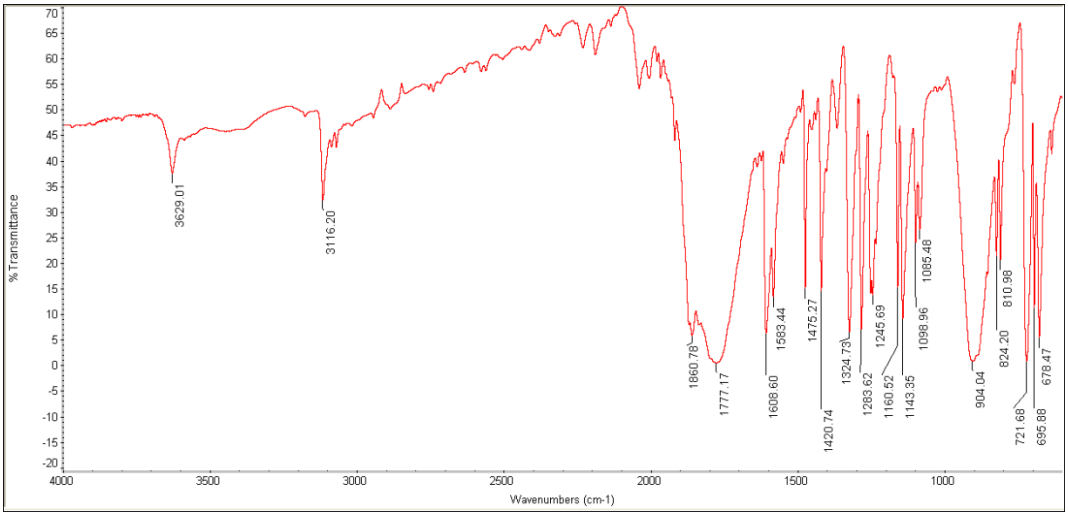

Naphthalene-1,4-diol (5.12):

Infrared absorption spectrum (KBr)

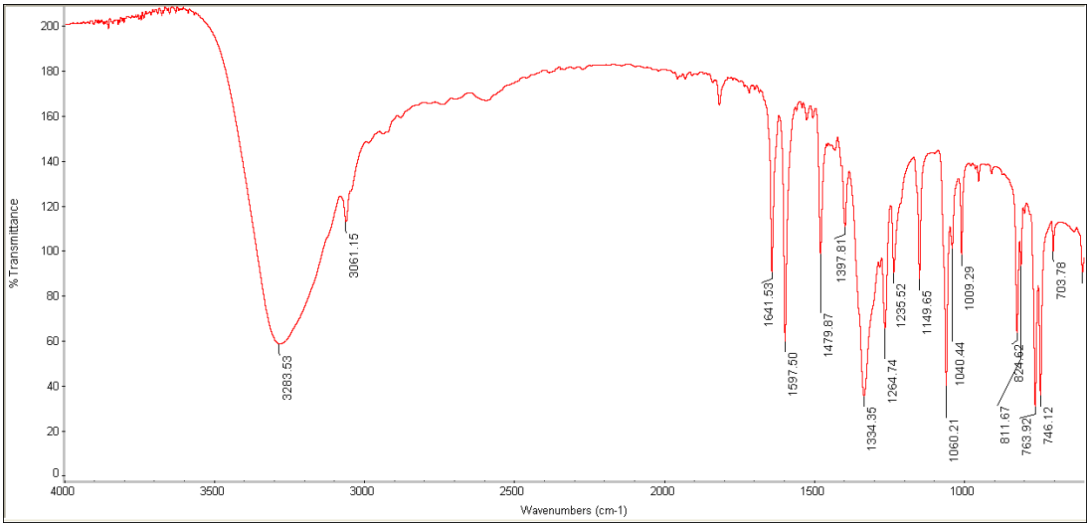

6,11-dihydroxynaphtho[2,3-*g*]quinoline-5,12-dione (5.11)

Infrared absorption spectrum (KBr)

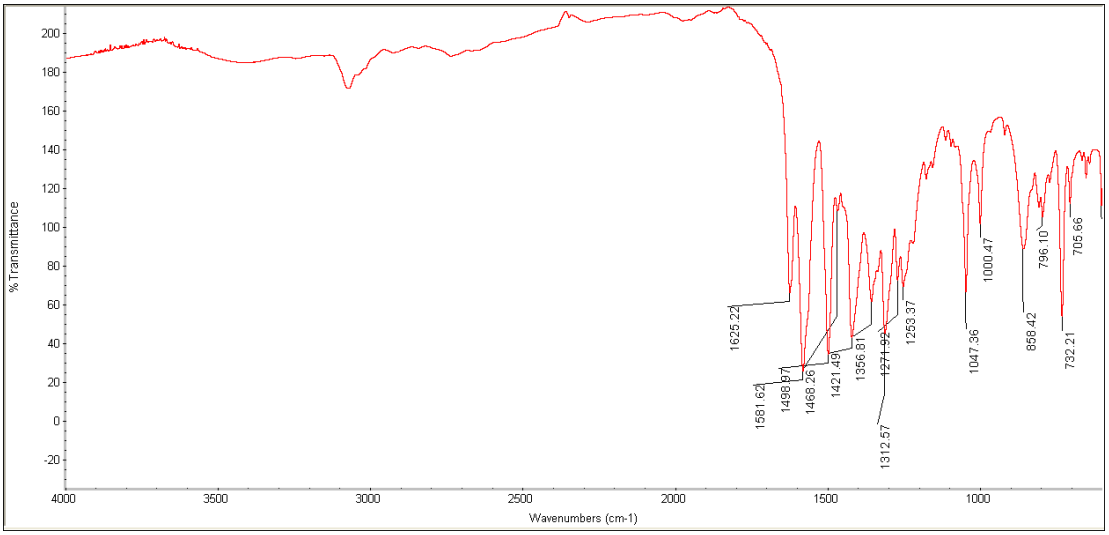

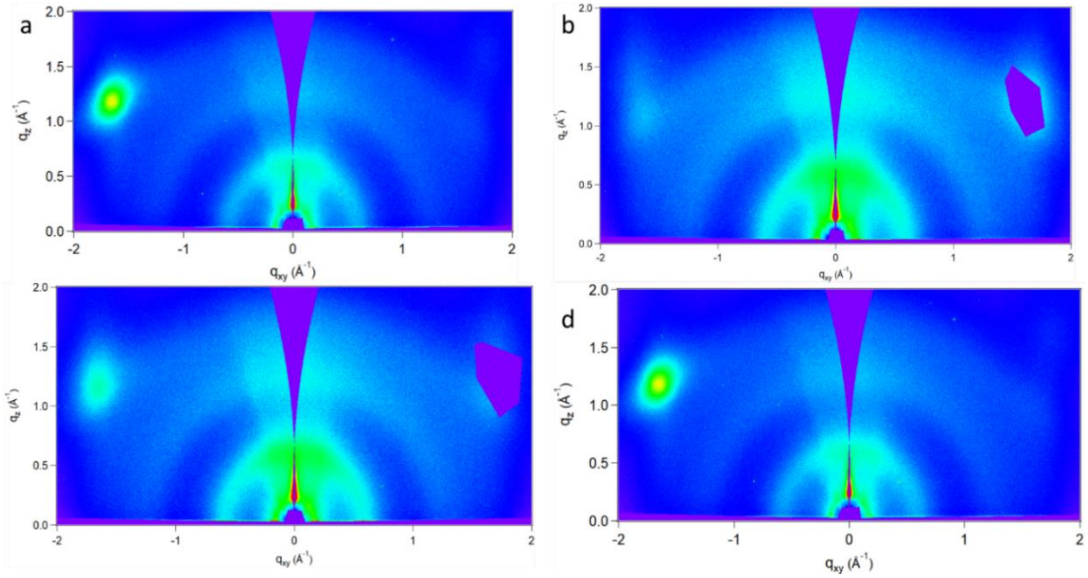

Figure A1: 2-D qzqxy patterns of compound **2.4b** thin film from $CHCl_3$:ODCB 20 mg/ml on Si/SiO_2, a) as-cast film b) film annealed at 60 ˚C c) thin film annealed at 100 ˚C d) thin film annealed at 150 ˚C

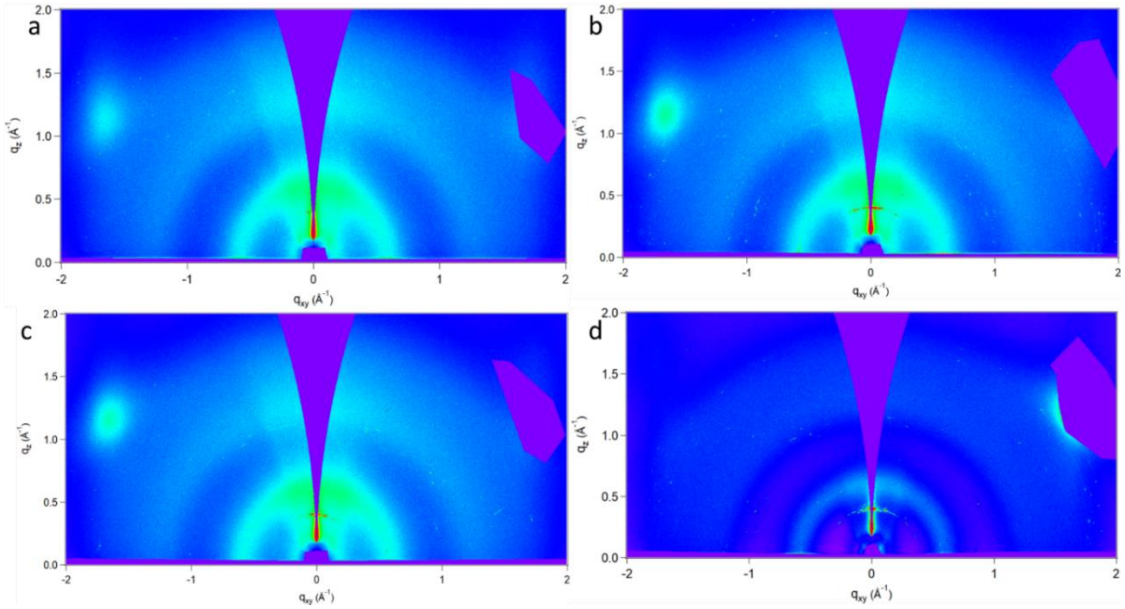

Figure A2: 2-D qzqxy patterns of compound **2.4b** thin film from MeTHF:toluene 20 mg/ml on Si/SiO_2, a) as-cast film b) film annealed at 60 ˚C c) thin film annealed at 100 ˚C d) thin film annealed at 150 ˚C

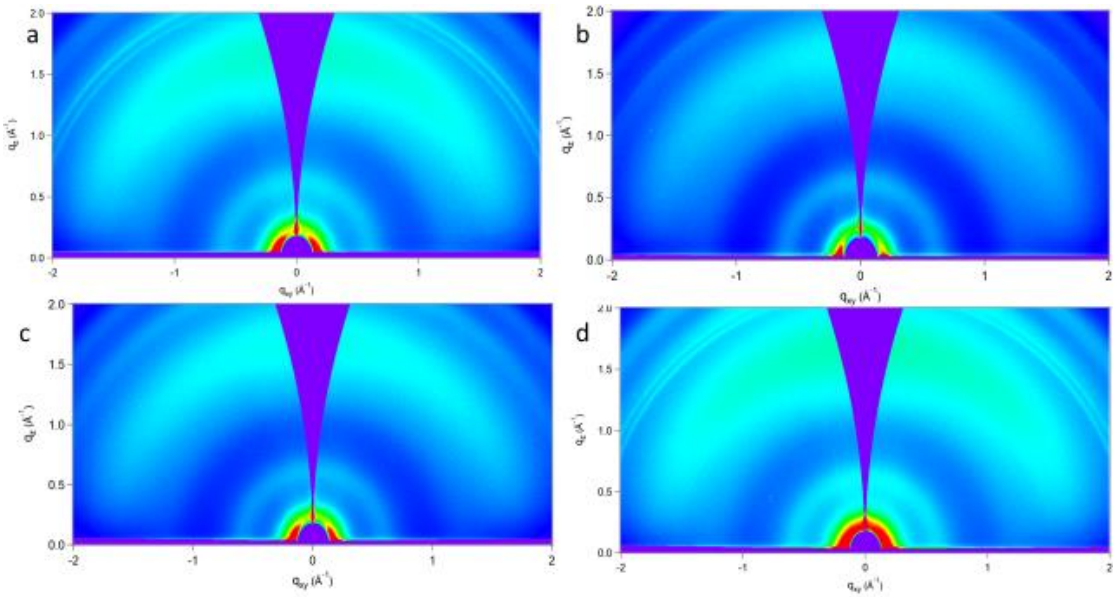

Figure A3: 2-D qzqxy patterns of compound **2.4b** thin film from $CHCl_3$:ODCB 20 mg/ml on ITO/ZnO, a) as-cast film b) film annealed at 60 ˚C c) thin film annealed at 100 ˚C d) thin film annealed at 150 ˚C

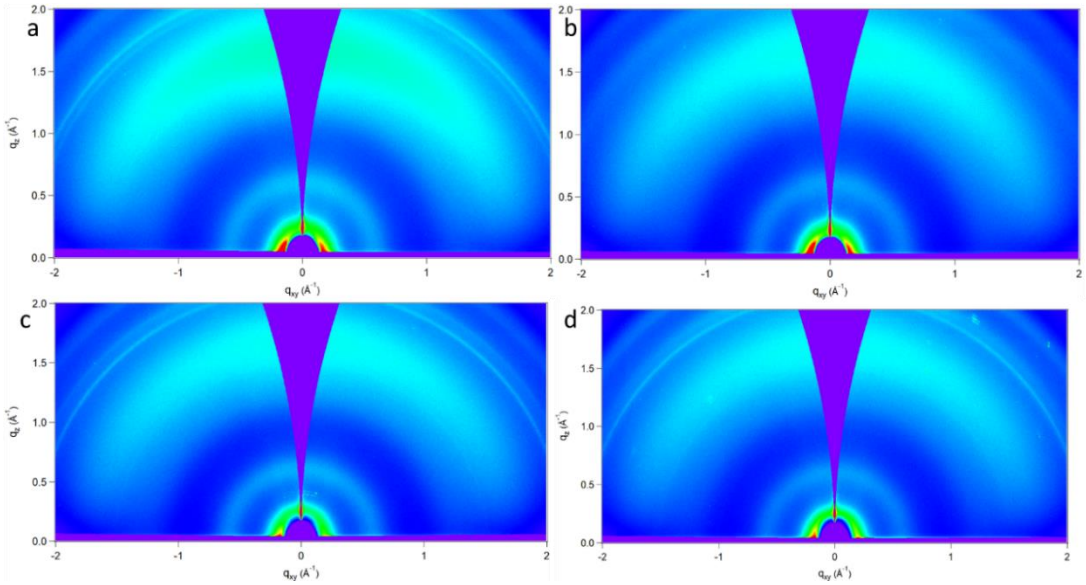

Figure A4: 2-D qzqxy patterns of compound **2.4b** thin film from MeTHF:toluene 20 mg/ml on ITO/ZnO, a) as-cast film b) film annealed at 60 ˚C c) thin film annealed at 100 ˚C d) thin film annealed at 150 ˚C

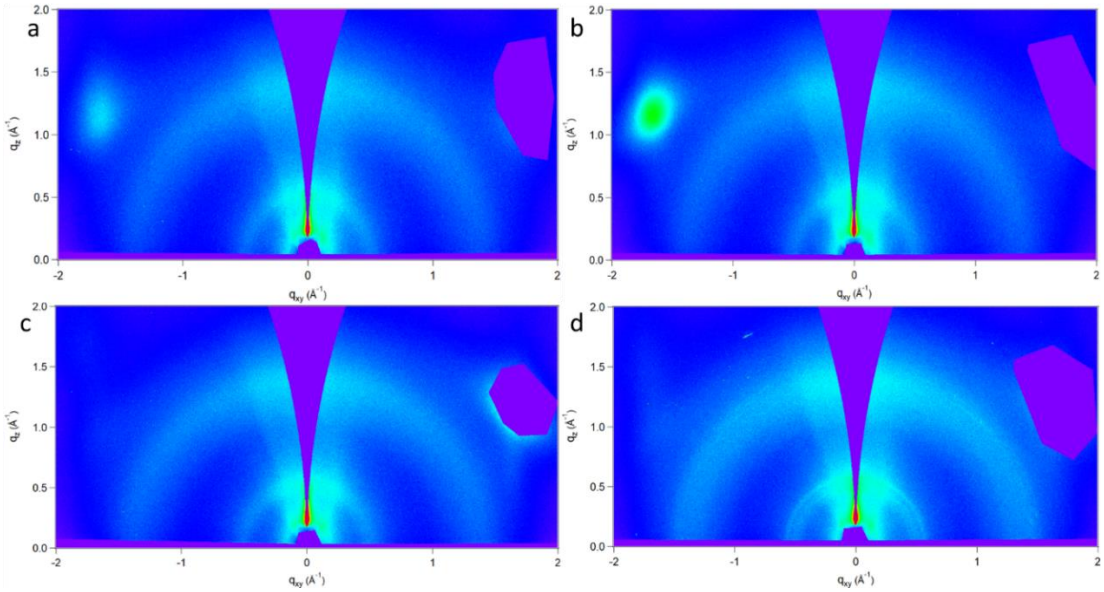

Figure A5: 2-D qzqxy patterns of compound **2.4d** thin film from $CHCl_3$:ODCB 20 mg/ml on Si/SiO_2, a) as-cast film b) film annealed at 60 ˚C c) thin film annealed at 100 ˚C d) thin film annealed at 150 ˚C

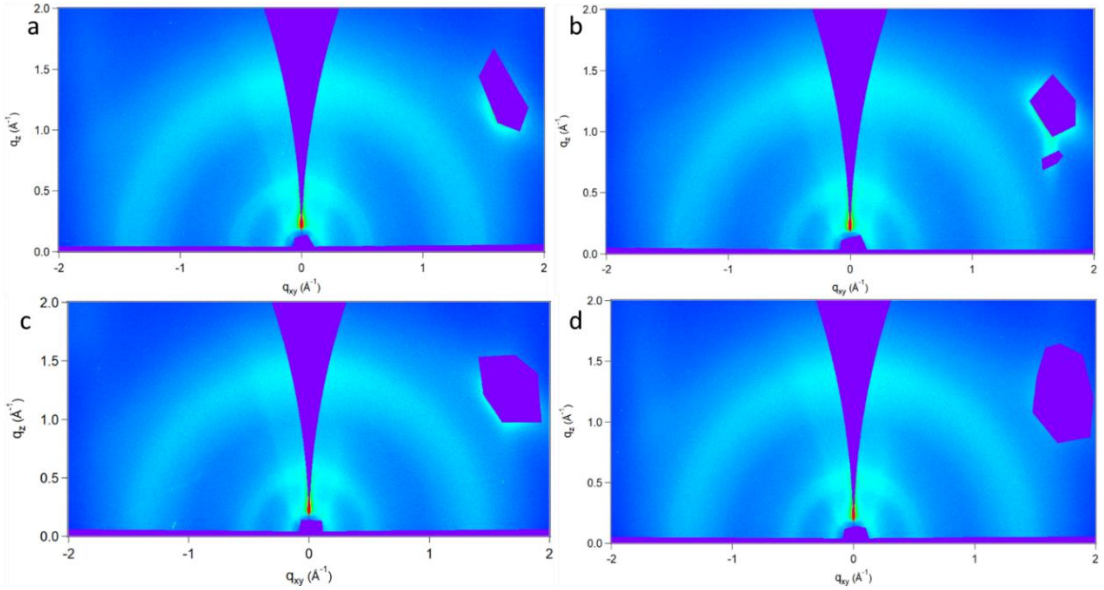

Figure A6: 2-D qzqxy patterns of compound **2.4d** thin film from MeTHF:toluene 20 mg/ml on Si/SiO_2, a) as-cast film b) film annealed at 60 ˚C c) thin film annealed at 100 ˚C d) thin film annealed at 150 ˚C

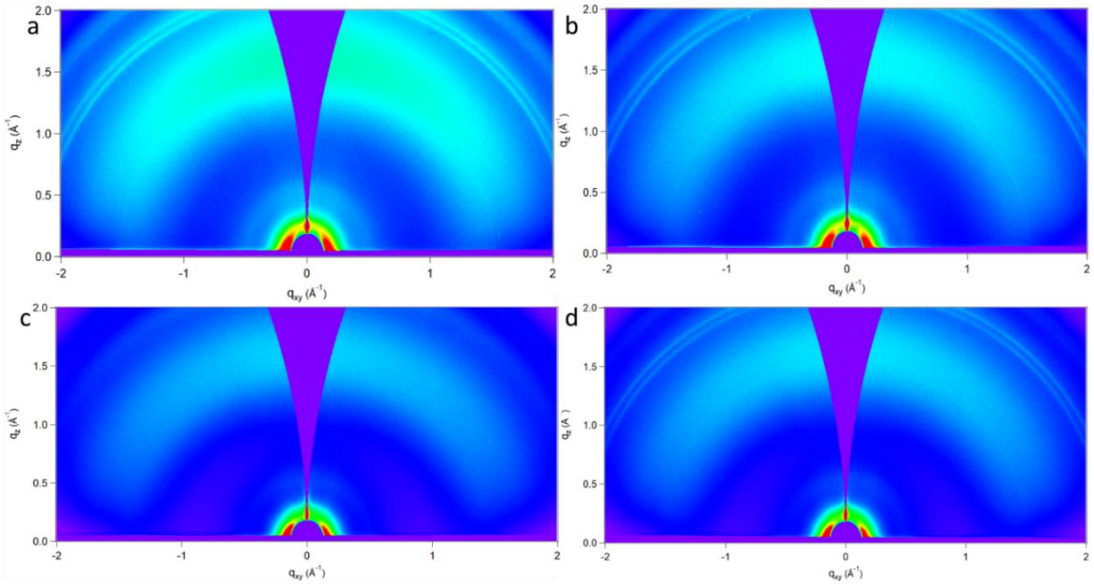

Figure A7: 2-D qzqxy patterns of compound **2.4d** thin film from $CHCl_3$:ODCB 20 mg/ml on ITO/ZnO, a) as-cast film b) film annealed at 60 ˚C c) thin film annealed at 100 ˚C d) thin film annealed at 150 ˚C

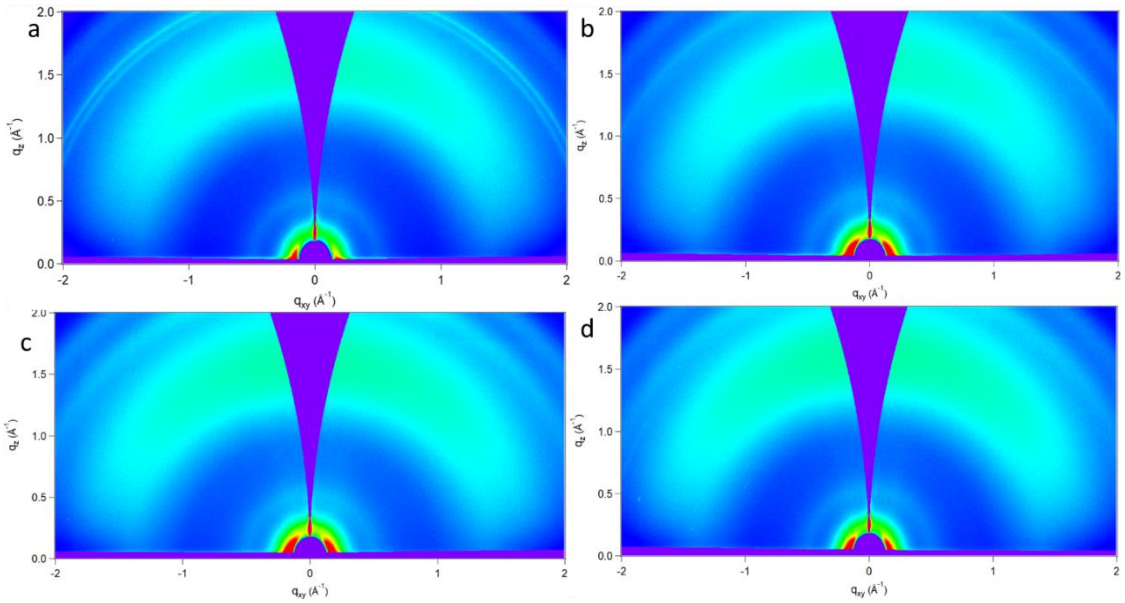

Figure A8: 2-D qzqxy patterns of compound **2.4d** thin film from MeTHF:toluene 20 mg/ml on ITO/ZnO, a) as-cast film b) film annealed at 60 ˚C c) thin film annealed at 100 ˚C d) thin film annealed at 150 ˚C

Thin film crystal structure determination:

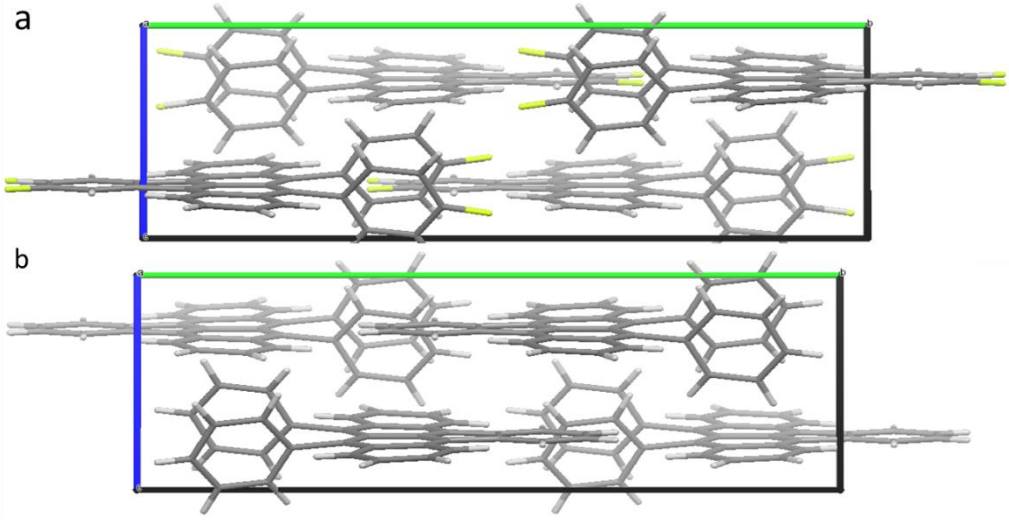

Figure A9: Monoclinic C2/c crystal structures a) compound **2.4a** b) compound **2.4c**

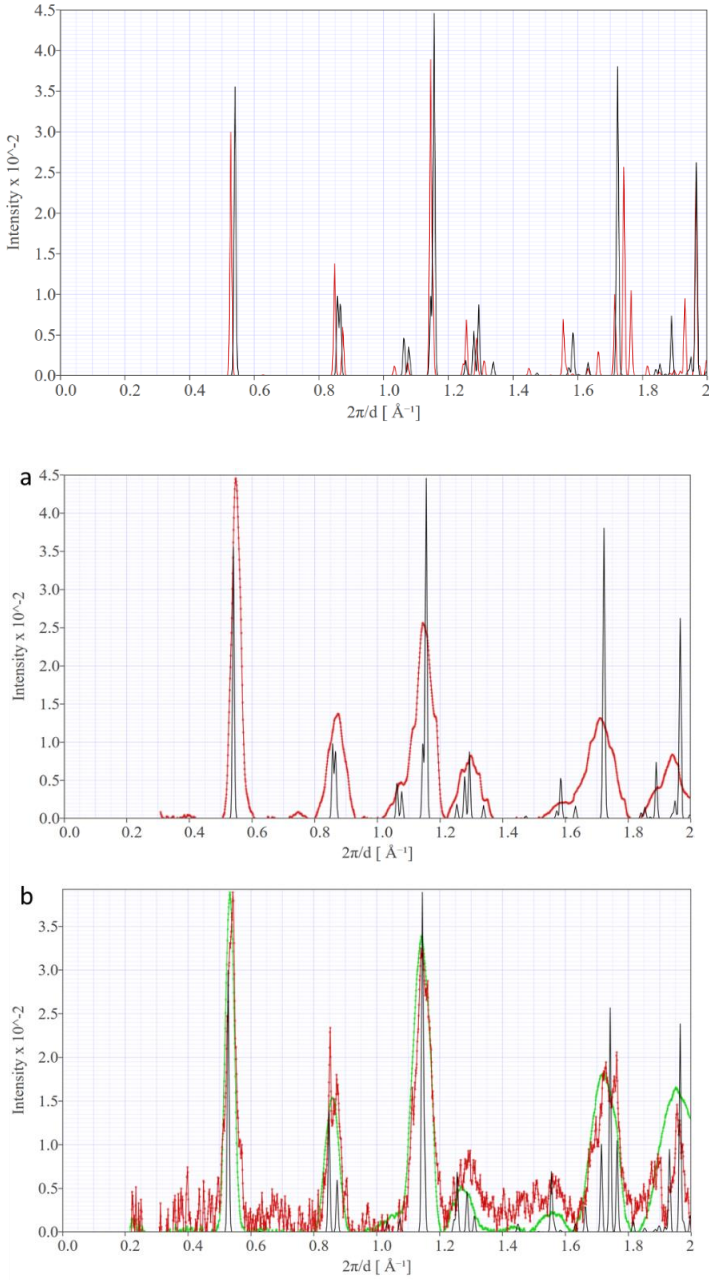

Figure A10: Overlaid experimental and theoretical I vs q patterns of the single crystal. a) Compound **2.4a** MeTHF:toluene processed thin film on Si/SiO_2 b) Compound **2.4c** $CHCl_3$:ODB processed thin films on Si/SiO_2, calculated C2/*c* powder diffraction pattern, as-cast thin film, green thin film annealed 150 ˚C

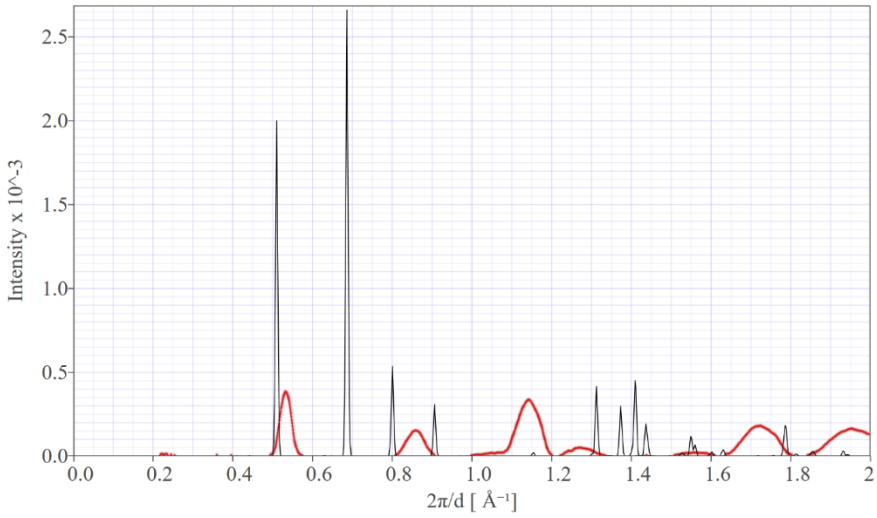

Figure A11: Calculated diffraction patters for triclinic P1 crystal system overlaid with experimentally determined I vs q of compound **2.4c** prepared from $CHCl_3$:ODCB on Si/SiO_2 annealed at 150 ˚C

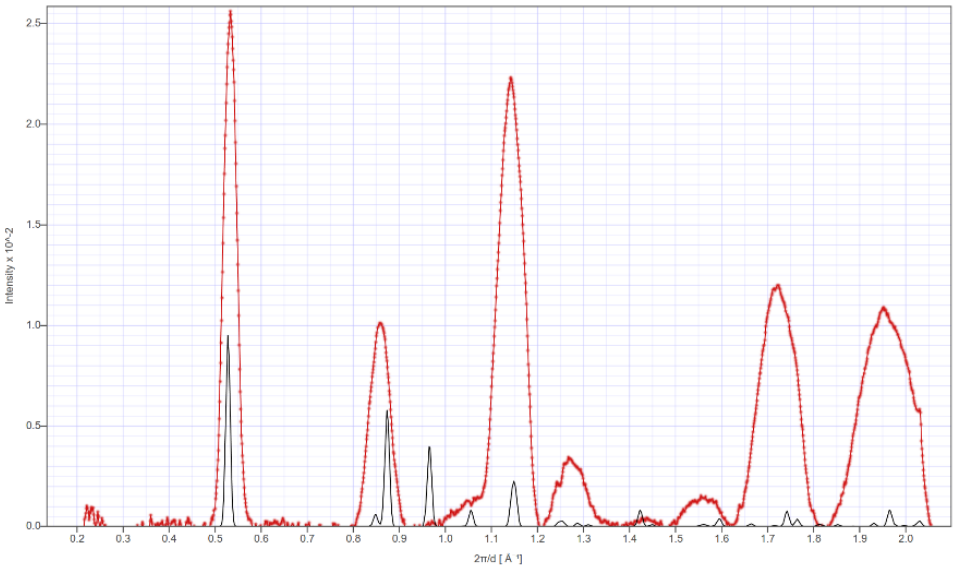

Figure A12: Calculated diffraction patters for triclinic C2 crystal system overlaid with experimentally determined I vs q of compound **2.4c** prepared from $CHCl_3$:ODCB on Si/SiO_2 annealed at 150 ˚C

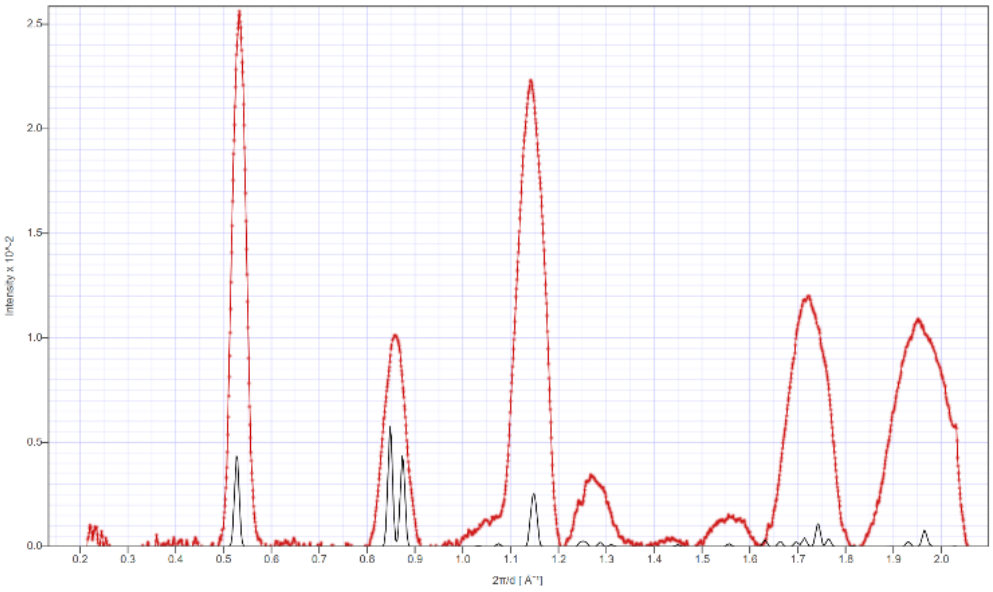

Figure A13: Calculated diffraction patters for triclinic Cc crystal system overlaid with experimentally determined I vs q of compound **2.4c** prepared from $CHCl_3$:ODCB on Si/SiO_2 annealed at 150 ˚C

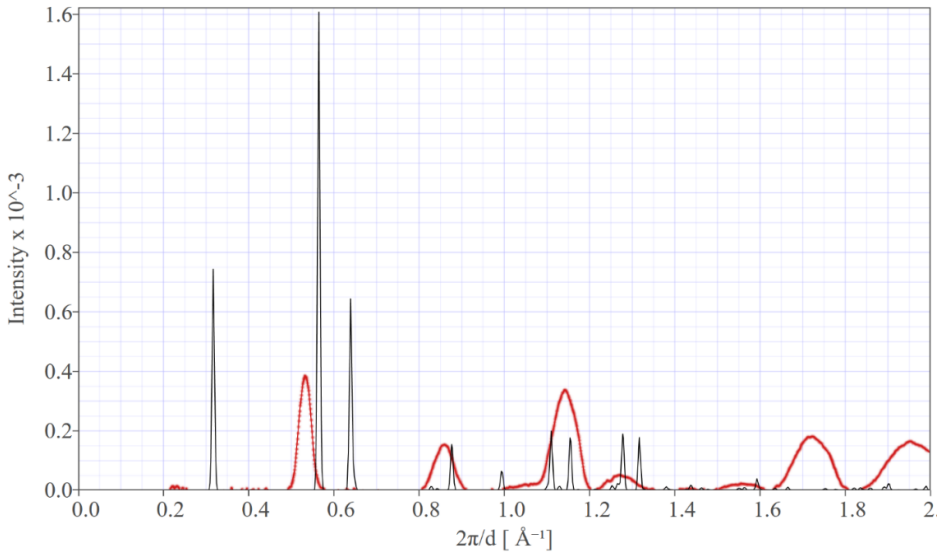

Figure A14: Calculated diffraction patters for triclinic P2/c crystal system overlaid with experimentally determined I vs q of compound **2.4c** prepared from $CHCl_3$:ODCB on Si/SiO_2 annealed at 150 ˚C

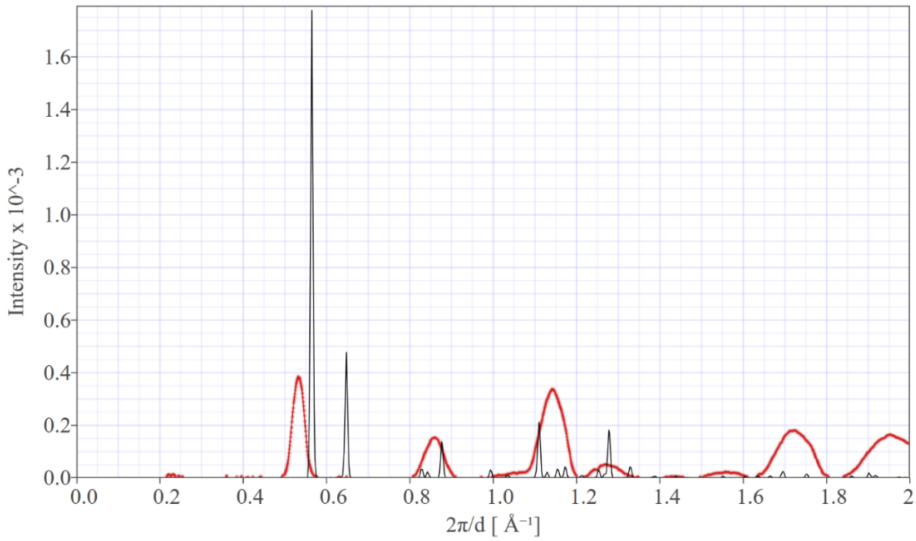

Figure A15: Calculated diffraction patters for triclinic $P2_1/c$ crystal system overlaid with experimentally determined I vs q of compound **2.4c** prepared from $CHCl_3$:ODCB on Si/SiO_2 annealed at 150 ˚C

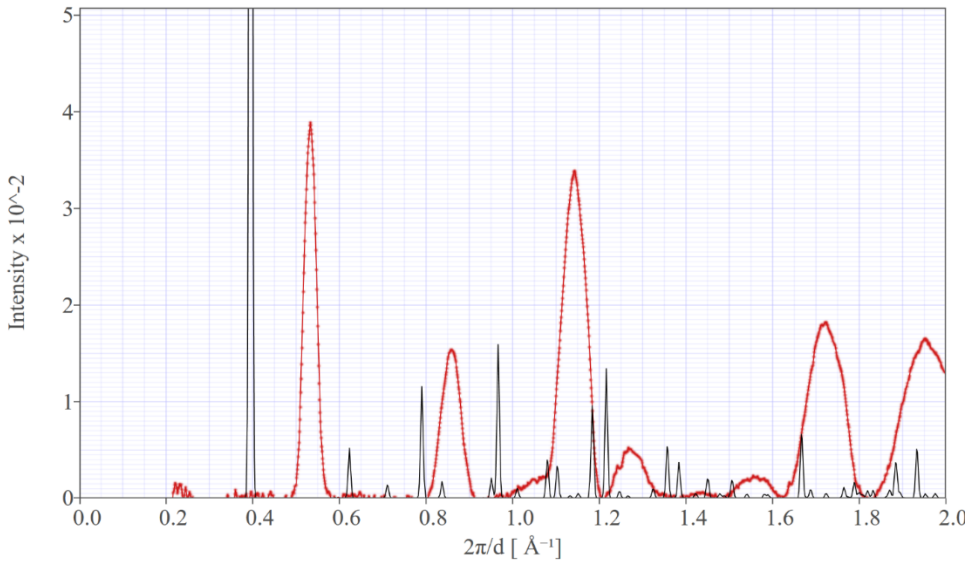

Figure A16: Calculated diffraction patters for triclinic Pbca crystal system overlaid with experimentally determined I vs q of compound **2.4c** prepared from $CHCl_3$:ODCB on Si/SiO_2 annealed at 150 ˚C

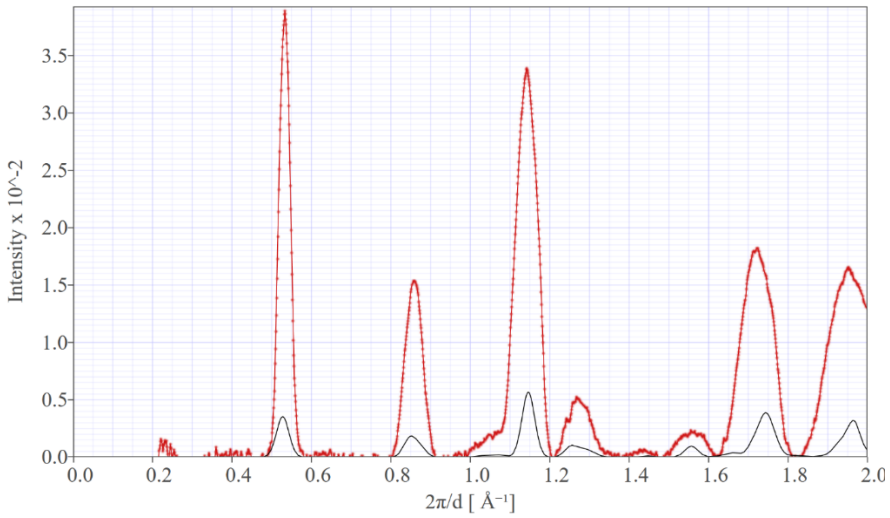

Figure A17: Experimental diffraction pattern over laid with simulated diffraction accounting for both the high energy X-ray source, 0.974 Å, and small crystallite size, 0.0158 μm crystallite size used.

Table A1: Relative intensity of theoretical and measured diffraction signals. It must be noted, that an accurate experimental intensity of the 112 signal could not be determined due to substrate interference.

Compound **2.4a**		
110 Plane compared to planes	Measured relative intensity	Calculated relative intensity
200	4.97	4.043
11$\bar{1}$	2.74	3.683
(200+11$\bar{1}$)	1.77	1.92
111	0.99	0.797
002	1.51	1.47
Compound **2.4c**		
110 Plane compared to planes	Measured relative intensity	Calculated relative intensity
200	1.615	1.522
111	0.786	0.724
002	1.203	1.171

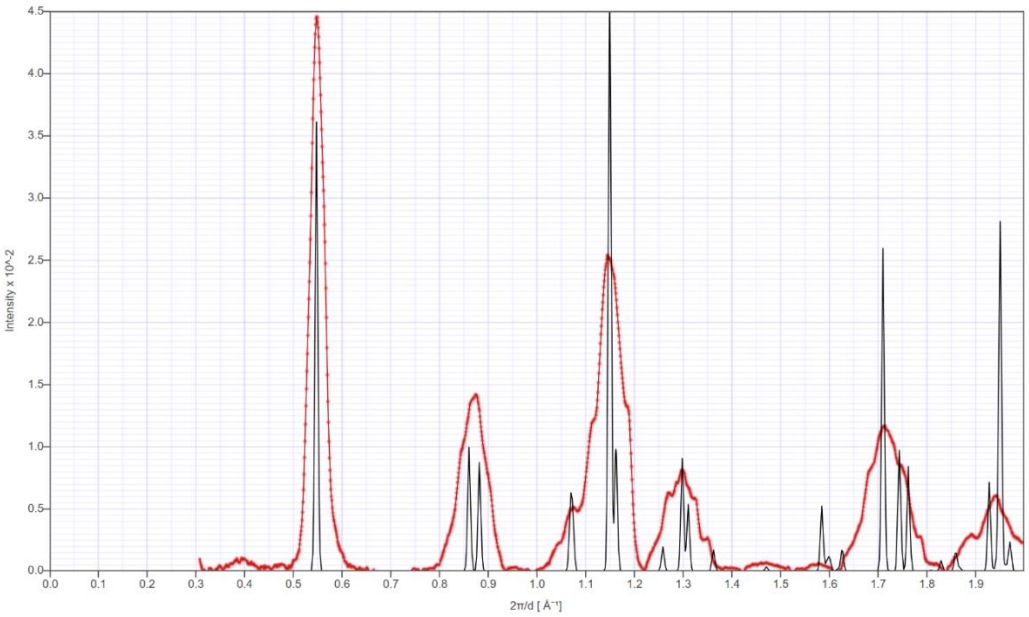

Figure A18: The theoretical powder diffraction patterns with the modified lattice parameters of compound **2.4a** thin films prepared from MeTHF:toluene on Si/SiO_2 as-cast.

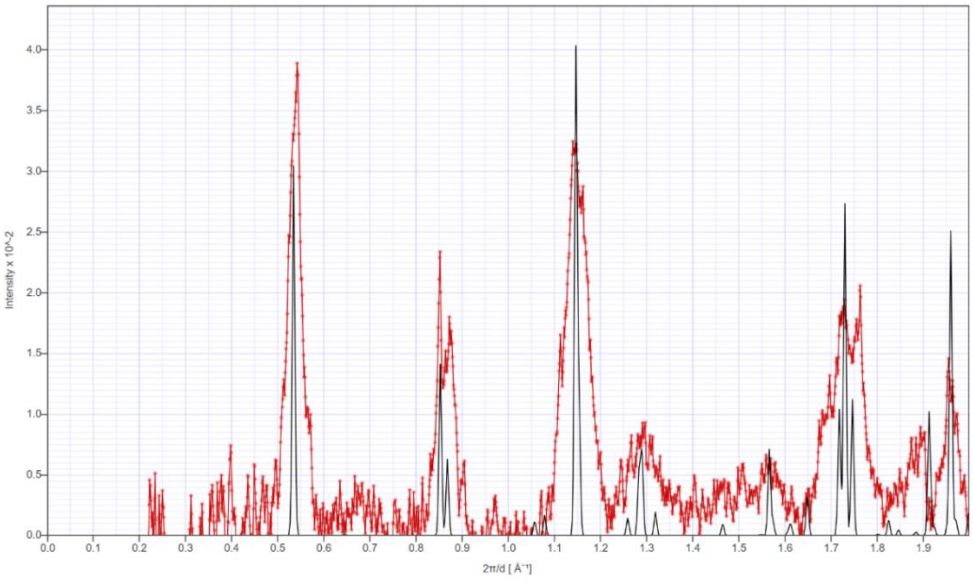

Figure A19: The theoretical powder diffraction patterns with the modified lattice parameters of compound **2.4c** thin films prepared from $CHCl_3$:ODCB on Si/SiO_2, as-cast.

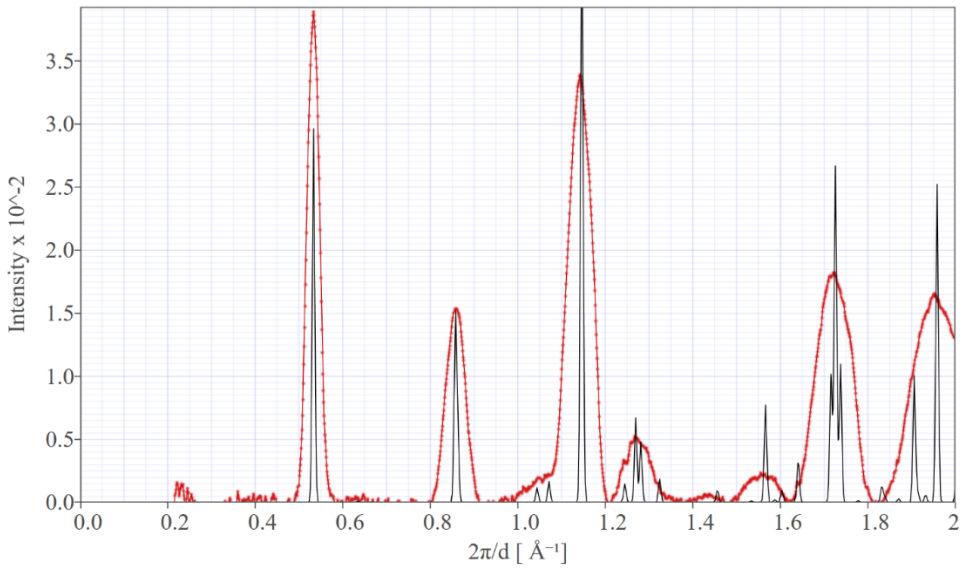

Figure A20: The theoretical powder diffraction patterns with the modified lattice parameters of compound **2.4c** thin films prepared from $CHCl_3$:ODCB on Si/SiO_2, annealed 150 ˚C.

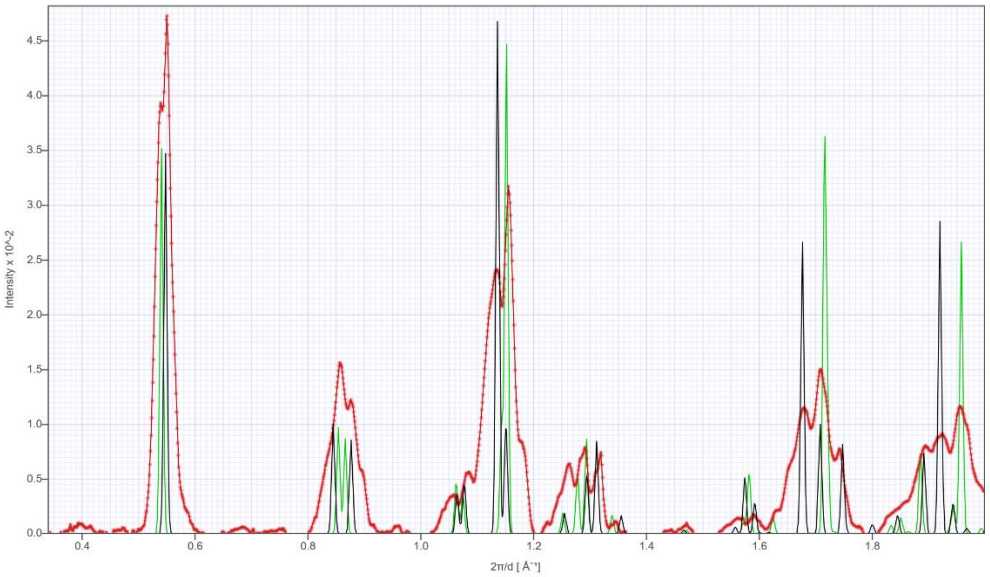

Figure A21: The theoretical powder diffraction patterns with the modified lattice parameters of compound **2.4a** thin films prepared from MeTHF:toluene on Si/SiO_2 annealed at 150 ˚C.

Intermolecular Interactions on Si/SiO_2:

Compound 2.4a:

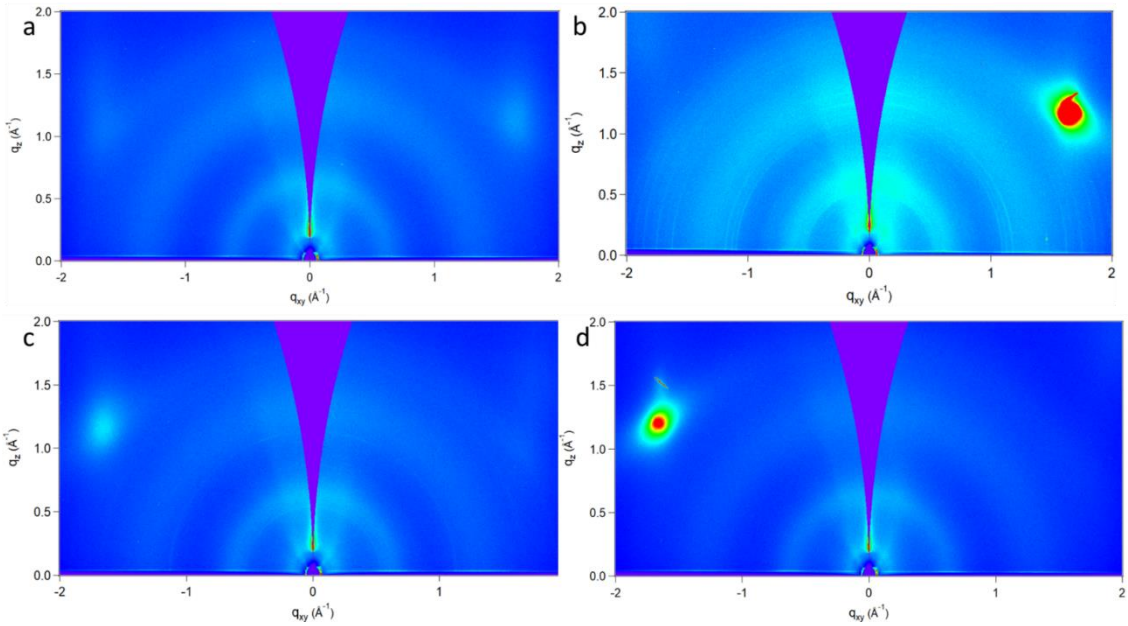

Figure A22: 2-D qzqxy patterns of compound **2.4a** thin film from $CHCl_3$:ODCB on Si/SiO_2, a) as-cast film b) film annealed at 60 ˚C c) thin film annealed at 100 ˚C d) thin film annealed at 150 ˚C

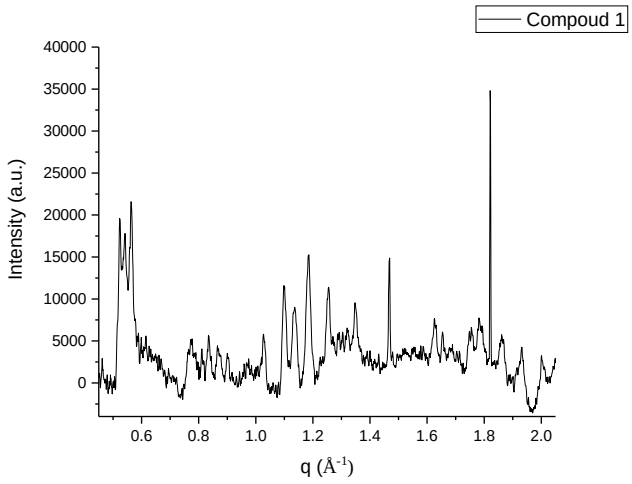

Figure A23: I vs q of compound **2.4a** annealed at 60 ˚C prepared form $CHCl_3$:ODCB on Si/SiO_2

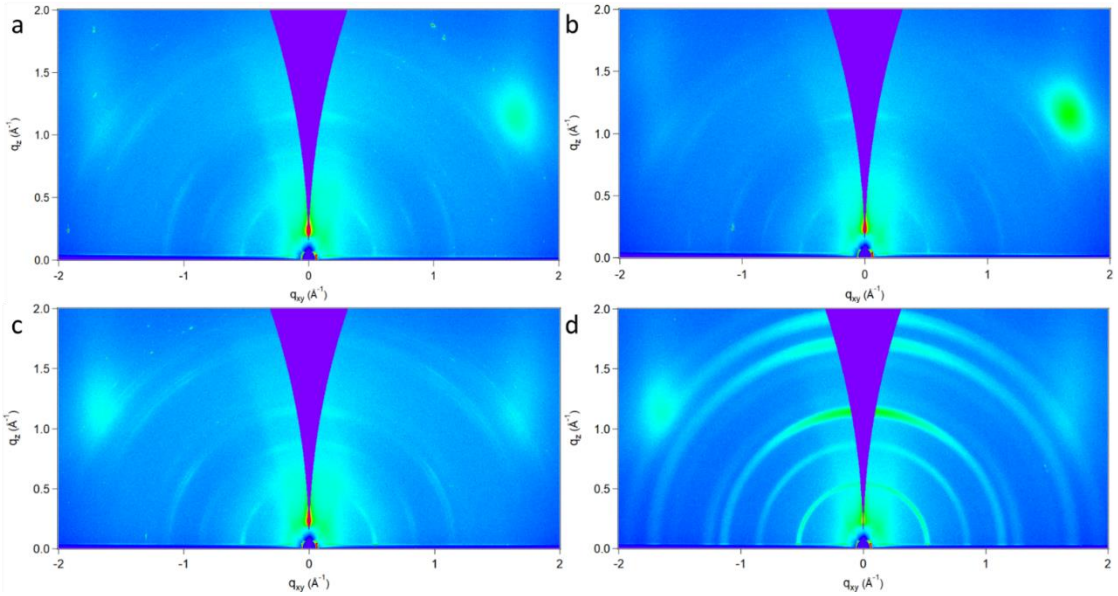

Figure A24: 2-D qzqxy patterns of compound **2.4c** thin film from $CHCl_3$:ODCB on Si/SiO_2, a) as-cast film b) film annealed at 60 ˚C c) thin film annealed at 100 ˚C d) thin film annealed at 150 ˚C

Compound 2.4c:

As-Cast Films:

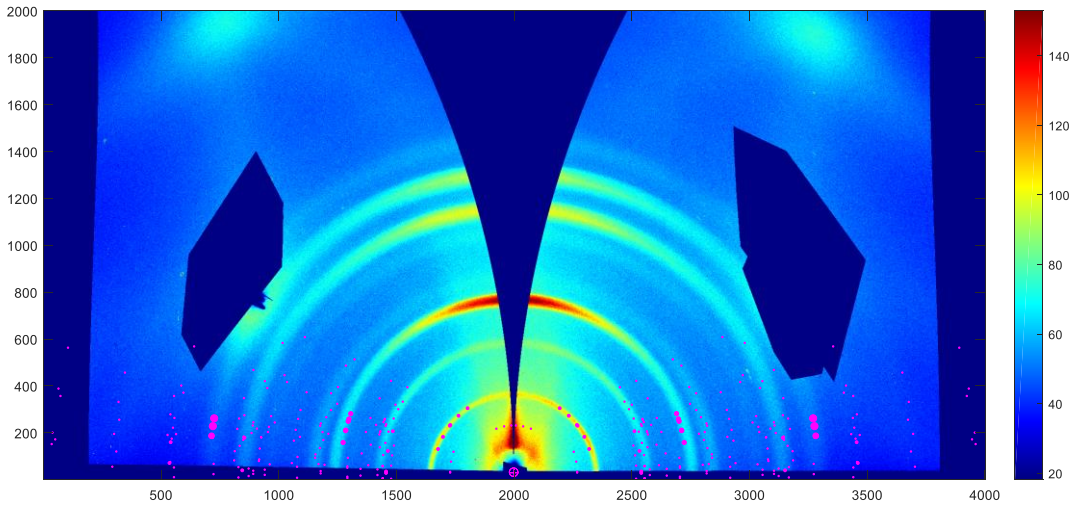

Figure A25: Thin film qzqxy diffraction patterns of compound **2.4c** from $CHCl_3$:ODCB on Si/SiO_2 annealed at 150 ˚C 110, 200 oriented perpendicular to the Si/SiO_2 substrate and tilted 70 to 90 degrees.

Analysis of Hirschfeld surfaces and finger print map:

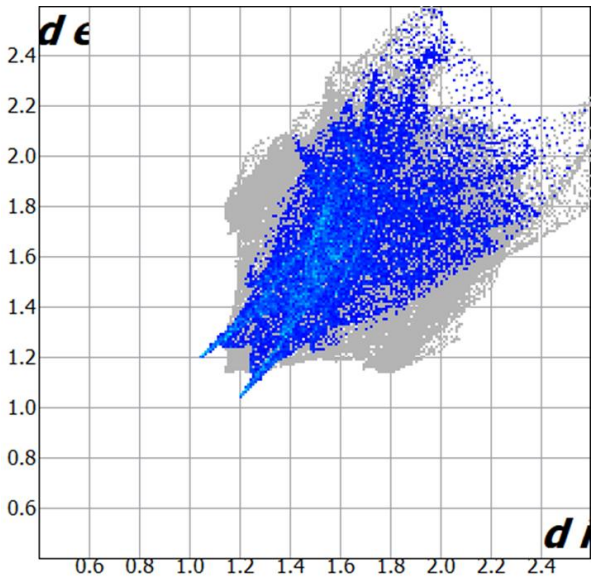

Figure A26: Figure print map of C-F-H interaction of compound **2.4c**

Intermolecular C–F··X Interactions on ITO/ZnO:

Compound 2.4a:

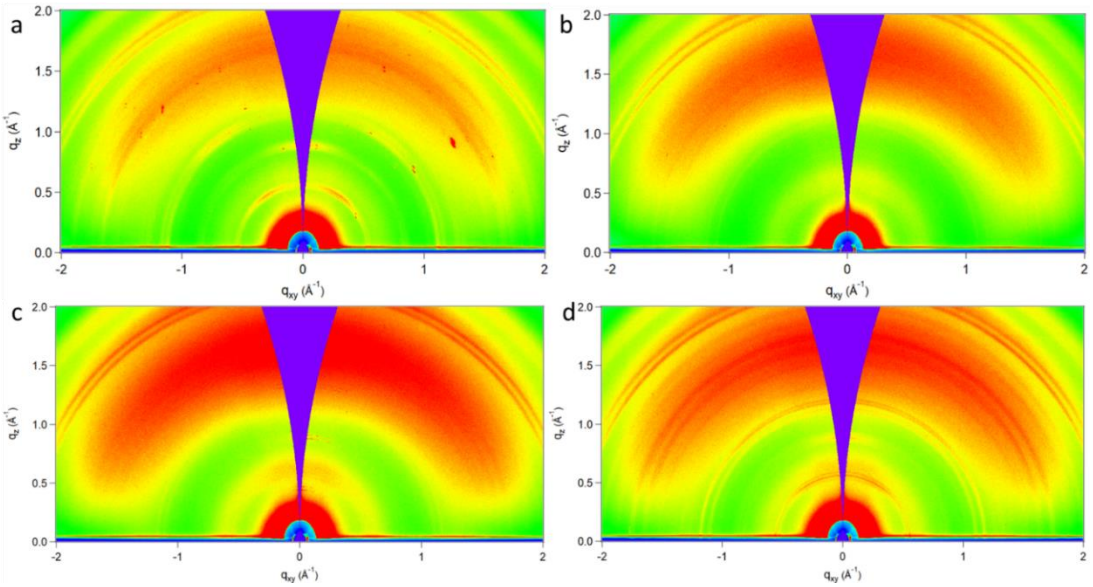

Figure A27: 2-D qzqxy patterns of compound **2.4a** thin film from $CHCl_3$:ODCB on ITO/ZnO, a) un-annealed film b) film annealed at 60 ˚C c) thin film annealed at 100 ˚C d) thin film annealed at 150 ˚C

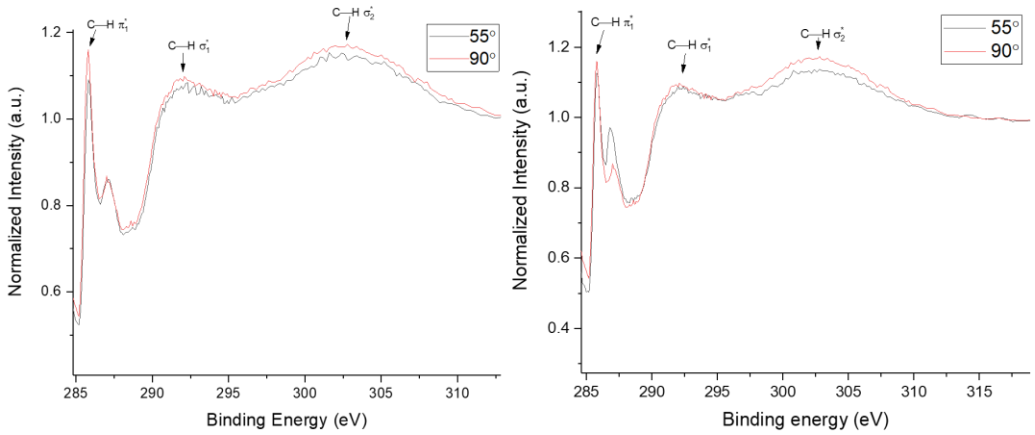

Figure A28: Normalized NEXAFS spectra of compound **2.4a** prepared from the $CHCl_3$:ODCB solvent system on ITO/ZnO a) as-cast and annealed at 150 ˚C

Compound 2.4c:

As-cast thin film:

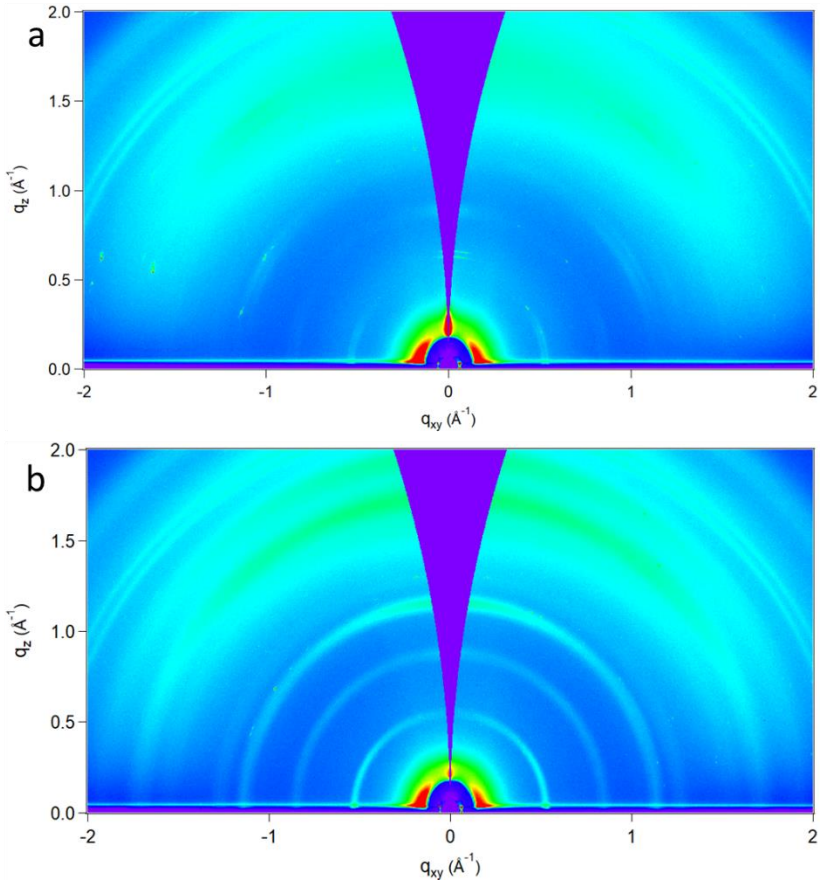

Figure A29: 2-D qzqxy patterns of compound **2.4c** thin film from $CHCl_3$:ODCB on ITO/ZnO, a) un-annealed film, b) thin film annealed at 150 ˚C

Annealed Thin Films:

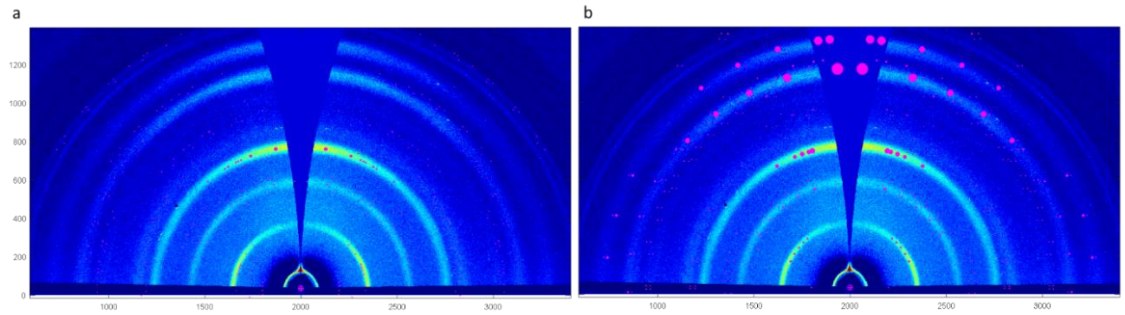

Figure A30: The 2-D diffraction patterns of compound **2.4c** thin films prepared from $CHCl_3$:ODCB on ITO/ZnO annealed at 150 ˚C and the overlaid modeled diffraction patterns a) 11ī plane tilted from 40 to 60˚ b) 200 plane tilted from 40 to 60˚.

Solvent effects:

Compound 2.4a on SiO_2 and ITO/ZnO as-cast and annealed:

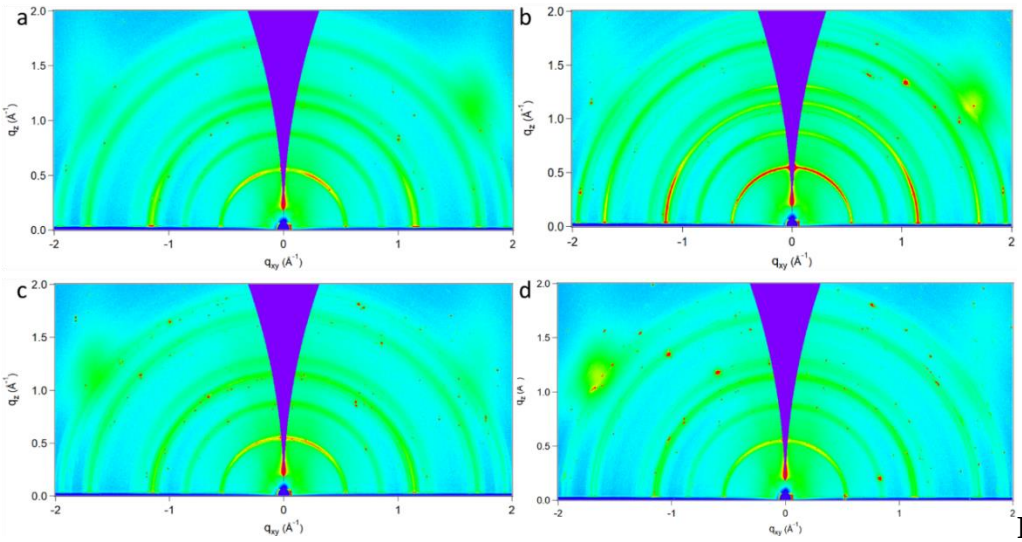

Figure A31: 2-D qzqxy patterns of compound **2.4a** thin film from MeTHF:toluene on Si/SiO_2 20 mg/ml, a) as-cast film b) film annealed at 60 ˚C c) thin film annealed at 100 ˚C d) thin film annealed at 150 ˚C

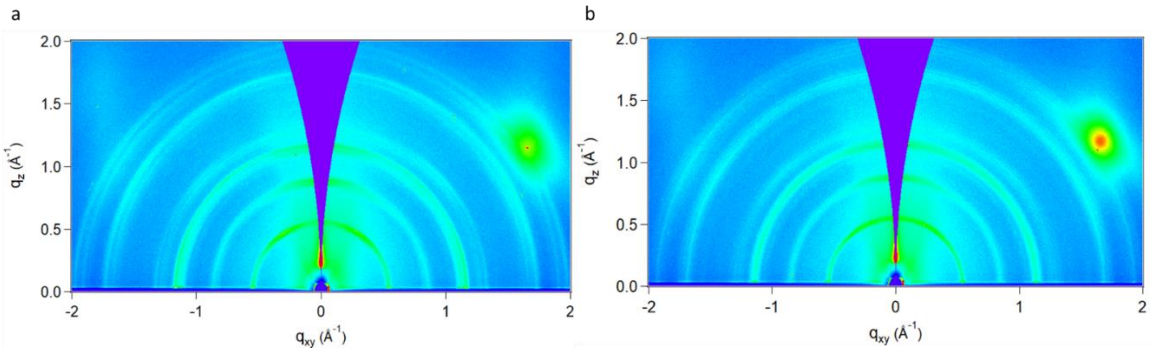

Figure A32: 2-D qzqxy patterns of compound **2.4a** thin film from MeTHF:toluene on Si/SiO_2 10 mg/ml, a) as-cast film, b) thin film annealed at 150 ˚C

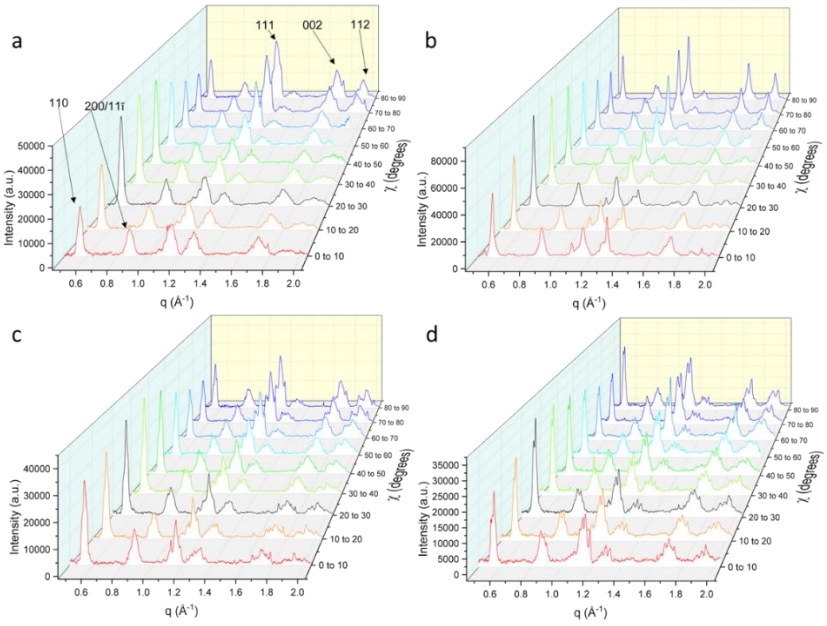

Figure A33: Waterfall plots of I vs q form 0 to 90˚ of compound **2.4a** thin films produced from MeTHF:toluene on Si/SiO_2, a) as-cast, b) annealed at 60 ˚C, c) annealed at 100 ˚C, d) annealed at 150 ˚C

Compound 2.4c on Si/SiO_2 and ITO/ZnO as-cast and annealed:

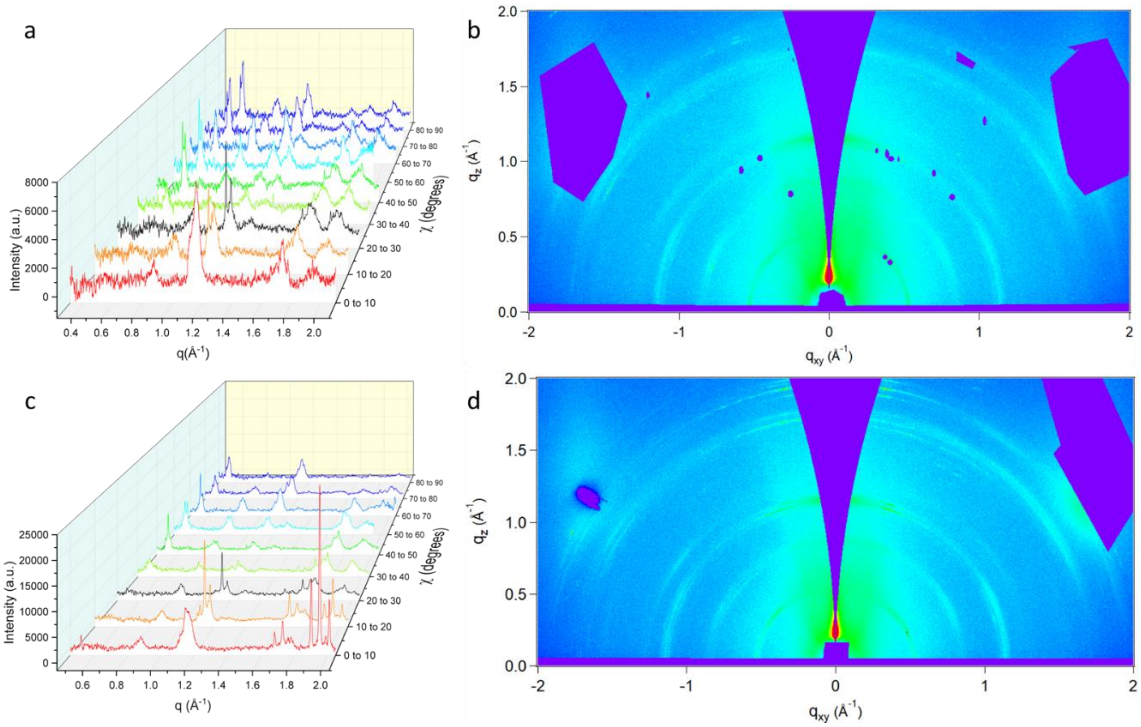

Figure A34: Data of 2- diffraction patterns of thinfilms of compound **2.4c** prepared from MeTHF:toluene on Si/SiO_2; as-cast thin films a) I vs q waterfall pot b) 2-D qzqxy diffraction pattern; thin films annealed at 150 ˚C c) I vs q waterfall pot d) 2-D qzqxy diffraction pattern; thin films annealed at 150 ˚C

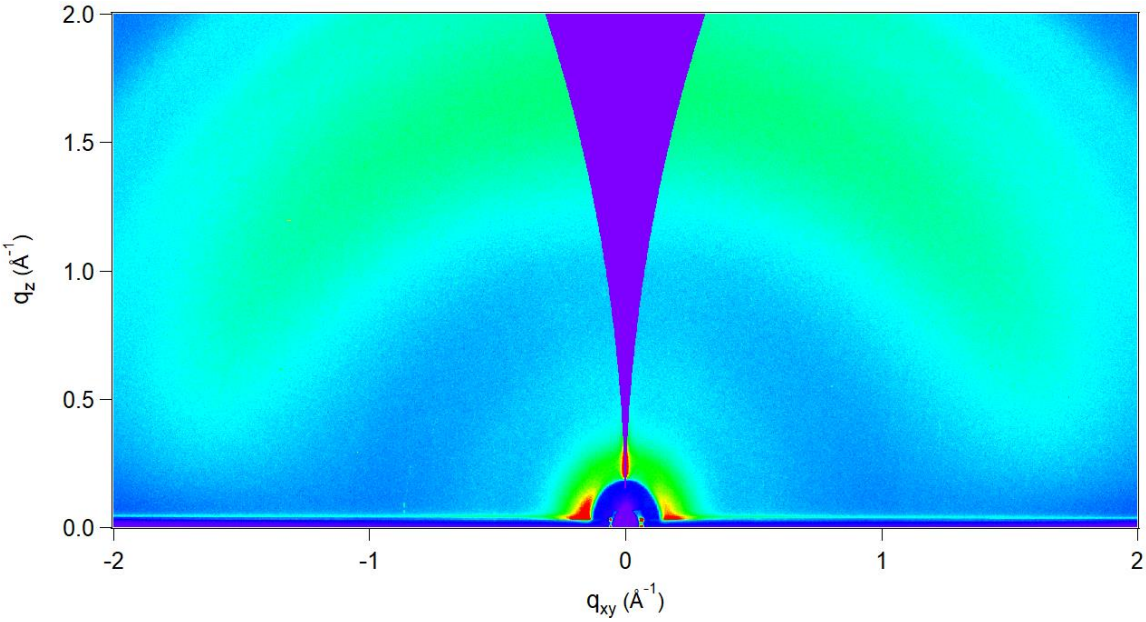

Figure A35: 2-D qzqxy patterns of compound **2.4c** thin film from 10mg/ml solution MeTHF:toluene on ITO/ZnO, 10 mgl/ml, as-cast film

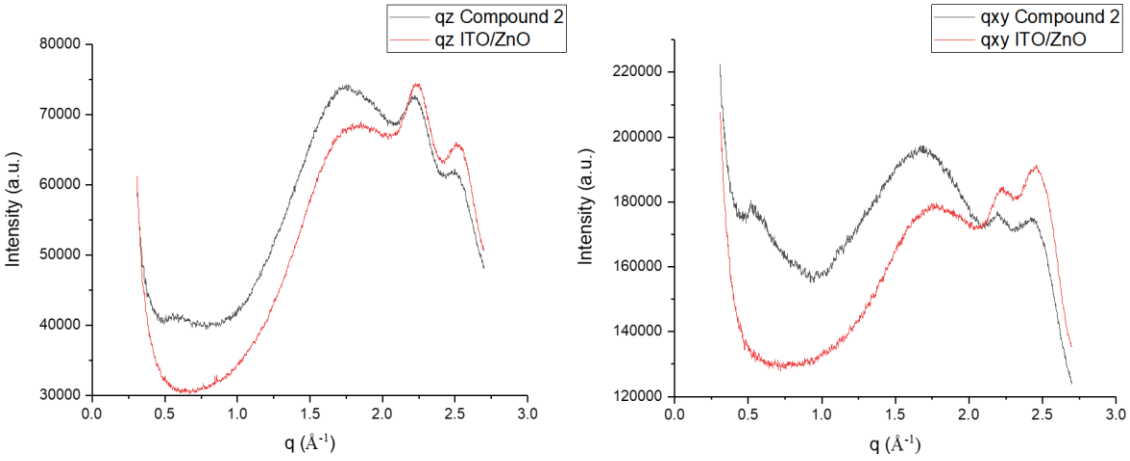

Figure A36: I vs q graphs of thin films of compound **2.4c** prepared from 10 mg/ml solution in MeTHF:toluene from χ = 0 to 20˚ and χ = 70 to 90˚, black, overlaid with I vs q graphs of blank ITO/ZnO from from χ = 0 to 20˚ and χ = 70 to 90˚, red.

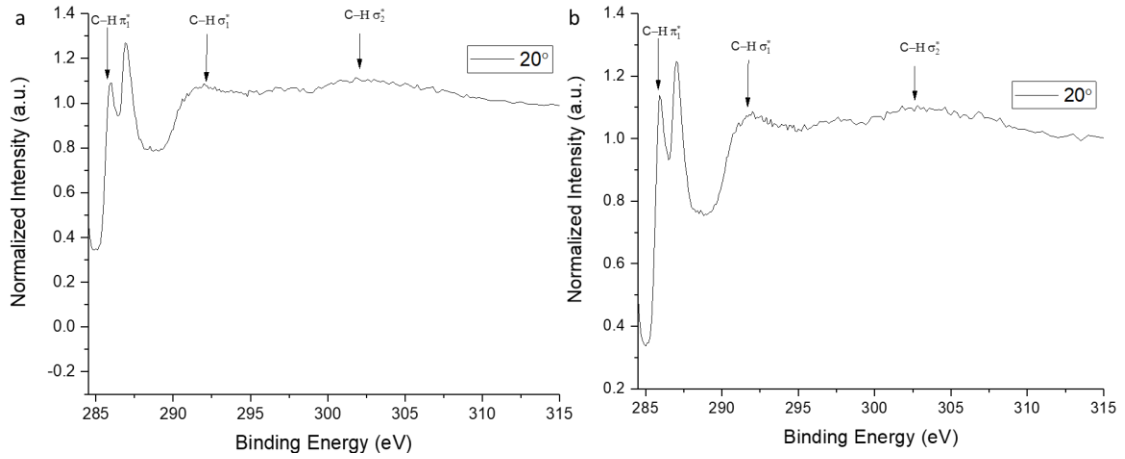

Figure A37: Shows the normalized NEXAFS data for incident angles of 20; of a) the as-cast thin films of compound **2.4b** on Si/SiO_2 and b) the 150 ˚C annealed thin films of compound **2.4b** on Si/SiO_2.

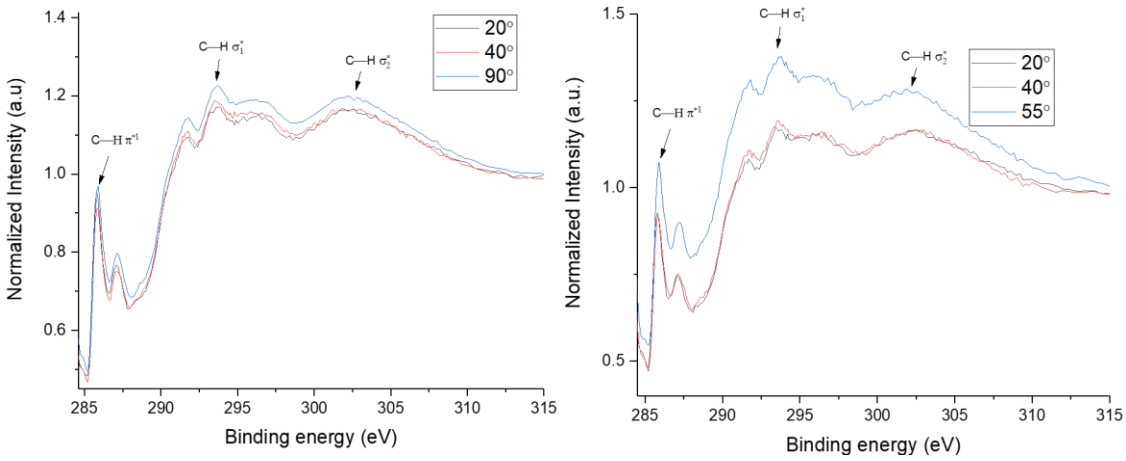

Figure A38: Shows the normalized NEXAFS data for incident angles; of a) of 20, 40, and 90˚ for the as-cast thin films of compound **2.4d** on Si/SiO_2 and b) of 20, 40, 55 and for the 150 ˚C annealed thin films of compound **2.4d** on Si/SiO_2.

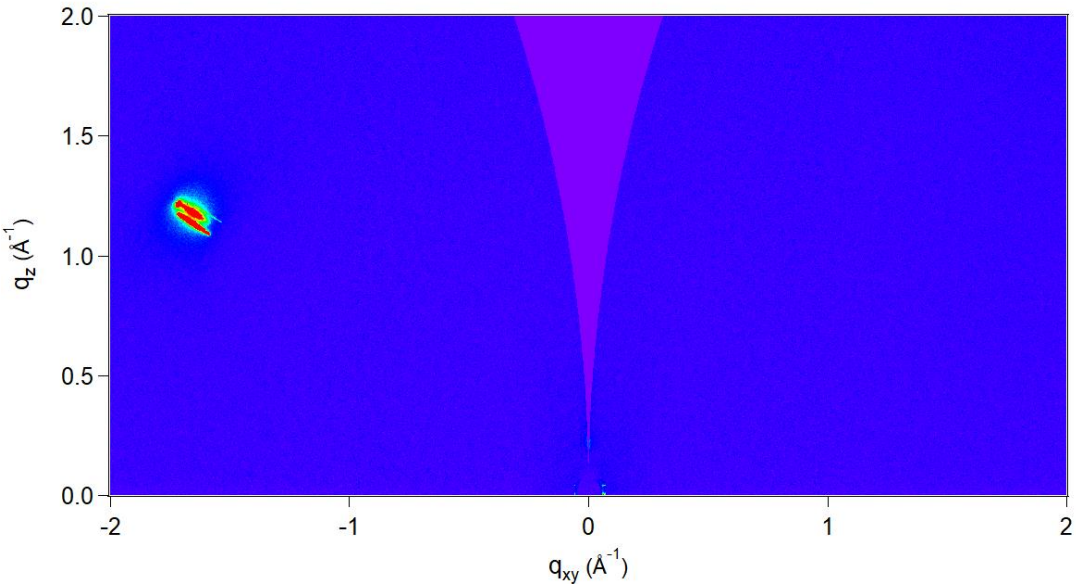

Figure A39: 2-D diffraction pattern of Si/SiO_2 substrate Blank

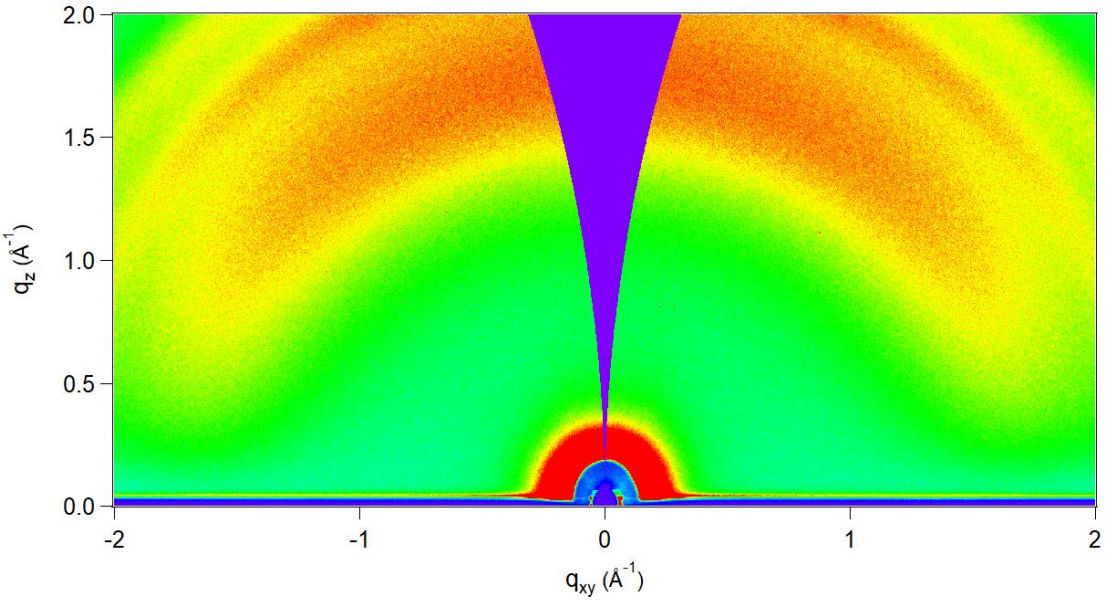

Figure A40: 2-D diffraction pattern of ITO/ZnO substrate blank.

Table A2: A summary of OPV parameters for ITO/ZnO/compound **2.4a**/MoO_3/Ag. Devices were prepared from 10 or 20 mg/ml solution of either (2:3) $CHCl_3$:ODBC or (2:3) MeTHF:toluene. Four different film processing temperatures were tested, as-cast, annealed at 60, 100 and 150 ˚C. J_{sc} is the short-circuit current, V_{oc} is the open-circuit voltage, and P_{max} is the maximum power output.

(2:3) $CHCl_3$:ODCB				
20mg/ml	J_{sc} (mA/cm$_2$)	V_{oc} (V)	P_{max} (mW/cm$_2$)	Fill Factor
as-cast	-3.15E-03	2.27E-05	0.00E+00	0.00E+00
Annealed 60 ˚C	-3.21E-03	6.67E-05	0.00E+00	0.00E+00
Annealed 100 ˚C	-2.12E-03	4.00E-03	-1.56E-06	5.78E-02
Annealed 150 ˚C	-4.67E-03	7.47E-05	0.00E+00	0.00E+00
10mg/ml				
As-cast	-7.42E-03	1.75E-03	0.00E+00	0.00E+00
Annealed 60 ˚C	-4.45E-03	2.78E-05	0.00E+00	0.00E+00
Annealed 100 ˚C	-8.96E-03	0.00E+00	0.00E+00	0.00E+00
Annealed 150 ˚C	-7.92E-03	1.29E-05	0.00E+00	0.00E+00
(2:3) MeTHF:Toluene				
20mg/ml	J_{sc} (mA/cm$_2$)	V_{oc} (V)	P_{max} (mW/cm$_2$)	Fill Factor
As-cast	-6.25E-03	6.69E-05	0.00E+00	0.00E+00
Annealed 60 ˚C	-3.14E-03	6.03E-02	-2.31E-05	7.30E-02
Annealed 100 ˚C	-6.47E-03	7.41E-05	0.00E+00	0.00E+00
Annealed 150 ˚C	-8.57E-03	3.58E-05	0.00E+00	0.00E+00
10mg/ml				
As-cast	-3.05E-03	2.73E-04	0.00E+00	0.00E+00
Annealed 60 ˚C	-7.57E-03	2.66E-05	0.00E+00	0.00E+00
Annealed 100 ˚C	-6.38E-03	4.30E-02	-6.21E-05	1.35E-01
Annealed 150 ˚C	-8.49E-03	2.50E-05	0.00E+00	0.00E+00

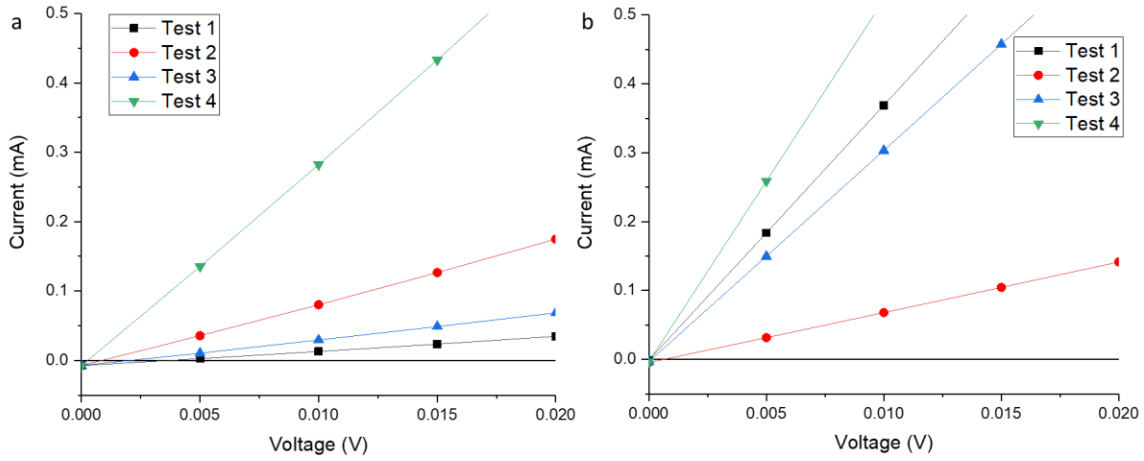

Figure A41: I-V experiments for OPVs using as-cast **2.4a** as the active layer molecule prepared from a) 10 mg/ml **2.4a** in (2:3) $CHCl_3$:ODCB b) 10 mg/ml **2.4a** in (2:3) MeTHF:toluene.

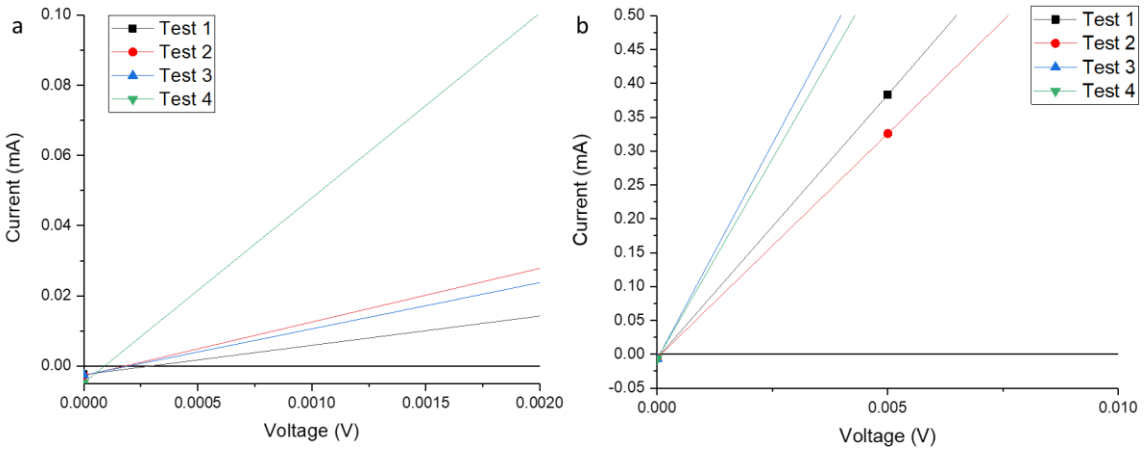

Figure A42: I-V experiments for OPVs using as-cast **2.4a** as the active layer molecule prepared from a) 20 mg/ml **2.4a** in (2:3) $CHCl_3$:ODCB b) 20 mg/ml **2.4a** in (2:3) MeTHF:toluene.

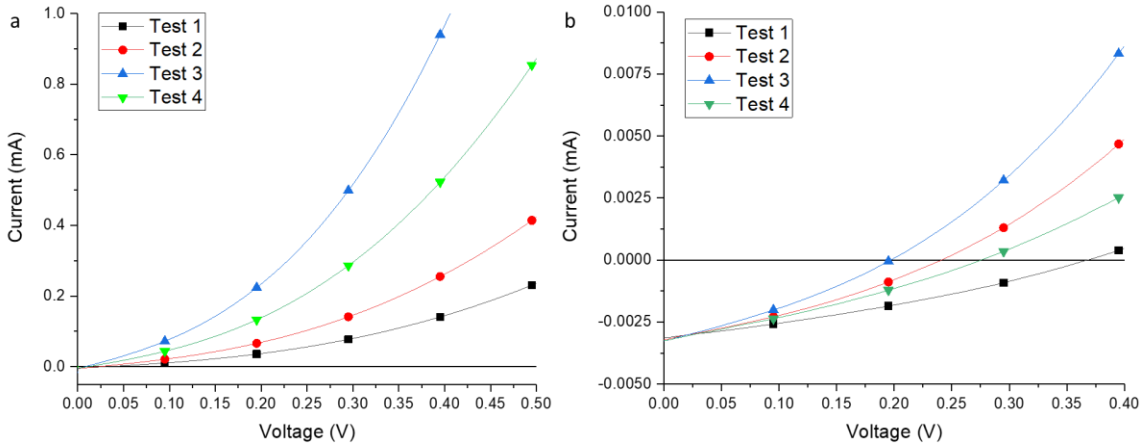

Figure A43: I-V experiments for OPVs using as-cast **2.4b** as the active layer molecule prepared from a) 10 mg/ml **2.4b** in (2:3) $CHCl_3$:ODCB b) 10 mg/ml **2.4b** in (2:3) MeTHF:toluene.

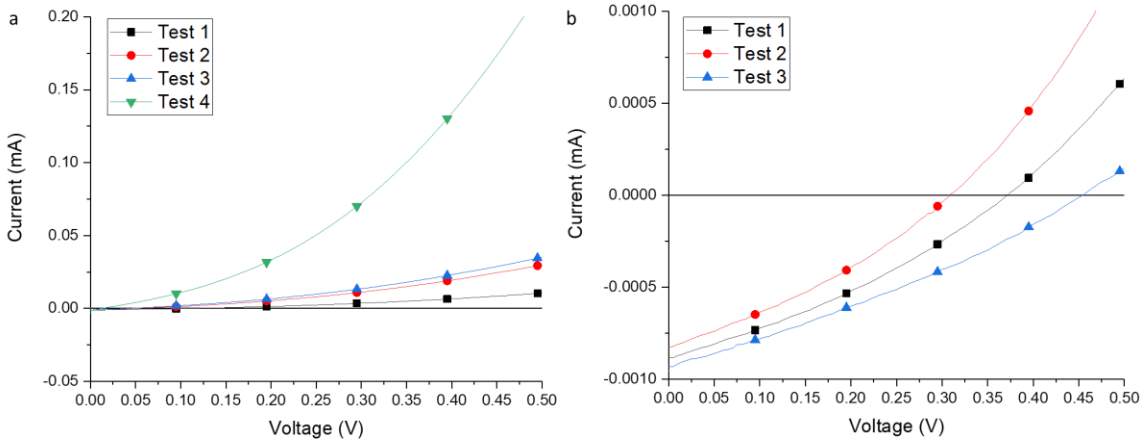

Figure A44: I-V experiments for OPVs using as-cast **2.4b** as the active layer molecule prepared from a) 20 mg/ml **2.4b** in (2:3) $CHCl_3$:ODCB b) 10 mg/ml **2.4b** in (2:3) MeTHF:toluene.

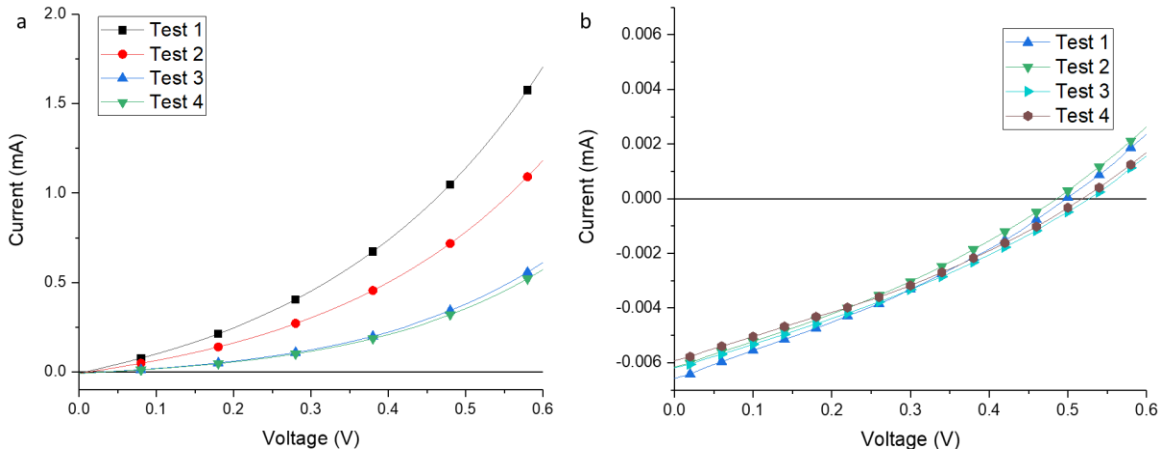

Figure A45: I-V experiments for OPVs using as-cast **2.4c** as the active layer molecule prepared from a) 10 mg/ml **2.4c** in (2:3) $CHCl_3$:ODCB b) 10 mg/ml **2.4c** in (2:3) MeTHF:toluene.

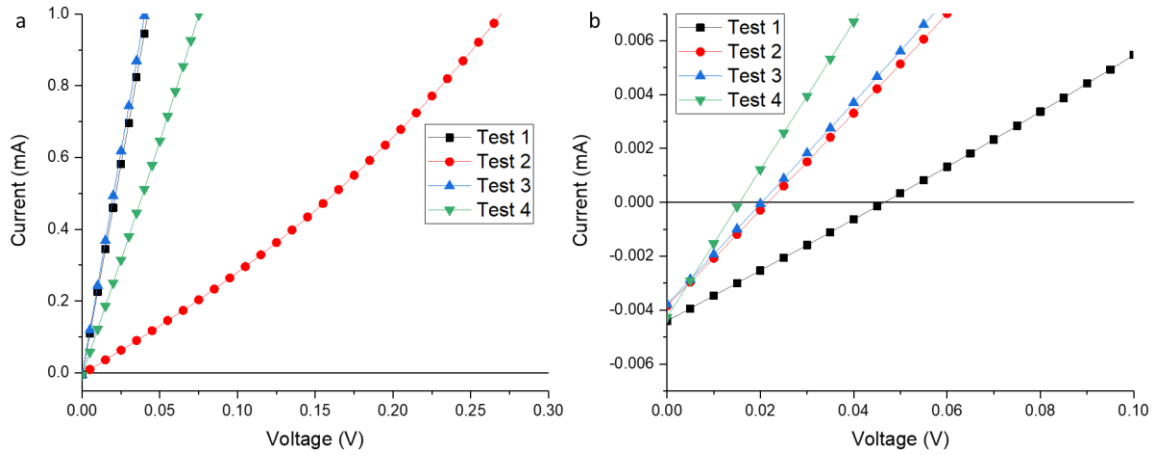

Figure A46: I-V experiments for OPVs using as-cast **2.4c** as the active layer molecule prepared from a) 20 mg/ml **2.4c** in (2:3) $CHCl_3$:ODCB b) 20 mg/ml **2.4c** in (2:3) MeTHF:toluene.

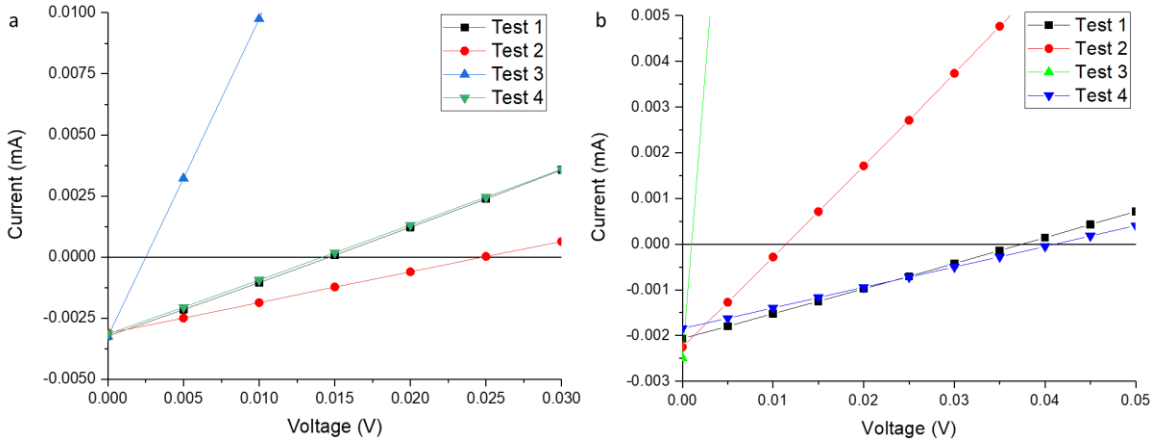

Figure A47: I-V experiments for OPVs using as-cast **2.4d** as the active layer molecule prepared from a) 10 mg/ml **2.4d** in (2:3) $CHCl_3$:ODCB b) 10 mg/ml **2.4d** in (2:3) MeTHF:toluene.

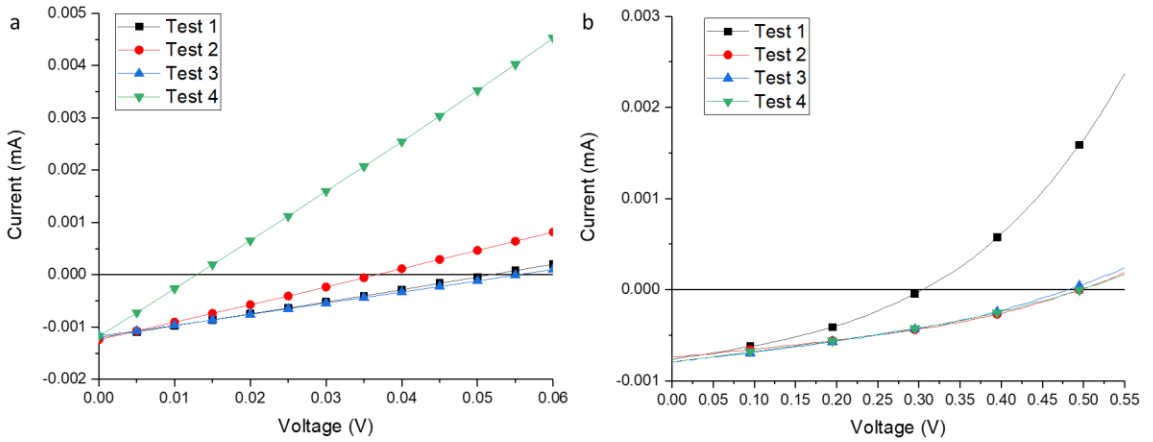

Figure A48: I-V experiments for OPVs using as-cast **2.4d** as the active layer molecule prepared from a) 20 mg/ml **2.4d** in (2:3) $CHCl_3$:ODCB b) 20 mg/ml **2.4d** in (2:3) MeTHF:toluene.

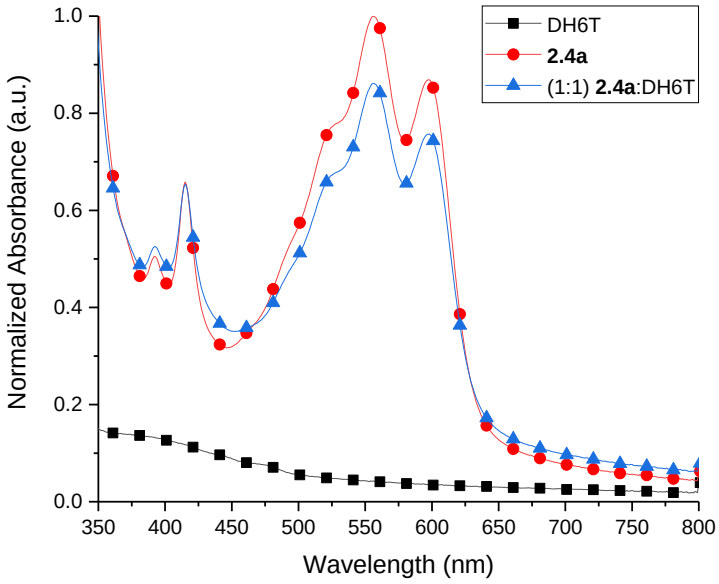

Figure A49: Absorption spectra of thin films neat DH6T, neat **2.4a**, and mixed (1:1) **2.4a**:DH6T

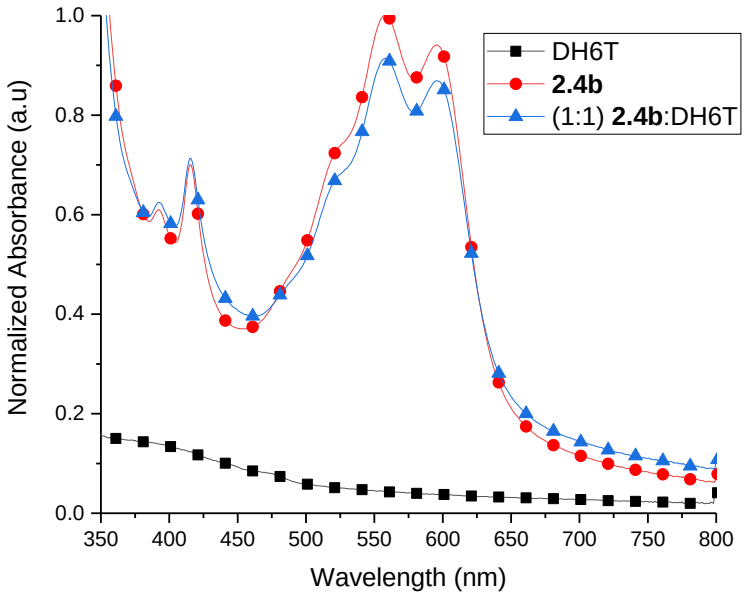

Figure A50: Absorption spectra of thin films neat DH6T, neat **2.4b**, and mixed (1:1) **2.4b**:DH6T

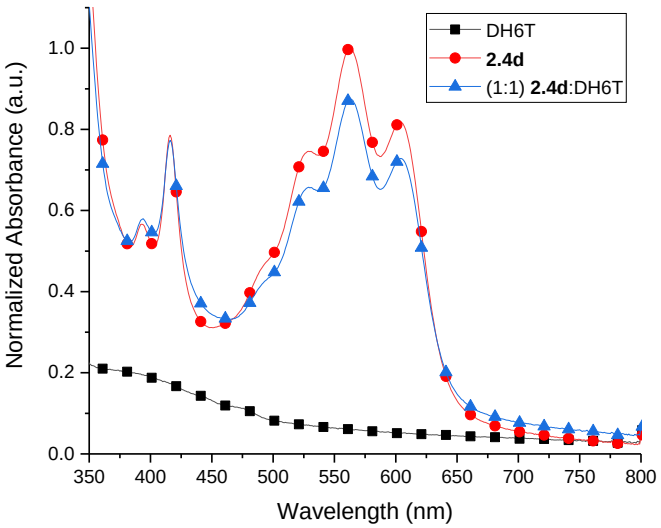

Figure A51: Absorption spectra of thin films neat DH6T, neat **2.4d**, and mixed (1:1) **2.4d**:DH6T

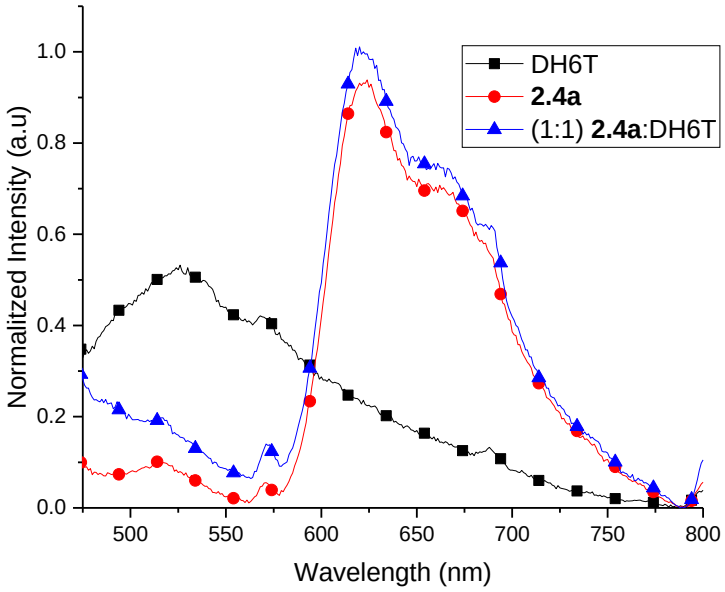

Figure A52: Fluorescence spectra of thin films neat DH6T, neat **2.4a**, and mixed (1:1) **2.4a**:DH6T

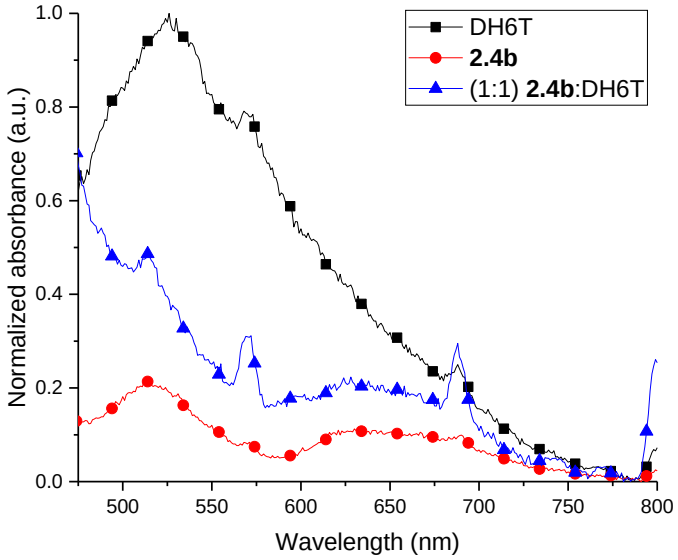

Figure A53: Fluorescence spectra of thin films neat DH6T, neat **2.4b**, and mixed (1:1) **2.4b**:DH6T

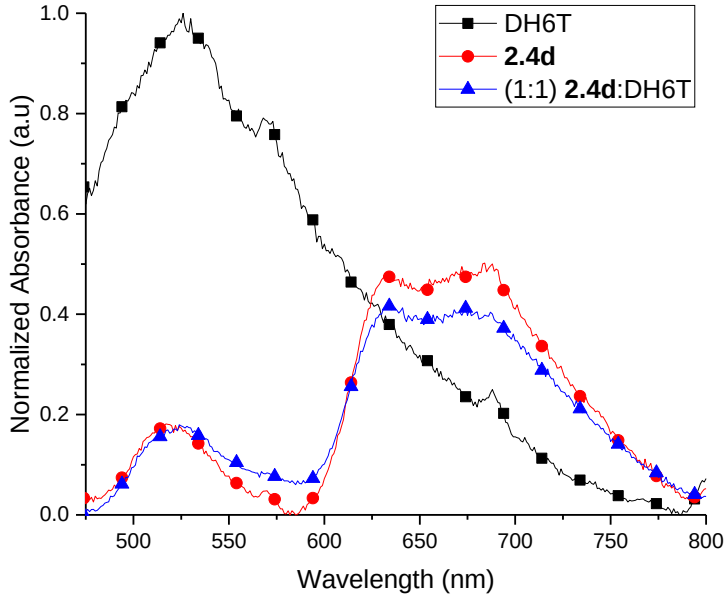

Figure A54: Fluorescence spectra of thin films neat DH6T, neat **2.4d**, and mixed (1:1) **2.4d**:DH6T

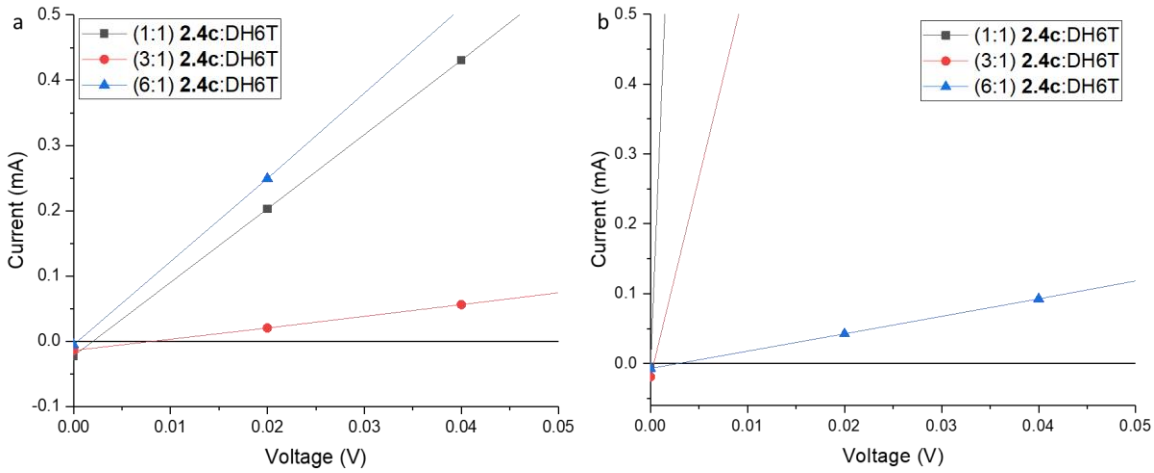

Figure A55: I-V curves for BHJ small molecule organic solar using **2.4c** as the electron acceptor and DH6T as the electron donor, ITO/ZnO/**2.4c**:DH6T/MoO_3/Ag

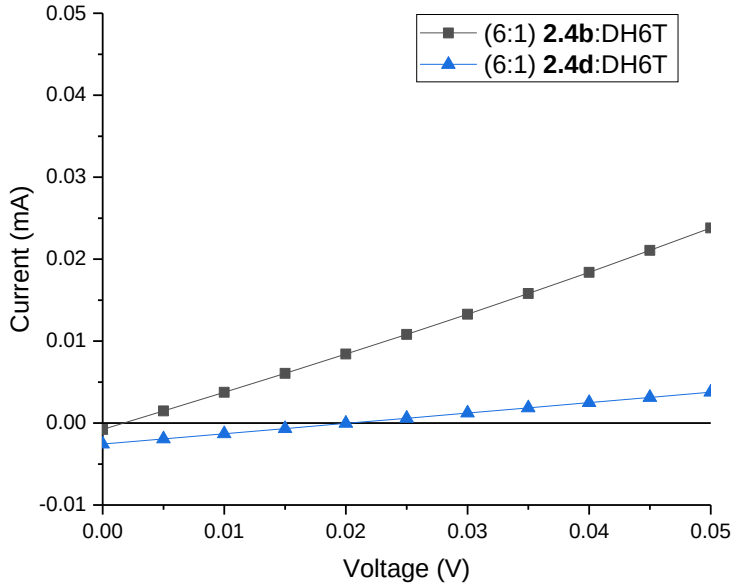

Figure A56: I-V curves for BHJ small molecule organic solar using **2.4b** or **d** as the electron acceptor and DH6T as the electron donor, ITO/ZnO/**2.4b** or **2.4d**:DH6T/MoO_3/Ag

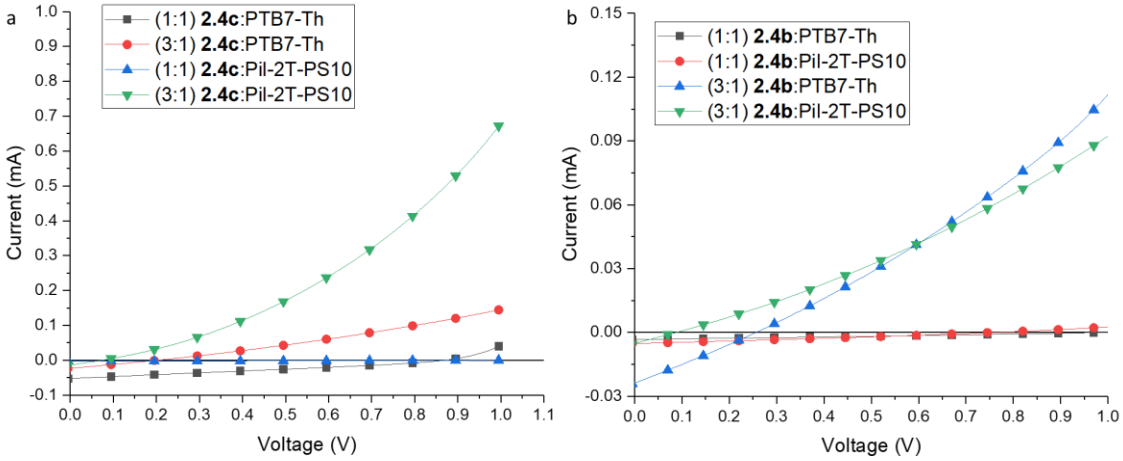

Figure A57: I-V curves for BHJ small molecule organic solar using; a) **2.4c** as the electron acceptor and PTB7-Th or PiI-2T-PS10 as the electron donor, ITO/ZnO/**2.4c**: PTB7-Th or PiI-2T-PS10 /MoO_3/Ag b) **2.4b** as the electron acceptor and PTB7-Th or PiI-2T-PS10 as the electron donor, ITO/ZnO/**2.4b**: PTB7-Th or PiI-2T-PS10 /MoO_3/Ag

9,10-diphenylindeno[1,2,3-*fg*]tetracene (2.4a):

X-ray CIF Atomic connectivity and bond lengths

C8 C7 1.425(2)

C8 C9 1.4326(12)

C8 C9 1.4326(12) 2_556

C9 C10 1.4175(14)

C9 C11 1.4959(14)

C7 C6 1.4096(13)

C7 C6 1.4097(13) 2_556

C5 C6 1.3952(14)

C5 C4 1.4312(14)

C5 C10 1.4490(15)

C10 C1 1.4383(14)

C6 C17 1.4758(14)

C11 C16 1.3891(15)

C11 C12 1.3945(15)

C1 C2 1.3616(16)

C1 H1 0.9500

C2 C3 1.4171(17)

C2 H2 0.9500

C16 C15 1.3877(15)

C16 H16 0.9500

C12 C13 1.3858(16)

C12 H12 0.9500

C3 C4 1.3561(16)

C3 H3 0.9500

C4 H4 0.9500

C14 C15 1.3830(17)

C14 C13 1.3862(17)

C14 H14 0.9500

C13 H13 0.9500

C18 C19 1.3901(16)

C18 C17 1.3951(15)

C18 H18 0.9500

C15 H15 0.9500

C19 C19 1.381(3) 2_556

C19 H19 0.9500

C17 C17 1.418(2) 2_556

2-methyl-10-phenyl-9-(*p*-tolyl)indeno[1,2,3-*fg*]tetracene (2.4b)

X-ray CIF Atomic connectivity and bond lengths

C1 C2 1.361(4)

C1 C18 1.435(3)

C1 H1A 0.9300

C2 C3 1.389(4)

C2 H2A 0.9300

C3 C4 1.350(3)

C3 H3A 0.9300

C4 C5 1.442(3)

C4 H4A 0.9300

C5 C6 1.408(3)

C5 C18 1.440(3)

C6 C7 1.428(3)

C6 C25 1.437(16)

C6 C25" 1.536(13)

C7 C16 1.419(3)

C7 C8 1.428(3)

C8 C9 1.409(3)

C8 C31" 1.410(18)

C8 C31 1.567(17)

C9 C10 1.425(3)

C9 C14 1.455(3)

C10 C11 1.360(3)

C10 H10A 0.9300

C11 C12 1.404(3)

C11 H11A 0.9300

C12 C13 1.354(3)

C12 H12A 0.9300

C13 C14 1.425(3)

C13 H13A 0.9300

C14 C15 1.392(3)

C15 C16 1.408(3)

C15 C24 1.480(3)

C16 C17 1.413(3)

C17 C18 1.392(3)

C17 C19 1.468(3)

C19 C20 1.389(3)

C19 C24 1.414(3)

C20 C21 1.357(4)

C20 H20A 0.9300

C21 C22 1.383(4)

C21 C38" 1.460(12)

C21 H21 1.15(5)

C22 C23 1.424(4)

C22 C38 1.469(4)

C22 H22 1.099(5)

C23 C24 1.386(3)

C23 H23A 0.9300

C25 C30 1.377(11)

C25 C26 1.389(11)

C26 C27 1.377(13)

C26 H26A 0.9300

C27 C28 1.370(13)

C27 H27A 0.9300

C28 C29 1.374(13)

C28 H28A 0.9300

C29 C30 1.392(12)

C29 H29A 0.9300

C30 H30A 0.9300

C31 C32 1.384(11)

C31 C36 1.402(10)

C32 C33 1.393(11)

C32 H32A 0.9300

C33 C34 1.368(14)

C33 H33A 0.9300

C34 C35 1.368(14)

C34 H34A 0.9300

C35 C36 1.399(11)

C35 H35A 0.9300

C36 H36A 0.9300

C25" C30" 1.377(11)

C25" C26" 1.381(11)

C26" C27" 1.378(12)

C26" H26B 0.9300

C27" C28" 1.372(13)

C27" H27B 0.9300

C28" C29" 1.374(13)

C28" H28B 0.9300

C29" C30" 1.394(9)

C29" H29B 0.9300

C30" H30B 0.9300

C31" C32" 1.377(12)

C31" C36" 1.400(11)

C32" C33" 1.388(12)

C32" H32B 0.9300

C33" C34" 1.367(14)

C33" H33B 0.9300

C34" C35" 1.374(14)

C34" H34B 1.101(5)

C35" C36" 1.404(12)

C35" H35B 0.9300

C36" H36B 0.9300

C37 H37B 1.0949

C37 H37C 1.0949

C37 H37A 1.0950

C37 H37J 1.0950

C37 H37K 1.0948

C37 H37L 1.0951

C37B H37D 1.0949

C37B H37E 1.0949

C37B H37F 1.0949

C37B H37M 1.0950

C37B H37N 1.0950

C37B H37O 1.0950

C37" H37H 1.0949

C37" H37G 1.0948

C37" H37I 1.0946

C37" H37P 1.0945

C37" H37Q 1.0948

C37" H37R 1.0954

C38 H22 0.628(5)

C38 H38A 0.9600

C38 H38B 0.9600

C38 H38C 0.9600

C38 H38J 0.9600

C38 H38K 0.9600

C38 H38L 0.9600

C38" H21 0.31(5)

C38" H38D 0.9600

C38" H38E 0.9600

C38" H38F 0.9600

C38" H38M 0.9600

C38" H38N 0.9600

C38" H38O 0.9600

2-fluoro-9-(4-fluorophenyl)-10-phenylindeno[1,2,3-*fg*]tetracene (2.4c):

X-ray CIF Atomic connectivity and bond lengths

C2 F2 1.313(2)

C2 C3 1.3811(19)

C2 C9 1.3851(19)

C2 H02 1.14(11)

C3 C4 1.3882(16)

C3 H11 0.9500

C4 C5 1.3942(16)

C4 H13 0.9500

C5 C8 1.4003(16)

C5 C6 1.4941(15)

C6 C10 1.4198(15)

C6 C7 1.4371(12)

C7 C17 1.426(2)

C7 C6 1.4372(12) 2_656

C8 C9 1.3876(17)

C8 H12 0.9500

C9 H3 0.9500

C10 C15 1.4424(16)

C10 C11 1.4511(16)

C11 C16 1.3976(16)

C11 C12 1.4360(16)

C12 C13 1.3591(18)

C12 H4 0.9500

C13 C14 1.4185(19)

C13 H5 0.9500

C14 C15 1.3606(17)

C14 H7 0.9500

C15 H6 0.9500

C16 C17 1.4132(14)

C16 C18 1.4750(15)

C17 C16 1.4131(14) 2_656

C18 C19 1.3958(16)

C18 C18 1.422(2) 2_656

C19 C20 1.3882(18)

C19 H8 0.9500

C20 C20 1.373(3) 2_656

C20 F1 1.386(2)

C20 H01 0.9386

10-phenyl-2-(trifluoromethyl)-9-(4-(trifluoromethyl)phenyl)indeno[1,2,3-*fg*]tetracene (2.4d):

X-ray CIF Atomic connectivity and bond lengths

C00C C00E 1.404(4)

C00C C00D 1.423(4)

C00C C00J 1.428(4)

C00D C00S 1.395(4)

C00D C013 1.474(4)

C00E C00Y 1.403(4)

C00E C00T 1.475(4)

C00F C00N 1.395(4)

C00F C01H 1.428(4)

C00F C014 1.452(4)

C00G C00W 1.411(4)

C00G C00N 1.418(4)

C00G C00Q 1.418(4)

C00H C01V 1.383(4)

C00H C019 1.386(4)

C00H C012 1.501(4)

C00I C00V 1.408(4)

C00I C00Q 1.438(4)

C00I C00K 1.497(4)

C00J C015 1.427(4)

C00J C00U 1.430(4)

C00K C01N 1.380(5)

C00K C00P 1.381(4)

C00L C01C 1.390(4)

C00L C00X 1.426(4)

C00L C00W 1.476(4)

C00M C015 1.419(4)

C00M C01F 1.435(4)

C00M C00S 1.453(4)

C00N C00X 1.464(4)

C00O C017 1.352(4)

C00O C00S 1.435(4)

C00O H00O 0.9500

C00P C01E 1.384(4)

C00P H00P 0.9500

C00Q C012 1.426(4)

C00R C023 1.380(5)

C00R C01K 1.386(4)

C00R C015 1.507(4)

C00T C01I 1.387(4)

C00T C013 1.428(4)

C00U C011 1.408(4)

C00U C00Z 1.508(4)

C00V C01B 1.438(4)

C00V C010 1.446(4)

C00W C010 1.404(4)

C00X C01P 1.396(4)

C00Y C01X 1.419(4)

C00Y C011 1.455(4)

C00Z C01Q 1.384(5)

C00Z C02D 1.386(5)

C010 C01M 1.429(4)

C011 C01Y 1.437(4)

C012 C014 1.420(4)

C013 C01A 1.393(4)

C014 C01Z 1.430(4)

C016 C018 1.382(5)

C016 C01A 1.393(4)

C016 H016 0.9500

C017 C01R 1.415(4)

C017 H017 0.9500

C018 C01I 1.407(4)

C018 C02C 1.487(4)

C019 C01T 1.387(4)

C019 H019 0.9500

C01A H01A 0.9500

C01B C01W 1.362(4)

C01B H01B 0.9500

C01C C01J 1.394(4)

C01C H01C 0.9500

C01D C01G 1.379(5)

C01D C01V 1.388(4)

C01D H01D 0.9500

C01E C01U 1.387(5)

C01E H01E 0.9500

C01F C01R 1.365(4)

C01F H01F 0.9500

C01G C01T 1.387(5)

C01G C02E 1.485(5)

C01H C026 1.357(4)

C01H H01H 0.9500

C01I H01I 0.9500

C01J C01O 1.389(4)

C01J C025 1.488(4)

C01K C01S 1.393(4)

C01K H01K 0.9500

C01L C01S 1.377(5)

C01L C029 1.377(5)

C01L C02F 1.493(4)

C01M C021 1.358(4)

C01M H01M 0.9500

C01N C022 1.386(5)

C01N H01N 0.9500

C01O C01P 1.382(4)

C01O H01O 0.9500

C01P H01P 0.9500

C01Q C028 1.397(4)

C01Q H01Q 0.9500

C01R H01R 0.9500

C01S H01S 0.9500

C01T H01T 0.9500

C01U C022 1.380(5)

C01U H01U 0.9500

C01V H01V 0.9500

C01W C021 1.419(5)

C01W H01W 0.9500

C01X C02A 1.365(5)

C01X H01X 0.9500

C01Y C027 1.352(5)

C01Y H01Y 0.9500

C01Z C024 1.362(5)

C01Z H01Z 0.9500

C021 H021 0.9500

C022 H022 0.9500

C023 C029 1.385(4)

C023 H023 0.9500

C024 C026 1.410(5)

C024 H024 0.9500

C025 F9 1.150(13)

C025 F6B 1.174(15)

C025 F8B 1.301(11)

C025 F8 1.313(10)

C025 F6 1.405(11)

C025 F9B 1.454(10)

C026 H026 0.9500

C027 C02A 1.408(5)

C027 H027 0.9500

C028 C02B 1.376(5)

C028 H028 0.9500

C029 H029 0.9500

C02A H02A 0.9500

C02B C02G 1.382(6)

C02B H02B 0.9500

C02C F2B 1.172(14)

C02C F7B 1.29(2)

C02C F3B 1.296(16)

C02C F7 1.34(2)

C02C F3 1.345(14)

C02C F2 1.439(12)

C02D C02G 1.387(5)

C02D H02D 0.9500

C02E F4 1.240(16)

C02E F5 1.314(14)

C02E F1 1.319(18)

C02E F1B 1.332(14)

C02E F5B 1.349(13)

C02E F4B 1.392(13)

C02F F11B 1.25(2)

C02F F10 1.279(17)

C02F F12B 1.329(18)

C02F F10B 1.338(17)

C02F F12 1.345(15)

C02F F11 1.41(2)

F11B F12B 1.63(3)

C02G H02G 0.9500

2-methoxy-9-(4-methoxyphenyl)-10-phenylindeno[1,2,3-*fg*]tetracene (2.4e):

X-ray CIF Atomic connectivity and bond lengths

O1 C22 1.365(5)

O1 C37 1.435(6)

O2 C28 1.368(5)

O2 C38 1.435(5)

C12 C13 1.416(5)

C12 C7 1.431(5)

C12 C11 1.446(6)

C16 C15 1.410(6)

C16 C17 1.434(6)

C16 C3 1.445(6)

C19 C20 1.393(5)

C19 C24 1.420(6)

C19 C4 1.470(5)

C14 C5 1.417(5)

C14 C13 1.432(6)

C14 C15 1.435(6)

C7 C6 1.395(6)

C7 C8 1.423(6)

C24 C23 1.390(5)

C24 C6 1.476(5)

C31 C36 1.395(6)

C31 C32 1.399(6)

C31 C13 1.485(5)

C25 C26 1.387(6)

C25 C30 1.394(6)

C25 C15 1.488(5)

C11 C10 1.347(6)

C11 H11 0.9500

C26 C27 1.378(6)

C26 H26 0.9500

C10 C9 1.403(6)

C10 H10 0.9500

C23 C22 1.385(6)

C23 H23 0.9500

C28 C29 1.382(6)

C28 C27 1.389(6)

C17 C18 1.356(6)

C17 H17 0.9500

C8 C9 1.344(6)

C8 H8 0.9500

C22 C21 1.389(6)

C6 C5 1.405(5)

C20 C21 1.380(5)

C20 H20 0.9500

C21 H21 0.9500

C36 C35 1.382(6)

C36 H36 0.9500

C30 C29 1.378(6)

C30 H30 0.9500

C9 H9 0.9500

C18 C1 1.415(6)

C18 H18 0.9500

C29 H29 0.9500

C34 C33 1.381(6)

C34 C35 1.383(6)

C34 H34 0.9500

C35 H35 0.9500

C38 H38A 0.9800

C38 H38B 0.9800

C38 H38C 0.9800

C32 C33 1.378(5)

C32 H32 0.9500

C33 H33 0.9500

C27 H27 0.9500

C37 H37A 0.9800

C37 H37B 0.9800

C37 H37C 0.9800

C1 C2 1.346(6)

C1 H1 0.9500

C5 C4 1.410(6)

C4 C3 1.379(6)

C2 C3 1.434(6)

C2 H2 0.9500

9-(4-fluorophenyl)-10-phenylindeno[1,2,3-fg]tetracene (2.4.1):

X-ray CIF Atomic connectivity and bond lengths

C001 C004 1.410(3)

C001 C004 1.410(3) 2_656

C001 C002 1.423(3)

C002 C006 1.432(3) 2_656

C002 C006 1.432(3)

C003 C010 1.394(2)

C003 C003 1.420(4) 2_656

C003 C004 1.469(2)

C004 C007 1.395(3)

C005 C006 1.416(3)

C005 C00B 1.437(3) 2_656

C005 C007 1.446(2) 2_656

C006 C009 1.489(2)

C007 C00D 1.433(3)

C007 C005 1.446(2) 2_656

C008 C00F 1.383(2)

C008 C009 1.388(3)

C008 H008 0.9500

C009 C00C 1.395(3)

C010 C00E 1.389(3)

C010 H00A 0.9500

C00B C00G 1.361(3)

C00B C005 1.437(3) 2_656

C00B H00B 0.9500

C00C C00J 1.381(3)

C00C H00C 0.9500

C00D C00H 1.353(3)

C00D H00D 0.9500

C00E C00E 1.382(4) 2_656

C00E H00E 0.9500

C00F C00I 1.375(3)

C00F H00F 0.9500

C00G C00H 1.413(3)

C00G H00G 0.9500

C00H H00H 0.9500

C00I F0K 1.323(4)

C00I C00J 1.375(3)

C00I H16 0.9500

C00J H00J 0.9500

5,12-bis(3,5-bis(trifluoromethyl)phenyl)-6,11-bis(3,5-dimethylphenyl)tetracene (4.1.2.1):

X-ray CIF Atomic connectivity and bond lengths

C1 C2 1.346(7)

C1 C13 1.438(6)

C1 H1 0.9500

C2 C3 1.417(9)

C2 H2 0.9500

C3 C4 1.358(7)

C3 H3 0.9500

C4 C14 1.436(6)

C4 H4 0.9500

C14 C5 1.406(6)

C14 C13 1.437(7)

C5 C16 1.435(5)

C5 C25 1.494(6)

C16 C6 1.424(5)

C16 C15 1.445(5)

C6 C18 1.400(5)

C6 C37 1.489(5)

C18 C7 1.434(5)

C18 C17 1.445(5)

C7 C8 1.362(6)

C7 H7 0.9500

C8 C9 1.413(7)

C8 H8 0.9500

C9 C10 1.352(6)

C9 H9 0.9500

C10 C17 1.427(5)

C10 H10 0.9500

C17 C11 1.403(5)

C11 C15 1.420(5)

C11 C31 1.503(5)

C15 C12 1.425(5)

C12 C13 1.394(6)

C12 C19 1.495(6)

C25 C26 1.392(7)

C25 C30 1.398(6)

C26 C27 1.382(8)

C26 H26 0.9500

C27 C28 1.393(8)

C27 C50 1.510(9)

C28 C29 1.381(9)

C28 H28 0.9500

C29 C30 1.388(8)

C29 C49 1.516(8)

C30 H30 0.9500

C37 C38 1.382(6)

C37 C42 1.391(6)

C38 C39 1.392(6)

C38 H38 0.9500

C39 C40 1.384(7)

C39 C48 1.503(8)

C40 C41 1.390(7)

C40 H40 0.9500

C41 C42 1.395(6)

C41 C47 1.492(7)

C42 H42 0.9500

C31 C32 1.387(5)

C31 C36 1.394(6)

C32 C33 1.389(5)

C32 H32 0.9500

C33 C34 1.388(6)

C33 C46 1.505(6)

C34 C35 1.384(6)

C34 H34 0.9500

C35 C36 1.394(6)

C35 C45 1.494(7)

C36 H36 0.9500

C19 C24 1.390(6)

C19 C20 1.400(6)

C20 C21 1.383(8)

C20 H20 0.9500

C21 C22 1.399(9)

C21 C44 1.512(8)

C22 C23 1.377(8)

C22 H22 0.9500

C23 C24 1.394(7)

C23 C43 1.519(9)

C24 H24 0.9500

C50 F50D 0.97(4)

C50 F50B 1.07(3)

C50 F50C 1.28(4)

C50 F50A 1.44(4)

C50 H50A 0.9800

C50 H50B 0.9801

C50 H50C 0.9799

F50A F50B 1.62(7)

C49 F49C 1.12(2)

C49 F49A 1.42(3)

C49 F49B 1.49(3)

C49 H49A 0.9778

C49 H49B 0.9772

C49 H49C 0.9802

C48 F48F 1.284(9)

C48 F48D 1.328(7)

C48 F48E 1.358(9)

C48 H48A 0.9799

C48 H48B 0.9800

C48 H48C 0.9801

C47 F47C 1.218(9)

C47 F47A 1.238(8)

C47 F47B 1.255(11)

C47 F47E 1.337(14)

C47 H47A 0.9799

C47 H47B 0.9799

C47 H47C 0.9798

F47A F47B 1.756(16)

F47B F47C 1.730(16)

C46 F46A 1.321(6)

C46 F46C 1.325(6)

C46 F46E 1.331(6)

C46 H46A 0.9798

C46 H46B 0.9800

C46 H46C 0.9801

C45 F45B 1.300(9)

C45 F45A 1.315(8)

C45 F45C 1.317(7)

C45 H45A 0.9799

C45 H45B 0.9800

C45 H45C 0.9800

C44 F44A 1.01(3)

C44 F44C 1.18(3)

C44 F44B 1.32(3)

C44 H44A 0.9799

C44 H44B 0.9801

C44 H44C 0.9799

C43 F43B 1.11(2)

C43 F43A 1.38(3)

C43 F43C 1.69(3)

C43 H43A 0.9801

C43 H43B 0.9800

C43 H43C 0.9799

C1' C2' 1.354(6)

C1' C13' 1.436(6)

C1' H1' 0.9500

C2' C3' 1.428(6)

C2' H2' 0.9500

C3' C4' 1.357(6)

C3' H3' 0.9500

C4' C14' 1.444(5)

C4' H4' 0.9500

C14' C5' 1.391(5)

C14' C13' 1.445(5)

C5' C16' 1.426(5)

C5' C25' 1.502(5)

C16' C6' 1.435(5)

C16' C15' 1.445(5)

C6' C18' 1.391(5)

C6' C37' 1.499(6)

C18' C7' 1.437(5)

C18' C17' 1.444(6)

C7' C8' 1.350(6)

C7' H7' 0.9500

C8' C9' 1.419(7)

C8' H8' 0.9500

C9' C10' 1.354(7)

C9' H9' 0.9500

C10' C17' 1.427(6)

C10' H10' 0.9500

C17' C11' 1.409(6)

C11' C15' 1.413(5)

C11' C31' 1.499(6)

C15' C12' 1.429(5)

C12' C13' 1.392(6)

C12' C19' 1.503(6)

C25' C26' 1.383(6)

C25' C30' 1.403(5)

C26' C27' 1.395(6)

C26' H26' 0.9500

C27' C28' 1.384(6)

C27' C50' 1.513(7)

C28' C29' 1.393(6)

C28' H28' 0.9500

C29' C30' 1.388(6)

C29' C49' 1.504(6)

C30' H30' 0.9500

C37' C42' 1.386(6)

C37' C38' 1.388(6)

C38' C39' 1.392(7)

C38' H38' 0.9500

C39' C40' 1.376(7)

C39' C48' 1.504(7)

C40' C41' 1.391(7)

C40' H40' 0.9500

C41' C42' 1.388(7)

C41' C47' 1.508(7)

C42' H42' 0.9500

C31' C36' 1.384(6)

C31' C32' 1.397(6)

C32' C33' 1.390(7)

C32' H32' 0.9500

C33' C34' 1.397(8)

C33' C46' 1.509(8)

C34' C35' 1.372(8)

C34' H34' 0.9500

C35' C36' 1.403(7)

C35' C45' 1.508(8)

C36' H36' 0.9500

C19' C20' 1.389(6)

C19' C24' 1.394(7)

C20' C21' 1.391(6)

C20' H20' 0.9500

C21' C22' 1.377(8)

C21' C44' 1.519(7)

C22' C23' 1.394(8)

C22' H22' 0.9500

C23' C24' 1.388(7)

C23' C43' 1.508(8)

C24' H24' 0.9500

C50' F50G 1.256(10)

C50' F50H 1.271(12)

C50' F50I 1.301(11)

C50' H50D 0.9804

C50' H50E 0.9795

C50' H50F 0.9799

C49' F49H 1.213(9)

C49' F49G 1.370(10)

C49' F49I 1.406(12)

C49' H49D 0.9799

C49' H49E 0.9804

C49' H49F 0.9800

C48' F48K 1.289(9)

C48' F48J 1.305(9)

C48' F48L 1.417(11)

C48' H48D 0.9801

C48' H48E 0.9800

C48' H48F 0.9792

C47' F47K 1.258(9)

C47' F47J 1.280(10)

C47' F47L 1.373(9)

C47' H47D 0.9807

C47' H47E 0.9796

C47' H47F 0.9800

C46' F46G 1.177(11)

C46' F46H 1.315(12)

C46' F46I 1.361(14)

C46' F47J 1.440(14)

C46' H46D 0.9797

C46' H46E 0.9803

C46' H46F 0.9801

F46G F46I 1.729(18)

F46H F46I 1.765(18)

C45' F45G 1.234(11)

C45' F45I 1.250(11)

C45' F45H 1.355(10)

C45' H45D 0.9799

C45' H45E 0.9799

C45' H45F 0.9803

C44' F44I 1.119(11)

C44' F44G 1.311(12)

C44' F44H 1.379(14)

C44' H44D 0.9801

C44' H44E 0.9800

C44' H44F 0.9799

C43' F43I 1.039(13)

C43' F43H 1.416(14)

C43' F43G 1.616(16)

C43' H43D 0.9801

C43' H43E 0.9801

C43' H43F 0.9800

6,11-dihydroxynaphtho[2,3-*g*]quinoline-5,12-dione (5.1.2.5):

X-ray CIF Atomic connectivity and bond lengths

N1 C1 1.373(3)

N1 C5 1.384(2)

C1 C2 1.388(3)

C1 H1 0.9500

C2 C3 1.374(3)

C2 H2 0.9500

C3 C4 1.402(2)

C3 H3 0.9500

C4 C5 1.405(2)

C4 C8 1.457(2) 3_677

C5 C6 1.464(2)

C3' C1' 1.373(3)

C3' C5' 1.384(2)

C1' C2' 1.388(3)

C1' H1B 0.9500

C2' N1' 1.374(3)

C2' H2B 0.9500

N1' C4' 1.402(2)

C4' C5' 1.405(2)

C4' C8 1.457(2) 3_677

C5' C6 1.464(2)

C6 O1 1.2879(18)

C6 C7 1.417(2)

C7 C8 1.421(2)

C7 C7 1.441(3) 3_677

C8 O2 1.2877(19)

C8 C4' 1.457(2) 3_677

C8 C4 1.457(2) 3_677

O1 H4 1.33(4)

O2 H4 1.26(4)

6,11-dihydroxynaphtho[2,3-*g*]quinoline-5,12-dione (5.1.2.5):

CIFcheck

checkCIF/PLATON report

Structure factors have been supplied for datablock(s) 15187a

THIS REPORT IS FOR GUIDANCE ONLY. IF USED AS PART OF A REVIEW PROCEDURE

FOR PUBLICATION, IT SHOULD NOT REPLACE THE EXPERTISE OF AN EXPERIENCED

CRYSTALLOGRAPHIC REFEREE.

No syntax errors found. CIF dictionary Interpreting this report

Datablock: 15187a

Bond precision: C-C = 0.0019 A Wavelength=1.54178

Cell: a=3.6627(3) b=8.9442(7) c=18.3416(13)

alpha=90 beta=95.046(3) gamma=90

Temperature: 123 K

Calculated Reported

Volume 598.54(8) 598.54(8)

Space group P 21/n P 21/n

Hall group -P 2yn -P 2yn

Moiety formula C16 H7.44 N2 O4 C17H9O4

Sum formula C16 H7.44 N2 O4 C17 H9 N O4

Mr 291.68 291.25

Dx,g cm-3 1.618 1.616

Z 2 2

Mu (mm-1) 1.004 0.977

F000 298.9 300.0

F000’ 299.93

h,k,lmax 4,11,22 4,11,22

Nref 1235 1219

Tmin,Tmax 0.584,0.990 0.736,0.968

Tmin’ 0.359

Correction method= # Reported T Limits: Tmin=0.736 Tmax=0.968

AbsCorr = MULTI-SCAN

Data completeness= 0.987 Theta(max)= 74.829

R(reflections)= 0.0503(1063) wR2(reflections)= 0.1479(1219)

S = 1.122 Npar= 110

The following ALERTS were generated. Each ALERT has the format

test-name_ALERT_alert-type_alert-level.

Click on the hyperlinks for more details of the test.

Alert level C

PLAT041_ALERT_1_C Calc. and Reported SumFormula Strings Differ Please Check

PLAT043_ALERT_1_C Calculated and Reported Mol. Weight Differ by .. 0.43 Check

PLAT250_ALERT_2_C Large U3/U1 Ratio for Average U(i,j) Tensor .... 2.3 Note

PLAT303_ALERT_2_C Full Occupancy Atom H4 with # Connections 2.00 Check

PLAT772_ALERT_2_C Suspect O-H Bond in CIF: O1 --H4 .. 1.33 Ang.

PLAT911_ALERT_3_C Missing FCF Refl Between Thmin & STh/L= 0.600 8 Report

Alert level G

FORMU01_ALERT_1_G There is a discrepancy between the atom counts in the

_chemical_formula_sum and _chemical_formula_moiety. This is

usually due to the moiety formula being in the wrong format.

Atom count from _chemical_formula_sum: C17 H9 N1 O4

Atom count from _chemical_formula_moiety:C17 H9 O4

FORMU01_ALERT_2_G There is a discrepancy between the atom counts in the

_chemical_formula_sum and the formula from the _atom_site* data.

Atom count from _chemical_formula_sum:C17 H9 N1 O4

Atom count from the _atom_site data: C16 H7.44 N2 O4

CELLZ01_ALERT_1_G Difference between formula and atom_site contents detected.

CELLZ01_ALERT_1_G ALERT: Large difference may be due to a

symmetry error - see SYMMG tests

From the CIF: _cell_formula_units_Z 2

From the CIF: _chemical_formula_sum C17 H9 N O4

TEST: Compare cell contents of formula and atom_site data

atom Z*formula cif sites diff

C 34.00 32.00 2.00

H 18.00 14.88 3.12

N 2.00 4.00 -2.00

O 8.00 8.00 0.00

PLAT042_ALERT_1_G Calc. and Reported MoietyFormula Strings Differ Please Check

PLAT063_ALERT_4_G Crystal Size Likely too Large for Beam Size .... 1.00 mm

PLAT171_ALERT_4_G The CIF-Embedded .res File Contains EADP Records 6 Report

PLAT301_ALERT_3_G Main Residue Disorder .....(Resd 1) 51% Note

PLAT304_ALERT_4_G Non-Integer Number of Atoms in ..... Resd 1 29.44 Check

PLAT333_ALERT_2_G Large Aver C6-Ring C-C Dist. C4 -C8_a 1.43 Ang.

PLAT333_ALERT_2_G Large Aver C6-Ring C-C Dist. C6 -C5' 1.43 Ang.

PLAT333_ALERT_2_G Large Aver C6-Ring C-C Dist. C7 -C7_a 1.43 Ang.

PLAT811_ALERT_5_G No ADDSYM Analysis: Too Many Excluded Atoms .... ! Info

PLAT912_ALERT_4_G Missing # of FCF Reflections Above STh/L= 0.600 9 Note

PLAT978_ALERT_2_G Number C-C Bonds with Positive Residual Density. 6 Info

0 **ALERT level A** = Most likely a serious problem - resolve or explain

0 **ALERT level B** = A potentially serious problem, consider carefully

6 **ALERT level C** = Check. Ensure it is not caused by an omission or oversight

15 **ALERT level G** = General information/check it is not something unexpected

6 ALERT type 1 CIF construction/syntax error, inconsistent or missing data

8 ALERT type 2 Indicator that the structure model may be wrong or deficient

2 ALERT type 3 Indicator that the structure quality may be low

4 ALERT type 4 Improvement, methodology, query or suggestion

1 ALERT type 5 Informative message, check

Validation response form

Please find below a validation response form (VRF) that can be filled in and pasted into your CIF.

start Validation Reply Form

_vrf_PLAT041_15187a

;

PROBLEM: Calc. and Reported SumFormula Strings Differ Please Check

RESPONSE: ...

;

_vrf_PLAT043_15187a

;

PROBLEM: Calculated and Reported Mol. Weight Differ by .. 0.43 Check

RESPONSE: ...

;

_vrf_PLAT250_15187a

;

PROBLEM: Large U3/U1 Ratio for Average U(i,j) Tensor .... 2.3 Note

RESPONSE: ...

;

_vrf_PLAT303_15187a

;

PROBLEM: Full Occupancy Atom H4 with # Connections 2.00 Check

RESPONSE: ...

;

_vrf_PLAT772_15187a

;

PROBLEM: Suspect O-H Bond in CIF: O1 --H4 .. 1.33 Ang.

RESPONSE: ...

;

_vrf_PLAT911_15187a

;

PROBLEM: Missing FCF Refl Between Thmin & STh/L= 0.600 8 Report

RESPONSE: ...

;

end Validation Reply Form

It is advisable to attempt to resolve as many as possible of the alerts in all categories. Often the

minor alerts point to easily fixed oversights, errors and omissions in your CIF or refinement

strategy, so attention to these fine details can be worthwhile. In order to resolve some of the more

serious problems it may be necessary to carry out additional measurements or structure

refinements. However, the purpose of your study may justify the reported deviations and the more

serious of these should normally be commented upon in the discussion or experimental section of a

paper or in the "special_details" fields of the CIF. checkCIF was carefully designed to identify

outliers and unusual parameters, but every test has its limitations and alerts that are not important

in a particular case may appear. Conversely, the absence of alerts does not guarantee there are no

aspects of the results needing attention. It is up to the individual to critically assess their own

results and, if necessary, seek expert advice.

Publication of your CIF in IUCr journals

A basic structural check has been run on your CIF. These basic checks will be run on all CIFs

submitted for publication in IUCr journals (*Acta Crystallographica*, *Journal of Applied*

Crystallography, *Journal of Synchrotron Radiation*); however, if you intend to submit to *Acta*

Crystallographica Section C or *E* or *IUCrData*, you should make sure that full publication checks

are run on the final version of your CIF prior to submission.

Publication of your CIF in other journals

Please refer to the *Notes for Authors* of the relevant journal for any special instructions relating to

CIF submission.

PLATON version of 30/01/2018; check.def file version of 30/01/2018

Datablock 15187a - ellipsoid plot